Molecular Modeling of Ions in Biological Systems

Esam Abd El-Malek Abd-Allah Orabi

A Thesis

in

The Department

of

Chemistry and Biochemistry

Presented in Partial Fulfillment of the Requirements

For the Degree of

Doctor of Philosophy (Chemistry) at

Concordia University

Montréal, Québec, Canada

April 2015

© Esam Abd El-Malek Abd-Allah Orabi, 2015

CONCORDIA UNIVERSITY
SCHOOL OF GRADUATE STUDIES

This is to certify that the thesis prepared

By: Esam Abd El-Malek Abd-Allah Orabi

Entitled: Molecular Modeling of Ions in Biological Systems

and submitted in partial fulfillment of the requirements for the degree of

Doctor of Philosophy (Chemistry)

complies with the regulations of the University and meets the accepted standards with respect to originality and quality.

Signed by the final examining committee:

_____ Chair
Dr. W. Zerges

_____ External Examiner
Dr. C.N. Rowley

_____ External to Program
Dr. L. Kalman

_____ Examiner
Dr. G.H. Peslherbe

_____ Examiner
Dr. P.D. Pawelek

_____ Thesis Supervisor
Dr. G. Lamoureux

Approved by: _____
Dr. C. Skinner, Graduate Program Director

April 10, 2015 _____
Dr. A. Roy, Dean
Faculty of Arts and Science

ABSTRACT

Molecular Modeling of Ions in Biological Systems

Esam Abd El-Malek Abd-Allah Orabi, Ph.D.

Concordia University, 2015

Ions are ubiquitous in biological systems. Metal ions contribute to biological function as counter ions, as triggers to cellular response, and as catalytic cofactors. They play structural roles and are part of the catalytic active site of metalloenzymes. NH_4^+ ions provide a source of nitrogen for amino acid synthesis in plants and bacteria and help maintaining the acid-base balance in mammals. The cationic side chains of amino acids Lys and Arg contribute to the stability of proteins and protein-DNA complexes through cation–π interactions with the π electrons of aromatic amino acids.

Developing molecular models for ion-protein interactions is required to investigate and understand the various biological functions of ions and to complement and interpret experimental data. In this regard, the aims of this thesis are to: 1- Investigate the selectivity of alkali ions toward N, O, and S-containing ligands (a step toward understanding protein selectivity to metal ions). 2- Optimize new semiempirical quantum mechanical models for calcium and magnesium metalloproteins. 3- Study the strength and directionality of cation–π interactions involving inorganic and organic cations interacting with model compounds of aromatic amino acid side chains in both gas phase and aqueous solution. 4- Investigate the selectivity and binding affinity of AmtB and RhCG ammonium transport proteins toward various ions and study the function of amino acids that line the transport pathway of these proteins.

Proteins bind metal ions through N, O, and S atoms from the side chains of the amino acids His, Asp, Glu, Ser, Tyr, Asn, Gln, Cys, and Met and from main chain carbonyl and amino groups. NH_3, H_2O, and H_2S are used as minimal models for N, O, and S ligands to investigate the selectivity of alkali metal ions. Polarizable potential models for NH_3 and H_2S that accurately reproduce the experimental properties of the pure and aqueous liquids are developed. The models are used, together with a previously developed model for water, to study the solvation structures and solvation free energies of the ions in the pure liquids and to investigate the selectivity of alkali ions toward the three ligands. The models yield solvation structures and solvation free energies in good agreement with experiments and show a selectivity of alkali ions toward the three ligands that follows the order $H_2O > NH_3 > H_2S$.

Magnesium and Calcium are two of the most bioavailable metals and are known to play roles in signal transduction and in muscular contraction and are cofactors in many enzymes. Semiempirical models are optimized for the two metals based on the ab initio structures and binding energies of complexes formed between Mg^{2+} and Ca^{2+} with ligands that model binding groups in biological and chemical systems. Optimized models are tested on the ab initio properties of ~170 ion-ligand binary and ion-water-ligand ternary complexes. Optimized models of Mg underestimate the binding energies of S-containing complexes but give structures and binding energies of other complexes in agreement with ab initio data. Models for Ca reproduce the ab initio properties of all complexes, including S complexes.

Cation–π interactions are common among protein structures and are believed to play key roles in stabilizing proteins and protein complexes with ligands and DNA. Polarizable potential models for the interaction of Rb^+, Cs^+, Tl^+, ammonium, tetramethylammonium, and tetraethylammonium with aromatic amino acid side chains are calibrated based on the ab initio properties of the different cation–π complexes. The models are used to study the binding affinity and complexation geometry of the different pairs in water. Results are showing that cation–π interactions persist in aqueous solutions and are stronger than charge-dipole interactions (such as interactions of Rb^+, Cs^+, Tl^+ with ethanol and acetamide). It is also found that cation–π complexes have geometries in aqueous solution similar to gas phase. In addition, results suggest that cation–π interactions influence the solubility of aromatic compounds in aqueous solutions.

Proteins of the Amt/Mep/Rh family —ammonium transporters (Amt) in plants and bacteria, methylamine permease (Mep) in yeast, and rhesus (Rh) blood-group associated glycoproteins in animals— facilitate the permeation of ammonium across cell membranes. Crystal structures of AmtB and RhCG proteins reveal structural differences along the transport pathways. Amt proteins are selective toward NH_4^+ over Na^+ and K^+, yet their activity can be inhibited by ions such as Cs^+ and Tl^+. Polarizable potential models for NH_3, NH_4^+, Na^+, K^+, Rb^+, Cs^+, and Tl^+ interacting with model compounds to side chains of amino acids that line the transport pathway are optimized. The models are used to calculate the binding affinity of both proteins toward the various ligands and to study the functional roles of amino acids along the transport pathway. Results show that among the various ligands, only Cs^+ and Tl^+ can compete with NH_4^+ for binding the two proteins and hence inhibit the protein activity. Results also show that the large hydrophobicity of the pore lumen in RhCG protein destabilizes NH_4^+ and water molecules in the pore which suggests a net NH_3 transport mechanism of the protein.

To My Wife and Daughters, My Mom and Dad, My Sisters and Brothers

Acknowledgements

The present study was carried out in the Department of Chemistry and Biochemistry at Concordia University, Montreal, Quebec, Canada during the period 5/2011−4/2015.

I am most grateful to my supervisor, Professor Guillaume Lamoureux for the chance to work in his laboratory and for his guidance and financial support throughout the course of this research. Especially, I am indebted for his time and effort during the writing of this thesis.

I wish to thank Professor Gilles H. Peslherbe and Professor Peter D. Pawelek for being on my research committee and for their helpful suggestions during the course of my research.

I sincerely thank all my friends and colleagues in the Centre for Research in Molecular Modeling (CERMM) for the friendly atmosphere and the useful scientific discussions. In particular I am thankful to Bharat Sharma for helping me with optimization of the semiempirical models for magnesium and calcium.

Great thanks to my brothers, Dr. Mohamed Orabi and Mr. Abd-Allah Orabi for their encouragements and support.

The financial support from Concordia University, PROTEO, and GEPROM and the computational facilities from CERMM and RQCHP are gratefully acknowledged.

I dedicate this thesis to my wife for her love, support, encouragement, and understanding during the course of my degree, to my lovely daughters (Nadeen, Yasmeen, and Leen), to my father's spirit, to my mother, and to my brothers and sisters.

TABLE OF CONTENTS

List of Figures

List of Tables

Abbreviations

Ach	Acetylcholine
AChE	Acetylcholinesterase
Ala	Alanine
AM1	Austin Model 1
Amt	Ammonium Transporters
Arg	Arginine
Asn	Asparagine
Asp	Aspartic acid
B3LYP	Becke, Three-parameter, Lee-Yang-Parr
BSSE	Basis Set Superposition Error
CCSD(T)	Coupled cluster theory with single, double, and perturbative triple excitations
CHARMM	Chemistry at HARvard Macromolecular Mechanics
CN	Coordination Numbers
CP	Counterpoise
CDS	Cambridge Structural Database
Cys	Cysteine
DMPC	Dimyristoylphosphatidylcholine
DNA	Deoxyribonucleic Acid
FC	Frozen Core
FEP	Free Energy Perturbation
FF	Force Field
Gln	Glutamine
Glu	Glutamic acid
Gly	Glycine
His	Histidine
HSAB	Hard and Soft Acids and Bases
Ile	Isoleucine
Leu	Leucine
LJ	Lennard-Jones

Lys	Lysine
MC	Monte Carlo
MD	Molecular Dynamics
Mep	Methylamine Permease
Met	Methionine
MM	Molecular Mechanics
MP2	Second-order Møller–Plesset Perturbation Theory
MSD	Mean Square Deviation
NDDO	Neglect of Diatomic Differential Overlap
NDIS	Neutron Diffraction with Isotropic H/D Substitution
NMA	N-methylacetamide
NPT	Isothermal-Isobaric Ensemble
NVE	Microcanonical Ensemble
NVT	Canonical Ensemble
PDB	Protein Data Bank
PESs	Potential Energy Surface
Phe	Phenylalanine
PIMC	Path integral Monte Carlo
PM	Polarizable Mechanics
QM	Quantum Mechanics
RDF	Radial Distribution Function
Rh	Rhesus
RNA	Ribonucleic Acid
SE	Semiempirical
Ser	Serine
SWM4-NDP	Simple Water Model with 4 sites and Negative Drude Polarizability
TEA	Tetraethylammonium
Thr	Threonine
TI	Thermodynamic Integration
TIP3P	Transferable Intermolecular Potential 3 Point
TMA	Tetramethylammonium

Trp	Tryptophan
TS	Transition State
Tyr	Tyrosine
Val	Valine
WHAM	Weighted Histogram Analysis Method

1. Introduction

1.1. Ions in Biological Systems

Ions are ubiquitous in biological systems. Depending on their concentration, inorganic ions are typically classified into bulk, trace, and ultra-trace ions. Bulk mineral ions (Na^+, K^+, Mg^{2+}, Ca^{2+}, Cl^-, and HPO_4^{-2}) regulate electric potentials across membranes and provide electrostatic stabilization of a large variety of biomolecules.[1,2] Some metal ions (such as Zn^{2+}, Fe^{II}/Fe^{III}, Cu^{I}/Cu^{II}) are required in only small or trace amounts and typically interact with specific proteins.[2] These ions (also K^+, Mg^{2+}, Ca^{2+}) activate or regulate the function of these proteins by causing a change in the structure and/or serving as catalytic centers for chemical reactions.[2] Although metal ions vary in their chemistry, in large concentrations one metal ion may compete for another metal ion's binding sites, which usually results in a less active or inactive system.[2] Organic ions in biological systems are typically due to the side chains of cationic amino acids (Arg, His, and Lys) and anionic amino acids (Asp and Glu). Interactions of these ions (electrostatic, salt-bridges, and hydrogen bonding) with one another and with other amino acids as well as interactions of inorganic ions with proteins contribute to protein stabilization, protein-protein interaction, and protein-ligand binding. Beside experimental measurements, an accurate understanding of the roles of various ions and their mechanism of action will require studies at the microscopic level, possible only using molecular modeling.

1.2. Selectivity of Metal Ions Toward Ligands

Metal ions vary in their selectivity toward ligands. This selectivity is commonly described by Pearson's principle of Hard and Soft Acids and Bases (HSAB).[3] Acids (metal ions) and bases (ligands) are classified as hard, soft, or borderline based on their polarizability. Acids or bases that are small with high charge density are considered non-polarizable and classified as "hard". Polarizable acids and bases are large in size with small charge density and are classified as "soft". Acids and bases with intermediate hard/soft character are classified as "borderline".[3,4] The HSAB principle predicts that hard acids (e.g. Li^+, Na^+, K^+, Be^{2+}, Mg^{2+}, Ca^{2+}, Al^{3+}, Co^{3+}, Fe^{3+}) prefer hard bases (e.g. H_2O, RO^-, CH_3COO^-, NH_3, RNH_2), soft acids (e.g. Cu^+, Ag^+, Tl^+, Hg^+, Pd^{2+}, Cd^{2+}, Pt^{2+}, Hg^{2+}) prefer soft bases (e.g. RSH, RS^-, R_2S, H_2S), and borderline acids (e.g. Fe^{2+}, Co^{2+}, Cu^{2+}, Zn^{2+}, Pb^{2+}) prefer borderline bases (e.g. NO_2^-, Br^-, imidazole). While Pearson's classification is a useful starting point for predicting the selectivity of metal ions

toward ligands with various donor groups, it does not provide quantitative information about this selectivity. For example, while the HSAB theory predicts that Ca^{2+} binds H_2O in preference to H_2S, it does not quantify the extent of selectivity, i.e. is H_2S totally expelled from the ion coordination sphere? And if not, how many H_2O vs H_2S can bind Ca^{2+} at the same time? In addition, selectivity of a metal ion toward ligands with similar polarizabilities is hard to predict. Furthermore, the mechanism of selectivity remains unclear. Using molecular modeling to investigate and understand the mechanism and extent of selectivity is critical for understanding the selectivity of biological systems toward metal ions.

1.3. Calcium and Magnesium Binding to Proteins

Metal ions are ubiquitous in biological systems. The most important of these are Na^+, K^+, Mg^{2+}, Ca^{2+}, Fe^{2+}/Fe^{3+}, Cu^+/Cu^{2+}, Zn^{2+}, and Co^{3+}. Calcium and magnesium represent the first and fourth most abundant metals in the human body.[2] Ca^{2+} plays a crucial role in the physiology and biochemistry of the cell, in signal transduction pathways, and in the contraction of all muscle cell types.[1,2] Many enzymes require Ca^{2+} as a cofactor and extracellular calcium is required for proper bone formation. Mg^{2+} is an essential mineral nutrient for life and stabilizes polyphosphate compounds in the cell.[1,2] Both Ca^{2+} and Mg^{2+} are hard metals and thus coordinate O, rather than S-containing ligands. The coordination geometry and the stability of their complexes are however different. Mg^{2+} commonly binds 6 ligands while Ca^{2+} binds 6–8 ligands, and the ligand exchange process is slower for Mg^{2+}.[2] Investigating the coordination geometry and ligand's dynamic and selectivity of the two ions is important to understand the role of the two ions in biological systems. For this purpose, theoretical models that reproduce the binding affinity of the two ions toward various ligands and that reproduce the structural geometry of these complexes are required.

1.4. Noncovalent Interactions

Noncovalent interactions do not require orbital overlap between interacting atoms, ions, or molecules. Examples of noncovalent interactions are: hydrogen bonding, ion-pairing (salt-bridge), π–π, anion–π, and cation–π interactions. Compared to covalent bonds, which are generally shorter than 2 Å, noncovalent interactions function within a range of several angstroms.[5] These interactions play major roles in stabilizing biological macromolecules (e.g. proteins, DNA, and RNA), in receptor-ligand interactions, enzyme-substrate binding, and in molecular recognition in general.[6]

Cation–π interactions are defined as the noncovalent preferential association between cations or cationic moieties and π electrons, commonly from aromatic compounds.[6] Cations can be simple monatomic metal ions (e.g. Na^+, K^+, Mg^{2+}, Ca^{2+}) or complex organic cations (e.g. quaternary ammonium ions and acetylcholine (ACh)). In proteins, cation–π interactions are commonly due to: 1) The interaction between monatomic cations and the aromatic moieties of Phe, Tyr, and Trp (Figure 1.1**a**), 2) Association between cationic side chain of Lys or Arg with the aromatic side chains of Phe, Tyr, or Trp (Figure 1.1**b**). 3) The interaction between a cationic moiety of a ligand with the aromatic side chains of Phe, Tyr, or Trp (Figure 1.1**c**). and 4) The complexation between an aromatic moiety from ligands with the cationic side chains of Lys and Arg (Figure 1.1**d**). Cation–π interactions are largely observed in chemical and biological systems and are believed to play key roles in molecular recognition,[7] stabilization of protein and nucleic acid structures,[8,9] stability of protein-DNA[7,10] and protein-ligand[6,11] complexes. In addition, the investigation of these interactions can help in designing new ligands and drugs.[12] The study of cation–π interactions has thus become a research focus in many fields of chemistry and biology.

Electrostatic interactions between the cation and the aromatic system play the dominant role in the overall cation–π binding.[13] Electrostatic forces arise from ion-dipole and ion-quadrupole interactions. Polarization is also important in cation–π stability. Large polarizability of aromatic systems results in a large induced dipole moment upon binding to cations, and hence strengthens the binding.[14–16] Other forces such as dispersion are weaker and their contribution to cation–π attractions is minor.[16]

Development of polarizable molecular models for cation–π interactions is important to study the stability and roles of these interactions in chemical and biological systems. In particular understanding the factors that influence their strength and geometry is important for designing cation-selective receptors and to devise new separation strategies for toxic cationic or aromatic wastes.

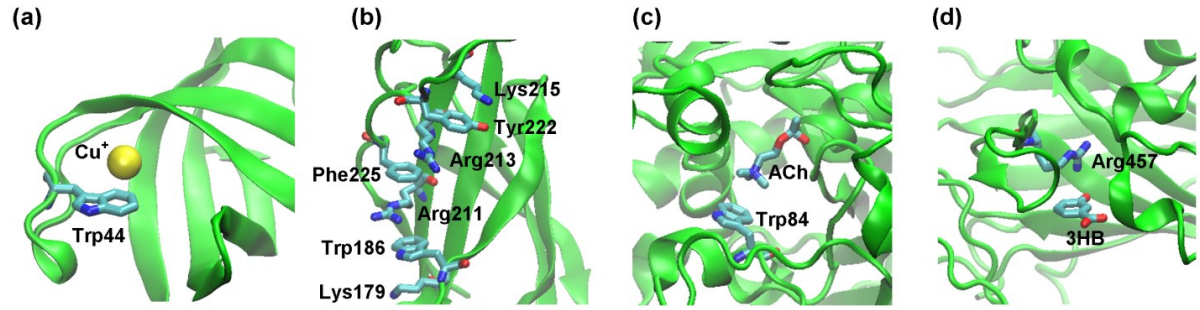

Figure 1.1. Examples of cation–π interactions in proteins: **(a)**, between Cu^+ and Trp44 in the structure of the copper and silver resistance protein CuSF (PDB code: 2VB2); **(b)**, of the cationic side chains of Lys and Arg with the aromatic side chains of Phe, Tyr, and Trp in the structure of a human growth hormone (hGH) bound to the extracellular domain of its receptor (PDB code: 3HHR); **(c)**, between the quaternary ammonium head of ACh and Trp84 in the X-ray structure of Torpedo California acetylcholinesterase (AChE) (PDB code: 2ACE); **(d)**, interaction of 3-hydroxybenzoate (3HB) with Arg457 in the structure of protocatechuate 3,4-dioxygenase (PDB code: 3PCB).

1.5. Ammonium Transport by AmtB and RhCG Proteins

Ammonia is a source of nitrogen for amino acid synthesis in plants and bacteria and helps to maintain the acid-base equilibrium in mammals.[17,18] The transport of ammonia through cellular membranes is mediated by ammonium transport proteins which are found in all domains of life (ammonium transporters (Amt) in plants and bacteria, methylamine permease (Mep) in yeast, and rhesus (Rh) blood-group associated glycoproteins in humans). The X-ray crystallographic structure of AmtB protein from *Escherichia coli*[19] and of the human RhCG protein[20] show that these proteins are homotrimers with a transport channel at the center of each monomer (see Figure 1.2**a** and 1.2**b** for AmtB). A comparison between the two channel structures reveals some conserved features and some structural differences (Figure 1.2**c**).

Experimental studies on various proteins of the Amt family are suggesting three possible transport mechanisms: electroneutral NH_3 transport,[19,21] NH_3/H^+ cotransport,[18,21–23] and NH_4^+ transport.[24,25] On the other hand, studies on Rh family proteins[20] are pointing toward an electroneutral transport mechanism. Structural variations along the transport pathway might influence the mechanism of function of the two proteins. Although mutagenesis studies can shed light on the importance of a certain amino acid, computational studies provide detailed information about the exact role of these amino acids. Experiments suggest that while the activity of Amt proteins is not inhibited by Na^+ and K^+ ions, it is inhibited by ions such as Cs^+ and Tl^+.[21] The mechanism of inhibition remains however unexplained. We aim in this work to measure the binding affinities of AmtB and RhCG proteins toward various ions and to investigate the influence of structural variation on the mechanism of transport.

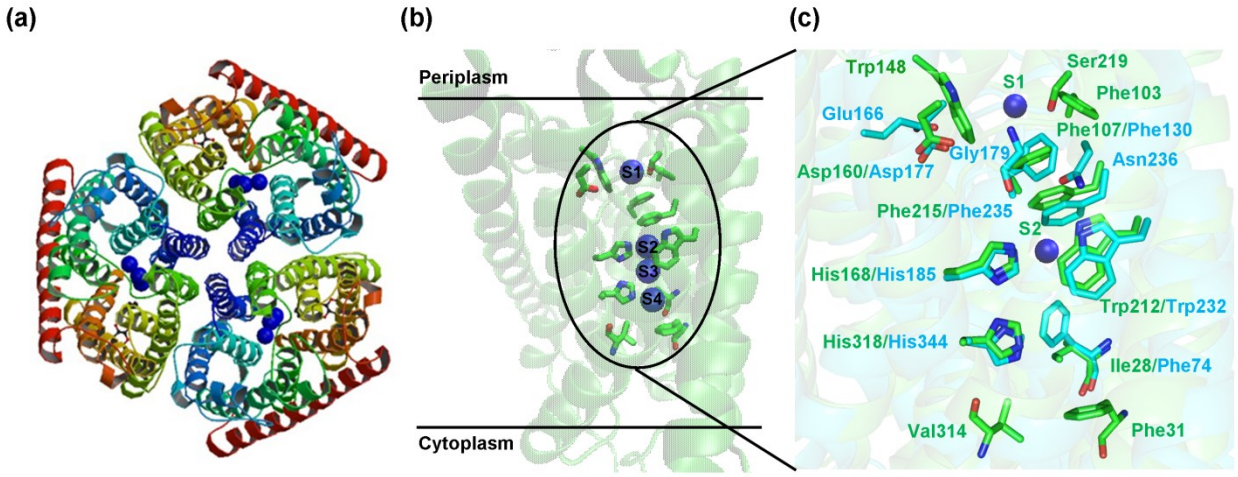

Figure 1.2. Three dimensional fold of: (a), the AmtB trimer; (b), the monomeric ammonium channel in AmtB (PDB code: 1U7G);[17] (c), amino acid side chains lining the transport pathway in AmtB (in green) and RhCG (in cyan). Blue spheres are crystallographically identified electronic density maxima (in the AmtB structure) that are thought to be occupied by water or ammonia.

1.6. Choice of the Model Compounds

With few exceptions (such as phosphorus and halides), ligands generally bind metal ions via N, O, or S atoms. In fact these are the only atoms that bind metal ions in proteins. Toward understanding protein selectivity toward metal ions, we study the selectivity of alkali metal ions (Li^+, Na^+, K^+, Rb^+, Cs^+). For the sake of reducing the computational cost of molecular dynamics (MD) simulations, NH_3, H_2O, and H_2S are used as minimal model compounds for N, O, and S containing ligands. These three molecules can also be considered minimal models for the side chains of some amino acids (NH_3 for Lys, H_2O for Ser and Thr, and H_2S for Cys and Met).

To investigate the strength and geometry of cation–π interactions involving inorganic metal ions in gas phase and in aqueous solution and to compare their strength with other interactions, we investigate the complexation of Rb^+, Cs^+, and Tl^+ with benzene and toluene (models to Phe), with phenol and 4-methylphenol (models for Tyr), with indole and 3-methylindole (models for Trp), with imidazole and 5-methylimidazole (models for His), with water and ethanol (models of Ser and Thr), with acetamide (model for Asn and Gln), and with N-methylacetamide (model for peptide backbone).

Cation–π interactions involving organic cations are investigated by studying the complexes of quaternary ammonium ions (ammonium, tetramethylammonium, and tetraethylammonium) with benzene, toluene, 4-methylphenol, and 3-methylindole.

We also optimize AM1-based semiempirical models for Ca^{2+} and Mg^{2+} metalloproteins. For this purpose we consider ligands that model groups that can coordinate the two metal ions in proteins. These model compounds are: water, methanol, ammonia, methylamine, hydrogen sulfide, methanethiol, formaldehyde, acetaldehyde, formamide, acetamide, formate ion, acetate ion, imidazole, 4-methylimidazole, and 5-methylimidazole.

1.7. Computational Chemistry Methods

Computational chemistry uses methods of theoretical chemistry to solve chemical problems, to determine properties that are inaccessible experimentally, and to interpret experimental data. It provides an advantage over experiments in exploring the mechanism of a physical or a chemical process at the molecular level. Depending on the approximation used, computational methods are typically classified into, ab initio quantum mechanics (QM), semiempirical QM, and molecular mechanics (also known as force fields).

1.7.1. Ab initio QM calculations

Ab initio QM methods use quantum physics to calculate the molecular structure by solving the Schrödinger equation. These methods deal explicitly with electrons and can thus be used to study chemical reactions and properties that depend on electronic structure such as aromaticity, transition states, and excited states. They are however computationally expensive and are thus typically used to study small systems (tens of atoms). Among QM methods that account for electronic correlations, the second-order Møller-Plesset perturbation theory (MP2) provides a compromise between computational cost and accuracy. With a few exceptions, ab initio calculations in this thesis are performed at the MP2 level. Ab initio calculations are performed using GAUSSIAN 09 program.[26] Two types of calculations are usually performed: geometry optimization and scan of some potential energy surface. Optimized geometries are typically subjected to frequency calculations to identify whether the optimized structure is an energy minima structure or a transition state. Potential energy surfaces are generated by scanning some intermolecular coordinates (distances, angles, or dihedrals).

1.7.2. Semiempirical QM Calculations

The high cost of ab initio calculations is mainly due to the many integrals that need to be calculated. Semiempirical (SE) QM methods are based on the ab initio Hartree-Fock formalism, but make many approximations and rely on empirical data for some parameters.[27] These

parameters are adjusted to improve the agreement with experimental data, which results in an implicit consideration of electronic correlations. SE methods use effective core potentials to treat core electrons together with the nuclei of an atom and use minimal basis set to treat valence electrons. They are thus computationally less demanding compared to ab initio methods and can be used for medium-sized systems (hundreds of atoms). SE methods can also be used for studying chemical reactions and calculating transition states and excited states. SE methods may however be inaccurate for molecules not similar to those used in the parameterization.

The Austin Model 1 (AM1)[28] is based on the Neglect of Diatomic Differential Overlap (NDDO) method and is one of the most popular SE models. The model is parametrized with particular emphasis on heats of formation, dipole moments, ionization potentials, and geometries of molecules.[28] The model is not parameterized for intermolecular interactions and might require reparameterization to reproduce structural and energetic properties of these interactions. We parameterize an AM1 SE model for Mg^{2+} and Ca^{2+} based on the ab initio properties (geometries and binding energies) of their complexes with various ligands at the MP2/6-311++G(d,p) level.

1.7.3. Molecular Mechanical Calculations

In molecular mechanics (MM), molecular systems are entirely modeled using classical mechanics and their potential energies are calculated using empirical force fields. All-atom FFs do not describe electrons explicitly; instead they treat atoms as single particles with a specific radius and charge. While this approximation allows for studying large systems with thousands of atoms, it does not allow for studying chemical reactions. All MM calculations of this work are performed with the program CHARMM.[29] Polarizable FFs are superior to pairwise-additive ones in a number of properties such as polarization-induced geometries and cooperativity between interactions[30,31] and are generally expected to give results in better agreement with experimental and ab initio calculations than conventional FFs.

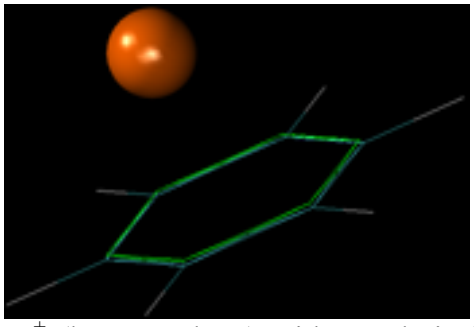

Figure 1.3. Complexation of K^+ (brown sphere) with a polarizable model of benzene. Drude particles (in green) are displaced from carbon atoms (in cyan) toward the metal ion.

Among different methods for describing polarization in FFs, the classical Drude oscillator model[32] is used in this study. In this model, molecular polarizability is implemented by attaching a light (0.4 amu) charged particle to all heavy (non-hydrogen) atoms (see Figure 1.3) via a harmonic spring with force constant k_D = 1000 kcal/mol/Å^2.[32] The partial charge q of a polarizable atom is then distributed between the Drude particle (q_D) and the atom core ($q_C = q - q_D$) with the Drude particle charge being determined from the atomic polarizability via the relation $\alpha = q_D^2/k_D$. A separation d between the Drude particle and the polarizable atom results in an induced dipole moment $q_D d$. The Drude particles are initially placed on the heavy atom and get displaced by electric fields from neighboring atoms (see Figure 1.3).

Molecular dynamics is a method used to generate successive configurations of a system by integrating the Newton's second law of motion. This results in a trajectory that describes the evolution of the positions and velocities of particles with time. Molecular mechanics MD simulations are done with the program CHARMM[29] with all bonds involving hydrogen atoms kept at their reference lengths using the SHAKE algorithm.[33]

1.8. Aims of the Thesis

One focus of the present work is to understand the selectivity of metal ions towards various ligands. Toward this, we optimize polarizable models for NH_3 and H_2S and for their interactions with alkali metal ions. The models are validated over properties of liquid ammonia and liquid hydrogen sulfide and over ab initio properties of alkali ion complexes with NH_3 and H_2S. The models are used to investigate the solvation structure and solvation free energy of alkali ions in pure ammonia and pure hydrogen sulfide and to investigate the preferential solvation of the ions in aqueous ammonia and aqueous hydrogen sulfide solutions.

Another aim of this work is to develop reliable SE models for Ca^{2+} and Mg^{2+} metalloproteins. For this purpose, new AM1-based SE models are optimized for the two metal

ions based on the ab initio properties of their complexes with various ligands that model the coordinating groups in proteins. The optimized models are useful in studying the ligand selectivity, complexation geometry and ligand exchange dynamics of the two metals ions. The models can also be used to calculate the binding affinity and selectivity of proteins toward the two cations and to study the mechanism of action of the two ions in their metalloproteins.

Due to the important roles of cation–π interactions in biological system, we aim to optimize polarizable potential models for the interaction of simple (Rb^+, Cs^+, Tl^+) and bulk (ammonium, tetramethylammonium, tetraethylammonium) cations with model compounds to the aromatic amino acid side chains. Optimized models are used to calculate the binding affinity and binding geometry of the different cation–π complexes in aqueous solution.

In addition, we also aim at measuring the selectivity and binding affinities of AmtB and RhCG proteins toward different ions. The structural function of amino acids lining the transport pathway of these proteins and the mechanism of inhibiton of protein acivity are also studied.

1.9. Structure of the Thesis

The thesis is written (in a manuscript-based format) based on the seven manuscripts listed below. Three of these (I–III) are published and the others are in preparation.

I. Orabi, E. A.; Lamoureux, G. Polarizable Interaction Model for Liquid, Supercritical, and Aqueous Ammonia. *J. Chem. Theory Comput.* **2013**, *9*, 2035−2051.

II. Orabi, E. A.; Lamoureux, G. Molecular Dynamics Investigation of Alkali Metal Ions in Liquid and Aqueous Ammonia. *J. Chem. Theory Comput.* **2013**, *9*, 2324–2338.

III. Orabi, E. A.; Lamoureux, G. Simulation of Liquid and Supercritical Hydrogen Sulfide and of Alkali Ions in the Pure and Aqueous Liquid. *J. Chem. Theory Comput.* **2014**, *10*, 3221–3235.

IV. Orabi, E. A.; Lamoureux, G. Optimization of AM1-based Semiempirical Quantum Mechanical Models for Ca^{2+} and Mg^{2+} Metalloproteins.

V. Orabi, E. A.; Lamoureux, G. Complexation of Rb^+, Cs^+, and Tl^+ with Aromatics, Alcohols, and Amides in Gas Phase and in Aqueous Solution.

VI. Orabi, E. A.; Lamoureux, G. Cation–π Interactions between Quaternary Ammonium Ions and Aromatic Amino Acid Side Chains in Gas Phase and in Aqueous Solutions.

VII. Orabi, E. A.; Lamoureux, G. Computational Investigation of the Selectivity and Inhibition of AmtB and RhCG Ammonium Transport Proteins.

2. Polarizable Interaction Model for Liquid, Supercritical, and Aqueous Ammonia*

* Adapted with permission from (Orabi, E. A.; Lamoureux, G. Polarizable Interaction Model for Liquid, Supercritical, and Aqueous Ammonia. *J. Chem. Theory Comput.* **2013**, *9*, 2035−2051) Copyright (2013) American Chemical Society.

Abstract

A polarizable model for ammonia is optimized based on the ab initio properties of the NH_3 molecule and the NH_3−NH_3 and NH_3−H_2O dimers calculated at the MP2 level. For larger $(NH_3)_m$, $NH_3(H_2O)_n$, and $H_2O(NH_3)_n$ clusters (m = 2−7 and n = 1−4), the model yields structural and binding energies in good agreement with ab initio calculations without further adjustments. It also reproduces the structure, density, heat of vaporization, self-diffusion coefficient, heat capacity, and isothermal compressibility of liquid ammonia at the boiling point. The model is further validated by calculating some of these properties at various temperatures and pressures spanning the liquid and supercritical phases of the fluid (up to 700 K and 200 MPa). The excellent transferability of the model suggests that it can be used to investigate properties of fluid ammonia at conditions for which experiments are not easy to perform. For aqueous ammonia solutions, the model yields liquid structures and densities in good agreement with experimental data, and allows the nonlinearity in the density-composition plot to be interpreted in terms of structural changes with composition. Finally, the model is used to investigate the solvation structure of ammonia in liquid water and of water in liquid ammonia, and to calculate the solvation free energy of NH_3 and H_2O in aqueous ammonia as a function of solution composition and temperature. The simulation results suggest the presence of a transition around 50% molar NH_3/H_2O compositions, above which water molecules are preferably solvated by ammonia.

2.1. Introduction

Ammonia is an amphiprotic molecule often described as "water-like", due to the considerable similarity of its solvent properties to those of water.[34,35] Both molecules can function as hydrogen bond donor and acceptor and have comparable ability to dissolve a variety of compounds such as ionic and molecular compounds and elemental metals and nonmetals.[34,35] Compared to water, ammonia has a lower dielectric constant, which results in ammonia being generally a poorer solvent for ionic compounds but a better solvent for covalent compounds.[35] However, the power of ammonia in dissociating electrolytes closely approaches that of water; some salts conduct electricity even better in ammonia than in water.[34,35] Ammonia is used as a solvent for organic reactions and in many industrial sectors as refrigerant, fertilizer, cleaner, and as precursor to high-energy nitrogenous compounds. In both its neutral (NH_3) and ionic (NH_4^+) forms, it is a source of nitrogen for amino acid synthesis in bacteria and plants, supports the growth of yeast cells, and helps maintain the acid-base equilibrium in mammals.[36–40]

Ammonia is one of the weakest and simplest hydrogen-bonded liquids.[41–44] Structural data of liquid ammonia from x-ray[41,42] and neutron[43,44] diffraction experiments, as well as abundant experimental data on the physical properties of the fluid (such as density,[45] heat capacity,[46] self-diffusion coefficient,[47–49] dielectric constant,[50] viscosity,[51] and heat of vaporization[46,52]) have prompted computational chemists to develop molecular models for understanding the properties of liquid ammonia. Experimental studies[53–57] and ab initio investigations[25–27] of ammonia clusters have also been reported. These studies are important for understanding the structure and stability of the clusters and can provide insight on the transition toward the bulk fluid as the cluster size increases. They also provide useful benchmark data to test and validate new molecular models. The weak nature of the intermolecular interaction in the ammonia dimer[53–60] suggests however that accurate experiments and high level ab initio calculations might be required for reliable determination of the structure and binding energy in ammonia clusters.

A number of intermolecular potentials have been used to explore the structure and binding energies of $(NH_3)_m$ ammonia clusters.[61–65] Sagarik *et al.* have developed a pairwise-additive potential to calculate the structure and interaction energies of the ammonia dimer and to compute static and dynamic properties of liquid NH_3.[61] This potential was used by Greer *et al.* to investigate ammonia clusters with $m = 3-7$.[62] Using the rigid-ammonia pairwise-additive model

of Impey and Klein,[66] Beu and Buck[63] have performed geometry optimization and binding energy calculations of clusters with m = 2–18. Using a rigid-ammonia model with an explicit description of induction parameterized by fitting to ab initio data, Janeiro-Barral *et al.*[64] have investigated the structure and energetics of ammonia clusters with m = 2−20. Yu and Yang[65] have used an eight-point intermolecular potential including fluctuating charges and flexible bonds to study the structure, binding energies, and vibrational frequencies of ammonia clusters with m = 1−5 and to explore the dynamical properties of liquid ammonia. Although binding energies calculated with both nonpolarizable[61−63] and polarizable[64,65] models have comparable performance relative to ab initio results, the contributions of non-additive effects such as induction forces are important for providing more accurate total interaction energies.[64,65] Almedia *et al.*[67] have investigated the electronic properties of ammonia clusters electrostatically embedded in liquid ammonia (sampled using the Impey and Klein potential), and found a 27% increase in the average dipole moment of liquid ammonia compared to the gas-phase value, suggesting again the importance of induction forces.

Over the last decades, several theoretical studies[61,65,66,68−84] have contributed to molecular-level understanding of the structure, thermodynamics, and rheology of fluid ammonia. Different approaches have been used, going from computationally inexpensive simulations using non-polarizable[61,66,68−73,77−83] and polarizable[65,84] force fields to time-consuming quantum mechanical/molecular mechanical (QM/MM)[76] and ab initio[71,73−75] simulations.

Mixtures of ammonia and water have various industrial applications and play an important role in refrigeration and power generation cycles.[85] The NH_3–H_2O dimer itself, represents the simplest system containing an N···H−O hydrogen bond (ubiquitous in biological molecules), has been the subject of several experimental[86−90] and theoretical studies.[91−96] Experimental investigations on mixtures of the two fluids have similarly been performed.[41,97,98] Using x-rays scattering experiments, Narten[8] has reported the structure of aqueous ammonia solutions with two compositions (x_{NH_3}= 18.3 and 28.5%) at 4°C. Ammonia adsorption at the air-water interface[97] and its adsorption on and diffusion into ice[98] have also been studied experimentally. A number of theoretical studies have been performed to investigate the solvation of ammonia in water clusters,[94,97,99–101] and the properties of aqueous ammonia and its liquid/vapor interface.[69,84,102−110]

With a few exceptions,[70,77,79–83] most studies have so far focused on fluid ammonia under a limited range of thermodynamic conditions (around standard temperature and pressure), and few potential models have been used to study aqueous ammonia solutions.[106–109] Although in principle ab initio simulations are expected to provide the best description of fluids properties, a reliable sampling of the configuration space requires long simulations using highly correlated ab initio methods, which are computationally prohibitive. Potential models that reproduce various experimental properties under different thermodynamic conditions, especially those for which experiments are difficult to perform, can thus provide a convenient alternative. The fact that polarization has been found essential to model cluster and liquid ammonia,[64,65,67] to reproduce the ab initio properties in ammonia-water clusters,[94] and to reproduce the hydration free energy of NH_3[109] suggests that, for such purpose, polarizable potential models are preferable to nonpolarizable ones.

In this work we aim to parameterize a polarizable potential model for NH_3 that can be reliably used to simulate liquid and aqueous ammonia solutions under different thermodynamic conditions. For this purpose, MP2-level geometry optimizations are performed on $(NH_3)_m$, $NH_3(H_2O)_n$, and $H_2O(NH_3)_n$ clusters (m = 1−7 and n = 1−4). We also calculate various ab initio energy surfaces of the NH_3−NH_3 and NH_3−H_2O dimers. A polarizable model based on classical Drude oscillators[32] is then generated for ammonia-ammonia and ammonia-water interactions. The model is parameterized based on the ab initio properties of the NH_3 monomer and its dimers with H_2O and NH_3. The model is validated by calculating the structure and interaction energies of the larger clusters, and by simulating properties of fluid ammonia at temperatures and pressures for which experimental data are available. It is then used to calculate the hydration structure and hydration free energy of ammonia, and to explore the properties of aqueous ammonia solutions at various compositions and temperatures.

2.2. Methods

2.2.1. Ab initio Calculations

Ab initio calculations on $(NH_3)_m$, $NH_3(H_2O)_n$, and $H_2O(NH_3)_n$ clusters (m = 1−7 and n = 1−4) are carried out at the MP2/6-311++G(d,p) level with frozen-core (FC) electrons, using Gaussian 09 program.[26] Calculations at the MP2(full)/6-311++G(d,p) level give almost the same results as FC calculations. Except for the transition state structures of the NH_3−NH_3 and NH_3−H_2O dimers and the O···H−N hydrogen-bonded NH_3−H_2O dimer, geometry optimizations

are carried out without imposing any symmetry constraints. Frequency calculations are performed on all resulting structures to confirm that they are energy minima. Interaction energies are corrected for basis set superposition error (BSSE) using the counterpoise (CP) procedure proposed by Boys and Bernardi.[111] For the ammonia monomer, geometry optimization and frequency calculations are also performed using coupled cluster theory with single, double, and perturbative triple excitations (CCSD(T)) on 6-311++G(d,p), 6-311++G(2d,2p), and Dunning's aug-cc-pV5Z[112] basis sets. In order to assess the accuracy of the MP2 results, the minimum energy and transition state conformers in the NH_3−NH_3 and NH_3−H_2O dimers are also optimized at the CCSD(T)/6-311++G(d,p) and CCSD(T)/6-311++G(2d,2p) levels.

For the NH_3−NH_3 dimer (see Figure 2.1), potential energy surfaces (PESs) are generated by scanning the following parameters in the eclipsed isomer (Figure 2.1a): N···N distance (from 2 to 8 Å), N···N−H angle (from 20 to 160°), and H−N···N−H dihedral (from 0 to 180°). The bond angle scan describes deviations from the optimal orientation of one molecule relative to the other and the dihedral scan describes the relative orientation of hydrogen atoms in the two molecules, going from the eclipsed to the staggered configurations. For the NH_3−H_2O dimer (see Figure 2.2), PESs are generated by scanning the N···O distance in the N···H−O and O···H−N hydrogen-bonded complexes (from 2.0 to 8.0 Å), the N···O−H angle in the N···H−O hydrogen-bonded complex (from 30 to 180°), and the N···H−O−H dihedral in the N···H−O hydrogen-bonded complex (from 0 to 180°). As for the ammonia dimer, the angle and dihedral scans target the position and hydrogen atoms orientations in the two molecules. All curves are computed at the MP2(FC)/6-311++G(d,p) level with rigid monomers maintained in their gas-phase optimal geometries, and are corrected for BSSE.

2.2.2. Molecular Mechanical Calculations

Molecular mechanics (MM) calculations are performed with the program CHARMM.[29] Electronic polarization is described using the classical Drude oscillator model.[32] The ammonia model is calibrated based on the ab initio MP2(FC)/6-311++G(d,p) properties of the ammonia monomer, ammonia dimer, and ammonia-water dimer. The polarizable SWM4-NDP water model[113] is used in all MM calculations involving water.

2.2.2.1. Potential Energy Function and Parameterization Strategy

Molecular polarizability is implemented by attaching a light (0.4 amu) charged particle to all heavy (non-hydrogen) atoms via a harmonic spring with force constant k_D = 1000

kcal/mol/Å^2.[32] The partial charge q of a polarizable atom is then distributed between the Drude particle (q_{D}) and the atom core ($q_{\mathrm{c}} = q - q_{\mathrm{D}}$) with the Drude particle charge being determined from the atomic polarizability via the relation $\alpha = {q_{\mathrm{D}}}^2/k_{\mathrm{D}}$. A separation d between the Drude particle and the polarizable atom results in an induced dipole moment $q_{\mathrm{D}}d$. To account for induction, the functional form of the CHARMM additive empirical potential energy[114] is modified to include electrostatic interactions with the Drude oscillators. A term describing the self-energy of a polarizable atom ($\frac{1}{2}k_{\mathrm{D}}d^2$) is also added.[32,30] Similarly to our recently developed polarizable model for NH_4^+,[30] NH_3 is modeled by four atomic sites and an auxiliary Drude particle attached to the nitrogen atom. The polarizable potential energy function that describes the interaction energy in liquid and aqueous ammonia solutions can be written as following:[32,114,30]

$$
\begin{aligned}
U(R) = & \sum_{i=1}^{N} \frac{1}{2} k_{\mathrm{D}} |\mathbf{r}_i - \mathbf{r}_{Di}|^2 + \sum_{\text{HNH angles}} k_\theta (\theta - \theta_0)^2 \\
& + \sum_{\text{nonbond}} E_{\min,ij} \left[\left(\frac{R_{\min,ij}}{|\mathbf{r}_i - \mathbf{r}_j|} \right)^{12} - 2 \left(\frac{R_{\min,ij}}{|\mathbf{r}_i - \mathbf{r}_j|} \right)^{6} \right] \\
& + \sum_{\text{nonbond}} \left(\frac{q_i q_j}{|\mathbf{r}_i - \mathbf{r}_j|} + \frac{q_{\mathrm{D}i}\, q_j}{|\mathbf{r}_{\mathrm{D}i} - \mathbf{r}_j|} + \frac{q_i q_{\mathrm{D}j}}{|\mathbf{r}_i - \mathbf{r}_{\mathrm{D}j}|} + \frac{q_{\mathrm{D}i} q_{\mathrm{D}j}}{|\mathbf{r}_{\mathrm{D}i} - \mathbf{r}_{\mathrm{D}j}|} \right)
\end{aligned}
\qquad (2.1)
$$

where N is the number of interacting molecules, and $\mathbf{r}_i$ and $\mathbf{r}_{\mathrm{D}i}$ are the positions of the core particle i and its corresponding Drude particle, respectively. k_θ, θ, and θ_0 are respectively the force constant, angles, and equilibrium angle parameters for the HNH angles. q_i is the partial charge on the core particles i and $q_{\mathrm{D}i}$ is the partial charge of its Drude particle. $E_{\min,\mathrm{ij}}$ and $R_{\min,\mathrm{ij}}$ are the mixed Lennard-Jones (LJ) parameters between nonbonded atoms i and j, defined by the Lorentz–Berthelot combination rules:

$$
E_{\mathbf{min},\mathrm{ij}} = \sqrt{E_{\min,\mathrm{i}} \times E_{\min,\mathrm{j}}} \qquad \text{and} \qquad R_{\min,\mathrm{ij}} = \frac{R_{\min,\mathrm{i}} + R_{\min,\mathrm{j}}}{2} \qquad (2.2)
$$

The potential energy term that describes deviations in bonds:

$$
E_{\mathrm{bond}} = \sum_{\text{bonds}} k_b (b - b_0)^2 \qquad (2.3)
$$

where k_b, b, and b_0 are the force constant, bond, and equilibrium bond parameters for NH and OH bonds, is not included in Eq. (2.1) because these bonds are constrained to their equilibrium

values in all MM calculations using the SHAKE/Roll-RATTLE/Roll algorithm.[33] Water is described using the polarizable SWM4-NDP model, in which the HOH angle is rigid[113] and thus excluded from the angle-bending term of Eq. (2.1).

The equilibrium bonded parameters for NH_3 (b_0 for NH bonds and θ_0 for HNH angles) are based on MP2(FC)/6-311++G(d,p) optimization of the monomer. The bond and angle force constants, k_b and k_θ, are set to reproduce the ab initio vibration frequencies of the monomer and to minimize distortions in its pyramidal structure during molecular dynamics (MD) simulations.[30] The electrostatic parameters (partial atomic charges and polarizability) are similarly based on the ab initio properties of the NH_3 monomer, with the partial atomic charges on N and H atoms fitted to reproduce the MP2 dipole moment and the polarizability of the N atom calculated from the trace of the MP2 polarizability tensor.[30]

Optimization of the polarizable model for ammonia-ammonia and ammonia-water interactions follows our previous approach.[30] In particular, the model is optimized based on the ab initio properties (complexation energies and PESs) of the dimers. The "generic" LJ parameters of N and H of NH_3 are optimized based on the properties of the ammonia-water complex. The ammonia dimer's potential model is adjusted by optimizing pair-specific LJ parameters between N atoms, introduced via the NBFIX[29] facility of CHARMM. Following our previously reported parameterization approach,[30] optimization of the atomic and pair-specific LJ parameters initially targets the ab initio PESs of the two dimers. Each point of the energy surfaces contributes to the error function χ^2 to be minimized by a Boltzmann-weighted error term.[30] Since the PESs are computed using the rigid monomer geometries of H_2O and NH_3, parameters obtained from the minimization of χ^2 are further refined to reproduce the complexation energies of the fully relaxed ab initio dimers.[30] This slight modification of the parameters improves the complexation energy of the dimers, but creates small deviations in the position of the energy minimm on the rigid-monomer PESs.

2.2.2.2. Molecular Dynamics

Most previously published computational studies on liquid ammonia are artificially imposing the experimental density by performing simulations in the canonical (NVT)[61,65,66,68,71–73,76,80,83,84] or the microcanonical (NVE)[67,75,78,79] ensembles for which the volume of the system corresponds to the experimental density of the liquid at the studied thermodynamic conditions. By contrast, all MD simulations reported in this work are performed

in the isothermal-isobaric ensemble (*NPT*). Unless otherwise specified, the total number of molecules (ammonia and/or water) is 250 in each system. All simulations are performed with cubic periodic boundary conditions using previously reported simulation protocol.[30] The SWM4-NDP polarizable water model[113] is used for simulations of aqueous ammonia. Electrostatic interactions are computed using the particle-mesh Ewald method[115] with $\kappa = 0.34$ for the charge screening and a 1.0 Å grid spacing with fourth-order splines for the mesh interpolation. The real-space interactions (Lennard-Jones and electrostatic) are cut off at 15 Å and the long range contribution from the Lennard-Jones term is introduced as an average density-dependent term.[116] The temperature of the system is controlled with a two-thermostats algorithm, where atoms are kept at the desired temperature and auxiliary Drude particles are kept at low temperature (1 K) to ensure self-consistent dipole induction.[32] The equations of motion are integrated using a 1 fs time step, with all bonds involving hydrogen atoms kept at their reference lengths using the SHAKE/Roll-RATTLE/Roll algorithm.[33]

2.2.2.3. Free Energy Calculations

The optimized polarizable potential model for ammonia-water interaction is validated by calculating the hydration free energy of NH_3 at $T = 298.15$ K and $p = 1$ atm = 0.1013 MPa. The hydration free energy of H_2O relative to NH_3 in bulk water ($\Delta\Delta G_{\mathrm{hyd}} = \Delta G_{\mathrm{hyd}}(\mathrm{H_2O}) - \Delta G_{\mathrm{hyd}}(\mathrm{NH_3})$) is calculated using a previously reported thermodynamic integration approach.[30] Specifically, we use a special hybrid residue in which virtual NH_3 and H_2O groups are linked through their heavy atoms via a weak harmonic bond of force constant 5 kcal/mol/Å^2.[30] This residue is composed of one original "real" molecule linked to a "dummy" molecule having no interactions with the real particles (apart from the harmonic tether). The relative solvation free energy is evaluated from the conventional thermodynamic cycle for solute transformation

$$\Delta\Delta \mathrm{G_{hyd}} \equiv \Delta G_{\mathrm{hyd}}(\mathrm{H_2O}) - \Delta G_{\mathrm{hyd}}(\mathrm{NH_3}) = \Delta G^{\mathrm{aq}}_{\mathrm{mut}}(\mathrm{NH_3} \rightarrow \mathrm{H_2O}) \qquad (2.4)$$

where $\Delta G^{\mathrm{aq}}_{\mathrm{mut}}$ is the relative free energy for the alchemical solute $\mathrm{NH_3} \rightarrow \mathrm{H_2O}$ "mutation" performed in water. The transformation in performed in 17 steps, controlled by a scaling parameter λ which takes the following values: 0, 0.005, 0.02, 0.04, 0.1, 0.2, 0.3, 0.4, 0.5, 0.6, 0.7, 0.8, 0.9, 0.96, 0.98, 0.995, and 1. Each λ window is equilibrated for 150 ps followed by subsequent data collection for 350 ps. Each mutation is performed in the forward and backward

directions in six independent replicates in order to confirm the convergence and estimate the error in the calculated values.

The solvation free energy of H_2O and NH_3 in aqueous ammonia is calculated as a function of the mixture composition and temperature. For this purpose we initially calculate the solvation free energy of H_2O, $\Delta G_{\mathrm{solv}}(\mathrm{H_2O})$, by mutating one water molecule into a dummy molecule, having no charges and no LJ parameters, using free energy perturbation (FEP) theory. The transformation is performed in 21 steps with the scaling parameter λ taking the values 0, 0.00001, 0.0001, 0.001, 0.01, 0.05, 0.1, 0.2, 0.3, 0.4, 0.5, 0.6, 0.7, 0.8, 0.9, 0.95, 0.99, 0.999, 0.9999, 0.99999, and 1. A slow growth of λ near its extreme values is used to avoid sampling errors created by the sudden appearance or disappearance of the solute. This integration scheme is equivalent to the previously reported free energy perturbation protocol, in which the solvation free energy is decomposed into three components, each being calculated from independent simulations:[117,118]

$$\Delta G_{\mathrm{solv}} = \Delta G_{\mathrm{elec}} + \Delta G_{\mathrm{disp}} + \Delta G_{\mathrm{rep}} \qquad (2.5)$$

where ΔG_{elec} is the electrostatic component of the solvation free energy and ΔG_{disp} and ΔG_{rep} are the attractive (dispersive) and repulsive components of the LJ interaction. Our preliminary tests show that the integration scheme yields hydration free energy of water (–5.9 kcal/mol) and alkali ions (–109.6 kcal/mol for Li^+, –85.4 kcal/mol for Na^+, –68.1 kcal/mol for K^+, –63.2 kcal/mol for Rb^+, and –56.1 kcal/mol for Cs^+) in excellent agreement with the results from the decomposition scheme of Eq. (2.5) (–5.9 kcal/mol for H_2O,[113] and –109.8, –85.6, –67.9, –63.0, and –55.8 kcal/mol for Li^+, Na^+, K^+, Rb^+, and Cs^+, respectively[118]). To reduce the computing effort associated with having that many λ values, the solvation free energy of NH_3 is calculated relative to that of H_2O:

$$\Delta G_{\mathrm{solv}}(\mathrm{NH_3}) = \Delta G_{\mathrm{solv}}(\mathrm{H_2O}) - \Delta\Delta \mathrm{G_{solv}} \qquad (2.6)$$

The solvation free energy calculations are performed in aqueous ammonia solutions composed of a total of 251 molecules (one solute + 250 solvent molecules), with various ammonia mole fraction, $0.0 \leq x_{\mathrm{NH_3}} \leq 1.0$. The simulations are performed at three temperatures, T = 239.8, 273.15, and 298.15 K, and at the corresponding vapor pressures of liquid ammonia, p = 0.1013, 0.4294, and 1.0030 MPa.

2.3. Results and Discussion

2.3.1. Ab initio Optimized Geometries

The enumeration of all stable conformers of $(NH_3)_m$ and $NH_3(H_2O)_n$ clusters is outside the scope of this study and can be found elsewhere.[59,60,94,97,99−101] Except for the dimers (m = 2, n = 1), only the minimum-energy conformers of these clusters are considered, solely for the purpose of validating the NH_3 potential model. However, since to the best of our knowledge no ab initio investigations have been reported on $H_2O(NH_3)_n$ clusters larger than the trimer (n = 2), we report all stable conformers we have identified in clusters with n = 1−4.

2.3.1.1. Ammonia Monomer

The MP2(FC)/6-311++G(d,p), CCSD(T)/6-311++G(d,p), CCSD(T)/6-311++G(2d,2p), and CCSD(T)/aug-cc-pV5Z optimized geometries, gas-phase dipole moments, and vibrational frequencies of the isolated ammonia molecule are reported in Table 2.1. The calculated internal geometry of ammonia at the MP2 level shows r_{NH} = 1.0135 Å and θ_{HNH} = 107.29°, in good agreement with the experimental data[119] (r_{NH} = 1.0124 Å, θ_{HNH} = 107.67°) and the higher-level calculations results. The MP2-optimized structure possesses a dipole moment of 1.782 D, comparable to the CCSD(T)/6-311++G(d,p) value (1.808 D) but larger than the CCSD(T)/6-311++G(2d,2p) value (1.682 D), the CCSD(T)/aug-cc-pV5Z value (1.622 D), and the experimental gas-phase value (1.561 D).[57] Table 2.1 also shows that frequencies calculated at the MP2 level are close to the experimental[120] and the CCSD(T) values.

Table 2.1. Properties of the ammonia monomer calculated at various ab initio levels and corresponding experimental values. Values from the optimized Drude model are also given (see Section 2.3.3).

Property	MP2(FC)/ 6-311++G(d,p)	CCSD(T)/ 6-311++G(d,p)	CCSD(T)/ 6-311++G(2d,2p)	CCSD(T)/ aug-cc-pV5Z	Drude	Expt.
NH bond (Å)	1.0135	1.0167	1.0120	1.0122	1.0135	1.0124[a]
HNH angle (°)	107.29	106.84	106.69	106.60	107.29	106.67[a]
HNHH dihedral (°)	114.03	114.13	113.74	113.56	114.03	112.15[a]
Dipole (D)	1.782	1.808	1.682	1.622	1.782	1.561[b]
Vibration frequencies (cm^{-1})						
ν_1	3530	3485	3491	3479	3556	3337[c]
ν_2	1069	1094	1086	1056	1614	950[c]
ν_3	3681	3621	3613	3611	3667	3444[c]
ν_4	1665	1662	1693	1674	2218	1627[c]

[a] Reference 119. [b] Reference 57. [c] Reference 120.

2.3.1.2. $(NH_3)_m$ (m = 2−7) Clusters

Figure 2.1 shows structures of the $(NH_3)_m$ clusters (m = 2−7) obtained from geometry optimization at the MP2(FC)/6-311++G(d,p) level. Table 2.2 lists the intermolecular structural properties and the interaction energies of three structures of the dimer, with and without correction for BSSE (E^{CP} and E, respectively). Table 2.3 reports the MP2 interaction energies of the clusters and the corresponding energies calculated with the optimized Drude model (see section 2.3.3), along with literature data from ab initio calculations, empirical potential functions, and experiments.

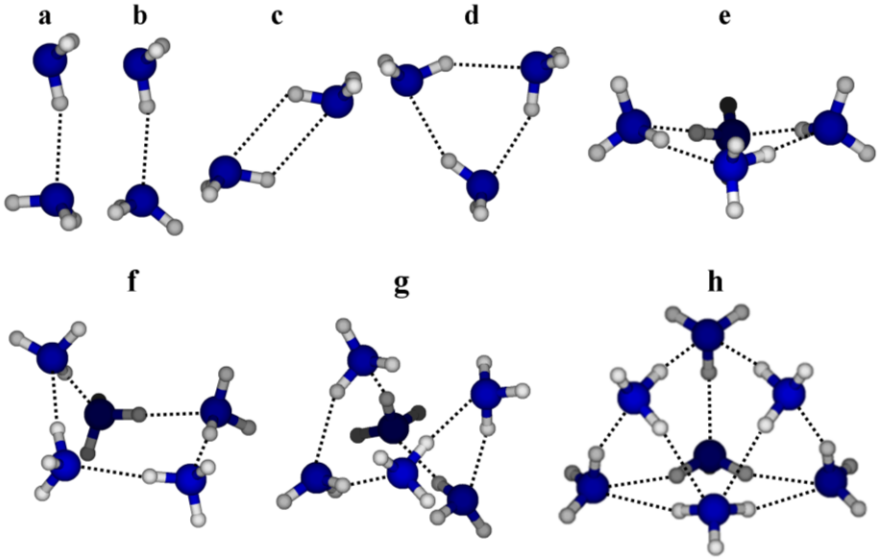

Figure 2.1. Geometries of ammonia clusters optimized at the MP2(FC)/6-311++G(d,p) level: (a) eclipsed dimer, (b) staggered dimer, (c) cyclic dimer (transition state), (d) trimer, (e) tetramer, (f) pentamer, (g) hexamer, and (h) heptamer.

Table 2.2. Intermolecular geometrical parameters, $r_{N\cdots N}$ (Å) and ∠N···H−N (°), and interaction energies with and without correction for BSSE (E^{CP} and E, respectively, in kcal/mol) for the three structures of the ammonia dimer (a, eclipsed; b, staggered; c, cyclic TS), optimized at the MP2 and CCSD(T) levels of theory.

Structure	MP2(FC)/6-311++G(d,p)				CCSD(T)/6-311++G(d,p)				CCSD(T)/6-311++G(2d,2p)			
	E	E^{CP}	$r_{N\cdots N}$	∠N···H−N	E	E^{CP}	$r_{N\cdots N}$	∠N···H−N	E	E^{CP}	$r_{N\cdots N}$	∠N···H−N
a	−3.80	−2.73	3.258	165.5	−3.74	−2.62	3.277	167.0	−3.28	−2.81	3.282	161.9
b	−3.80	−2.68	3.261	167.4	−3.74	−2.61	3.264	165.4	−3.21	−2.70	3.304	165.8
c	−3.55	−2.78	3.172	121.6	−3.52	−2.68	3.181	121.4	−3.17	−2.76	3.195	121.7

Table 2.3. Uncorrected (E) and CP-corrected (E^{CP}) binding energies of the $(NH_3)_m$ clusters (m = 2–7) calculated at the MP2(FC)/6-311++G(d,p) level compared with computational and experimental data from the literature. All energies are in kcal/mol.

m	Ab initio				Potential models					Expt.[h]
	E [a]	E^{CP} [a]	Kulkarni and Pathak (E)[b]	J.-Barral and Mella (E^{CP})[c]	Greer *et al.*[d]	Beu and Buck[e]	J.-Barral *et al.*[f]	Yu and Yang[g]	E^{Drude} [a]	
2(a)	−3.80	−2.73	−4.03	−2.74		−2.78		−2.93	−2.64 (0.045)	2.57−3.15[i], < 2.8[j], < 2.72[k], 2.77[l]
2(b)	−3.80	−2.68							−2.63 (0.025)	
2(c)	−3.55	−2.78		−2.74				−2.92	−2.40 (0.190)	
3	−12.31	−9.34	−13.02	−9.24	−8.44	−8.26	−9.06	−9.76	−8.13 (0.403)	
4	−19.32	−14.17	−20.12	−14.30	−13.10	−12.62	−14.91	−15.12	−13.24 (0.233)	
5	−24.66	−17.88	−25.48	−18.16	−16.93	−16.72	−19.45	−18.91	−17.30 (0.116)	
6	−31.32	−22.56	−31.90*		−22.74*	−22.70*	−24.29*		−22.11 (0.075)	
7	−38.91	−28.27			−28.55	−28.22	−30.14		−28.50 (−0.033)	

[a]This work. Values in parentheses represent the error per molecule compared to E^{CP}, calculated as $(E^{Drude} - E^{CP})/m$. [b]Reference 59, at the MP2/6-31++G(d,p) level and uncorrected for BSSE. [c]Reference 60, at the MP2/aug-cc-pVDZ level and corrected for BSSE. [d]Reference 62, using an additive rigid potential model. [e]Reference 63, using an additive rigid potential model. [f]Reference 64, using a rigid-polarizable potential model. [g]Reference 65, using the ABEEM ammonia-8P potential. [h]Experimental data are not for a specific dimer geometry. [i]Infrared photodissociation energy from Ref. 53. [j]Infrared photodissociation energy from Ref. 54. [k]Infrared photodissociation energy from Ref. 55. [l]Dissociation energy using threshold photoelectron photoion coincidence time-of-flight method.[56] *Binding energy refers to a conformer different from the one reported in this study.

Geometry optimizations of the dimer show that both the eclipsed and staggered isomers (Figures 2.1a and 2.1b, respectively) are stable and that the doubly hydrogen-bonded cyclic dimer (Figure 2.1c) is a first-order transition state (TS), in accord with previous ab initio results.[58,60] The very weak stability of the eclipsed isomer relative to the staggered one (0.05 kcal/mol at the MP2 level) is consistent with a very low rotation barrier of the hydrogen bond acceptor about its C_3 axis.[58]

The counterpoise procedure appears to overestimate the BSSE of some conformers, and yields E^{CP} values lower for the TS structure (Figure 2.1c) than for some of the stable isomers (see Table 2.2). For instance the MP2(FC)/6-311++G(d,p) calculations show a BSSE of 0.77 kcal/mol for the TS structure, compared to 1.07 kcal/mol for the eclipsed isomer and 1.12

kcal/mol for the staggered one. On the other hand, the eclipsed isomer is 0.05 kcal/mol more stable than the TS structure at the CCSD(T)/6-311++G(2d,2p) level, which represents an energy barrier to proton donor-acceptor interchange comparable to the 0.02 kcal/mol value reported by Lee and Park at the MP2/aug-cc-pVQZ//MP2/aug-cc-pVTZ level[58] and the 0.007 kcal/mol value reported by Janeiro-Barral and Mella at the MP2/aug-cc-pVQZ level.[60]

Table 2.2 shows good agreement between the structural and energetic properties of the minimum-energy isomer at MP2 and CCSD(T) levels, with discrepancies of at most 0.11 kcal/mol for binding energies, 0.024 Å for N···N distances, and 3.6° for N···H−N angles. The MP2 binding energy of the dimer, $E^{CP} = -2.73$ kcal/mol, is in agreement with the experimentally reported infrared photodissociation energies of the dimer (2.57−3.15 kcal/mol,[53] < 2.8 kcal/mol,[54] and < 2.72 kcal/mol[55]). The overall good agreement between the monomer and dimer properties calculated at the MP2 level and those calculated at the higher CCSD(T) level suggests that the MP2(FC)/6-311++G(d,p) level of theory is suitable for studying ammonia clusters.

The lowest-energy conformation of the trimer is a C_{3h}-symmetric cyclic isomer (Figure 2.1d), in agreement with previous ab initio results.[59,60] The N···N separation in the trimer is 3.173 Å, significantly shorter than the distance observed in the minimum-energy dimer (3.258 Å). This shortening indicates binding cooperativity: despite the frustration induced in the individual hydrogen bonds, each dimer is strengthened upon binding of a third NH_3 molecule.

The most stable ammonia tetramer is a cyclic "boat" structure[60] (Figure 2.1e) with a binding energy $E^{CP} = -14.17$ kcal/mol. Molecules in direct contact are separated by an equal N···N distance of 3.160 Å, which is 0.013 Å shorter than in the trimer.

The most stable pentamer is a non-planar cyclic structure[59,60] with four quasi-planar ammonia molecules and a fifth molecule above the plane (Figure 2.1f). The CP-corrected interaction energy of the complex is −17.88 kcal/mol and the N···N separation between H-bonded ammonia molecules varies between 3.145 Å and 3.171 Å.

Kulkarni and Pathak[59] have reported cyclic and chair-like conformers as the two most stable hexamers, with CP-uncorrected binding energies (E) of −31.90 and −30.96 kcal/mol, respectively (calculated at the MP2/6-31++G(d,p) level). Model potential studies on the hexamer however have suggested various other non-symmetric conformations as global minima.[62−64] Our MP2 calculations suggest the minimum-energy hexamer to be a C_1 symmetry conformation with distorted tetragonal bipyramidal geometry (Figure 2.1g). This conformer possesses a binding

energy E^{CP} = −22.56 kcal/mol, 0.45 and 0.99 kcal/mol lower than the cyclic and chair-like hexamers optimized at the same level (structures not shown).

Similarly to previous potential models results,[62–64] the global energy minimum of the heptamer is a C_s symmetrical isomer (Figure 2.1h) with a binding energy E^{CP} = −28.27 kcal/mol.

2.3.1.3. $NH_3(H_2O)_n$ (n = 1−4) Clusters

Figure 2.2 shows the geometries for ammonia in complex with one to four water molecules optimized at the MP2(FC)/6-311++G(d,p) level. The corresponding ab initio binding energies are reported in Table 2.4. As for the ammonia dimer, MP2 calculations on the NH_3−H_2O dimer are compared to CCSD(T)/6-311++G(d,p) and CCSD(T)/6-311++G(2d,2p) calculations.

The minimum-energy isomer of the ammonia-water dimer possesses a trans N···H−O hydrogen-bonded structure (Figure 2.2a; E^{CP} = −5.89 kcal/mol). The cis conformer (Figure 2.2b) is a first order TS with a binding energy E^{CP} = −5.88 kcal/mol. The 0.01 kcal/mol difference between the cis and trans isomers represents the barrier height to internal rotation of NH_3 around its C_3 axis and is in agreement with microwave and far-infrared experimental results (0.03 ± 0.001 kcal/mol).[87] The third structure reported for the dimer (Figure 2.2c) is an unstable O···H−N hydrogen-bonded structure obtained from an optimization in which the O···H−N angle is constrained at 180°. It is 3.80 kcal/mol less stable than the N···H−O bonded dimer, showing that ammonia is a better H-bond acceptor than donor.[86–90] The N···O separation is 2.937 Å in conformer a, 2.940 Å in conformer b, and 3.211 Å in conformer c. The N···H−O angle is 171° in both isomers a and b, indicating a non-linear hydrogen bond in agreement with experimental results.[87] Optimization of conformer a at the CCSD(T)/6-311++G(d,p) level shows an N···O distance of 2.955 Å, an N···H−O angle of 171°, and E^{CP} = −5.90 kcal/mol, while optimization at the CCSD(T)/6-311++G(2d,2p) level shows an N···O distance of 2.958 Å, an N···H−O angle of 171°, and E^{CP} = −5.95 kcal/mol, in good agreement with the MP2 results. The MP2-calculated binding energy and structural parameters of the global minimum isomer are also in good agreement with Lane *et al.* calculations at the CCSD(T)/aug-cc-pVQZ level ($r_{N\cdots O}$ = 2.938 Å, ∠N···H−O = 170°, and E^{CP} = −6.33 kcal/mol).[96]

By comparison, MP2(FC)/6-311++G(d,p) geometry optimization on the water dimer, $(H_2O)_2$, shows a more linear hydrogen-bonded complex with an O···O distance of 2.914, O···H–O angle of 177°, and a binding energy E^{CP} = −5.15 kcal/mol. The water dimer is 0.74 kcal/mol

less stable than the ammonia-water dimer, which indicates that ammonia is a better hydrogen bond acceptor than water.

The optimal trimer, tetramer, and pentamer structures are cyclic complexes with two hydrogen bonds per molecule (Figures 2.2d, 2.2e, and 2.2f).[94,97,99–101] Due to the cooperative nature of the interactions, distances between hydrogen-bonded molecules are shorter in larger clusters. For example, the $r_{O\cdots N}$ distance for the N···H−O bond is 2.937 Å for the dimer (Figure 2.2a), but becomes 2.916 Å for the trimer (Figure 2.2d), 2.788 Å for the tetramer (Figure 2.2e), and 2.780 Å for the pentamer (Figure 2.2f). Similarly, the $r_{O\cdots N}$ distance for the O···H−N bond goes from 3.211 Å for the constrained dimer (Figure 2.2c) to 3.006 Å for the pentamer (Figure 2.2f). The $r_{O\cdots O}$ distance follows a similar trend: 2.914 Å for the water dimer (not shown), 2.799 Å for the trimer (Figure 2.2d), 2.747–2.777 Å for the tetramer (Figure 2.2e), and 2.717–2.762 Å for the pentamer (Figure 2.2f).

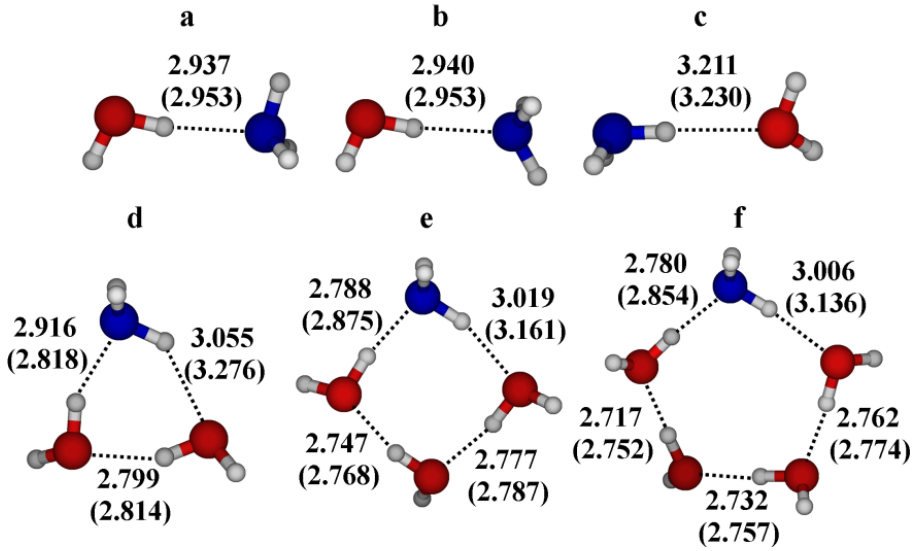

Figure 2.2. Geometries of $NH_3(H_2O)_n$ (n = 1−4) clusters optimized at the MP2(FC)/6-311++G(d,p) level. Numbers represent $r_{O\cdots O}$ and $r_{N\cdots O}$ distances (in Å) for the ab initio optimal structures and in brackets for the Drude model optimal geometries (see section 2.3.3).

Table 2.4. Uncorrected (E) and CP-corrected (E^{CP}) binding energies of the $NH_3(H_2O)_n$ (n = 1−4) clusters at MP2(FC)/6-311++G(d,p) level in comparison with Drude models and literature ab initio data. All energies are in kcal/mol.

n	This work			Literature
	E	E^{CP}	E^{Drude}	
1(a)	−7.46	−5.89	−5.68	−5.99[a], −6.17[b], −6.30[c], −6.37[d], −5.99[e], −6.33[f], −6.03[g]
1(b)	−7.43	−5.88	−5.68	−6.17[b], −6.36[d]
1(c)	−3.22	−2.09	−2.38	
2	−18.06	−14.12	−13.06	−15.52[d]
3	−30.10	−23.00	−22.60	−21.35[h]
4	−41.29	−31.27	−30.81	−29.00[h]

[a]Reference 91 CP-corrected binding energy calculated at the MP2/TZ2P level. [b]Reference 92 CP-corrected binding energies calculated at MP2/aug-cc-pVTZ//CCSD(T)/aug-cc-pVTZ level. [c]Reference 93 CP-corrected binding energy at the MP2/cc-pV5Z level. [d]Reference 94 CP-corrected binding energies at the MP2/aug-cc-pVTZ level. [e]Reference 95 CP-corrected binding energy at the MP2/6-31G* level. [f]Reference 96 CP-corrected binding energy at the CCSD(T)/aug-cc-pVQZ level. [g]Reference 97 CP-corrected binding energy at the MP2/6-61G(d,p)//MP4SDTQ/6-311++G(3df,2pd) level. [h]Reference 99 Binding energies corrected for zero-point energy at the MP2/6-311+G(d,p) level but uncorrected for BSSE.

2.3.1.4. $H_2O(NH_3)_n$ (n = 2−4) Clusters

MP2(FC)/6-311++G(d,p) geometry optimizations are performed on the clusters formed of one water molecule complexed with two, three, and four ammonia molecules. To the best of our knowledge, the only theoretical investigation on $H_2O(NH_3)_n$ clusters larger than the dimer was reported on the $H_2O(NH_3)_2$ complex by Rzepkowska *et al.* at the MP2/aug-cc-pVTZ level.[94] The minimum energy conformers of these clusters are shown in Figure 2.3. Binding energies are reported in Table 2.5.

As for the $(NH_3)_3$ and $NH_3(H_2O)_2$ trimers, the minimum-energy conformation of $H_2O(NH_3)_2$ is a cyclic isomer with two H-bonds per molecule (Figure 2.3a). Separations of heavy atoms in the O···H−N, N···H−N, and N···H−O hydrogen bonds of the trimer are 0.153, 0.126, and 0.099 Å shorter than the corresponding separations in the isolated dimers. In comparison to the calculated value E^{CP} = −12.44 kcal/mol, Rzepkowska *et al.* have reported a value E^{CP} = −13.58 kcal/mol at the MP2/aug-cc-pvTZ level.[94]

Three conformers are optimized for the tetramer (Figures. 2.3b, 2.3c, and 2.3d), with conformer b 1.30 kcal/mol more stable than conformer c and 3.14 kcal/mol more stable than conformer d. Structures b and c are quasi-planar and structure d is pyramidal.

Four stable conformations are identified for the pentamer. In the most stable one (Figure 2.3e), water and three ammonia molecules form a planar cyclic structure and the fourth, out-of plane, ammonia molecule acts as a proton donor to water and acceptor to one ammonia molecule. The other pentamer structures (Figures 2.3f, 2.3g, and 2.3h) are all characterized by water and three ammonia molecules in "boat" conformations and are respectively 0.47, 0.73, and 1.18 kcal/mol less stable than the global minimum.

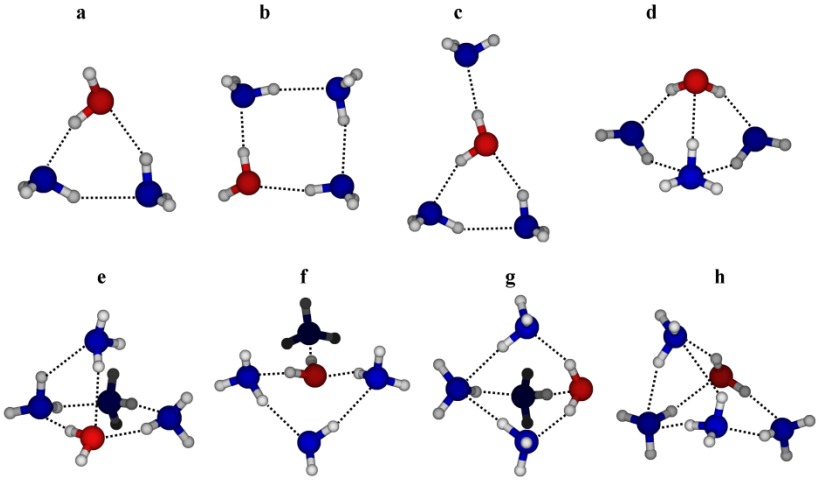

Figure 2.3. Geometries of $H_2O(NH_3)_n$ (n = 2−4) clusters optimized at the MP2(FC)/6-311++G(d,p) level.

Table 2.5. Uncorrected (E) and CP-corrected (E^{CP}) binding energies of the $H_2O(NH_3)_n$ clusters (n = 2−4) at MP2(FC)/6-311++G(d,p) level. Binding energies calculated with the Drude model (E^{Drude}) are also reported. All energies are in kcal/mol.

Complex	Conformer	E	E^{CP}	E^{Drude}
$H_2O(NH_3)_2$	a	−15.87	−12.44	−10.75
$H_2O(NH_3)_3$	b	−23.99	−18.18	−16.66
	c	−21.81	−16.88	−15.70
	d	−19.60	−15.04	−15.33
$H_2O(NH_3)_4$	e	−30.10	−22.41	−20.80
	f	−29.00	−21.94	−21.46
	g	−28.94	−21.68	−21.71
	h	−28.19	−21.23	−21.15

2.3.2. Potential Energy Surfaces

Ab initio potential energy curves for NH_3 in complex with NH_3 and with H_2O are reported as dashed lines in Figure 2.4, along with the corresponding solid curves calculated with the Drude model (see section 2.3.3). Three curves are calculated for the ammonia homodimer. Curve 2.4a is calculated by scanning the N···N separation between the two molecules in the eclipsed conformation from 2.0 to 8.0 Å. Curve 2.4b is calculated by scanning the angle N···N−H from 20 to 160° at the equilibrium N···N separation (3.258 Å) and describes the rotation of the hydrogen bond donor molecule in the mirror-symmetry plane of the dimer. Curve 2.4c is calculated by scanning the dihedral angle H−N···N−H from 0 to 180° at N···N separation of 3.261 Å and shows the change in energy as the staggered conformer is transformed into the eclipsed one. While the 0° structure corresponds to the exact staggered conformer, the structure at 180° is not the exact eclipsed conformer, which explains the 1.1 kcal/mol difference observed in curve 2.4c instead of the expected 0.05 kcal/mol (see Table 2.1). Similarly, three potential energy curves are calculated for the NH_3–H_2O dimer. The first curve (Figure 2.4d) is calculated by scanning the distance between N and O atoms in both the trans N···H−O and the O···H−N hydrogen-bonded conformers from 2.0 to 8.0 Å. Curve 2.4e is calculated by scanning the O···N−H angle from 30 to 180° at an N···O distance of 2.937 Å. Curve 2.4f is calculated by scanning the H−N···H−O dihedral angle from 0 to 180° at 2.937 Å. While the conformer at 180° in curve 2.4f is the exact trans isomer, the one at 0° is a distorted cis structure, which results in a 0.25 kcal/mol energy difference between the two structures instead of the 0.01 kcal/mol expected for the fully relaxed structures (see Table 2.4).

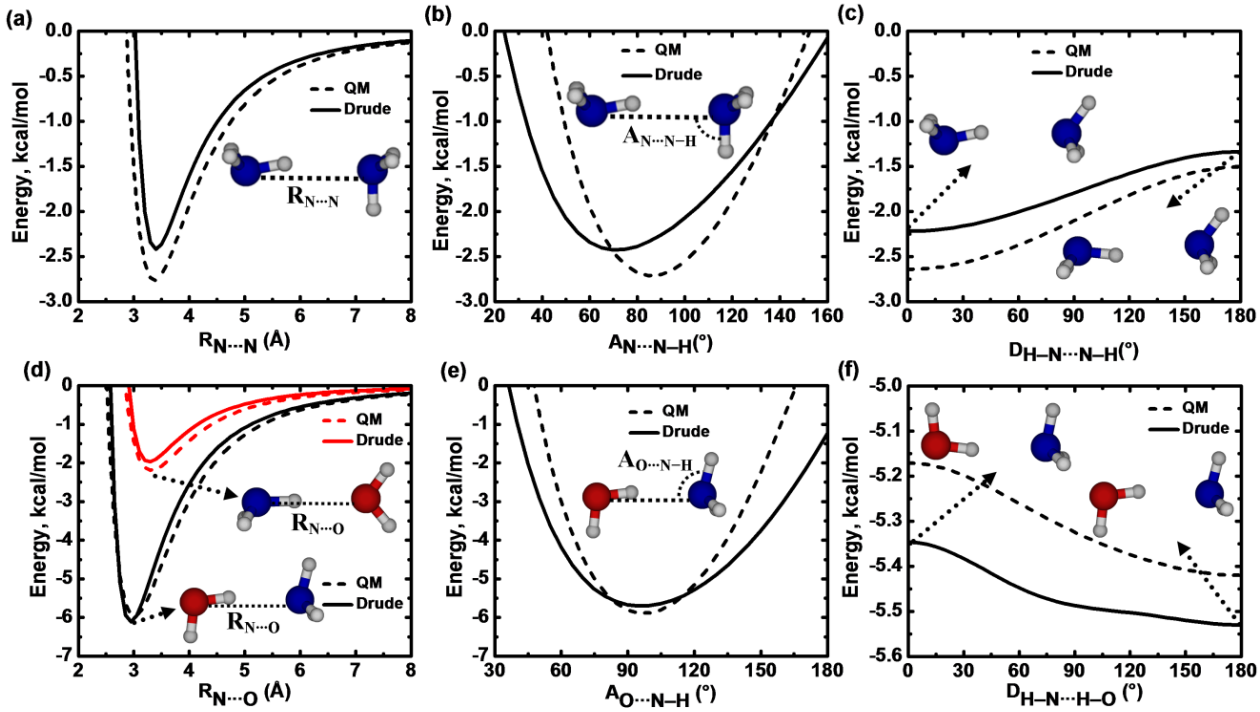

Figure 2.4. Potential energy curves for NH_3−NH_3 and NH_3−H_2O complexes from ab initio MP2(FC)/6-311++G(d,p) calculations (dashed lines) and from polarizable models (solid lines). For the ammonia dimer the following coordinates are scanned: (a) N···N distance in the eclipsed conformer; (b) N···N−H angle at N···N distance of 3.258 Å; (c) H−N···N−H dihedral at N···N distance of 3.261 Å. For ammonia-water dimer, the scanned curves are: (d) N···O distance in the trans N···H−O and the O···H−N hydrogen-bonded isomers; (e) the O···N−H angle at N···O distance of 2.937 Å; (f) H−N···H−O dihedral at N···O distance of 2.937 Å.

2.3.3. Optimized Force Field

In previous work,[30] we have optimized a polarizable model for NH_4^+−H_2O and NH_4^+−benzene interactions based on the ab initio properties of the two complexes. Following this work, we now optimize a polarizable model for NH_3−NH_3 and NH_3−H_2O interactions based on the ab initio properties of NH_3 and its dimers with NH_3 and H_2O. The equilibrium structural parameters for NH_3 (see section 2.3.1.1) are those from the MP2(FC)/6-311++G(d,p) optimized monomer: b_0 = 1.0135 Å and θ_0 = 107.29°. The corresponding force constants are chosen as k_b = 525.0 kcal/mol/Å^2 and k_θ = 84.0 kcal/mol/rad^2 and result in the following vibrational frequencies for the gaseous monomer: ν_1 (N–H asymmetric stretching) = 3556 cm^{-1}, ν_2 (N–H wagging) = 1614 cm^{-1}, ν_3 (N–H symmetric stretching) = 3667 cm^{-1}, and ν_4 (H–N–H scissoring) = 2218 cm^{-1}. While the bond force constant is chosen to reproduce the MP2(FC)/6-311++G(d,p) bond-stretching frequencies (ν_1 and ν_3, see Table 2.1), the angle force constant is set larger in order to

avoid unphysical distortions of the NH_3 geometry during MD simulations. Although our ab initio calculations show that ammonia molecules retain their gas-phase monomeric structure in small clusters (with a maximum deviation of 0.011 Å for the NH bond length and of 1.5° for the NHN angle), the angle potential for ammonia was reported to be particularly important for the vapor-to-liquid equilibrium properties of ammonia.[82] For this reason, we use an ammonia model with rigid bonds but flexible angles.

The optimized nonbonded parameters are as follows: q_{H} = 0.33192 e, q_{N} = –0.99576 e, α_N = 1.6905 Å^3, $E_{\mathrm{min,N}}$ = 0.10434 kcal/mol, $R_{\mathrm{min,N}}/2$ = 2.07801 Å, $E_{\mathrm{min,H}}$ = 0.06995 kcal/mol, and $R_{\mathrm{min,H}}/2$ = 0.55582 Å. The partial atomic charges reproduce the MP2-calculated dipole moment of gaseous NH_3 (1.782 D) and the isotropic Drude polarizability is set to the orientational average of the MP2-calculated molecular polarizability tensor. The LJ parameters for N and H are optimized to reproduce the binding energy and PESs of the NH_3–H_2O dimer (see Table 2.4 and Figure 2.4). These parameters are used for all N–O, N–H, H–O, and H–H pairs (based on the Lorentz–Berthelot combination rules, Eq. (2.2)), but separate LJ parameters are adjusted for N–N pairs, based on the ab initio properties of the ammonia dimer (see Table 2.3 and Figure 2.4): $E_{\mathrm{min,NN}}$ = 0.15418 kcal/mol and $R_{\mathrm{min,NN}}/2$ = 2.00607 Å. Note that H atoms in the SWM4-NDP water model have no LJ parameters and therefore do not contribute to the LJ energy. In both cases the parameters are first optimized based on the PESs of the dimers (calculated with rigid monomer geometries), then refined to reproduce their CP-corrected binding energies.[30] This latter refinement results in a slight disagreement between the Drude and ab initio PESs (see Figure 2.4).

As seen from Table 2.3, the optimized model gives binding energies for the various ammonia clusters in good agreement with ab initio data and with previous potential models.[62–65] It correctly reproduces the trend from the uncorrected energies E of dimer structures a, b, and c. The trend observed for the CP-corrected energies (E^{CP}) is likely due to overestimation of the BSSE of the stable dimer conformations. In comparison, the polarizable models of Janeiro-Barral *et al.*[64] and Yu and Yang[65] give binding energies in close agreement with E^{CP} for the dimer and trimer, but tend to overestimate the energies of larger clusters. The optimized Drude model also reproduces the binding cooperativity in these clusters. For example, while the N···N separation in the eclipsed ammonia dimer is 3.366 Å, it is 3.340 Å in the trimer and 3.301 Å in the tetramer.

The NH_3 model displays good transferability when combined with the SWM4-NDP H_2O model,[113] as indicated by the close agreement between E^{Drude} and E^{CP} energies for $NH_3(H_2O)_n$ and $H_2O(NH_3)_n$ clusters (see Tables 2.4 and 2.5). The model also reproduces the binding cooperativity in $NH_3(H_2O)_n$ (see Figure 2.2) and $H_2O(NH_3)_n$ clusters. For example, the Drude-optimized $H_2O(NH_3)_2$ complex shows separations between the heavy atoms in the O···H–N, N···H–N, and N···H–O hydrogen-bonded molecules that are 0.038, 0.051, and 0.023 Å shorter than the corresponding distances in the isolated dimers.

2.3.4. Liquid Ammonia

The Drude model for NH_3–NH_3 interaction is validated by calculating the structural, thermodynamic, and dynamic properties of liquid ammonia at its boiling point. For this purpose a system of 250 ammonia molecules is simulated at the normal boiling point of liquid ammonia (T = 239.8 K[34] and p = 1 atm = 0.1013 MPa). Four simulations with different initial configurations are run for 10 ns (40 ns total) and the liquid properties are calculated from the last 8 ns of each simulation. Under these thermodynamic conditions, the model yields an average molecular volume of 41.42 Å^3 and a density of 0.683 ± 0.001 g/cm^3, in better agreement with the experimental value[121] (0.682 g/cm^3) than the values reported by Rizzo and Jorgensen[69] (0.697 g/cm^3), Honda[74] (0.690 g/cm^3 at 277 K), Ren *et al.*[84] (0.676 g/cm^3), and Eckl *et al.*[77] (0.686 g/cm^3 at 240 K and 0.1196 MPa).

Enthalpy of vaporization, ΔH_{vap}, is calculated from the average net gain of potential energy $\langle \Delta u \rangle$ upon formation of the dense system.[102]

$$\Delta H_{\mathrm{vap}} = RT - \Delta u = RT - \left(\langle u \rangle_{\mathrm{l}} - \langle u \rangle_{\mathrm{g}}\right) = RT - \left(\langle u \rangle_{\mathrm{l}} - \frac{3}{2}RT\right) \qquad (2.7)$$

where R is the gas constant, T is the temperature, $\langle u \rangle_{\mathrm{l}}$ is the average potential energy per mole in the liquid phase, and $\langle u \rangle_{\mathrm{g}}$ is the average potential energy of gaseous NH_3. For an NH_3 model with fixed NH bond lengths, only the angle-bending modes contribute to the gas-phase potential energy:

$$\langle u \rangle_{\mathrm{g}} = \frac{3}{2}RT \qquad (2.8)$$

The average potential energy of the simulated system is found to be $\langle u \rangle_{\mathrm{l}}$ = –4.714 kcal/mol, which corresponds to ΔH_{vap}= 5.90 ± 0.005 kcal/mol, in good agreement with the experimental value, 5.58 kcal/mol.[121] Again, it should be emphasized that the model was not adjusted for any

of the bulk properties. By comparison, the AMOEBA force field of Ren *et al.*,[84] calibrated specifically to reproduce both the density and the enthalpy of vaporization, yields ΔH_{vap}= 5.54 kcal/mol.

The self-diffusion coefficient of an ammonia molecule in the liquid state is obtained from the long-time limit of the mean-square displacement of the nitrogen atoms:[122]

$$D_{\mathrm{PBC}} = \lim_{t\to\infty} \frac{1}{6t} \langle \frac{1}{N} \sum_{i=1}^{N} \left[\mathbf{r}_{\mathrm{N},i}(t) - \mathbf{r}_{\mathrm{N},i}(0)\right]^2 \rangle \qquad (2.9)$$

The resulting diffusion coefficient, obtained from a least-square linear fit of the last 8 ns of the trajectories, is corrected for system-size dependence using the formula of Yeh and Hummer:[123]

$$D = D_{\mathrm{PBC}} + \frac{2.837297\, k_{\mathrm{B}}T}{6\pi\eta L} \qquad (2.10)$$

where k_{B} is Boltzmann constant, η the shear viscosity of the solvent, and L is the average length of the cubic simulation box.[123] Using a value of 0.254 cP for the shear viscosity,[34] the self-diffusion coefficient of the bulk liquid is D = 5.90 ± 0.02 × 10^{-9} m^2 s^{-1}, in close agreement with the experimental value of 5.6 × 10^{-9} m^2 s^{-1} reported by Garroway and Cotts[47] and in excellent agreement with the experimental value of 5.83 × 10^{-9} m^2 s^{-1} reported by O'Reilly *et al.*[48] Compared to our calculated value, Impey and Klein reported a D_{PBC} value of 5.0 × 10^{-9} m^2 s^{-1} (at T = 260 K), which would correspond to a size-corrected D value of 6.6 × 10^{-9} m^2 s^{-1}.[66] Using two different potential models, Sagarik *et al.*[61] reported D_{PBC} values of 4.2 × 10^{-9} m^2 s^{-1} and 4.4 × 10^{-9} m^2 s^{-1} (at T = 237 K) which would correspond to size-corrected D values of 5.28 × 10^{-9} m^2 s^{-1} and 5.48 × 10^{-9} m^2 s^{-1}.

Isothermal compressibility measures the relative volume change accompanying any change in pressure:

$$\beta_T = -\frac{1}{V}\left(\frac{\partial V}{\partial P}\right)_T \qquad (2.11)$$

The isothermal compressibility of a system of N particles in equilibrium at constant temperature and pressure is directly related to the volume fluctuations around its average value:[124]

$$\beta_T = \frac{1}{k_{\mathrm{B}}T} \frac{\langle \Delta V^2 \rangle_{NPT}}{\langle V \rangle_{NPT}} \qquad (2.12)$$

where $\langle V \rangle_{NPT}$ is the average volume and $\langle \Delta V^2 \rangle_{NPT}$ are the average volume fluctuations. The isothermal compressibility of liquid ammonia at its boiling point (239.8 K) calculated using the

Drude model is 0.74 ± 0.05 GPa^{-1}, in excellent agreement with the experimental value of 0.74 GPa^{-1} at 238.0 K.[125]

The dielectric constant of the liquid, ε, was calculated following the procedure reported for the SWM4-NDP water model.[122] The model shows a value of 122, which is overestimated compared to the experimental value of 22.6 at 238.15 K.[50] This overestimation may be attributed to the higher dipole moment obtained from MP2 calculations of gaseous ammonia compared to the experimental value (see Table 2.1).

The molar heat capacity at constant pressure, C_p, is calculated from five simulations at different temperatures (219.8, 224.8, 229.8, 234.8, and 239.8 K) and at a constant pressure of 0.1013 MPa. The total energy U_{tot} and the volume V are averaged over time and C_p at 239.8 K is calculated from a linear fit of $\langle U_{\mathrm{tot}}\rangle + p\langle V\rangle$ versus T.[124]

$$C_p = \frac{1}{N}\left(\frac{\partial(\langle U_{\mathrm{tot}}\rangle + p\langle V\rangle)}{\partial T}\right)_{T=239.8\ \mathrm{K},\ \ p=0.1013\ \mathrm{MPa}} \qquad (2.13)$$

The model shows a value of C_p = 19.6 cal mol^{-1} K^{-1}, in good agreement with the experimental value of 18.12 cal mol^{-1} K^{-1}.[46]

Ricci *et al.*[43] conducted neutron diffraction experiments with isotropic H/D substitution (NDIS) to investigate the microscopic structure of liquid ammonia at two sets of temperatures and pressures, one at T = 213 K and p = 0.121 MPa and the other at T = 273 K and p = 0.483 MPa. A similar experiment was performed by Thompson *et al.*[44] to investigate the structure of ammonia and metallic lithium-ammonia solutions at 230 K. To compare with the Ricci *et al.* experiment, a system of 250 ammonia molecules is simulated for 10 ns at T = 213 K and p = 0.121 MPa. The structure of the liquid is analyzed from the $g_{\mathrm{NN}}(r)$, $g_{\mathrm{NH}}(r)$, and $g_{\mathrm{HH}}(r)$ radial distribution functions (RDFs), shown in Figure 2.5. The agreement between the calculated and experimental RDFs is very good, especially given the fact that no adjustments were made to reproduce the liquid structure data.

The $g_{\mathrm{NN}}(r)$ function (Figure 2.5a) shows three peaks centered at 3.37, 6.6, and 9.6 Å, indicating three well-defined solvation shells. The narrow shape of the first peak in the calculated $g_{\mathrm{NN}}(r)$ is likely due to the steepness of the Lennard-Jones repulsive potential.[122] The coordination number (up to the first minimum in the $g_{\mathrm{NN}}(r)$ curve, at 4.91 Å) is 12.5, in agreement with the experimental values of ~14 ammonia molecules reported by Ricci *et al.*[43] and of ~12 reported by Thompson *et al.*[44]

The $g_{NH}(r)$ function (Figure 2.5b) is similarly characterized by three peaks, located at 3.64, 6.6, and 9.6 Å. The high and narrow peak at $r \sim 1.0$ Å corresponds to the intramolecular NH bonds. The density at $r \sim 1.6$ Å in the experimental curve of Figure 2.5b corresponds to residual signal from intramolecular HH pairs.[43] Integration of $g_{NH}(r)$ over the range 1.9 Å $\leq r \leq$ 4.91 Å shows 37.5 neighboring H atoms around a central nitrogen, consistent with the NN coordination number at the same distance range (37.5 ÷ 3 = 12.5). The shoulder at $r \sim 2.44$ Å matches the experimental shoulder observed at ~2.25 Å by Ricci *et al.*[43] and at ~2.4 Å by Thompson *et al.*[44] and represents N···H pairs directly involved in hydrogen bonds.[43] The number of hydrogen bonds formed between a central nitrogen atom and its nearest neighbors can be estimated by integrating the function from 2.0 Å to the shallow minimum observed at 2.67 Å, which yields 2.0 hydrogen bonds per nitrogen atom, in agreement with the experimental numbers reported by Ricci *et al.*[43] (less than 2) and by Thompson *et al.*[44] (2.1 ± 0.5).

The $g_{HH}(r)$ function (Figure 2.5c) has the same characteristic features as the experimental function. The peak at $r \sim 1.6$ Å corresponds to the intramolecular HH pairs. Although the calculated function does not display a distinct peak at ~2.7 Å, its broad profile and the very weak shoulder at almost same position is consistent with experiment. This shoulder corresponds to the shortest intermolecular HH separation in the hydrogen-bonded dimers.[43]

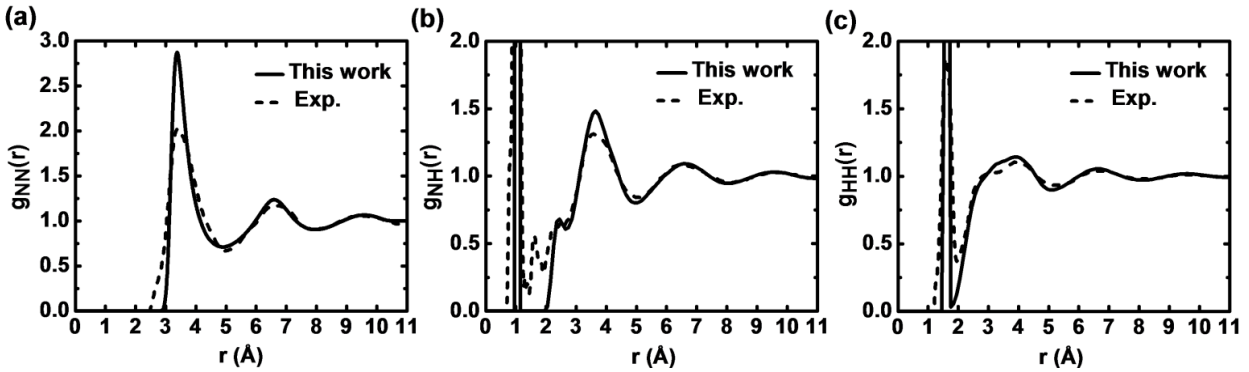

Figure 2.5. Radial distribution functions of ammonia at T = 213.0 K and p = 0.121 MPa calculated from MD simulation using the Drude model (solid lines) in comparison with NDIS experiment[43] at the same conditions (dashed lines).

Since the number of first-shell molecules is much larger in liquid ammonia (12.5) than in liquid water (4.63),[122] the fraction of molecules forming a hydrogen bond with a central molecule is much smaller in ammonia than in water.

Although the model overestimates the dielectric constant and is slightly overestimating the vaporization enthalpy of fluid ammonia (by 6%), it yields density, diffusion coefficient, isothermal compressibility, heat capacity, and structure in very good agreement with the experimental results. We have therefore not re-optimized the model for better agreement in the calculated enthalpy of vaporization since this deteriorates the performance on the other properties. It will be shown in the following section that the discrepancy in ΔH_{vap} is approximately uniform over a wide range of pressures, and therefore can be easily corrected.

2.3.5. Ammonia at Various p and T

The transferability of the NH_3 model is further tested by calculating the densities, vaporization enthalpies, diffusion coefficients, and structure of fluid ammonia at different thermodynamic conditions and comparing the results to available experimental data. See Figure 2.6 for an overview of the pressure and temperature conditions simulated in this work.

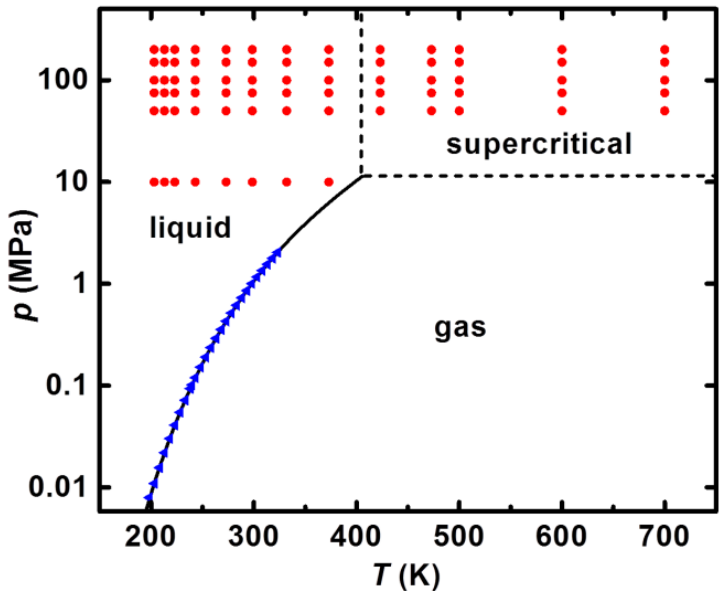

Figure 2.6. Phase diagram of NH_3. The solid and dashed lines are phase boundaries and their intersection is the critical point (T_c = 405.55 K, p_c = 11.38 MPa).[34] Red circles are the conditions at which densities, vaporization enthalpies, and self-diffusion coefficients are investigated (see Tables 2.6, and 2.9). Blue triangles are the pressure and temperature conditions at which densities and vaporization enthalpies are investigated (see Table 2.7). The pink square represents the normal boiling point of NH_3 (T = 239.8 K, p = 1 atm = 0.1013 MPa)[34] and the green square represents one of Ricci *et al.*'s NDIS experimental conditions[43] (T = 213 K, p = 0.121 MPa), at which the liquid structure of ammonia is investigated.

2.3.5.1. Density and Vaporization Enthalpy

The ammonia model is used in a total of 99 simulations: along the liquid-vapor phase boundary, and in the liquid and supercritical phases of fluid ammonia (under the thermodynamic conditions shown in blue and red in Figure 2.6). Each of the 99 systems is composed of 250 ammonia molecules and is simulated for 2 × 10 ns.

Figure 2.7a shows the calculated versus experimental[126] densities (see also Tables 2.6 and 2.7). The simulations show an average unsigned error of 3.6% for densities of simulations at $p \geq p_c$ (red circles on Figure 2.6; density values reported in Table 2.6) and of 1.5% for densities at the liquid-vapor boundary (blue triangles on Figure 2.6; density values reported in Table 2.7). The average overall unsigned error for all 99 simulations is 3.2%.

Figure 2.7b shows the calculated vaporization enthalpies from simulations at the liquid-vapor phase boundary *versus* the available corresponding experimental values[127] (see also Table 2.7). (No experimental data are available for ΔH_{vap} at the conditions shown in red in Figure 2.6, but calculated values are reported in Table 2.6.) Although the model systematically overestimates ΔH_{vap} (see Figure 2.7b and Table 2.7), the deviation from experimental data is approximately uniform over a wide range of temperatures and pressures and never more than 7.6%. Based on Figure 2.7b, we derive a correction for the calculated ΔH_{vap} as:

$$\Delta H_{vap}^{expt} = 0.971 \times \Delta H_{vap}^{calc} - 0.154 \text{ kcal/mol} \qquad (2.14)$$

This correction reduces the average unsigned error to one tenth of its uncorrected value (0.6% instead of 6.2%).

Table 2.6. Density (ρ, in g/cm^3) and vaporization enthalpy (ΔH_{vap}, in kcal/mol) of liquid ammonia at different temperatures and pressures.

T (K)	10 MPa[a]			50 MPa			75 MPa		
	ρ		ΔH_{vap}	ρ		ΔH_{vap}	ρ		ΔH_{vap}
	MD	Expt.[b]	MD	MD	Expt.[b]	MD	MD	Expt.[b]	MD
203	0.728	0.728	6.40	0.742	0.741	6.49	0.749	0.748	6.52
213	0.717	0.718	6.22	0.731	0.731	6.36	0.740	0.739	6.40
223	0.705	0.706	6.09	0.720	0.721	6.22	0.728	0.730	6.27
243	0.678	0.683	5.75	0.694	0.701	5.95	0.708	0.710	6.03
273	0.635	0.645	5.29	0.657	0.668	5.57	0.671	0.680	5.65
298.5	0.595	0.610	4.95	0.627	0.639	5.28	0.641	0.653	5.36
332	0.524	0.558	4.38	0.579	0.599	4.87	0.600	0.617	4.99
373	0.402	0.473	3.54	0.515	0.547	4.37	0.546	0.572	4.56
423[c]	–	–	–	0.429	0.475	3.54	0.477	0.513	4.06
473[c]	–	–	–	0.341	0.393	2.98	0.412	0.452	3.62
500[c]	–	–	–	0.299	0.347	2.84	0.379	0.419	3.41
600[c]	–	–	–	0.197	0.221	1.91	0.279	0.309	2.84
700[c]	–	–	–	0.153	0.164	1.73	0.219	0.237	2.57
T (K)	100 MPa			150 MPa			200 MPa		
	ρ		ΔH_{vap}	ρ		ΔH_{vap}	ρ		ΔH_{vap}
	MD	Expt.[b]	MD	MD	Expt.[b]	MD	MD	Expt.[b]	
203	0.756	-	6.56	0.769	-	6.63	0.780	-	6.69
213	0.746	0.747	6.44	0.759	0.760	6.51	0.771	0.772	6.57
223	0.735	0.738	6.31	0.749	0.752	6.39	0.762	0.765	6.46
243	0.715	0.719	6.08	0.731	0.735	6.16	0.745	0.749	6.24
273	0.682	0.691	5.72	0.701	0.709	5.83	0.719	0.725	5.93
298.5	0.654	0.666	5.44	0.676	0.687	5.57	0.696	0.705	5.68
332	0.617	0.632	5.09	0.642	0.657	5.24	0.665	0.678	5.37
373	0.568	0.591	4.69	0.602	0.622	4.88	0.628	0.646	5.03
423[c]	0.510	0.540	4.24	0.555	0.579	4.49	0.585	0.608	4.66
473[c]	0.453	0.489	3.85	0.508	0.538	4.15	0.546	0.572	4.35
500[c]	0.423	0.461	3.66	0.485	0.516	3.99	0.524	0.553	4.21
600[c]	0.332	0.367	3.13	0.407	0.439	3.52	0.455	0.487	3.77
700[c]	0.271	0.295	2.84	0.347	0.375	3.22	0.400	0.429	3.47

[a] At 10 MPa and at $T \geq 423$ K, NH_3 is a gas.[b] Reference 126. [c] Supercritical ammonia under all studied pressures.[126]

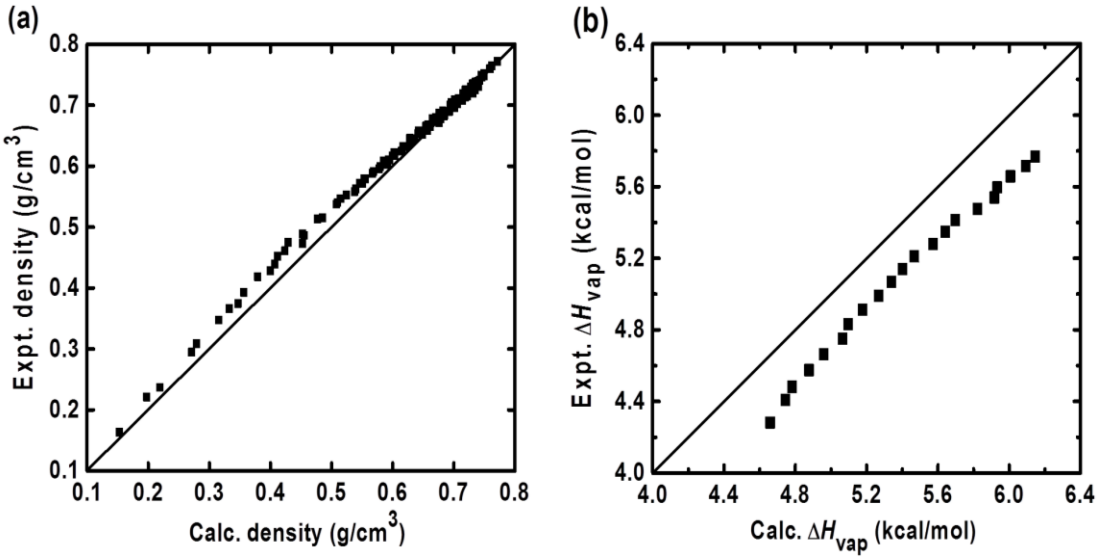

Figure 2.7. (a) Calculated versus experimental[126] densities of fluid ammonia under the thermodynamic conditions shown in red and blue in Figure 2.6 (also reported in Tables 2.6 and 2.7). (b) Calculated versus experimental[127] enthalpy of vaporization under the thermodynamic conditions shown in blue in Figure 2.6 (see also Table 2.7).

Table 2.7. Calculated densities and vaporization enthalpies of fluid ammonia at the liquid-vapor phase boundary in the temperature range 198.15 K $\leq T \leq$ 323.15 K and the pressure range 0.00793 MPa $\leq p \leq$ 2.032 MPa and corresponding experimental values.[127] The uncertainties in the reported densities and vaporization enthalpies are estimated to be 0.001 g/cm^3 and 0.005 kcal/mol, respectively.

T (K)	p (MPa)	ρ (g/cm^3)		ΔH_{vap} (kcal/mol)		T (K)	p (MPa)	ρ (g/cm^3)		ΔH_{vap} (kcal/mol)	
		MD	Expt.	MD	Expt.			MD	Expt.	MD	Expt.
323.15	2.03200	0.539	0.563	4.659	4.279	258.15	0.23630	0.656	0.659	5.642	5.345
318.15	1.78100	0.551	0.571	4.744	4.405	253.15	0.19020	0.661	0.665	5.697	5.410
313.15	1.55400	0.554	0.579	4.781	4.479	248.15	0.15160	0.676	0.671	5.821	5.471
308.15	1.35000	0.567	0.588	4.877	4.572	243.15	0.11960	0.679	0.678	5.864	5.536
303.15	1.16600	0.577	0.595	4.959	4.662	238.15	0.09319	0.685	0.684	5.932	5.593
298.15	1.00300	0.591	0.603	5.064	4.747	233.15	0.07177	0.693	0.690	6.007	5.654
293.15	0.85710	0.593	0.610	5.097	4.828	228.15	0.05454	0.701	0.696	6.092	5.711
288.15	0.72830	0.603	0.618	5.177	4.910	223.15	0.04087	0.705	0.702	6.145	5.764
283.15	0.61490	0.614	0.625	5.268	4.987	218.15	0.03016	0.714	0.708	6.231	–
278.15	0.51570	0.623	0.632	5.340	5.064	213.15	0.02190	0.719	0.714	6.293	–
273.15	0.42940	0.629	0.639	5.402	5.138	208.15	0.01516	0.731	0.719	6.409	–
268.15	0.35480	0.636	0.645	5.467	5.207	203.15	0.01092	0.735	0.725	6.461	–
263.15	0.29080	0.649	0.652	5.573	5.276	198.15	0.00793	0.740	0.731	6.532	–

Since the NH_3 model reproduces the experimental densities of liquid and supercritical ammonia within an average error of 3.2% over a wide range of temperature and pressure, it is expected to reliably describe the influence of temperature and pressure on the microscopic structure of the fluid.

We report in Figure 2.8 the $g_{NN}(r)$, $g_{NH}(r)$, and $g_{HH}(r)$ functions calculated at 50 MPa and at six different temperatures: 213, 273, 332, 423, 500, and 600 K. While the three functions display three intermolecular peaks (in addition to a shoulder in the $g_{NH}(r)$ function), only the first peak persists at high temperatures. The shoulders in the $g_{NH}(r)$ and $g_{HH}(r)$ functions at ~2.4 Å and ~2.7 Å, respectively, which indicate hydrogen bonding between ammonia molecules, decrease with increasing temperature. This indicates that preferential orientation of ammonia molecules—which allows for hydrogen bonding—decreases at high temperature.

Previous theoretical investigations have shown that while temperature strongly determines the local structure of liquid and supercritical ammonia, the influence of pressure is almost negligible.[78,80] Pressure and temperature-induced structural changes are analyzed by calculating the coordination number of the ammonia fluid at selected temperatures and pressures (see Table 2.8). The simulations show that the average coordination number decreases as the temperature increases, and that the decreasing trend is more pronounced at low pressure.[80] While pressure effect is minimal at low temperature, it has a significant influence on the local structure at high temperature. For example, a rise in pressure from 50 to 200 MPa increases the N–N coordination number by 0.4 at 203 K but by 5.3 at 700 K.

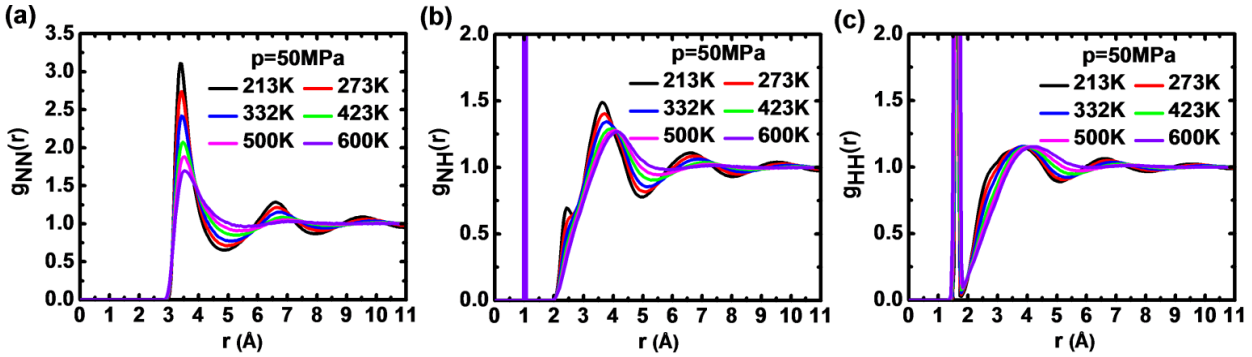

Figure 2.8. Temperature dependence of the (a) nitrogen–nitrogen, (b) nitrogen–hydrogen, and (c) hydrogen–hydrogen radial distribution functions in fluid NH_3 at p = 50 MPa.

Table 2.8. Average coordination number of NH_3 at different thermodynamic conditions, calculated by integrating the $g_{NN}(r)$ function up to 4.91 Å.

p (MPa)	203 K	273 K	332 K	423 K	500 K	600 K	700 K
50	12.7	11.6	10.3	8.1	5.9	3.6	2.6
200	13.1	12.3	11.6	10.3	9.2	8.0	7.9

2.3.5.2. Self-Diffusion Coefficient

Diffusion coefficients at high pressure have several applications in the chemical industry.[80] While diffusion data can be obtained from nuclear magnetic resonance and isotope trace techniques, experiments are difficult and time consuming.[49,80] Provided they are reliable, predictions from molecular dynamics simulations are therefore a valuable complement to experimental data.

Groß *et al.*[49] have measured the self-diffusion coefficients for fluid ammonia by NMR pulsed field gradient method at temperatures up to 473 K and pressures up to 200 MPa. To test the performance of the optimized ammonia model, MD simulations are performed at the different temperatures and pressures considered experimentally.[49] We also extend the investigation to higher temperatures, up to 700 K. A total of 73 thermodynamic conditions are simulated (see Figure 2.6 and Table 2.9). Each simulation is performed for a system of 2000 ammonia molecules for 8 ns in the *NPT* ensemble and the self-diffusion coefficient is calculated from the last 6 ns using Eq. (2.9). Such a large simulation system is necessary to prevent finite-size effects from speeding up the diffusion of large molecular clusters in the low-density supercritical phase and from causing an artificial non-Arrhenius behavior for the diffusivity. Whenever possible, the calculated self-diffusion coefficients are corrected for system-size dependence using Eq. (2.10),[123] with the shear viscosities of the fluid obtained from Ref. 126. The calculated self-diffusion coefficients are plotted against the experimental data in Figure 2.9.

Figure 2.9 and Table 2.9 show very good agreement between the calculated and experimentally measured self-diffusion coefficients. Excluding the point at 373 K and 10 MPa, which is significantly outside the Arrhenius trend, and is likely an aberration, the average unsigned error on the calculated D is 3.3%. This error is lower than the average error of 6.0% reported by Feng *et al.*,[80] which are calculated without the correction of Eq. (2.10). (With the correction of Eq. (2.10), the average unsigned error on Feng *et al*.'s results increases to 18%.) It should also be noted that the self-diffusion coefficients reported by Feng *et al.* at temperatures

higher than 332 K are based on *NVT* simulations using the experimental density rather than the density obtained from their model.[80,128] As in previous experimental[49] and theoretical[80,129] investigations, the data show a non-Arrhenius relation between ln D and $1/T$ at high temperatures and low pressures (see Table 2.9).

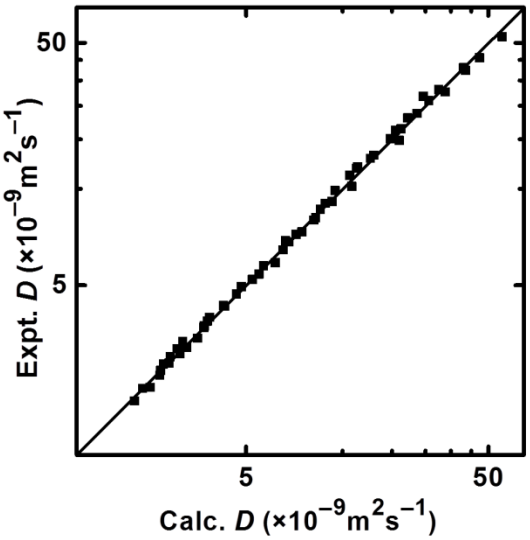

Figure 2.9. Log-log plot of the calculated versus experimental[49] self-diffusion coefficients of ammonia at some of the thermodynamic conditions shown in red in Figure 2.6 (see also Table 2.9).

Table 2.9. Self-diffusion coefficients, D, for NH_3 (in 10^{-9} m^2 s^{-1}).

T (K)	10 MPa[a]		50 MPa		75 MPa		100 MPa		150 MPa		200 MPa	
	MD	Expt.[b]	MD	Expt.[b]	MD	Expt.[b]	MD	Expt.[b]	MD	Expt.[b]	MD	Expt.[b]
203	2.66	2.61	2.28	2.37	2.20	2.1[d]	2.01[e]	1.90	1.73[e]	1.67	1.45[e]	–
213	3.36	3.40	2.74	2.93	2.60	2.7[d]	2.43	2.54	2.22	2.23	1.87	1.88
223	4.03	4.13	3.53	3.69	3.34	3.4[d]	3.15	3.03	2.84	2.77	2.40	2.39
243	5.90	6.02	5.30	5.29	4.78	4.9[d]	4.56	4.61	4.09	4.10	3.46	3.56
273	9.51	9.30	8.03	8.10	7.51	7.6[d]	7.11	7.01	6.60	6.20	5.65	5.57
298.5	13.65	12.8	11.33	11.1	10.13	10.3[d]	9.68	9.50	8.49	8.31	7.27	7.65
332	21.41	19.8	16.30	16.7	14.41	15.4[d]	13.38	14.2	11.64	12.3	10.62	10.9
373	41.43	49.2	25.35	25.6	21.77	22.1	19.69	20.1	16.83	17.2	14.27	15.2
423[c]	–	–	39.46	39.5	33.18	31.4	28.36	28.9	23.19	24.5	20.66	21.8
473[c]	–	–	56.92	53.0	45.94	43.4	40.19	38.5	31.16	32.1	29.26	30.1
500[c]	–	–	67.9	–	52.84	–	45.9	–	36.0	–	30.9	–
600[c]	–	–	125	–	91.0	–	74.4	–	56.9	–	45.9	–
700[c]	–	–	192	–	130	–	103.5	–	78.5	–	63.2	–

[a] At 10 MPa and $T \geq 423$ K, NH_3 is a gas. [b] Reference 49. [c] Supercritical ammonia under all studied pressures.[126] [d] Data extracted from Figure 3 of reference 49. [e] Data are uncorrected for the system-size dependence due to lack of experimental viscosities under these thermodynamic conditions.

2.3.6. Hydration of NH_3

As reported in sections 2.3.1.3 and 2.3.1.4, the NH_3 model (in combination with the SWM4-NDP water model[113]) reproduces the binding energies and structural properties of the $NH_3(H_2O)_n$ and $H_2O(NH_3)_n$ (n = 2–4) clusters. As a further test of transferability, the free energy of hydration of NH_3 relative to that of H_2O in bulk water, $\Delta\Delta G_{hydr}(NH_3 \rightarrow H_2O)$, is calculated at T = 298.15 K and p = 0.1013 MPa. The calculations show a value of −2.0 ± 0.1 kcal/mol. Taking into account the hydration free energy of the SWM4-NDP water molecule, –5.9 ± 0.1 kcal/mol,[113] this results in a hydration free energy of NH_3 equal to –3.9 ± 0.1 kcal/mol, in good agreement with the experimental value of –4.3 kcal/mol[130,131] and with hybrid QM/MM MD simulation results (–4.5 ± 0.2 kcal/mol).[109] By comparison, Rizzo and Jorgensen[69] have reported a value of –3.34 kcal/mol using a pairwise-additive model, Dang and Garrett[106] have reported a value of –5.6 ± 0.5 kcal/mol using a polarizable model, and Pártay *et al.*[108] have reported a value of –1.9 kcal/mol.

The hydration structure of NH_3 is investigated from the simulation of one ammonia molecule in 249 water molecules at 298.15 K and 0.1013 MPa. The $g_{NO}(r)$, $g_{NH}(r)$, $g_{HO}(r)$, and $g_{HH}(r)$ RDFs between the ammonia solute and its water solvent are reported in Figure 2.10. The $g_{NH}(r)$ RDF exhibits a narrow and well-separated peak at 1.93 Å that corresponds to N···H−O hydrogen-bonded pairs. Integration up to the minimum at 2.55 Å yields a coordination number of 1.8, indicating that the N atom acts as a hydrogen bond acceptor to about two water molecules. In comparison, Rizzo and Jorgensen[69] have calculated 1.23 N···H−O hydrogen bonds per N atom. A second peak centered at 3.43 Å depicts a more flexible solvation structure, as evidenced by the broader and less symmetric peak. Integration up to the second minimum (at 5.5 Å) results in a coordination number of ~46 hydrogen atoms, indicating ~23 water molecules in the first solvation shell of NH_3. The $g_{NO}(r)$ RDF exhibits a shoulder at 2.88 Å due to N···H−O hydrogen bonds, followed by a peak at 3.17 Å due to N–H···O bonds (see Figure 2.2). Integration up to the minimum at 5.53 Å confirms that the first solvation shell of NH_3 contains ~23 water molecules.

The RDFs are consistent with a picture of NH_3 hydration in which approximately two (1.8 on average) water molecules are forming strong N···H−O hydrogen bonds on the acceptor side of the ammonia molecule, while the donor side of the molecule is interacting with a large number (~21) of water molecules forming transient N−H···O hydrogen bonds.

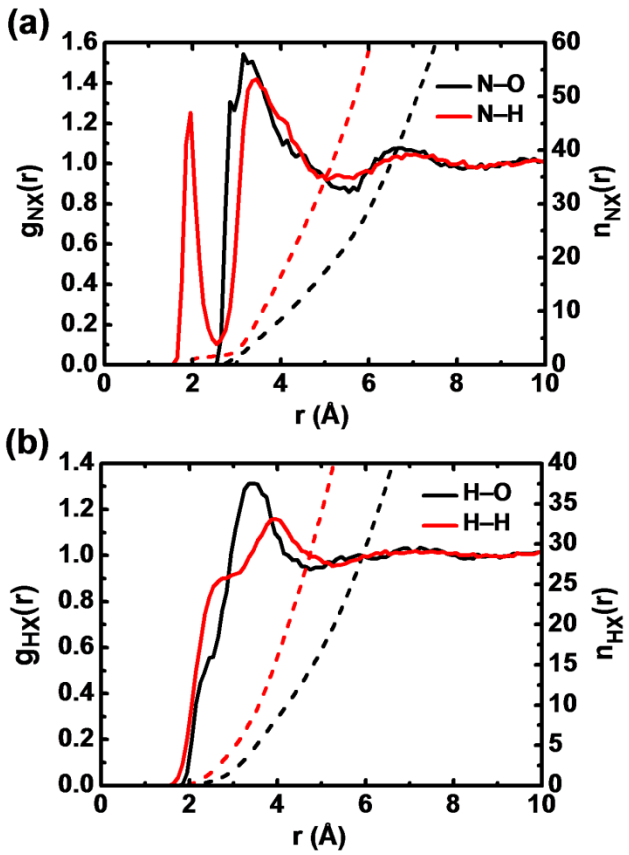

Figure 2.10. Radial distribution functions, $g(r)$, between a single ammonia molecule solvated by 249 water molecules at T = 298.15 K and p = 1 atm = 0.1013 MPa. Panel a shows nitrogen-oxygen (black) and nitrogen-hydrogen (red) RDFs and panel b shows hydrogen-oxygen (black) and hydrogen-hydrogen (red) RDFs. Dashed lines represent the corresponding running coordination numbers, $n(r)$.

2.3.7. Water Solvated in Ammonia

The $g_{ON}(r)$, $g_{OH}(r)$, $g_{HN}(r)$, and $g_{HH}(r)$ RDFs obtained from the simulation of one water molecule in 249 ammonia molecules at 239.8 K and 0.1013 MPa are reported in Figure 2.11. The $g_{ON}(r)$ RDF (Figure 2.11a) exhibits a peak with a maximum at 2.88 Å due to O–H···N hydrogen-bonded pairs and a shoulder at 3.17 Å due to O···H–N pairs. Integration up to the minimum at 4.48 Å shows 9.1 ammonia molecules in the first solvation shell of water. The $g_{OH}(r)$ RDF exhibits a peak at 2.31 Å (due to O···H–N pairs) that overlaps with a peak at 3.46 Å. Integration of $g_{OH}(r)$ up to the minimum at 2.67 Å shows 3.0 ammonia hydrogen atoms at coordinating distance from the water oxygen. Integration from 2.67 Å to 4.48 Å shows further 24.4 ammonia hydrogen atoms. The total number of ammonia hydrogen around the water molecule up to the first solvation shell, 3.0 + 24.4 = 27.4, is consistent with 9.1 ammonia molecules around water.

The $g_{HN}(r)$ RDF (Figure 2.11b) displays a narrow and well-separated first peak with a maximum at 1.95 Å, due to N···H–O hydrogen bonding. Integration up to the minimum at 2.60 Å results in a coordination number of 1.0, indicating that water is forming a total of two N···H–O hydrogen bonds with ammonia molecules in its first solvation shell. The $g_{HH}(r)$ RDF shows two peaks at 2.55 Å and 3.85 Å with their minima at 3.14 Å and ~4.7 Å, respectively.

To summarize, the first solvation shell of the water molecule if composed of ~9 ammonia molecules, including two acting as H-bond acceptors. The remaining seven ammonia molecules act as transient H-bond donors, three at a time.

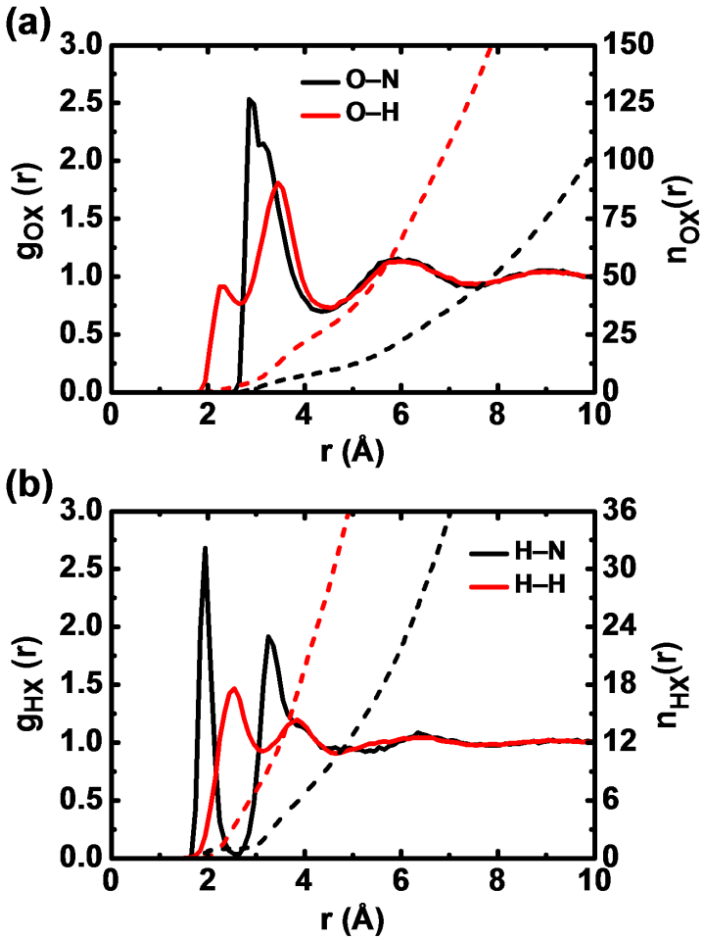

Figure 2.11. Radial distribution functions, $g(r)$, between a single water molecule solvated by 249 ammonia molecules at T = 239.8 K and p = 1 atm = 0.1013 MPa. Panel a shows oxygen-nitrogen (black) and oxygen-hydrogen (red) RDFs and panel b shows hydrogen-nitrogen (black) and hydrogen-hydrogen (red) RDFs. Dashed lines represent the corresponding running coordination numbers, $n(r)$.

2.3.8. Water-Ammonia Mixtures

We calculate the density and structure of various aqueous ammonia mixtures under different thermodynamic conditions: at T = 239.8, 273.15, and 293.15 K and at p corresponding to the vapor pressure of pure ammonia at the temperature simulated (0.1013, 0.4294, and 0.8571 MPa, respectively). The mixtures are composed of a total of 250 molecules with ammonia molar fraction, $x_{\mathrm{NH_3}}$, going from 0 to 100%. Two 10-ns simulations are performed for each system at each set of thermodynamic conditions. The water-rich systems at T = 239.8 K are simulated in the supercooled state. Figure 2.12 presents the calculated densities as a function of the composition (see also Table 2.10), together with the experimental densities measured by King *et al.*[132] at 293.15 K. The calculated densities are in excellent agreement with experiment, with a maximum error of 1.7%. Figure 2.12 shows a non-linear trend in the density-composition plot, with significant deviation from ideality for $x_{\mathrm{NH_3}}$ > 30–40%.

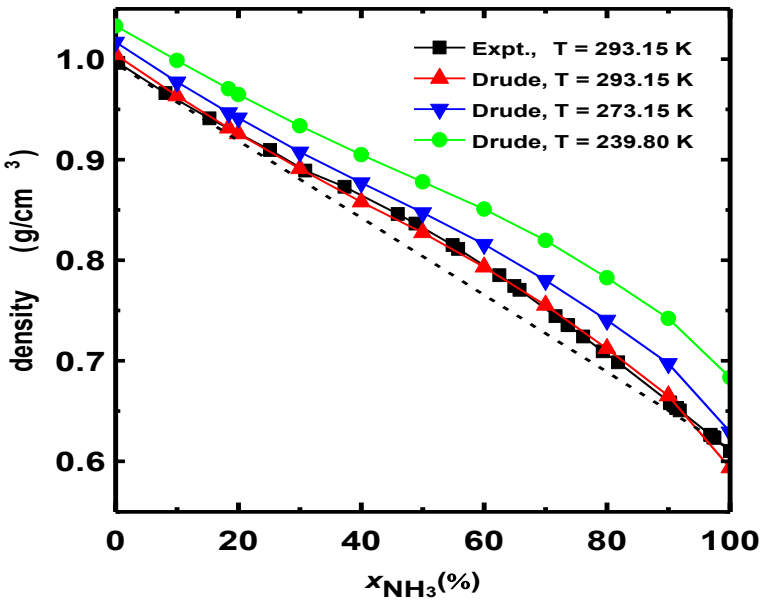

Figure 2.12. Densities of water-ammonia mixtures calculated using the Drude model at 239.8 K (green), 273.15 K (blue), and 293.15 K (red) and measured experimentally[132] at 293.15 K (black). The straight, dashed black line connects the experimental densities at $x_{\mathrm{NH_3}}$ = 0 and 100%.

Table 2.10. Density (in g/cm^3) of ammonia-water mixtures at different NH_3 mole fraction and at different temperatures and pressures, calculated from MD simulations.

T(K)/p(MPa)	x_{NH_3} (%)											
	0	10	18.4	20	30	40	50	60	70	80	90	100
239.80/0.1013	1.033	0.998	0.970	0.965	0.934	0.905	0.878	0.851	0.820	0.783	0.742	0.683
273.15/0.4294	1.017	0.977	0.947	0.942	0.908	0.878	0.847	0.816	0.780	0.740	0.697	0.629
293.15/0.8571	1.004	0.963	0.931	0.926	0.891	0.858	0.827	0.793	0.755	0.712	0.665	0.593

We plot in Figure 2.13 the total pair distribution function $g_{(N+O)-(N+O)}(r)$ for some of the compositions simulated at 273.15 K, along with the experimental function reported by Narten[41] for x_{NH_3}= 18.4% at 277.15 K. The figure shows that, as x_{NH_3} increases, the intensity of the band centered at ~2.8 Å decreases while the intensity of the band centered at ~3.4 Å increases. In comparison, the experimental $g_{(N+O)-(N+O)}(r)$ RDF displays a first maximum that shifts from 2.82 Å for water to 3.4 Å for ammonia.[41] The first peak corresponds to hydrogen-bonded O···O and N···O pairs. Its position is almost unaffected by x_{NH_3} (2.79 Å in pure water and only 2.85 Å at x_{NH_3}= 80%) because the water-water and ammonia-water dimers have comparable molecular separations (see section 2.3.1.3). The second peak, at ~3.4 Å, is due to N···N pairs. The pair distribution function calculated for x_{NH_3}= 18.4% follows the experimental distribution very closely. The only significant difference is the higher intensity of the calculated first peak, which (again) is likely the result of the steepness of the Lennard-Jones repulsive potential,[122] in addition to the packing of molecules being slightly closer at 273.15 K than at 277.15 K (the experimental temperature).

The weak intensity of the peak at ~3.4 Å at low ammonia concentrations (see Figure 2.13) confirms the absence of ammonia aggregation, in agreement with the experimental x-ray diffraction results.[8] The results also agree with previous theoretical investigations.[102] Tanabe and Rode have simulated the structure of an 18.45% aqueous ammonia solution at 293.15 K and 0.1013 MPa, and found that hydrogen bonding between ammonia molecules is hardly present at this concentration.[102]

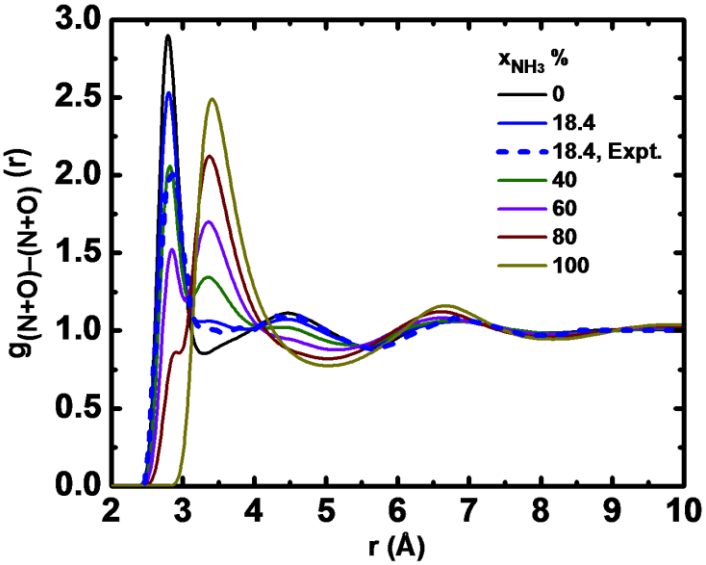

Figure 2.13. Total pair distribution function for aqueous ammonia solutions at different ammonia concentrations calculated from simulations at 273.15 K and 0.4294 MPa, The experimental[41] x-ray function for $x_{NH_3} = 18.4\%$ at 277.15 K is shown as dashed line.

In order to understand the microscopic structure giving rise to the observed non-ideal mixing properties, we plot in Figure 2.14 the numbers of H-bonds formed between ammonia and water molecules due to N···H–O, N···H–N, O···H–O, and O···H–N interactions, as a function of ammonia mole fraction at 273.15 K and 0.4294 MPa (see also Table 2.11). These are calculated by integrating functions $g_{\mathrm{N\text{-}H(H_2O)}}(r)$, $g_{\mathrm{N\text{-}H(NH_3)}}(r)$, $g_{\mathrm{O\text{-}H(H_2O)}}(r)$, and $g_{\mathrm{O\text{-}H(NH_3)}}(r)$ up to r = 2.55, 2.67, 2.45, and 2.67 Å, respectively. These distances represent the minimum of the first intermolecular peak of each function, and are almost composition-independent. The dashed lines in Figure 2.14 represent the trends expected for ideal mixing. The plot shows large deviations from ideal mixing in the numbers of N···H–O and O···H–N hydrogen bonds for x_{NH_3}> 20–30%. On the other hand, it shows smaller deviations in the numbers of O···H–O and N···H–N hydrogen bonds: water-water pairs are slightly enriched for x_{NH_3}< 50–60%, and ammonia-ammonia pairs slightly enriched for x_{NH_3}> 50–60%. In other words, water-ammonia association is stronger in ammonia-rich mixtures than in water-rich mixtures. This is consistent with the fact that O–H···N hydrogen bonds are significantly stronger than N–H···N bonds but comparable to O–H···O bonds—at least in gas phase. Using a more stringent definition of hydrogen bonding, Paul and Chandra[107] find 1.3 hydrogen bonds per ammonia molecule in neat ammonia, compared to 1.56 from the present simulations.

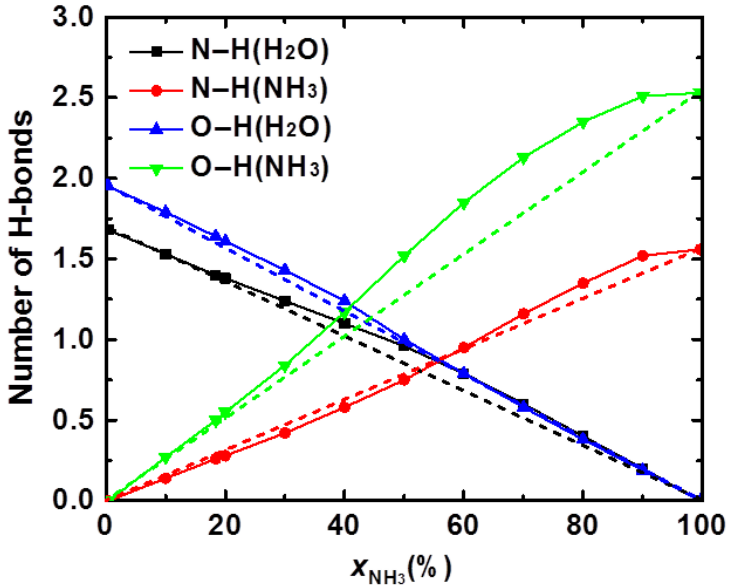

Figure 2.14. Number of hydrogen bonds per ammonia molecule due to N···H–O and N···H–N interactions, and per water molecule due to O···H–O and O···H–N interactions, as a function of ammonia molar fraction. Numbers are calculated by integrating the corresponding RDFs (see text). The highest coordination numbers in the black and green curves are calculated from the simulation of one ammonia molecule in 249 water molecules and of one water molecule in 249 ammonia molecules, respectively (at T = 273.15 K and p = 0.4294 MPa).

Table 2.11. Number of H-bonds between a central ammonia or water molecule and surrounding water and ammonia molecules due to N···H–O, N···H–N, O···H–O, and O···H–N interactions, at various percent ammonia molar fractions at 273.15 K and 0.4294 MPa.*

x_{NH_3} (%)	N···H–O	N···H–N	O···H–O	O···H–N
0	1.68	0	1.95	0
10	1.53	0.14	1.79	0.27
18.4	1.40	0.26	1.64	0.50
20	1.38	0.28	1.61	0.55
30	1.24	0.42	1.43	0.84
40	1.10	0.58	1.24	1.17
50	0.96	0.75	1.00	1.52
60	0.79	0.95	0.79	1.85
70	0.60	1.16	0.58	2.13
80	0.40	1.35	0.38	2.35
90	0.20	1.52	0.19	2.51
100	0.00	1.56	0	2.53

* See text for details of the calculations. The number of H-bonds from N···H–O interactions at x_{NH_3}= 0% is from simulation of one ammonia molecule in 249 water molecules, and the number of H-bonds from O···H–N interactions at x_{NH_3}= 100% is from simulation of one water molecule in 249 ammonia molecules.

The features observed in the density-composition plot (Figure 2.12) can thus be interpreted in terms of the local structure of the aqueous mixtures as follows: At low NH_3 concentrations (x_{NH_3}< 20–30%), in the composition range where excess density ($\rho - \rho_{ideal}$) is negligible, ammonia molecules are dispersed in solution and ammonia-water interactions are non-specific. However, at higher concentrations, ammonia-water pairs—particularly those forming O–H···N bonds, which are significantly more energetic and shorter than N–H···N bonds—become more pronounced and result in a positive excess density.

$\Delta G_{solv}(H_2O)$, the solvation free energy of H_2O, and $\Delta G_{solv}(NH_3)$, the solvation free energy of NH_3, are calculated at different mixture composition and temperatures. The results, along with the free energy difference $\Delta\Delta G_{solv} = \Delta G_{solv}(H_2O) - \Delta G_{solv}(NH_3)$ are shown in Figure 2.15 (see also Table 2.12). Figure 2.15a shows $\Delta G_{solv}(H_2O)$ to be approximately constant for x_{NH_3}< 50% and to increase (in absolute value) at higher ammonia concentrations. While solvation free energy is not easily decomposable into contributions from the various components of the mixture, this trend is consistent with the fact that, for ammonia-rich mixtures, each water molecule is involved in an excess of O–H···N hydrogen bonds, which are stronger. The slight decrease in the solvation free energy in pure ammonia can likely be attributed to the complete absence of N···H–O bonds and their replacement by weaker N···H–N bonds. The solvation free energy decreases with temperature, with the influence of temperature being more pronounced at higher ammonia mole fractions.

The solvation free energy of ammonia (Figure 2.15b) decreases almost uniformly with ammonia concentration. This trend can probably be attributed to the gradual replacement of strong N···H–O bonds by weaker N···H–N bonds (see Figure 2.14, black and red curves).

The relative free energy, $\Delta\Delta G_{solv}$ (Figure 2.15c), shows a systematic preference for water that increases with ammonia concentration and is maximum for x_{NH_3} around 80–90%. The preference for water over ammonia becomes more temperature-dependent for x_{NH_3}> ~50%, due mostly to the temperature-dependence of $\Delta G_{solv}(H_2O)$.

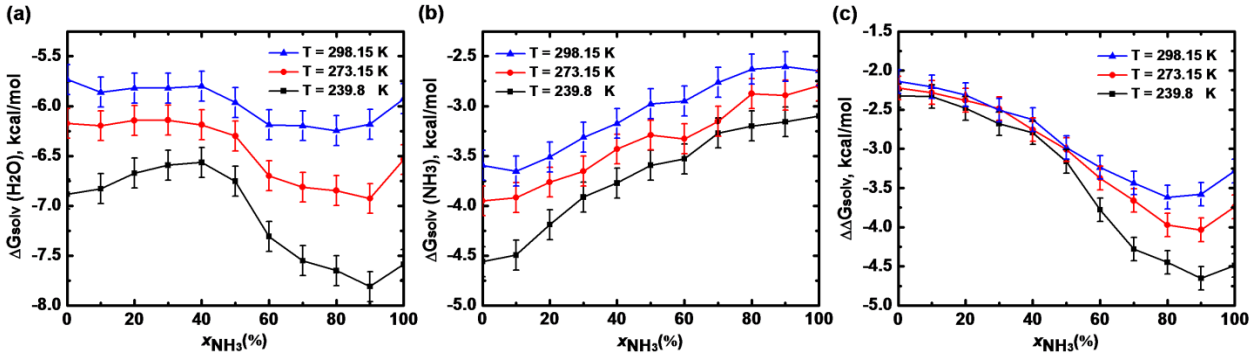

Figure 2.15. Solvation free energies of H_2O (a), NH_3 (b), and of H_2O relative to NH_3 (c) as a function of temperature and ammonia molar fraction. Three thermodynamic conditions are studied: T = 239.8, 273.15, and 298.15 K (with p = 0.1013, 0.4294, and 1.0030 MPa, respectively). Error bars are typically equal to ± 0.15 kcal/mol.

Table 2.12. Solvation free energy of H_2O, $\Delta G_{\mathrm{solv}}(H_2O)$, and NH_3, $\Delta G_{\mathrm{solv}}(NH_3)$, and the relative solvation free energy, $\Delta\Delta G_{\mathrm{solv}} = \Delta G_{\mathrm{solv}}(H_2O) - \Delta G_{\mathrm{solv}}(NH_3)$, in aqueous ammonia solutions of various ammonia molar fraction. Calculations are performed at three temperatures, T = 239.8, 273.15, and 298.15 K, and at the corresponding vapor pressure of liquid NH_3, 0.1013, 0.4294, and 1.003 MPa. Free energies are in kcal/mol.

x_{NH_3} (%)	$\Delta G_{\mathrm{solv}}(H_2O)$			$\Delta G_{\mathrm{solv}}(NH_3)$			$\Delta\Delta G_{\mathrm{solv}}$		
	239.8	273.15	298.15	239.8	273.15	298.15	239.8	273.15	298.15
0	−6.88	−6.17	−5.73	−2.32	−2.22	−2.14	−4.56	−3.95	−3.59
10	−6.83	−6.20	−5.86	−2.33	−2.28	−2.21	−4.50	−3.92	−3.65
20	−6.67	−6.14	−5.82	−2.48	−2.38	−2.31	−4.19	−3.76	−3.51
30	−6.59	−6.14	−5.82	−2.68	−2.49	−2.51	−3.91	−3.65	−3.31
40	−6.57	−6.19	−5.80	−2.79	−2.76	−2.63	−3.77	−3.43	−3.17
50	−6.75	−6.30	−5.96	−3.16	−3.01	−2.99	−3.59	−3.29	−2.98
60	−7.31	−6.70	−6.19	−3.78	−3.37	−3.24	−3.53	−3.33	−2.95
70	−7.55	−6.81	−6.20	−4.28	−3.66	−3.44	−3.27	−3.15	−2.76
80	−7.65	−6.85	−6.25	−4.45	−3.97	−3.62	−3.20	−2.87	−2.63
90	−7.81	−6.93	−6.18	−4.65	−4.04	−3.58	−3.16	−2.89	−2.60
100	−7.59	−6.54	−5.93	−4.49	−3.74	−3.28	−3.10	−2.80	−2.64

2.4. Conclusion

Unlike the previously developed SWM4-NDP polarizable model for water,[113] which was adjusted explicitly to reproduce bulk properties of water, the present model for ammonia is adjusted solely based on ab initio properties of the NH_3 monomer and the NH_3–NH_3 and NH_3–H_2O dimers. The model reproduces the structure, density, self-diffusion coefficient, heat capacity, and compressibility of liquid ammonia, as well as the hydration free energy of NH_3. It also reproduces experimental properties of liquid ammonia over a wide range of temperatures and pressures. As further indication of its transferability, it accurately reproduces the experimental structure and densities of aqueous ammonia solutions. While this strictly ab-initio approach to force field parameterization has been reported to give results in agreement with ab initio and experimental data,[18,30,31] it may not be generally applicable.

The model provides a powerful tool to investigate the properties of fluid ammonia at thermodynamic conditions for which experiments are difficult to perform. It has been used in combination with the SWM4-NDP water model to analyze the structure of aqueous ammonia mixtures, and will be used in future work to simulate ion solvation in liquid and aqueous ammonia solutions, and gain insight into the general phenomenon of preferential solvation.

3. Molecular Dynamics Investigation of Alkali Metal Ions in Liquid and Aqueous Ammonia*

* Adapted with permission from (Orabi, E. A.; Lamoureux, G. Molecular Dynamics Investigation of Alkali Metal Ions in Liquid and Aqueous Ammonia. *J. Chem. Theory Comput.* **2013**, *9*, 2324–2338). Copyright (2013) American Chemical Society.

Abstract

A polarizable potential model for M^+–NH_3 interactions ($M^+ = Li^+$, Na^+, K^+, Rb^+, Cs^+) is optimized based on the ab initio properties of the ion–ammonia dimers calculated at the MP2 level of theory. The optimized model reproduces the ab initio binding energies of $M^+(NH_3)_n$ (n = 2–4) and $M^+(NH_3)_n(H_2O)_m$ (n, m = 1–3 and $n + m \leq 4$) clusters and gives relative solvation free energies in liquid ammonia in good agreement with experimental data, without further adjustments. It also reproduces binding cooperativity in ion-ammonia and ion-ammonia-water clusters. The model is used in molecular dynamics simulations of isolated ions in liquid ammonia and in aqueous ammonia solutions with various ammonia molar fractions ($0.0 \leq x_{NH_3} \leq 1.0$). Simulations in liquid ammonia show coordination numbers of 4.0 for Li^+, 5.3 for Na^+, 6.1 for K^+, 6.7 for Rb^+, and 7.7 for Cs^+, in very good agreement with available experimental results. Simulations of ions in aqueous ammonia show preferential solvation by water in their first solvation shells and preferential solvation by ammonia in their second shells. Potentials of mean force are calculated between each ion and NH_3 in liquid water, and between each ion and H_2O in liquid ammonia. The results suggest that, in liquid water, Li^+ and Na^+ bind NH_3 in their second solvation shells only, while Cs^+ binds NH_3 in its first solvation shell only (K^+ and Rb^+ ions show only weak affinity for NH_3 in water). In liquid ammonia, the ions bind H_2O in their first solvation shells with an affinity following the trend $Li^+ > Na^+ > K^+ \approx Rb^+ > Cs^+$.

3.1. Introduction

Ammonia is a good solvent for many metals, nonmetals, and electrolytes and has a widespread use in many industrial sectors.[133] Alkali metals dissolve in anhydrous ammonia through dissociation into positive metal ions and free electrons.[133,134] The conductivity of alkali ions in liquid ammonia increases with concentration of the metal.[134] At low concentrations, the solutions are nonmetallic and blue-colored (a hallmark of solvated electrons) but they become metallic and bronze-colored at high concentrations. The dissolution of alkali metals in liquid ammonia is also characterized by a decrease in the density of the solution with the metal concentration.[134–136] At high metal concentrations, the density of the solution is markedly lower than that of either of its components.[134–136] The unusual electric and volumetric properties of these solutions have been the subject of various experimental[44,137–141] and theoretical investigations.[127,142–158] While electrons must be treated as quantum particles, in dilute solutions the alkali metal cores are decoupled from the free electrons and can be investigated using classical simulations.[127,142–144,146–148,150,152]

Solvation of alkali ions in liquid ammonia has been the subject of various computational approaches such as quantum path integral Monte Carlo (PIMC),[143] hybrid quantum mechanics/molecular mechanics (QM/MM),[15,20] classical Monte Carlo (MC),[143,147,148] and molecular dynamics (MD)[127,142,144,146,152] simulations. However few of these theoretical investigations have shown consistent agreement with experimental data. For instance, simulations of Li^+ in liquid ammonia have yielded first-shell coordination numbers of either 4[143,145,154] or 6,[142,144,145,148,152] compared to the experimentally reported tetrahedral arrangement of 4 NH_3 molecules.[44,138,140] Coordination numbers of 5,[143,150] 7,[127] 8,[127,147,150] and 9[147] have been reported for Na^+, compared to the experimental coordination number of ~5.5.[138] Using MD simulations, Tongraar *et al.*[146] have reported a coordination number of 8.7 for K^+, which seems overestimated since the experimental coordination number reported for the larger Rb^+ ion is 6.4 NH_3 molecules.[139] Using classical MC simulations, Marchi *et al*.[143] have reported a coordination number of 10 for Cs^+ in liquid ammonia at 260 K, which again seems overestimated. Although some of the reported potential models have shown agreement with experimental results (especially for Li^+), none have been used to systematically study the solvation of the whole alkali series. Even with the computationally expensive QM/MM simulations, the coordination number and the solvation structure have been observed to depend on the level of theory used to treat the

QM region. For instance, Tongraar and Hannongbua[159] have studied the solvation structure of NH_4^+ and reported a coordination number of 5.1 from QM(HF)/MM simulations and of 4.3 from QM(B3LYP)/MM simulations.

While the majority of published theoretical studies focus on metal ions in pure solvents, the solvation of alkali ions in liquid mixtures has received less attention.[160–166] Such studies are important to elucidate the phenomenon of preferential solvation, which plays an important role in the solubility of ions in mixed solvents and in understanding ion-ligand binding selectivity. Preferential solvation of the alkali ions Li^+, Na^+, and K^+ in 18.4% NH_3 (mole fraction) has been studied by classical MC and MD techniques[160–164] and by QM/MM simulations.[162–165] The solvation of a Li atom in 25 water molecules and 6 ammonia molecules (19.4% NH_3) has also been studied by first-principles Car–Parrinello molecular dynamics simulations.[166] At 18.4% NH_3 mole fraction, classical simulations have suggested the following first solvation shell structures: $Li^+(H_2O)_4(NH_3)_2$,[161] $Li^+(H_2O)_3(NH_3)_3$,[162] $Na^+(H_2O)_{2.4}(NH_3)_4$,[160] $Na^+(H_2O)_{4.9}(NH_3)_{2.2}$,[163] and $K^+(H_2O)_{5.3}(NH_3)_{3.4}$.[164] QM/MM simulations from Tongraar and Rode show different structures: $Li^+(H_2O)_3(NH_3)$,[162] $Li^+(H_2O)_4$,[165] $Na^+(H_2O)_{3.7}(NH_3)_{1.8}$,[163] and $K^+(H_2O)_{6.7}(NH_3)_{0.9}$.[164] Car–Parrinello MD simulations of a lithium atom in a 19.4% NH_3 solution show spontaneous ionization of Li and a first solvation shell structure $Li^+(H_2O)_4$.[166] While the structures are different, the accuracy of the method cannot be determined unless experimental results are available.

Ab initio MD simulations can in principle provide a physically accurate picture of ions in solution and of hydrogen bonds between solvent molecules, but may require a level of quantum theory that is not always amenable to extensive sampling. This is especially problematic for solvent mixtures in which the various components exchange in and out of the ion solvation shell at a slow rate. In contrast, force fields are computationally inexpensive and can be used for reliable sampling of the configuration space. They however do not represent electrons explicitly and often neglect polarization effects, which have been shown to contribute significantly to cation-ammonia interactions.[151,153] Ab initio energy decomposition analysis on the Li^+–NH_3 complex[151] has shown that polarization contributes to 16.3% of the total interaction energy—a fraction comparable to that of the Li^+–H_2O complex (19.9%).[167] Corral *et al.*[153] have similarly investigated the nature of binding of alkali and alkaline-earth cations with a series of oxygen and nitrogen ligands and found that polarization effects are important to reproduce the correct

basicity trend. In addition, non-additive terms may largely affect the simulation results of ion-containing solutions.[149,162–164]

In this work, we aim to develop a reliable polarizable potential model for alkali ion-ammonia interactions and investigate ion solvation in both pure and aqueous ammonia solutions. The model is optimized to reproduce the ab initio properties of ion-ammonia dimers (geometries, binding energies, and potential energy surfaces) calculated at the MP2 level. It is then validated using the ab initio binding energies of $M^+(NH_3)_n$ (n = 2–4) and $M^+(NH_3)_n(H_2O)_m$ (n, m = 1–3 and $n + m \leq 4$) clusters, and the solvation free energies of the ions in liquid ammonia. The model is used to investigate the solvation structure of the ions in liquid ammonia and, in combination with a model for ion-water interactions developed previously,[113,118] to investigate preferential solvation in aqueous ammonia solutions with various ammonia mole fractions ($0 \leq x_{NH_3} \leq 1$).

3.2. Methods

3.2.1. Ab initio Calculations

The structures of alkali ion-ammonia binary clusters, $M^+(NH_3)_n$ (n = 1–4), and alkali ion-ammonia-water ternary clusters, $M^+(NH_3)_n(H_2O)_m$ (n, m = 1–3 and $n + m \leq 4$), are optimized at the MP2 level of theory using Gaussian 09.[26] For complexes of Li^+, Na^+, and K^+, calculations are performed at the frozen core (FC) MP2/6-311++G(d,p) level and yield binding energies for the ion-ammonia dimers in very good agreement with experimental data. It should be noted that the MP2(FC) calculations yield binding energies for ion-ammonia dimers in close agreement with MP2(full) results. Complexes of the heavier alkali cations (Rb^+ and Cs^+) are calculated at the full-electron MP2 level with the 6-311+G(3df,2p) basis set for H, N, and O and with effective core potentials (ECPs) and valence basis sets for the metal ions. We use the Stuttgart RSC 1997 (ECP) basis set[168] to which d and f polarization functions are added with exponents 0.39 and 0.55 for Rb^+, and 0.29 and 0.44 for Cs^+.[169] The basis sets used to study Rb^+ and Cs^+ clusters were shown to give binding energies for the benzene-ion complexes in good agreement with experimental results.[169] They also yield ion-water binding energies in very good agreement with experimental results (see below). All calculations are done without symmetry constraints and frequency calculations are performed on the resulting structures to confirm that they are energy minima. Interaction energies are corrected for basis set superposition error (BSSE) using the counterpoise (CP) procedure of Boys and Bernardi.[111] Potential energy surfaces (PESs) for the M^+–NH_3 dimers are generated by scanning the $M^+\cdots N$ distance from 1 to 8 Å and the $M^+\cdots N$–H

angle from 0 to 180°. The surfaces are computed using rigid ammonia geometry, calculated at the MP2(FC)/6-311++G(d,p) level (r_{NH} = 1.0135 Å and θ_{HNH} = 107.29°),[170] and are corrected for BSSE.

3.2.2. Molecular Mechanics Calculations

Molecular mechanics (MM) calculations are performed with the program CHARMM.[29] Polarizable potential models based on classical Drude oscillators[32] have been reported for H_2O,[113] alkali ions,[118] and NH_3.[170] The SWM4-NDP water model was calibrated to reproduce the main properties of liquid water, including self-diffusion coefficient and dielectric constant.[113] The alkali cation model reproduces the experimental solvation structure and hydration free energies of the ions.[118] The ammonia model reproduces the properties of liquid, supercritical, and aqueous ammonia solutions.[170] Following our previous work,[170,18,30,31] a polarizable model for alkali ion-ammonia interactions is optimized based on the ab initio properties of the ion-ammonia dimers.

3.2.2.1. Potential Energy Function and Parameterization Strategy

Molecular polarizability is described by attaching a light (0.4 amu), negatively charged "Drude" particle to all non-hydrogen atoms using a harmonic spring with force constant $k_D = 1000\ \mathrm{kcal/mol/Å^2}$.[32] The partial charge q_i of a polarizable atom i is then distributed between the Drude particle (q_{Di}) and the atomic core ($q_{ci} = q_i - q_{Di}$) with the Drude particle charge being determined from the atomic polarizability via the relation $\alpha_i = {q_{Di}}^2/k_D$. A displacement d between the Drude particle and the polarizable atom results in an induced dipole moment $q_{Di}d$. The polarizable potential energy function that describes the interaction energy in liquid and aqueous ammonia solutions containing alkali ions is given as:[30,170]

$$
\begin{aligned}
U(R) = & \sum_{i=1}^{N} \frac{1}{2} k_D |\mathbf{r}_{ci} - \mathbf{r}_{Di}|^2 + \sum_{\text{HNH angles}} k_\theta (\theta - \theta_0)^2 \\
& + \sum_{\text{nonbond}} E_{\min,ij} \left[\left(\frac{R_{\min,ij}}{|\mathbf{r}_{ci} - \mathbf{r}_{cj}|} \right)^{12} - 2 \left(\frac{R_{\min,ij}}{|\mathbf{r}_{ci} - \mathbf{r}_{cj}|} \right)^{6} \right] \\
& + \sum_{\text{nonbond}} \left(\frac{q_{ci} q_{cj}}{|\mathbf{r}_{ci} - \mathbf{r}_{cj}|} + \frac{q_{ci}\, q_{Dj}}{|\mathbf{r}_{ci} - \mathbf{r}_{Dj}|} + \frac{q_{Di}\, q_{cj}}{|\mathbf{r}_{Di} - \mathbf{r}_{cj}|} + \frac{q_{Di} q_{Dj}}{|\mathbf{r}_{Di} - \mathbf{r}_{Dj}|} \right)
\end{aligned}
\tag{3.1}
$$

where N is the number of interacting molecules, $\mathbf{r}_{ci}$ and $\mathbf{r}_{Di}$ are positions of the core particle i and its Drude particle, respectively. k_θ and θ_0 are respectively the force constant and equilibrium

angle for the HNH angles θ. $E_{\min,ij}$ and $R_{\min,ij}$ are the mixed Lennard-Jones (LJ) parameters between non-bonded atoms i and j, defined by the Lorentz–Berthelot combination rules:

$$E_{\min,ij} = \sqrt{E_{\min,i} \times E_{\min,j}} \qquad \text{and} \qquad R_{\min,ij} = \frac{R_{\min,i} + R_{\min,j}}{2} \qquad (3.2)$$

Equation (3.1) does not include bond stretching energy terms since for both water and ammonia, bonds are constrained to their equilibrium values using the SHAKE/Roll-RATTLE/Roll algorithm.[33] It also does not include HOH angle bending terms since the SWM4-NDP water model has a rigid molecular geometry.[113] A polarizable model for alkali ion-ammonia interactions is optimized following our previously reported approach.[30,170] In particular, pair-specific LJ parameters between each ion and the nitrogen atom of NH_3 are optimized based on the ab initio properties of the ion-ammonia dimers. Parameters are first optimized to reproduce the calculated ab initio PESs.[30] Since these PESs are calculated with rigid ammonia geometry, we further refine the obtained parameters to give complexation energies of the relaxed ion-ammonia dimers in agreement with the ab initio minimum energy structures.[170] (For the dimers calculated with the force field, $M^+\cdots N$ distance and HNH angles are allowed to relax but NH bonds are constrained at their equilibrium values.)

3.2.2.2. Molecular Dynamics

Simulations are performed with cubic periodic boundary conditions in the isothermal-isobaric ensemble (*NpT*). All MD simulations are performed at the normal boiling point of ammonia (T = 239.8 K and p = 1 atm), except those for calculating the solvation free energies of the ions, which are performed at T = 298.15 K and p = 9.9 atm (the corresponding vapor pressure of liquid ammonia). The water-rich solutions at 239.8 K remain in the supercooled state for the duration of all simulations. The total number of molecules (one ion + ammonia + water) is 251 in all simulations. Eleven ammonia mole fractions are simulated: x_{NH_3} = 0, 0.1, 0.2, 0.3, 0.4, 0.5, 0.6, 0.7, 0.8, 0.9, and 1 (calculated without considering the ion). Electrostatic interactions are computed using the particle-mesh Ewald method[115] with κ = 0.34 for the charge screening and a 1.0 Å grid spacing with fourth-order splines for the mesh interpolation. The real-space interactions (Lennard-Jones and electrostatic) are cut off at 15 Å and the long range contribution from the Lennard-Jones term is introduced as an average density-dependent term.[116] The temperature of the system is controlled with a two-thermostats algorithm, where atoms are kept at the desired temperature and oscillations of the Drude particles are kept at low temperature (1

K) to ensure self-consistent dipole induction.[32] The equations of motion are integrated using a 1 fs time step, with all bonds involving hydrogen atoms kept at their reference lengths using the SHAKE/Roll and RATTLE/Roll algorithms.[33] Simulations in liquid ammonia are run for 20 ns while those in aqueous ammonia are run for 70 ns. The first 5 ns are excluded from the analysis.

3.2.2.3. Free Energy Calculations

The transferability of the polarizable ion–NH_3 model to bulk solutions is assessed by calculating the intrinsic free energy of solvation of each ion in liquid ammonia at T = 298.15 K and p = 9.9 atm. Two approaches are used for this purpose. In the first, the intrinsic solvation free energies are calculated using free energy perturbation (FEP). Specifically, the solvation free energy is evaluated from the transformation of one alkali ion, M^+, into a "dummy" atom having no charge and no LJ parameters:

$$\Delta G_{\mathrm{solv}}^{\mathrm{intr}} \equiv \Delta G_{\mathrm{solv}}(\mathrm{M}^+) - \Delta G_{\mathrm{solv}}(\mathrm{dummy}) = -\Delta \mathrm{G}_{\mathrm{mut}}(\mathrm{M}^+ \rightarrow \mathrm{dummy}) \qquad (3.3)$$

where $\Delta \mathrm{G}_{\mathrm{mut}}$ is the relative free energy for the alchemical $\mathrm{M}^+ \rightarrow \mathrm{dummy}$ "mutation" and $\Delta G_{\mathrm{solv}}(\mathrm{dummy}) = 0$. The transformation in performed in 21 steps, controlled by a scaling parameter λ which takes the following values: 0, 0.00001, 0.0001, 0.001, 0.01, 0.05, 0.1, 0.2, 0.3, 0.4, 0.5, 0.6, 0.7, 0.8, 0.9, 0.95, 0.99, 0.999, 0.9999, 0.99999, and 1.[170] Each λ window is equilibrated for 150 ps, followed by subsequent data collection for 350 ps. Each mutation is performed in the forward and backward directions in three independent replicates, in order to confirm the convergence and estimate the error on the calculated values.

In the second approach, the solvation free energy is decomposed into three contributions calculated following a free energy perturbation protocol established previously[117,118,171]

$$\Delta G_{\mathrm{solv}}^{\mathrm{intr}} = \Delta G_{\mathrm{elec}} + \Delta G_{\mathrm{disp}} + \Delta G_{\mathrm{rep}} \qquad (3.4)$$

where ΔG_{elec} is the electrostatic component of the solvation free energy and ΔG_{disp} and ΔG_{rep} are respectively the attractive (dispersive) and repulsive components of the LJ interaction. Each of the three components is calculated from independent simulations. The electrostatic and dispersive components are computed using thermodynamic integration, with the λ parameter takes the values 0, 0.1, 0.2, 0.3, 0.4, 0.5, 0.6, 0.7, 0.8, 0.9, and 1. The repulsive term is computed using a soft-core scheme[117] and unbiased using the weighted histogram analysis method (WHAM).[172] Values of λ = 0, 0.05, 0.1, 0.15, 0.2, 0.25, 0.3, 0.35, 0.4, 0.5, 0.6, 0.7, 0.8, 0.9, and 1 are used to calculate ΔG_{rep}.[118] Solvation free energies calculated from both approaches are within statistical error. On the basis of multiple runs, the error on the calculated values is ± 0.2 kcal/mol.

3.2.2.4. Potential of Mean Force Calculations

Potentials of mean force (PMFs) between each ion (Li^+, Na^+, K^+, Rb^+, or Cs^+) and one ammonia molecule in pure water and between each ion and one water molecule in pure ammonia are calculated using umbrella sampling, according to a previously reported procedure.[30] For these simulations, each system is composed of one alkali ion and one ligand (ammonia or water) solvated in 249 solvent molecules (water for the ammonia ligand and ammonia for the water ligand). The distance between the ion and the heavy atom of the ligand (N for ammonia or O for water) is used as reaction coordinate, and is sampled from 1 to 10 Å using 0.5-Å separated windows. A harmonic potential of force constant 10 kcal/mol/Å^2 is applied to bias the sampling. Each window is simulated for 2.3 ns and the last 2 ns are used to construct the unbiased PMF using WHAM.[173] To facilitate comparison, all PMFs are evaluated at the normal boiling point of ammonia (239.8 K and 1 atm).

3.3. Results and Discussion

3.3.1. Ab initio Optimized Structures

High-level ab initio calculations of small alkali ion-ammonia (binary) and alkali ion-ammonia-water (ternary) clusters can help in understanding the onset of bulk solvation as the size of the cluster increases. Only a limited number of ab initio studies have been published on alkali ion-ammonia clusters larger than the dimer[148,149,151,154,157,158] and to the best of our knowledge, no ab initio investigations have been reported on alkali ion-ammonia-water ternary clusters to date. Since the purpose of studying the binary and ternary complexes is simply to validate the optimized potential model, not all stable conformers will be reported for all systems.

3.3.1.1. $M^+(NH_3)_n$ Clusters

While previous ab initio investigations considered mainly the global energy minima,[149,151,157,158] in this study local energy minima of $M^+(NH_3)_n$ clusters (n = 1–4) are considered as well. Figure 3.1 shows the various optimized geometries and some of their characteristic parameters and Table 3.1 lists binding energies with (E^{CP}) and without (E) correction for BSSE, in addition to binding energies calculated with the optimized Drude model (E^{MM}, see section 3.3.3). The distance between the alkali cation and directly coordinated ammonia molecules increases on going from Li^+ to Cs^+, due to increasing ion size (see Figure 3.1). The distance also increases with the number of ammonia molecules in the ion's first coordination shell (see Figures 3.1a, 3.1b, 3.1e, and 3.1h).

Optimization of M^+–NH_3 dimers shows stable structures with C_{3v} symmetry. The optimized structures of alkali ions Li^+, Na^+, and K^+ show uncorrected binding energies E = –40.85, –28.22, and –20.71 kcal/mol, respectively. In comparison, Kerdcharoen and Hannongbua[149] reported values E = –45.5, –33.1, and –21.2 kcal/mol, respectively, at the MP2/6-31G(d,p) level of theory. The BSSE-corrected values E^{CP} = –38.71, –26.43, and –19.56 kcal/mol are in good agreement with the experimental binding enthalpies at room temperature (ΔH_{298}) of –39.1,[174] –25.4 ± 1.3,[175] and –18.9 ± 1.7 kcal/mol[176] reported for NH_3 in complex with Li^+, Na^+, and K^+, respectively. Full-electron calculations on dimers of Li^+, Na^+, and K^+ with ammonia yield E^{CP} = –38.98, –26.73, and –19.58 kcal/mol, respectively, in very close agreement with the FC calculations. The calculated binding energies of Rb^+ and Cs^+ complexes with NH_3 (E^{CP} = –16.69 and –14.94 kcal, respectively) are in good agreement with the dissociation energies of –16.2 and –14.2 kcal/mol calculated by Lim *et al.* at the CCSD(T) level of theory.[156]

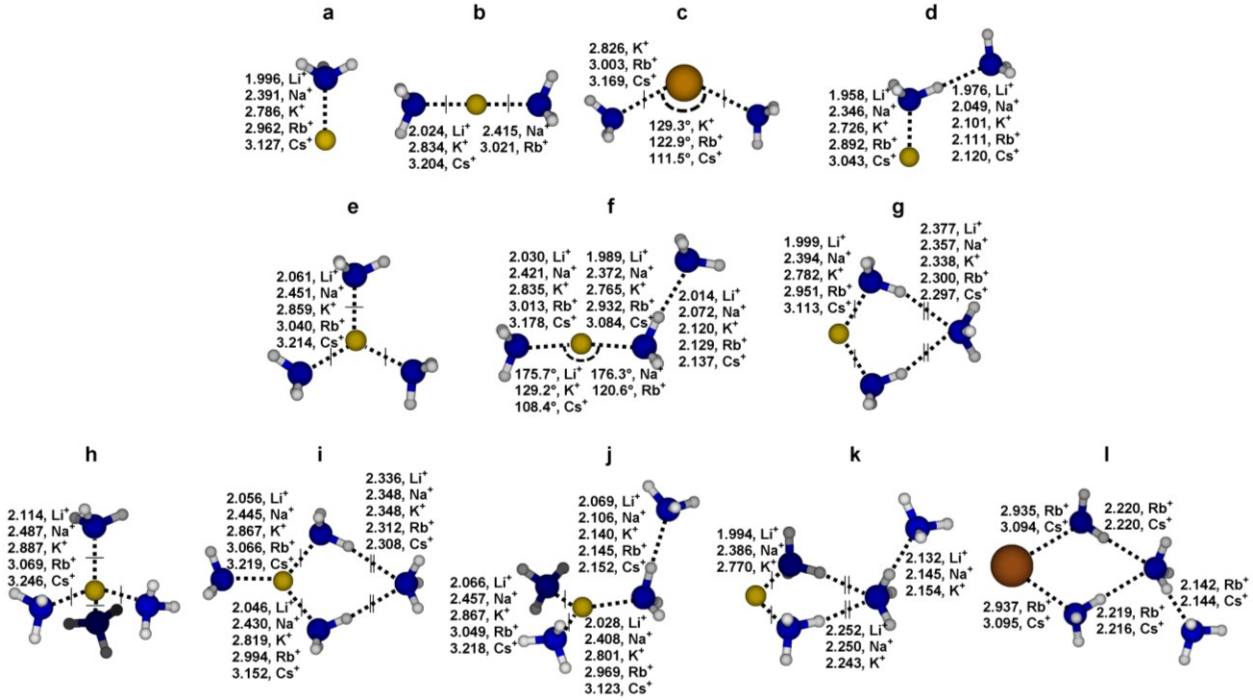

Figure 3.1. Optimized structures of alkali ion-ammonia clusters $M^+(NH_3)_n$ (M^+ = Li^+, Na^+, K^+, Rb^+, Cs^+ and n = 1–4) at the MP2 level (see the Methods section for details). Selected geometrical parameters ($M^+\cdots N$ and $H\cdots N$ distances in Å and $N\cdots M^+\cdots N$ angles in degrees) are reported. Equal atom-atom distances are indicated with single or double dashes. The structures are illustrated with Li^+ complexes, except for panels *c* (illustrated with K^+) and *l* (illustrated with Rb^+). Corresponding parameters for other alkali ions are reported.

Table 3.1. Binding energies without and with correction for BSSE (E and E^{CP}, respectively) and the corresponding binding energy calculated using the optimized Drude model (E^{MM}) for the alkali ion-ammonia clusters [$M^+(NH_3)_n$; M^+ = Li^+, Na^+, K^+, Rb^+, Cs^+ and n = 1–4]. All energies are in kcal/mol.

Complex (n)	Li^+			Na^+			K^+			Rb^+			Cs^+		
[structure] [a]	E	E^{CP}	E^{MM}	E	E^{CP}	E^{MM}	E	E^{CP}	E^{MM}	E	E^{CP}	E^{MM}	E	E^{CP}	E^{MM}
1a (1) [1+0]	–40.85	–38.71	–38.74	–28.22	–26.43	–26.43	–20.71	–19.56	–19.59	–17.10	–16.69	–16.89	–15.55	–14.94	–15.07
1b (2) [2+0]	–76.08	–71.23	–69.94	–53.45	–49.55	–49.19	–38.60	–36.46	–36.42	–31.87	–31.16	–31.44	–28.67	–27.62	–27.87
1c (2) [2+0]	–	–	–	–	–	–	–38.73	–36.53	–36.43	–32.03	–31.27	–31.55	–29.10	–27.95	–28.14
1d (2) [1+1]	–55.59	–51.72	–51.98	–40.65	–37.27	–37.21	–31.68	–28.91	–29.08	–26.83	–25.76	–25.82	–25.00	–23.70	–23.62
1e (3) [3+0]	–101.88	–94.58	–91.22	–73.49	–67.90	–67.14	–54.47	–51.17	–50.89	–45.15	–44.06	–44.32	–40.94	–39.32	–39.63
1f (3) [2+1]	–89.13	–82.59	–81.26	–64.84	–59.37	–58.92	–48.86	–45.09	–45.13	–41.05	–39.65	–39.78	–37.87	–36.06	–36.10
1g (3) [2+1]	–86.38	–80.56	–77.20	–62.88	–57.86	–57.20	–48.96	–44.84	–44.86	–41.72	–40.03	–39.94	–38.80	–36.69	–36.60
1h (4) [4+0]	–120.35	–110.38	–106.06	–89.68	–82.07	–81.26	–67.89	–63.37	–62.96	–56.46	–55.05	–55.30	–51.38	–49.31	–49.64
1i (4) [3+1]	–113.25	–104.40	–100.09	–83.77	–76.60	–75.58	–64.11	–58.99	–58.81	–54.21	–52.26	–52.23	–50.10	–47.52	–47.58
1j (4) [3+1]	–113.18	–104.24	–100.81	–83.73	–76.58	–75.79	–63.78	–58.96	–58.96	–53.46	–51.76	–51.89	–49.11	–46.81	–46.97
1k (4) [2+1+1]	–95.96	–88.37	–84.60	–71.93	–65.17	–64.20	–57.60	–51.71	–51.78	–	–	–	–	–	–
1l (4) [2+1+1]	–	–	–	–	–	–	–	–	–	–49.67	–47.24	–47.55	–46.63	–43.77	–44.05

[a] Total number of ammonia molecules in parenthesis. In square brackets are the numbers of ammonia molecules in the ion's first, second, and third (if any) coordination shells (see Figure 3.1). The dashes indicate that the conformation is unstable.

Alkali ions are reported to bind water less strongly than ammonia.[153,174,175] For the purpose of comparison, the interaction energies of Li^+, Na^+, K^+, Rb^+, and Cs^+ with water are calculated at the same level of theory. We find E^{CP} = –33.40, –23.09, –17.88, –15.24, and –13.73 kcal/mol, respectively, weaker than the corresponding ion-ammonia binding energies (see Table 3.1). The optimized ion-water dimers also show $M^+\cdots O$ distances of 1.866 Å for Li^+, 2.266 Å for Na^+, 2.631 Å for K^+, 2.794 Å for Rb^+, and 2.960 Å for Cs^+, shorter than the corresponding $M^+\cdots N$ distances (see Figure 3.1). The calculated ion-water binding energies are in good agreement with the experimentally reported[177] binding enthalpies ΔH_{298} = –34.0, –24.0, –17.9, –15.9, and –13.7 kcal/mol. This agreement is further supporting the choice of basis sets employed in this study.

Li^+ and Na^+ show only two stable conformers for the $M^+(NH_3)_2$ cluster (Figures 3.1b and 3.1d), but K^+, Rb^+, and Cs^+ stabilize an additional "bent" isomer (Figure 3.1c). Conformer 3.1b possesses D_{3d} symmetry, with the two NH_3 molecules in staggered orientation, and is the global minimum conformer for both Li^+ and Na^+, in accord with previous ab initio results.[151,154] A previously reported linear structure in which the two ammonia molecules are in eclipsed orientation[158] (D_3 symmetry, not shown in Figure 3.1) corresponds to a transition state.

Conformer 3.1c is a bent, C_s-symmetric structure and represents the global minimum energy for K^+, Rb^+, and Cs^+ (see Table 3.1). Conformer 3.1d, with only one ammonia molecule coordinating the ion, is the least stable of the three structures. The E^{CP} value for the ground-state $Li^+(NH_3)_2$ conformer (3.1b), –71.23 kcal/mol, is in agreement with MP2(full)/6-311+G(d,p) results from the literature (E^{CP} = –71.23 kcal/mol).[151]

Three conformers are identified for the $M^+(NH_3)_3$ tetramer (see Figures 3.1e, 3.1f, and 3.1g). Isomer 3.1e possesses C_{3h} symmetry and is the global energy minimum. The E^{CP} value for the $Li^+(NH_3)_3$ global minimum is –94.58 kcal/mol, compared to –92.06 kcal/mol calculated at the MP2(full)/6-311+G(d,p) level of theory.[151] Both isomers 3.1f and 3.1g have C_s symmetry, and only two NH_3 molecules are directly coordinating the metal ion. Structure 3.1f is more stable than structure 3.1g for Li^+, Na^+, and K^+, but less stable for Rb^+ and Cs^+ (see Table 3.1).

Four conformers are located for the $M^+(NH_3)_4$ pentamer (see Figures 3.1h to 3.1l). In the global minimum structure (3.1h), the four ammonia molecules coordinate the ion in a T_d symmetry. Structures 3.1i and 3.1j, with the ion coordinated by only three ammonia molecules, have comparable stabilities (see Table 3.1). For these structures, the coordination geometry is determined by the size of the ion: trigonal quasi-planar for Li^+ and Na^+ (as depicted in Figure 3.1i) but trigonal pyramidal for the larger ions (with the ammonia molecule not involved in a hydrogen bond bent out of the trigonal plane; structure not shown). For conformer 3.1j, the coordination is trigonal quasi-planar for Li^+, Na^+, and K^+ but trigonal pyramidal for Rb^+ and Cs^+ (with the ion displaced towards the second-shell ammonia molecule; structure not shown). In the least stable conformer (3.1k, for Li^+, Na^+, and K^+ and 3.1l for Rb^+ and Cs^+), only two ammonia molecules are bonded to the cation.

As shown in Figures 3.1d, 3.1f, and 3.1j the distance between hydrogen-bonded ammonia molecules, represented by the H···N distance, increases on going from Li^+ to Cs^+, yet is always shorter than in the isolated ammonia dimer (which has an H···N distance of 2.263 Å at the MP2(FC)/6-311++G(d,p) level). Comparison between structures 3.1a and 3.1d, between structures 3.1b/3.1c and 3.1f, and between structures 3.1e and 3.1j shows that the presence of a second-shell ammonia molecule reduces the M^+···N distance between the ion and its coordinating ammonia molecules. The shortening of N···N and M^+···N distances in "M^+···N–H···N" motifs indicates binding cooperativity: The ion and second-shell ammonia enhance the polarity of first-shell ammonia molecule, which strengthens both ion-ammonia and ammonia-

ammonia interactions. On the other hand, comparison between structures 3.1a, 3.1b/3.1c, 3.1e, and 3.1h shows that adding ammonia molecules to the ion's first shell increases the $M^+\cdots N$ distance. While steric factors might contribute to the elongation of $M^+\cdots N$ bonds in larger clusters, in smaller clusters the elongation is mostly due to the "$N\cdots M^+\cdots N$" motif creating binding anti-cooperativity: The ion induces opposite dipoles in the ammonia molecules, which creates a repulsive electrostatic force between them.[30,31]

To analyze the binding cooperativity or anti-cooperativity between ion-ammonia and ammonia-ammonia interactions, we calculate the E^{coop} parameter for complexes 3.1b and 3.1d, in accord with previous approach:[30,31]

$$E^{\mathrm{coop}} = E^{\mathrm{tot}} - E^{1}_{\mathrm{M^+-NH_3}} - E^{2}_{\mathrm{M^+-NH_3}} - E_{\mathrm{NH_3-NH_3}} \qquad (3.5)$$

where E^{tot} is the total binding energy of the trimer, $E^{1}_{\mathrm{M^+-NH_3}}$ and $E^{2}_{\mathrm{M^+-NH_3}}$ are the binding energies between the ion and each of the ammonia molecules (labeled 1 and 2), and $E_{\mathrm{NH_3-NH_3}}$ is the binding energy between the two ammonia molecules. All energy terms are calculated in the geometry found in the optimized trimers (see Figures 3.1b and 3.1d). Binding energies of the ammonia dimers, $E_{\mathrm{NH_3-NH_3}}$, are calculated at the MP2(FC)/6-311++G(d,p) level for trimer complexes of Li^+, Na^+, and K^+ and at the MP2(full)/6-311+G(3df,2p) level for Rb^+ and Cs^+ trimers. The calculated data, together with those from the Drude model, are reported in Table 3.2.

According to *Eq.* (3.5), a negative E^{coop} indicates that the total interaction energy is greater (more negative) than the sum of the pairwise interactions, showing cooperativity between the individual interactions. On the other hand, a positive E^{coop} indicates binding anti-cooperativity. Table 3.2 shows cooperativity between ion-ammonia and ammonia-ammonia interactions for complex 3.1d and anti-cooperativity between the two ion-ammonia interactions in complex 3.1b. The shortening of $M^+\cdots N$ distances in complexes 3.1b and 3.1e when a second-shell ammonia molecule is added (see Figures 3.1f and 3.1j) is similarly reflecting cooperativity between the individual interactions.

Table 3.2. BSSE-corrected complexation energies calculated at the MP2 level and corresponding interaction energies calculated using the optimized Drude model (in parentheses). All energies are in kcal/mol.

Energy[a]	Complex 3.1b					Complex 3.1d				
	Li^+	Na^+	K^+	Rb^+	Cs^+	Li^+	Na^+	K^+	Rb^+	Cs^+
E^{tot}	–71.23	–49.55	–36.46	–31.16	–27.62	–51.72	–37.27	–28.91	–25.76	–23.70
	(–69.94)	(–49.19)	(–36.42)	(–31.55)	(–28.18)	(–51.98)	(–37.21)	(–29.08)	(–25.82)	(–23.62)
$E^1_{\mathrm{M^+-NH_3}}$	–38.68	–26.44	–19.58	–16.65	–14.91	–38.59	–26.24	–19.26	–16.42	–14.60
	(–39.11)	(–26.82)	(–19.87)	(–17.15)	(–15.30)	(–39.86)	(–27.22)	(–20.17)	(–17.38)	(–15.49)
$E^2_{\mathrm{M^+-NH_3}}$	–38.68	–26.44	–19.58	–16.65	–14.91	–9.80	–7.99	–6.81	–6.06	–5.78
	(–39.11)	(–26.82)	(–19.87)	(–17.15)	(–15.30)	(–6.41)	(–5.65)	(–5.08)	(–4.79)	(–4.56)
$E_{\mathrm{NH_3-NH_3}}$	2.73	1.54	0.93	0.60	0.49	–1.03	–1.51	–1.75	–2.08	–2.10
	(1.52)	(0.99)	(0.68)	(0.71)	(0.71)	(–1.82)	(–2.27)	(–2.40)	(–2.43)	(–2.45)
E^{coop}	3.41	1.79	1.77	1.55	1.72	–2.30	–1.53	–1.08	–1.20	–1.22
	(6.76)	(3.46)	(2.64)	(2.04)	(1.71)	(–3.89)	(–2.07)	(–1.43)	(–1.22)	(–1.12)

[a] E^{tot} is the total binding energy, $E^1_{\mathrm{M^+-NH_3}}$ and $E^2_{\mathrm{M^+-NH_3}}$ are the binding energies between the metal ion and each ammonia molecule, and $E_{\mathrm{NH_3-}NH_3}$ is the interaction energy between the two ammonia molecules. While E^{tot} is obtained from relaxed trimer geometries (with NH bonds constrained with the SHAKE algorithm in Drude model calculations), the other three terms are calculated using coordinates extracted from the trimer geometries. $E_{\mathrm{NH_3-NH_3}}$ is calculated at the MP2(FC)/6-311++G(d,p) level for complexes of Li^+, Na^+, K^+, and at the MP2(full)/6-311+G(3df,2p) level for complexes of Rb^+ and Cs^+. E^{coop} is the energy due to cooperativity or anti-cooperativity between molecular interactions, calculated according to *Eq.* (3.5).

To understand the origin of preferential solvation, it is instructive to compare the energies of Table 3.1 with those of analogous ion-water clusters. Glendening and Feller[178] have reported CP-corrected binding energies for alkali ions hydrates, $M^+(H_2O)_n$ (n = 1–6), calculated at the MP2/6-31+G*//RHF/6-31+G* level, with effective core potentials for Rb^+ and Cs^+. For Li^+, they find E^{CP} = –34.5 kcal/mol for the monohydrate (n = 1), –64.4 kcal/mol for the dihydrate (n = 2), –87.5 kcal/mol for n = 3, and –104.1 kcal/mol for n = 4.[178] While these binding energies are weaker than those for ammonia complexes (see Table 3.1), they fall less rapidly as the lithium ion's first solvation shell gets populated. Each additional ammonia molecule (going from n = 1 to 4) increases the complexation energy of the cluster by –38.71, –32.52, –23.35, and –15.80 kcal/mol (see Table 3.1), while each water molecule increases the energy by –34.5, –29.9, –23.1, and –16.6 kcal/mol.[178] The reversal in the relative ammonia/water affinity between tri- and tetra-coordinated Li^+ ions is due to the larger size of ammonia molecules, which creates greater steric hindrance at high coordination numbers. A similar trend is observed for the other alkali metal

ions. For instance, binding of the first water molecule results in E^{CP} = –24.3 kcal/mol for Na^+, –18.9 kcal/mol for K^+, –16.1 kcal/mol for Rb^+, and –14.1 kcal/mol for Cs^+,[178] which is systematically weaker than the corresponding ion-ammonia energies (see Table 3.1), but binding of the fourth water molecule (from "[3+0]" to "[4+0]" ion-water clusters) increases E^{CP} by –14.0 kcal/mol for Na^+, –12.8 kcal/mol for K^+, –11.4 kcal/mol for Rb^+, and –14.8 kcal/mol for Cs^+,[178] which is comparable or *stronger* than the corresponding increases in E^{CP} from "[3+0]" to "[4+0]" ion-ammonia clusters (Figures 3.1e and 3.1h): –14.17 kcal/mol for Na^+, –12.20 kcal/mol for K^+, –10.99 kcal/mol for Rb^+, and –9.99 kcal/mol for Cs^+ (see Table 3.1).

3.3.1.2. $M^+(NH_3)_n(H_2O)_m$ Clusters

The optimized structures of ternary $M^+(NH_3)_n(H_2O)_m$ clusters (n, m = 1–3 and $n + m \leq 4$) are presented in Figure 3.2. Table 3.3 shows the ab initio binding energies of the structures, together with binding energies calculated with the optimized Drude model. All stable conformers are identified for the trimer and tetramer Li^+ clusters (Figures 3.2a to 3.2h) but for the sake of comparison only structurally similar isomers are considered for other alkali ions. For the "$n + m$ = 4" mixed clusters, only isomers derived from the tetrahedral arrangement of four molecules around the ion are considered.

Two stable isomers are presented for the $M^+(NH_3)(H_2O)$ trimer (Figures 3.2a and 3.2b). Structure 3.2a is quasi-linear for Li^+ and Na^+, but bent for the other alkali ions. The global minimum is structure 3.2a for Li^+, Na^+, and K^+ and structure 3.2b for Rb^+ and Cs^+ (see Table 3.3). Optimization of the structure in which H_2O is in the second coordination shell of the ion did not show a stable conformer, likely due to N–H···O hydrogen bonds being weaker than O–H···N bonds.[170] The di-coordinated trimers of Li^+, Na^+, K^+, Rb^+, and Cs^+ (Figure 3.2a) are respectively 4.49, 2.87, 1.36, 1.16, and 0.95 kcal/mol less stable than the equivalent complexes of one ion and two ammonia molecules (Figures 3.1b and 3.1c). On the other hand, the trimers of Figure 3.2b are respectively 4.20, 3.59, 4.32, 4.59, and 4.67 kcal/mol *more* stable than the corresponding ammonia-only complexes (Figure 3.1d).

Three stable conformations of the $M^+(NH_3)(H_2O)_2$ tetramer are shown in Figures 3.2c to 3.2e. The structures have quasi-planar geometries, except for the K^+, Rb^+, and Cs^+ complexes of structure 3.2d, for which the O···M^+···O···N dihedral angle significantly deviates from zero. The stability of the complexes follows the order 3.2c > 3.2d > 3.2e for Li^+, Na^+ and K^+, 3.2d > 3.2c > 3.2e for Rb^+, and 3.2d > 3.2c ≈ 3.2e for Cs^+ (see Table 3.3).

Equivalent stable conformations for the $M^+(NH_3)_2(H_2O)$ tetramer are shown in Figures 3.2f to 3.2h. Comparison of the binding energies of tri-coordinated structures 3.1e, 3.2f, and 3.2c (see Tables 3.1 and 3.3) shows a decrease in stability as first-shell ammonia molecules are replaced with water (3.1e > 3.2f > 3.2c). Ammonia is more stable than water in the first solvation shell of the ion if it is not involved in a hydrogen bond with a second-shell molecule (3.2g > 3.2d) but is *less* stable than water if it is (3.2h < 3.2d). Comparison between binding energies reported for structures 3.2g and 3.2e shows that water in the ion's first solvation shell is preferably bound to ammonia from the second solvation shell, due to O–H···N hydrogen bonds being slightly stronger than O–H···O bonds.[170]

The clusters obtained by substituting ammonia molecules with water in the tetrahedral $M^+(NH_3)_4$ pentamer are reported in Figures 3.2i to 3.2k. Similarly to what is observed for the tetramer (3.1e > 3.2f > 3.2c), the stability of the tetrahedral pentamer decreases as NH_3 molecules are replaced by water (3.1h > 3.2i > 3.2j > 3.2k) (see Tables 3.1 and 3.3).

In summary, alkali metal ions are preferentially coordinated by ammonia relative to water at least up to tetra-coordinated structures. Higher coordination numbers might however favor H_2O over NH_3, due to steric effects. The ammonia preference is partially reversed when molecules are added to the ion's second solvation shell. While an NH_3 molecule in the first solvation shell will form weak N–H···N or N–H···O hydrogen bonds with NH_3 or H_2O molecules in the second solvation shell, a first-shell H_2O molecule will form strong O–H···N or O–H···O hydrogen bonds. The presence of a second shell therefore enhances the stability of H_2O in the first solvation shell relative to NH_3.

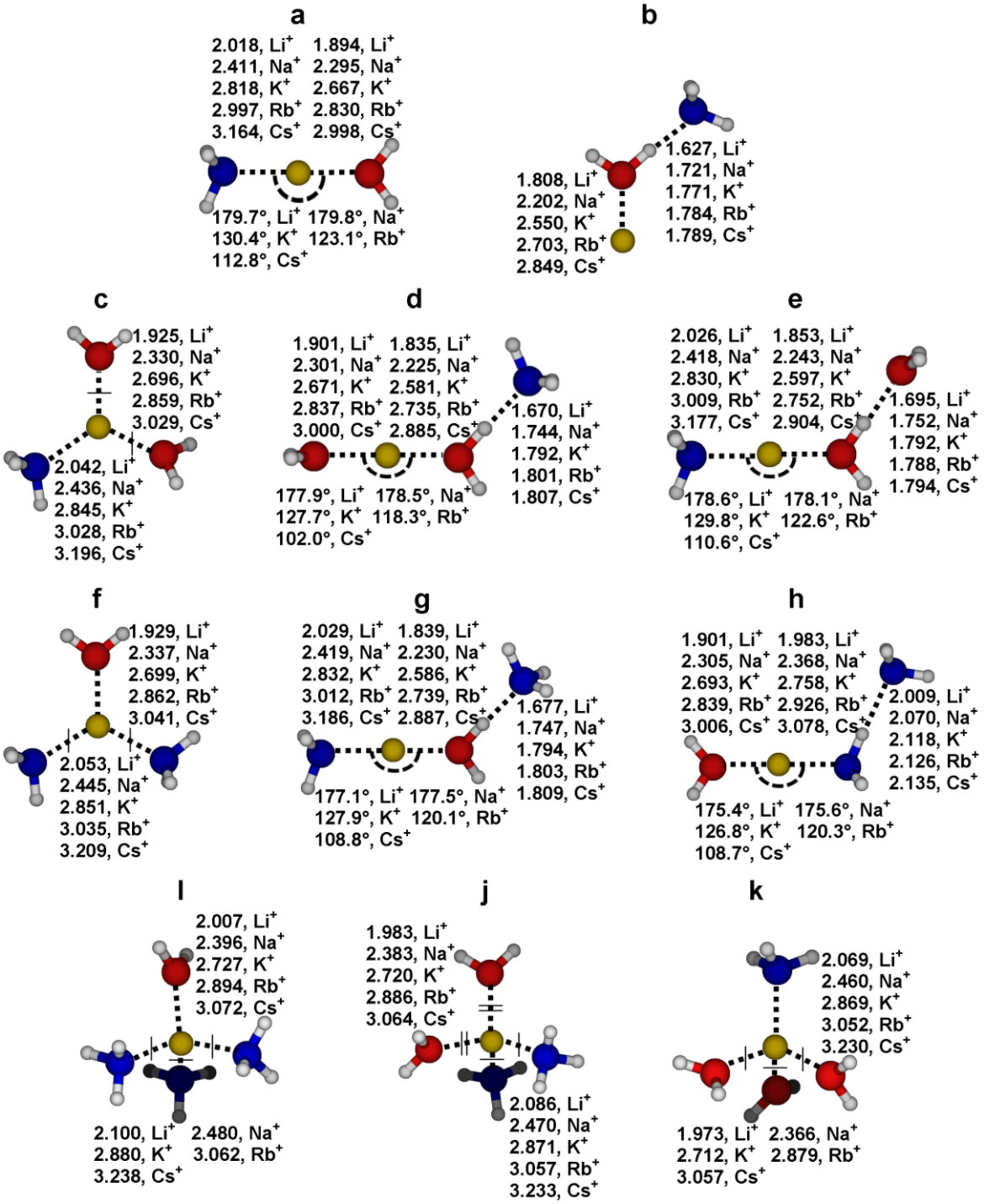

Figure 3.2. Optimized structures of the alkali ion-ammonia-water ternary clusters $M^+(NH_3)_n(H_2O)_m$ ($M^+ = Li^+$, Na^+, K^+, Rb^+, Cs^+, with n, m = 1–3 and $n + m \leq 4$) at the MP2 level (see the Methods section for details). Selected geometrical parameters are reported ($M^+\cdots N$, $M^+\cdots O$, $H\cdots N$, and $H\cdots O$ distances in Å, and $N\cdots M^+\cdots O$ and $O\cdots M^+\cdots O$ angles in degrees). Equal atom-atom distances are crossed with single or double bars. The structures are illustrated with Li^+ complexes but corresponding parameters for other alkali ion complexes are reported.

Table 3.3. Binding energies with and without correction for BSSE (E and E^{CP}, respectively) and the corresponding binding energy calculated using the optimized Drude model (E^{MM}) for the alkali ion-ammonia-water ternary clusters $[M^+(NH_3)_n(H_2O)_m$, $M^+ = Li^+$, Na^+, K^+, Rb^+, Cs^+, with n, m = 1–3 and $n + m \leq 4]$. All energies are in kcal/mol.

Complex	Li^+			Na^+			K^+			Rb^+			Cs^+		
	E	E^{CP}	E^{MM}	E	E^{CP}	E^{MM}	E	E^{CP}	E^{MM}	E	E^{CP}	E^{MM}	E	E^{CP}	E^{MM}
2a	–71.64	–66.74	–68.09	–50.36	–46.68	–47.86	–37.35	–35.17	–35.20	–30.91	–30.11	–30.86	–28.14	–27.00	–27.03
2b	–60.69	–55.92	–56.22	–44.79	–40.80	–41.52	–36.68	–33.23	–32.62	–31.95	–30.35	–29.85	–30.20	–28.37	–26.70
2c	–95.49	–88.14	–89.50	–68.66	–63.45	–65.55	–52.28	–49.02	–49.10	–43.37	–42.19	–43.44	–39.46	–37.78	–37.87
2d	–89.47	–82.05	–84.18	–65.99	–60.12	–62.12	–52.50	–48.11	–47.73	–45.05	–43.09	–43.34	–42.08	–39.74	–38.34
2e	–88.56	–81.36	–82.59	–65.26	–59.39	–60.79	–50.82	–46.59	–46.83	–43.24	–41.35	–42.06	–40.18	–37.90	–37.69
2f	–98.74	–91.54	–90.35	–71.10	–65.74	–66.35	–53.39	–50.07	–50.02	–44.27	–43.14	–43.89	–40.21	–38.58	–38.76
2g	–93.59	–86.11	–85.73	–68.91	–62.86	–63.29	–53.77	–49.36	–48.86	–46.10	–44.18	–43.93	–42.97	–40.63	–39.40
2h	–84.90	–78.30	–79.66	–61.86	–56.61	–57.72	–47.58	–43.87	–44.01	–40.02	–38.59	–39.20	–37.00	–35.18	–35.07
2i	–118.06	–107.94	–105.69	–87.78	–80.41	–80.83	–67.04	–62.55	–62.38	–55.80	–54.32	–55.08	–50.81	–48.69	–49.00
2j	–116.07	–105.77	–105.49	–86.05	–78.61	–80.48	–66.49	–61.38	–61.82	–55.14	–53.60	–54.88	–50.24	–48.08	–48.36
2k	–114.32	–103.57	–105.50	–84.27	–77.01	–80.22	–65.48	–60.93	–61.28	–54.49	–52.89	–54.69	–49.67	–47.48	–47.70

Comparison between the $M^+\cdots N$, $M^+\cdots O$, and $N\cdots H(H_2O)$ distances in the ion-ammonia, ion-water (see section 3.3.1.1), and ammonia-water (1.974 Å at the MP2(FC)/6-311++G(d,p) level) dimers, and the corresponding distances in complexes 3.2a and 3.2b, signals cooperativity between ion-water and ammonia-water interactions in complex 3.2b ($E^{coop} < 0$) and anti-cooperativity between ion-ammonia and ion-water interactions in complex 3.2a ($E^{coop} > 0$). The E^{coop} parameter in the two complexes is again calculated as the difference between the total interaction energy and the sum of the different pairwise interactions:

$$E^{coop} = E^{tot} - E_{M^+-H_2O} - E_{M^+-NH_3} - E_{H_2O-NH_3} \qquad (3.6)$$

Table 3.4 shows positive E^{coop} for complexes 3.2a and negative E^{coop} for complexes 3.2b. Similarly, comparing the structural parameters of complex 3.2a with those of complexes 3.2e, 3.2g, and 3.2h, shows cooperativity between first and second shell interactions.

Table 3.4. BSSE-corrected complexation energies calculated at the MP2 level and corresponding interaction energies calculated using the optimized Drude model (in parentheses). All energies are in kcal/mol.

Energy[a]	Complex 3.2a					Complex 3.2b				
	Li^+	Na^+	K^+	Rb^+	Cs^+	Li^+	Na^+	K^+	Rb^+	Cs^+
E^{tot}	−66.74	−46.68	−35.17	−30.12	−27.00	−55.92	−40.80	−33.23	−30.35	−28.37
	(−68.09)	(−47.86)	(−35.20)	(−30.86)	(−26.70)	(−56.22)	(−41.52)	(−32.62)	(−29.85)	(−27.03)
$E_{\mathrm{M^+-H_2O}}$	−33.39	−23.11	−17.91	−15.25	−13.74	−33.35	−22.93	−17.94	−15.04	−13.43
	(−35.74)	(−24.59)	(−17.86)	(−15.84)	(−13.54)	(−35.55)	(−24.45)	(−17.73)	(−15.70)	(−13.37)
$E_{\mathrm{M^+-NH_3}}$	−38.69	−26.44	−19.57	−16.67	−14.94	−10.56	−8.25	−6.86	−5.91	−5.55
	(−39.19)	(−26.85)	(−19.91)	(− 17.17)	(−15.34)	(−8.90)	(−7.65)	(−6.51)	(−6.07)	(−5.54)
$E_{\mathrm{H_2O-NH_3}}$	2.31	1.35	1.04	0.71	0.67	−3.81	−4.52	−4.84	−5.46	−5.49
	(1.38)	(0.91)	(0.70)	(0.66)	(0.64)	(−3.84)	(−4.70)	(−5.04)	(−5.13)	(−5.22)
E^{coop}	3.03	1.52	1.27	1.09	1.01	−8.20	−5.10	−3.59	−3.94	−3.90
	(5.46)	(2.67)	(1.87)	(1.49)	(1.54)	(−7.93)	(−4.72)	(−3.34)	(−2.95)	(−2.90)

[a] E^{tot} is the total binding energy, $E_{\mathrm{M^+-H_2O}}$ and $E_{\mathrm{M^+-NH_3}}$ are the binding energies between the metal ion and the individual molecules, and $E_{\mathrm{H_2O-NH_3}}$ is the interaction energy between water and ammonia. While E^{tot} is obtained from relaxed trimer geometries (with NH bonds constrained with the SHAKE algorithm in Drude model calculations), the other three terms are calculated using coordinates extracted from the trimer geometries. $E_{\mathrm{H_2O-NH_3}}$ is calculated at the MP2(FC)/6-311++G(d,p) level for complexes of Li^+, Na^+, K^+, and at the MP2(full)/6-311+G(3df,2p) level for complexes of Rb^+ and Cs^+. E^{coop} is the energy due to cooperativity between molecular interactions, calculated according to *Eq.* (3.6).

3.3.2. Ab initio Potential Energy Curves

Figure 3.3 shows ab initio potential energy surfaces together with the corresponding surfaces calculated with the optimized Drude model (see section 3.3.3). These curves are calculated by scanning the $M^+\cdots N$ distance and the $M^+\cdots H–N$ angle in the $M^+(NH_3)$ dimers, while keeping the NH_3 geometry fixed. Curve 3.3a represents the binding energy as a function of the distance between the ion and NH_3 in their C_{3v}-symmetric orientation. Curve 3.3b shows that the binding energy decreases as the $M^+\cdots H–N$ angle deviates from the equilibrium value, ~116°. These two curves are used to optimize the Drude model for the ion-ammonia interactions.

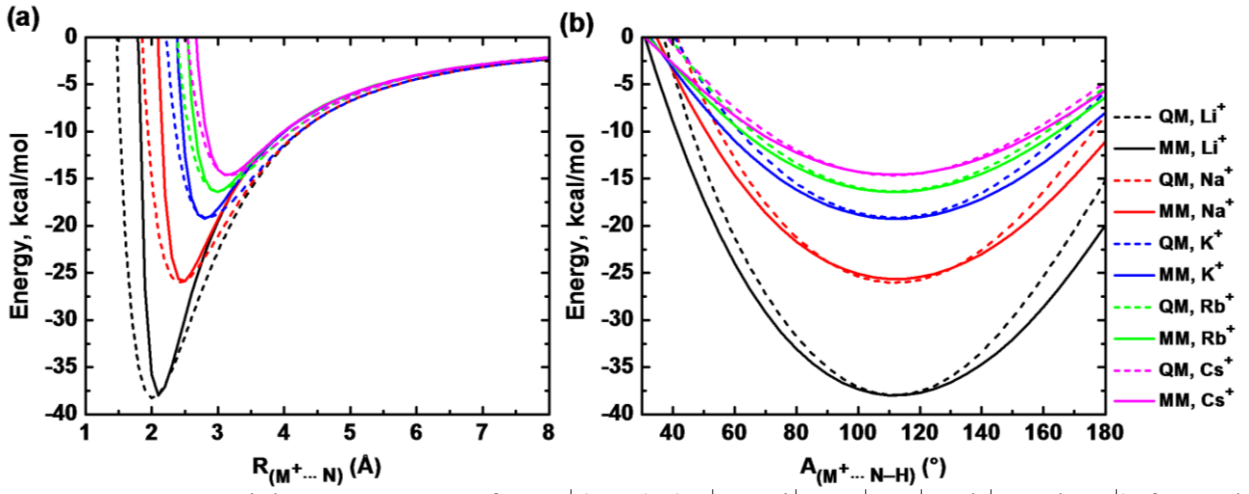

Figure 3.3. Potential energy curves for $M^+(NH_3)$ (M^+ = Li^+, Na^+, K^+, Rb^+, and Cs^+) from ab initio MP2 calculations (dashed line) and from polarizable model (solid line). The following coordinates are scanned: (a) $M^+\cdots N$ distance in the direction of ammonia's C_3 axis and (b) $M^+\cdots H–N$ angle at $M^+\cdots N$ distances of 2.1 Å for Li^+, 2.4 Å for Na^+, 2.8 Å for K^+, 3.0 Å for Rb^+, and 3.2 Å for Cs^+.

3.3.3. Optimized Drude Model

The optimized pair-specific LJ parameters of the polarizable potential model for alkali ion-ammonia interactions are reported in Table 3.5. As shown in Figure 3.3, the Drude-model PESs are in good agreement with ab initio results. The narrow shape of the Drude-model distance PESs (Figure 3.3a) is likely due to the steepness of the Lennard-Jones $1/r^{12}$ repulsive potential.[123] Although "softer" functional forms have been proposed,[179] we use the $1/r^{12}$ form to retain compatibility with the other components of the Drude polarizable force field and with standard non-polarizable force fields.

Table 3.1 shows that the Drude model gives binding energies of ion-ammonia binary clusters in good agreement with ab initio calculations: For all Li^+, Na^+, K^+, Rb^+, and Cs^+ clusters (Figure 3.1), maximum errors of respectively 4.3, 1.5, 0.6, 1.2, and 0.9%, and average unsigned errors of respectively 2.7, 0.9, 0.3, 0.5, and 0.5% are found. For ion-ammonia dimers, the model yields $M^+\cdots N$ separations of 2.105 Å for Li^+, 2.456 Å for Na^+, 2.788 Å for K^+, 2.972 Å for Rb^+, and 3.129 Å for Cs^+, in good agreement with MP2 results (see Figure 3.1a). It also captures the geometric variations of clusters as ammonia molecules are added. For instance the $Li^+\cdots N$ distance increases with the metal coordination number from 2.105 Å for the dimer (Figure 3.1a) to 2.148 Å for the trimer (Figure 3.1b), 2.204 Å for the tetramer (Figure 3.1e), and 2.260 Å for the pentamer (Figure 3.1h). For complex 1d, the Drude model shows a $Li^+\cdots N$ distance of 2.072

Å and an H···N distance of 2.167 Å, which are respectively 0.033 Å and 0.185 Å shorter than the corresponding distances in the isolated dimers, in line with the ab initio trend. As for the ab initio geometries, hydrogen bonds between first and second-shell ammonia molecules are longer for large ions (Rb^+, Cs^+) than for small ions (Li^+, Na^+) when the second-shell ammonia forms a single hydrogen bond (as in complexes 3.1d, 3.1f, and 3.1j) but are shorter for large ions when it forms two (as in complexes 3.1g and 3.1i). The Drude model also reproduces the cooperativity and anti-cooperativity observed in ion-ammonia clusters (see Table 3.2).

In combination with the SWM4-NDP water model, the Drude model for NH_3 yields binding energies of ion-ammonia-water clusters in good agreement with ab initio MP2 results (see Table 3.3). For all Li^+, Na^+, K^+, Rb^+, and Cs^+ clusters (Figure 3.2), maximum errors of 2.6, 4.2, 1.8, 3.4, and 3.5% and average unsigned errors of 1.4, 2.2, 0.6, 1.9, and 1.4% are found. The models reproduce the MP2 relative stabilities of the various structural arrangements of ligands around the metal ion. They also reproduce the cooperative and anti-cooperative binding observed in the ternary trimers (see Table 3.4).

The Drude model for alkali ion-water interactions[118] shows binding energies of the ion-water dimer of –35.92, –24.64, –17.90, –15.87, and –13.54 kcal/mol, and $M^+\cdots O$ distances of 1.906, 2.242, 2.620, 2.791, and 3.018 Å (going from Li^+ to Cs^+). While the ion-ammonia model is optimized to reproduce MP2 binding energies of M^+–NH_3 dimers, the ion-water model[118] was optimized to reproduce the experimental hydration free energies of the ions. For the Li^+ and Na^+ monohydrates, the Drude model slightly overestimates the MP2-calculated binding energies (by 2.5 kcal/mol for the lithium-water pair and by 1.55 kcal/mol for the sodium-water pair; see section 3.3.1.1). This is likely the reason why the combined Drude models for NH_3 and H_2O underestimate the increase in stability going from Li^+ or Na^+ ions coordinated by 1 ammonia and 3 water molecules (conformer 3.2k) to ions coordinated by 4 ammonia molecules (conformer 3.1h). For Li^+, the complexation energy goes from –103.57 to –110.38 kcal/mol for the MP2 calculations, but from –105.50 to –106.06 kcal/mol for the Drude model. For Na^+, the complexation energy goes from –77.01 to –82.07 kcal/mol for the MP2 calculations, but from –80.22 to –81.26 kcal/mol for the Drude model (see Tables 3.1 and 3.3). Since both the ion-water and ion-ammonia models yield solvation free energies in good agreement with experimental data and produce the expected trend for preferential solvation (see sections 3.3.4 and 3.3.6), we expect the solvation structures of ions in bulk solvent—whether pure or mixed—to be relatively unaffected by this discrepancy in the gas phase.

Table 3.5. Pair-specific LJ parameters for the interactions of Li^+, Na^+, K^+, Rb^+, and Cs^+ with NH_3.

Ion	Ion-N LJ parameters[a]		Generic LJ parameters[b]	
	$E_{min,ion-N}$ (kcal/mol)	$R_{min,ion-N}/2$ (Å)	E_{min} (kcal/mol)	$R_{min}/2$ (Å)
Li^+	0.01560	1.84419	0.03000	1.10000
Na^+	0.04637	1.88857	0.03151	1.46168
K^+	0.04787	2.08204	0.14193	1.68665
Rb^+	0.04875	2.18748	0.27307	1.78551
Cs^+	0.04982	2.27937	0.27660	2.02382

[a] This work. [b] Reproduced from Ref. 118. Parameters for ion-oxygen and ion-hydrogen interactions are obtained using the Lorentz–Berthelot mixing rules.

The ability of the polarizable model to describe the E^{coop} parameter (as defined in equations 3.5 and 3.6) represents a qualitative advantage over pairwise-additive force fields, which give $E^{coop} = 0$ by definition.[30,31] In light of the overall good performance of the models, it should be noted that, while the ion-ammonia model is adjusted to reproduce the properties of the ion-ammonia dimer, the ion-water,[118] ammonia-ammonia,[170] and ammonia-water[170] models have not been further adjusted. This suggests that the models can be reliably used to investigate properties of the ion solvated in liquid and aqueous ammonia solutions.

3.3.4. Solvation Free Energy of Alkali Ions in Liquid Ammonia

To further validate the M^+–NH_3 potential model, we calculate the free energy of solvation of alkali ions in liquid ammonia. The results are reported in Table 3.6 together with corresponding literature data.[180,181] The data show fair agreement for the solvation free energies of one ion relative to the next in the series. In comparison to liquid ammonia, calculations on alkali ions dissolved in SWM4-NDP water at 298.15 K and 1 atm show intrinsic solvation free energies, ΔG_{solv}^{intr} of –109.8, –85.6, –67.9, –63.0, and –55.8 kcal/mol for Li^+, Na^+, K^+, Rb^+, and Cs^+, respectively.[118] Despite M^+–NH_3 dimers having higher binding energies compared to corresponding M^+–OH_2 dimers, the polarizable model suggests that solvation free energies in water and in ammonia are comparable: $\Delta G_{solv,H_2O}^{intr} - \Delta G_{solv,NH_3}^{intr} = -0.3$ kcal/mol for Li^+, 0.0 kcal/mol for Na^+, 0.6 kcal/mol for K^+, −1.8 kcal/mol for Rb^+, and −0.4 kcal/mol for Cs^+.

Table 3.6. Absolute ($\Delta G_{\mathrm{solv}}^{\mathrm{intr}}$) and relative ($\Delta\Delta G_{\mathrm{solv}}$) solvation free energies of alkali ions in liquid ammonia,[a] with corresponding experimental values (in brackets). All values are in kcal/mol.

Ion	ΔG_{elec}	ΔG_{disp}	ΔG_{rep}	$\Delta G_{\mathrm{solv}}^{\mathrm{intr}}$	$\Delta\Delta G_{\mathrm{solv}}$
Li^+	−111.4	−0.2	2.1	−109.5	−23.9 (−28.0[b], −28.2[c])
Na^+	−87.9	−0.6	2.9	−85.6	−17.1 (−19.0[b], −18.8[c])
K^+	−71.4	−1.0	3.9	−68.5	−7.3 (−4.5[b], −5.1[c])
Rb^+	−64.2	−1.4	4.4	−61.2	−5.8 (−5.2[b])
Cs^+	−58.8	−1.7	5.1	−55.4	

[a] $\Delta\Delta G_{\mathrm{solv}}$ represents the difference in hydration free energies between consecutive alkali ions. Statistical error on the calculated values is ± 0.2 kcal/mol. [b] Reference 180. [c] Reference 181.

This finding—that alkali ions have comparable solvation free energies in water and in ammonia—is supported by experimental results.[180,181] Using thermodynamic data of ions in water and liquid ammonia, Plambeck reported $\Delta G_{\mathrm{solv,H_2O}} - \Delta G_{\mathrm{solv,NH_3}}$ to be 2.2 kcal/mol for Li^+, −0.4 kcal/mol for Na^+, −1.8 kcal/mol for K^+, −1.0 kcal/mol for Rb^+, and −0.8 kcal/mol for Cs^+.[180] By comparison, using a cluster pair method, Tuttle and Malaxos[181] have calculated solvation free energies of Li^+, Na^+, K^+, and Rb^+ in liquid ammonia that are 7.3, 4.3, 2.6, and 2.9 kcal/mol greater (more negative) than the corresponding hydration free energies of Tissandier *et al.*[182] (calculated using a similar cluster pair method).

3.3.5. Solvation Structure of Alkali Ions in Liquid Ammonia

The ion-ammonia Drude model is used to investigate the solvation structure of the alkali ions in liquid ammonia. For this purpose, systems composed of 250 NH_3 molecules and one alkali ion are simulated at 239.8 K and 1 atm for 20 ns. The structure of ammonia molecules around each ion is analyzed from the atom-atom correlation functions $g_{\mathrm{ion-N}}(r)$ and $g_{\mathrm{ion-H}}(r)$. The functions are calculated from the last 15 ns of each MD simulation, and shown in Figure 3.4. Characteristics of the different functions are summarized in Table 3.7.

The $g_{\mathrm{ion-N}}(r)$ function is characterized by a first peak that decreases in amplitude and shifts away from the ion on going from Li^+ to Cs^+. For lithium, the first minimum falls almost to zero, indicating that the first solvation shell is well structured and that exchange between ammonia molecules in the first and second solvation shells of Li^+ is rare. The analysis of the last 15 ns of a 20-ns simulation for the Li^+ system shows a minimum of 54 exchange events between molecules of the first and second solvation shells, which is large enough to ensure complete

equilibration of the solvation structure. The coordination number up to the minimum of the first peak, which is the average number of ammonia molecules in the cation's first solvation shell, is 4.0 for Li^+, 5.3 for Na^+, 6.1 for K^+, 6.7 for Rb^+, and 7.7 for Cs^+ (see Table 3.7). The calculated coordination numbers for Li^+, Na^+, and Rb^+ are in good agreement with experimental estimates (4.0 for Li^+,[44,138,140] ~5.5 for Na^+,[138] and 6.4 for Rb^+[139]). To our knowledge, no experimental data are available for K^+ and Cs^+. Compared to our results, previous theoretical calculations have reported coordination numbers of 4[143,145,154] and 6[142,144,145,148,152] for Li^+, 5,[143,150] 7,[127] 8,[127,147,150] and 9[147] for Na^+, 8.7 for K^+,[146] and 10 for Cs^+.[143] This shows that, with the exception of previous theoretical investigations on Li^+,[143,145,155] the Drude model represents a significant improvement in describing the solvation structures. It should also be noted that some of the coordination numbers reported in the literature are calculated at higher temperatures (260 K[143] and 277 K[147,148]) and might be larger at the temperature considered in this work (239.8 K).

Compared to ammonia, the solvation of the alkali ions in SWM4-NDP water at 239.8 K and 1 atm shows coordination numbers of 4.0, 5.7, 7.1, 8.5, and 10.3 water molecules in the first solvation shell of Li^+, Na^+, K^+, Rb^+, and Cs^+, respectively. These numbers are obtained from MD simulations of one alkali ion in 250 water molecules, by integrating the $g_{ion-O}(r)$ function up to its first minimum (at 2.56 Å for Li^+, 3.24 Å for Na^+, 3.56 Å for K^+, 3.80 Å for Rb^+, and 4.10 Å for Cs^+). Except for Li^+, the coordination numbers are slightly larger at 239.8 K than at room temperature.[118] Except for Li^+, they are also higher than the equivalent numbers for ammonia, due to the smaller size of H_2O compared to NH_3.

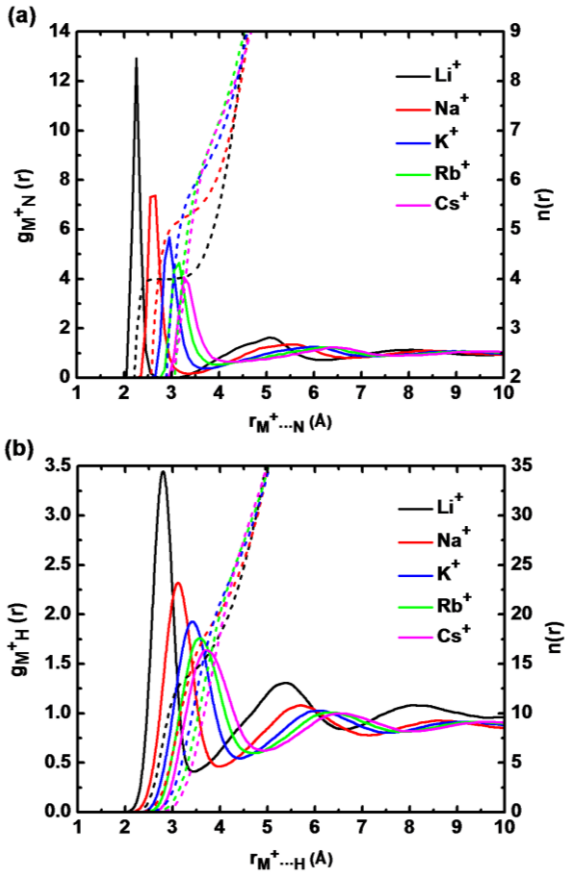

Figure 3.4. Ion−N (a) and ion−H (b) radial distribution functions (solid curves) and running integration numbers (dashed lines) from molecular dynamics simulations of Li^+ (black), Na^+ (red), K^+ (blue), Rb^+ (green), or Cs^+ (pink) in 250 NH_3 molecules at 239.8 K and 1 atm.

Table 3.7. Characteristic data of the radial distribution functions, $g_{ion-N}(r)$ and $g_{ion-H}(r)$, for a single ion in liquid ammonia.[a]

Ion	$g_{ion-N}(r)$						$g_{ion-H}(r)$					
	r_{M1}	r_{m1}	$n(r_{m1})$	r_{M2}	r_{m2}	$n(r_{m2})$	r_{M1}	r_{m1}	$n(r_{m1})$	r_{M2}	r_{m2}	$n(r_{m2})$
Li^+	2.25	2.83	4.0	5.03	6.2	25.7	2.79	3.43	14.1	5.39	6.68	92
Na^+	2.61	3.35	5.3	5.56	6.8	32.7	3.11	3.93	19.8	5.70	7.16	111
K^+	2.94	3.63	6.1	6.06	7.3	39.6	3.41	4.43	25.6	6.08	7.62	132
Rb^+	3.12	3.85	6.7	6.22	7.6	44.4	3.57	4.73	30.0	6.34	7.97	150
Cs^+	3.29	4.13	7.7	6.48	7.9	49.5	3.71	4.93	34.0	6.58	8.07	156

[a] r_{M1} and r_{M2} are the distances (Å) where the function has its first and second maximum, respectively. At r_{m1} and r_{m2} (in Å), the function has its first and second minimum. $n(r)$ is the running integration numbers evaluated at $r = r_{m1}$ and r_{m2}.

3.3.6. Alkali Ions in Aqueous Ammonia

To investigate the preferential solvation of alkali ions in ammonia-water mixtures, simulations are performed on systems composed of a single alkali cation solvated by $(1 - x_{NH_3})$ × 250 water molecules and x_{NH_3} × 250 ammonia molecules, with x_{NH_3} ranging from 0 to 1. Each simulation is run for 70 ns and the analysis is based on the last 65 ns.

Table 3.8 reports the number of ammonia and water molecules in the first and first + second solvation shells of each cation. These coordination numbers are calculated by integrating the $g_{ion–N}(r)$ and $g_{ion–O}(r)$ RDFs up to the minimum following the first (or second) peak in the total, $g_{ion–(N+O)}(r)$ RDF. The positions of these minima are weakly dependent on the mixture composition, with the first minimum at 2.80 Å for Li^+, 3.18 Å for Na^+, 3.56 Å for K^+, 3.80 Å for Rb^+, and 4.10 Å for Cs^+ and the second minimum at 5.06 Å for Li^+, 5.40 Å for Na^+, 5.74 Å for K^+, and 5.90 Å for both Rb^+ and Cs^+. For pure solvents (x_{NH_3} = 0 or 1), integration is performed up to the first and second minima of $g_{ion–O}(r)$ and $g_{ion–N}(r)$ RDFs. (The second minimum in the $g_{ion–O}(r)$ function is at 5.06 Å for Li^+, 5.40 Å for Na^+, 5.67 Å for K^+, 5.80 Å for Rb^+, and 5.88 Å for Cs^+. The first minima are reported in Section 3.3.5.)

Table 3.8. Average numbers of NH_3 and H_2O molecules in the first solvation shell of alkali cations in aqueous ammonia solutions at 239.8 K and 1 atm. The numbers of molecules in the first and second shells combined are reported within brackets.

x_{NH_3}	Li^+		Na^+		K^+		Rb^+		Cs^+	
	$n(NH_3)$	$n(H_2O)$	$n(NH_3)$	$n(H_2O)$	$n(NH_3)$	$n(H_2O)$	$n(NH_3)$	$n(H_2O)$	$n(NH_3)$	$n(H_2O)$
0.0	0 (0)	4 (20.2)	0 (0)	5.7 (24.0)	0 (0)	7.1 (26.8)	0 (0)	8.5 (28.5)	0 (0)	10.3 (29.0)
0.1	0 (2.2)	4 (17.6)	0.0 (2.0)	5.7 (21.9)	0.0 (1.8)	7.1 (25.6)	0.1 (1.7)	8.4 (27.7)	0.2 (1.7)	10.1 (27.1)
0.2	0 (4.1)	4 (15.3)	0.1 (3.8)	5.6 (19.7)	0.2 (4.0)	6.9 (22.9)	0.2 (4.0)	8.1 (24.7)	0.5 (3.7)	9.7 (24.4)
0.3	0 (6.0)	4 (13.0)	0.1 (6.1)	5.4 (16.9)	0.3 (6.5)	6.7 (19.8)	0.5 (6.6)	7.8 (21.4)	0.9 (5.7)	9.3 (21.7)
0.4	0 (8.3)	4 (10.3)	0.2 (8.1)	5.2 (14.3)	0.6 (8.9)	6.3 (16.6)	0.7 (8.8)	7.4 (18.6)	1.6 (8.5)	8.4 (18.0)
0.5	0 (9.6)	4 (8.7)	0.3 (10.4)	5.0 (11.3)	0.9 (11.3)	5.8 (13.6)	1.1 (11.6)	6.8 (15.0)	2.3 (11.0)	7.5 (14.8)
0.6	0 (11.5)	4 (6.6)	0.5 (12.4)	4.6 (8.7)	1.3 (13.7)	5.2 (10.4)	1.7 (14.3)	6.0 (11.4)	3.2 (14.4)	6.3 (11.5)
0.7	0 (12.2)	4 (5.8)	0.7 (13.8)	4.2 (6.7)	1.9 (15.5)	4.4 (7.8)	2.2 (16.2)	5.2 (8.8)	4.1 (15.4)	5.1 (8.6)
0.8	0 (12.8)	4 (4.8)	1.0 (14.6)	3.8 (5.3)	2.6 (16.7)	3.6 (5.9)	2.9 (17.5)	4.3 (6.5)	5.1 (17.1)	3.8 (5.8)
0.9	0 (13.3)	4 (4.4)	1.6 (15.3)	3.2 (3.8)	3.8 (17.8)	2.4 (3.5)	3.8 (18.6)	3.3 (4.4)	6.0 (18.3)	2.5 (3.5)
1.0	4 (25.7)	0 (0)	5.3 (32.7)	0 (0)	6.1 (39.6)	0 (0)	6.7 (44.4)	0 (0)	7.7 (49.5)	0 (0)

Preferential solvation of the ions is monitored using the following parameter:[183]

$$\delta x_{\mathrm{M^+,\,H_2O}} = x^{\mathrm{local}}_{\mathrm{M^+,\,H_2O}} - x_{\mathrm{H_2O}} = x_{\mathrm{NH_3}} - x^{\mathrm{local}}_{\mathrm{M^+,\,NH_3}} \qquad (3.7)$$

where $x^{\mathrm{local}}_{\mathrm{M^+,\,H_2O}}$ and $x^{\mathrm{local}}_{\mathrm{M^+,\,NH_3}}$ represent the local mole fractions of water and ammonia in the first, second, or first + second solvation shells of the ion, and $x_{\mathrm{H_2O}}$ and $x_{\mathrm{NH_3}}$ are the bulk mole fractions of water and ammonia.[183] Figure 3.5 shows the preferential water solvation of the various solvation shells of each ion as a function of $x_{\mathrm{NH_3}}$.

The positive sign of $\delta x_{\mathrm{M^+,\,H_2O}}$ in the first solvation shell (Figure 3.5a) indicates that alkali ions are preferentially solvated by water over the entire composition range. For any given composition, the preferential hydration follows the trend $Li^+ > Na^+ > K^+ \approx Rb^+ > Cs^+$. For Li^+, $\delta x_{\mathrm{M^+,\,H_2O}}$ is exactly equal to $x_{\mathrm{NH_3}}$ up to $x_{\mathrm{NH_3}} = 0.9$ because the occupancy of NH_3 in the first solvation shell is too low to be sampled from free MD simulations (given the slow rate of exchange of molecules around lithium).

The number of ammonia and water molecules in the second solvation shells is calculated from the numbers in the first shell and in the first and second shells combined (see Table 3.8). Counterbalancing the first solvation shell, the second shell is more favorably occupied by ammonia than by water, as evidenced by the negative values of $\delta x_{\mathrm{M^+,\,H_2O}}$ for all ions over most of the composition range (see Figure 3.5b). The preferential solvation in the second solvation shell follows for NH_3 molecules the same trend it follows for H_2O molecules in the first solvation shell ($Li^+ > Na^+ > K^+ \approx Rb^+ > Cs^+$).

Because of the complementary affinities of the first and second shells, the two shells combined display no marked solvation preference for either water or ammonia (see Figure 3.5c). Over the first two solvation shells, Li^+ shows slight preferential solvation by NH_3 for $x_{\mathrm{HN_3}} < 0.7$, while Na^+, K^+, Rb^+, and Cs^+ show slight preferential solvation by water over the entire concentration range.

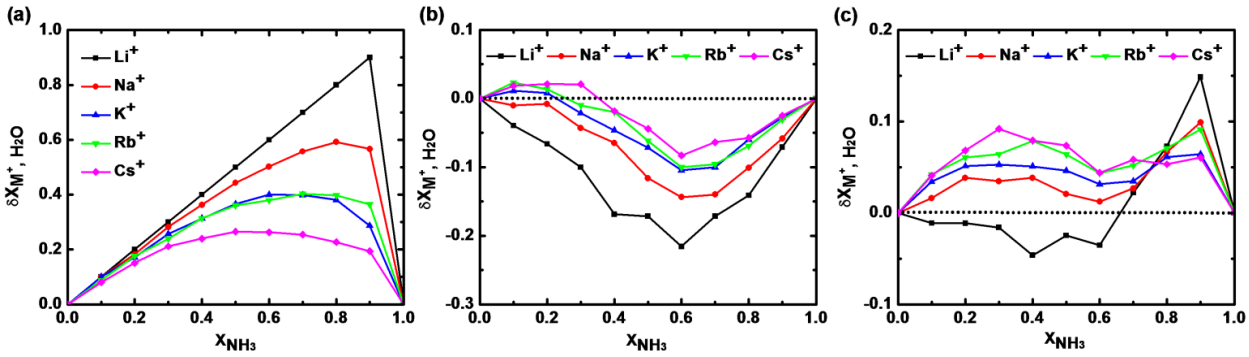

Figure 3.5. Preferential solvation by water of the first (a), second (b), and first + second (c) solvation shells of alkali ions, $\delta x_{\mathrm{M^+,\,H_2O}}$, as a function of the ammonia composition of the solution.

In aqueous ammonia solutions, alkali ions can therefore be viewed as water-selective in their first shells, ammonia-selective in their second shells, and, except for Li^+, slightly water-selective over both shells. Since the ion-ammonia dimer in gas phase has a greater binding energy than the ion-water dimer (see section 3.1.1), preferential solvation of the ions by ammonia might have been expected. Preferential solvation by water, however, could be attributed to the following two factors: (1) The smaller size of water relative to ammonia results in larger water coordination numbers (see Table 3.8) and in larger water clusters being more stable than the corresponding ammonia clusters. (2) Water molecules in the first solvation shell form strong O–H···N and O–H···O hydrogen bonds with ammonia and water molecules in the second solvation shell, while first-shell ammonia molecules form weak N–H···N and N–H···O hydrogen bonds.

Previous classical simulations on a single Li^+, Na^+, or K^+ solvated in 18.4% ammonia molar fraction have shown the following compositions for the first and second shells (using the notation "ion[first shell][second shell]"): $Li^+[(H_2O)_4(NH_3)_2][(H_2O)_8(NH_3)_4]$,[161] $Li^+[(H_2O)_3(NH_3)_3]$,[162] $Na^+[(H_2O)_{2.4}(NH_3)_4][(H_2O)_7(NH_3)_2]$,[160] $Na^+[(H_2O)_{4.9}(NH_3)_{2.2}]$,[163] and $K^+[(H_2O)_{5.3}(NH_3)_{3.4}]$.[164] QM/MM simulations of the same system show $Li^+[(H_2O)_3(NH_3)][(H_2O)_4(NH_3)_2]$,[162,165] $Li^+[(H_2O)_4][(H_2O)_4]$,[165] $Na^+[(H_2O)_{3.7}(NH_3)_{1.8}]$,[163] and $K^+[(H_2O)_{6.7}(NH_3)_{0.9}]$.[164] These QM/MM simulations have been performed using a QM region that includes either only the first solvation shell of the ion[162–164] or both the first and second solvation shells.[165] While QM/MM simulation results are expected to be more reliable, some of the structures they predict are questionable. First, it appears that the solvation structure is highly dependent on the size of the QM region.[165] Second, according to the hard-soft acid-base theory,

the hardness of the alkali ions decreases as the ion size increases and therefore should favor complexation with the softer base (NH_3). The QM/MM simulations of Tongraar and Rode[163–165] show affinities towards NH_3 following the trend $Na^+ > K^+ > Li^+$, inconsistent with the expected trend ($K^+ > Na^+ > Li^+$). By contrast, the Drude model shows the expected behavior: Larger ions have higher ammonia affinities (see Table 3.8 and Figure 3.5a). Ab initio MD simulations of a neutral Li atom in 20 water and 6 ammonia molecules[166] have shown ionization of Li and preferential coordination by four water molecules, in agreement with our results.

Based on the solvation structures reported for Li^+ and Na^+ from MC simulations,[160,161] we calculate a $\delta x_{M^+,\,H_2O}$ value of –0.15 for both shells of Li^+ and of –0.44 and –0.04 for the first and second shells of Na^+, respectively. Such preferential first-shell solvation by ammonia is at odd with the hardnesses of the two ions. The more recent QM/MM investigation of Li^+ solvation in 18.4% aqueous ammonia by Tongraar and Rode[165] shows a preferential hydration parameter of +0.184 for both solvation shells. While the preferential hydration of the first shell is consistent with our findings, Tongraar and Rode report that the Li^+ ion's second shell is populated by only ~4 molecules,[165] compared to 15.4 molecules from our simulations at 20% ammonia and 12.0 molecules from previous MC simulations.[161]

To further analyze the affinity of each solvent component for the ions, we calculate the PMF of association of an ion to a single NH_3 molecule in liquid water (see Figure 3.6a) and of an ion to a single H_2O molecule in liquid ammonia (see Figure 3.6c). These PMFs are computed under the thermodynamic conditions used to investigate preferential solvation (T = 239.8 K, p = 1 atm). Figure 3.6 also displays the number of first-shell solvent molecules as a function of the ion-ligand distance, which describes the influence of the ligand on first-shell solvent occupancy. Table 3.9 reports r_{m1} and r_{m2}, the ion-ligand distances corresponding respectively to the first- and second-shell PMF minima; n_1 and n_2, the numbers of first-shell solvent molecules when the ligand is respectively at distances r_{m1} and r_{m2} from the ion; as well as Δn_1 and Δn_2, the numbers of first-shell solvent molecules displaced when the ligand is at distances r_{m1} and r_{m2}. The coordination numbers are calculated from the pair distribution functions $g_{ion–O}$ and $g_{ion–N}$ up to their first minimum.

Figure 3.6a and Table 3.9 show that, while NH_3 binds the first solvation shell only for Cs^+ (PMF(r_{m1}) < 0), it mainly binds the second solvation shell only for Li^+ and Na^+ (PMF(r_{m2}) < 0). This is consistent with the "second-shell" values of $\delta x_{M^+,\,H_2O}$ when x_{NH_3} is close to 0 (see

Figure 3.5b): In dilute NH_3 aqueous solutions, $\delta x_{M^+,H_2O}$ is positive for K^+, Rb^+, and Cs^+ but negative for Li^+ and Na^+. Table 3.9 also shows that, while binding of NH_3 in the first solvation shell results in the displacement of at least 0.7 first-shell water molecules, binding in the second shell causes a depletion of no more than 0.1 first-shell molecules, indicating that the presence of NH_3 in the second shell does not significantly perturb the hydration structure.

In contrast to NH_3 in water, H_2O in ammonia shows a high affinity for the ion's first solvation shell that follows the trend $Li^+ > Na^+ > K^+ \approx Rb^+ > Cs^+$ (see Figure 3.6c and Table 3.9). This infinite-dilution result is consistent with the observed trend in preferential hydration over the entire composition range (see Figure 3.5a). The shallow minimum at 5–6 Å distances corresponds to solvent-separated pairs.

Table 3.9. Properties of the PMFs between alkali ions and NH_3 in water and between the ions and H_2O in ammonia, calculated at $T = 239.8$ K and $p = 1$ atm.*

Property	1 NH_3 in 250 H_2O					1 H_2O in 250 NH_3				
	Li^+	Na^+	K^+	Rb^+	Cs^+	Li^+	Na^+	K^+	Rb^+	Cs^+
r_{m1}	2.27	2.66	3.03	3.30	3.43	2.00	2.34	2.72	2.88	3.12
PMF(r_{m1})	0.1	0.5	0.2	0.2	−0.2	−3.7	−2.8	−2.1	−2.2	−1.6
n_1	3.0	4.8	6.4	7.8	9.4	3.0	4.1	5.0	5.7	6.8
Δn_1	–1.0	–0.9	–0.7	–0.7	–0.9	–1.0	–1.2	–1.1	–1.0	–0.9
r_{m2}	4.1	4.3	4.6	4.8	5.2	4.9	5.5	5.9	6.2	6.3
PMF(r_{m2})	−0.8	−0.4	0.0	0.0	0.0	−0.4	−0.3	−0.3	−0.3	−0.2
n_2	4.0	5.7	7.1	8.4	10.2	4.0	5.3	6.1	6.7	7.6
Δn_2	–0.0	–0.0	–0.0	–0.1	–0.1	–0.0	–0.0	–0.0	–0.0	–0.1

* r_{m1} and r_{m2} are ion-ligand distances (in Å) at which the PMF (in kcal/mol) possesses a minimum. n_1 and n_2 are numbers of first-shell solvent molecules at $r = r_{m1}$ and r_{m2}. Δn_1 and Δn_2 are numbers of first-shell solvent molecules displaced by ligand complexation at r_{m1} and r_{m2}.

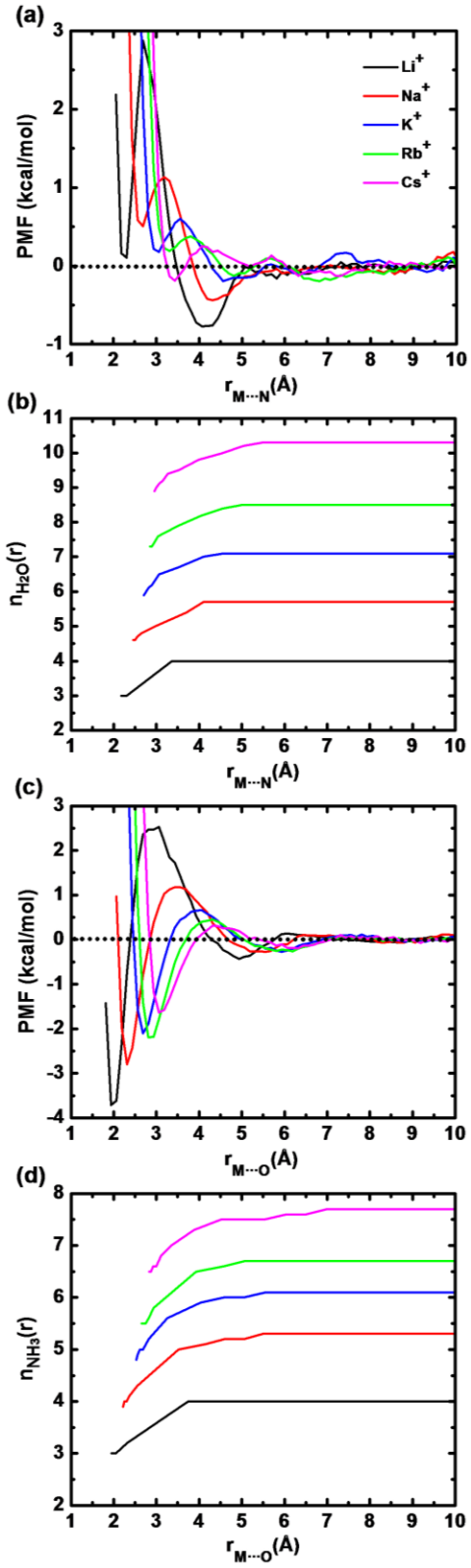

Figure 3.6. PMFs between alkali ions and an ammonia molecule in liquid water (a) and between alkali ions and a water molecule in liquid ammonia (c). The number of first-shell solvent molecules are shown in panels (b) and (d). Colors are as per panel (a).

3.4. Conclusion

A polarizable model based on classical Drude oscillators is optimized for alkali ions-ammonia interactions based on the ab initio properties of the individual dimers. The model gives binding energies for larger ion-ammonia and ion-ammonia-water clusters in very good agreement with ab initio MP2 results, gives relative solvation free energies of ions in liquid ammonia in good agreement with experiments, and yields structures of ammonia-solvated ions in very good agreement with experimental structures. It also reproduces binding cooperativity in ion-ammonia and ion-ammonia-water clusters, an effect that cannot be captured by pairwise-additive force fields. The model is used to investigate the preferential solvation of alkali ions in aqueous ammonia solutions, and shows preferential binding for water in the first solvation shell and for ammonia in the second solvation shell.

In the present work, water-ammonia mixtures were used as a prototypical system to analyze ligand competition in the first and second coordination shells of metal ions. The concepts developed in this work will likely be applicable to preferential solvation involving more complex ligands. They will also likely help in rationalizing ion selectivity and ion coordination in biological molecules such as proteins and nucleic acids.

4. Simulation of Liquid and Supercritical Hydrogen Sulfide and of Alkali Ions in the Pure and Aqueous Liquid*

* Adapted with permission from (Orabi, E. A.; Lamoureux, G. Simulation of Liquid and Supercritical Hydrogen Sulfide and of Alkali Ions in the Pure and Aqueous Liquid. *J. Chem. Theory Comput.* **2014**, *10*, 3221–3235) Copyright (2014) American Chemical Society.

Abstract

A polarizable model for hydrogen sulfide (H_2S) is optimized based on the experimental properties of the monomer and of the bulk liquid. The model is characterized by rigid SH bonds but flexible HSH angle and the polarizability is based on the Drude oscillator model. Bonded parameters and atomic charges are based on the experimental properties of the gaseous monomer. Atomic Lennard-Jones (LJ) parameters are adjusted based on the density of H_2S around the critical point (in the temperature range 363–393 K and pressure range 8.023–10.013 MPa). The model gives binding energies for H_2S dimers, trimers, and tetramers in good agreement with ab initio MP2(full)/6-311++G(d,p) results. It shows a liquid structure in very good agreement with neutron diffraction data. The model also gives density, self-diffusion coefficient, heat of vaporization, and dielectric constant of liquid hydrogen sulfide at the normal boiling point in good agreement with experimental data. In addition, the model is transferable to high temperature and pressure conditions, as evidenced from simulations up to 542.2 K and 40 MPa. The model is used in combination with the SWM4-NDP water model, with LJ parameters between the S and O atoms adjusted to reproduce the experimental hydration free energy of H_2S. Simulations suggest that, in its first solvation shell, a single H_2O molecule is solvated by 10 H_2S molecules while a single H_2S molecule is solvated by 20.5 H_2O molecules. Pair-specific LJ parameters between alkali ions (Li^+, Na^+, K^+, Rb^+, Cs^+) and the S atom are adjusted to reproduce ab initio binding energies of the ion-H_2S pairs at the CCSD(T) level. Simulations based on these parameters show that alkali ions have higher coordination numbers and lower solvation free energies in liquid H_2S than in liquid water or liquid ammonia. The model is also used to investigate the preferential solvation of the ions in aqueous solutions with a 10% H_2S mole fraction. Results show that the ions are preferentially solvated by water in their first solvation shell but have no significant selectivity to either ligands in their second shells.

4.1. Introduction

Hydrogen sulfide (H_2S) is a colorless gas known to be poisonous, highly corrosive to metals, flammable, and explosive.[184–186] The gas is primarily produced in nature by the bacterial decomposition of organic material, especially under low oxygen concentration, and is listed as a hazardous air pollutant.[186] It is a natural constituent of natural gas and petroleum, and the most common impurity in their hydrocarbon content. H_2S needs thus to be removed from oil and gas, in a process called sweetening.[186] While exposure to concentrated H_2S gas results in symptoms such as irritation, breathing disorder, nausea, diarrhea, rapid heart rate, and headaches, and can cause death,[184–186] H_2S is found to act as a neurotransmitter at very low concentrations.[187]

While H_2S and H_2O share some characteristic properties—both are polar molecules, have a bent molecular geometry, and are amphiprotic—their fluids display significantly different structural, dynamic, and thermodynamic properties. For example, while neutron diffraction experiments show strong hydrogen bonding between water molecules,[188] they indicate that H_2S lacks such hydrogen bonding network.[189] H_2S is also known to display dielectric constant and heat of vaporization lower than those of H_2O. Optimization of potential models for H_2S is thus important to understand the properties of the liquid and to study multicomponent natural-gas mixtures, in order to suggest effective H_2S-separation strategies. Such models would be valuable complements to experiment, given the care that should be taken when working with or in presence of H_2S (due to its toxicity). In addition, H_2S can be considered a minimal model for the side chains of the amino acids cysteine (Cys) and methionine (Met), and thus reliable potential models for H_2S can be transferred to higher thiol members. Molecular models can be benchmarked using a wealth of experimental data on the pure H_2S fluid: structure,[189] density,[190,191] heat of vaporization,[190,192,193] self-diffusion coefficient,[194] dielectric constant,[195] and heat capacity.[192,196]

The first potential model for liquid H_2S was reported by Jorgensen, as part of a series of intermolecular potential functions for sulfur-containing compounds.[197] This rigid three-site model is parameterized to reproduce the heat of vaporization and density of liquid H_2S at the normal boiling point. The model, published before neutron diffraction investigations of the liquid structure,[189] is suggesting significant hydrogen-bonding in liquid H_2S. Forester *et al.*[198] have parameterized a rigid four-site model, with three atomic sites and a point charge on the bisector of the HSH angle. This model gives heat of vaporization in satisfactory agreement with

experiment but underestimates the self-diffusion coefficient of the liquid in the temperature range examined (194–293 K).[198] Kristóf and Liszi[199] have re-parameterized the model of Forester *et al.* to reproduce the density and heat of vaporization over the temperature range 224–353 K of the liquid-vapor coexistence curve of H_2S. Kamath *et al.*[200] have parameterized a set of four three-site models for H_2S with flexible HSH angles. These four models were adjusted such that the density and vapor pressure in the temperature range 260-370 K are in close agreement with experiments.

Induced polarization is important for the accurate description of liquid water[113] and liquid ammonia,[67,170] which suggests that polarizable molecular models would be superior to pairwise-additive models for H_2S as well (given that polarizability increases in the sequence $H_2O < NH_3 < H_2S$). Most recently, Riahi and Rowley[201] have developed a polarizable model for H_2S composed of four sites (three atomic sites and a point charge at the bisector of the HSH angle) and a Drude oscillator on the sulfur atom. The model was parameterized to reproduce the structural, thermodynamic, and dielectric properties of liquid H_2S at the boiling point, and used to investigate properties of H_2S over the temperature range 212–298 K along the liquid-vapor coexistence curve.

While some of these models[197–200,201] are reported to reproduce experimental properties of H_2S, they have not been validated at temperatures higher than 400 K. Given the difficulty for performing experiments at high temperature and pressure, reliable models at such conditions are desirable.

The solvation structure and solvation thermodynamics of alkali ions in liquid water and liquid ammonia have received considerable attention over the past years.[118,180–182,202] In contrast, to the best of our knowledge, no experimental or computational studies of alkali ion solvation in liquid H_2S have ever been reported. Except for the Na^+–H_2S pair,[197] no ab initio studies of alkali ions in H_2S clusters have been reported either. A more systematic ab initio investigation is certainly desirable, given the lack of experimental data. Ab initio calculations can provide information on the geometry and energetics of ion-H_2S complexes, can help explaining the properties of ions in liquid H_2S, and can provide benchmark data for parameterization of potential models. Such models are important to understand the trend in solvation structure and solvation free energy as a function of the ligand hardness (going from the hard H_2O to the less hard NH_3 to the soft H_2S).

Studying the solvation of alkali ions in liquid mixtures is important to understand preferential solvation, which is a determinant factor in ion selectivity in biological systems. In a previous study,[202] we investigated the solvation of alkali ions in liquid ammonia and the ions preferential solvation in ammonia-water mixtures using a Drude polarizable model for ion-NH_3 interactions. Compared to other MM, QM/MM, and QM molecular dynamics (MD) simulation results, the model gave results more consistent with the hard-soft acid-base theory.[202]

In this work, we aim to develop a simple polarizable potential model for liquid H_2S. Compared to the Riahi and Rowley's model,[201] the present model is formed of three atomic sites and a Drude particle on sulfur but has no additional site to describe the electron lone pair. The model is optimized to minimize the error in density of H_2S in the temperature range 363–393 K and pressure range 8.023–10.013 MPa, and to reproduce the hydration free energy of H_2S and the ab initio binding energies of alkali ions-H_2S pairs calculated at the CCSD(T) level. It is then validated on the ab initio binding energies of $(H_2S)_n$ (n = 2–4) clusters calculated at the MP2 level, and on the properties of liquid hydrogen sulfide over a wide range of temperatures and pressures (that covers the liquid and supercritical phases of H_2S). The model is used to investigate the solvation structure and solvation free energy of alkali ions in liquid H_2S. In combination with models for water[113] and for ion-water interactions[118] developed previously, it is also used to investigate the solvation structure of a single H_2S solute in liquid H_2O, the solvation structure of a single H_2O solute in liquid H_2S, and the preferential solvation of alkali ions in aqueous hydrogen sulfide solution at mole fraction x_{H_2S} = 0.1.

4.2. Methods

4.2.1. Ab initio Calculations

All ab initio calculations are performed using the Gaussian 09 program.[26] Calculations on H_2S–H_2O pair and $(H_2S)_n$ clusters (n = 1−4) are carried out at the MP2/6-311++G(d,p) level. For $(H_2S)_2$, geometry optimization is also performed at the MP2 level using Dunning's aug-cc-pVXZ basis sets (X = D, T, Q, 5).[112] For M^+–H_2S pairs (M^+ = Li^+, Na^+, and K^+), calculations are performed at the MP2/6-311++G(d,p) level. For the M^+ = Rb^+ and M^+ = Cs^+ complexes, calculations are performed at the MP2 level with the 6-311+G(3df,2p) basis set for H, O, and S atoms, and with the Stuttgart RSC 1997 effective core potentials (ECP) and valence basis sets[168] for Rb and Cs atoms. Diffuse d and f polarization functions are added to the basis sets, with exponents 0.39 and 0.55 for Rb, and 0.29 and 0.44 for Cs.[202] Ab initio calculations on alkali ion-

H_2S pairs are also performed using coupled cluster theory with single, double, and perturbative triple excitations (CCSD(T)), with the same basis sets as for the MP2 calculations. All ab initio calculations are done using full-electron representation. Except for the transition state (TS) structures of the $H_2S{-}H_2S$ and $H_2S{-}H_2O$ pairs, geometry optimizations are carried out without imposing any symmetry constraints. Frequency calculations are performed on all optimized structures to confirm that they are either energy minima or TSs. The counterpoise (CP) procedure of Boys and Bernardi[111] is used to correct binding energies for basis set superposition error (BSSE).

Potential energy surfaces (PESs) for the $H_2S{-}H_2S$ and $H_2S{-}H_2O$ pairs are generated at the MP2/6-311++G(d,p) level by scanning the S···S and S···O distances in optimized structures from 2 to 10 Å. For $M^+{-}H_2S$ pairs, PESs are generated at the CCSD(T) level with basis sets as described earlier. These PESs are the result of scanning the $M^+{\cdots}S$ distance from 2 to 10 Å and the $M^+{\cdots}S{-}Y$ angle from 0° to 180° (where Y is a point on the bisector of the HSH angle). All surfaces are computed using the geometries of the optimized H_2S and H_2O monomers and are corrected for BSSE.

4.2.2. Molecular Mechanics Calculations

Molecular mechanics (MM) calculations are performed with the program CHARMM.[29] Polarizable potential models based on classical Drude oscillators[32] have been reported for H_2O[113] and alkali ions.[118] Following our previous work,[18,30,31,170,202] a polarizable model for liquid H_2S and alkali ion-H_2S interactions is optimized based on their experimental and ab initio properties.

4.2.2.1. Potential Energy Function and Parameterization Strategy

In the Drude oscillator model, molecular polarizability is described by attaching a light (0.4 amu), negatively charged "Drude" particle to all non-hydrogen atoms.[32] A harmonic spring with force constant $k_{\mathrm{D}} = 1000\ \mathrm{kcal/mol/Å^2}$ is used to tether the Drude particle to the heavy atom.[32] The partial charge q_i of a polarizable atom i is distributed between the Drude particle ($q_{\mathrm{D}i}$) and the atomic core ($q_{ci} = q_i - q_{\mathrm{D}i}$) with the Drude particle charge being determined from the atomic polarizability via the relation $\alpha_i = {q_{\mathrm{D}i}}^2/k_{\mathrm{D}}$. A displacement d of the Drude particle from the polarizable atom results in a dipole moment $q_{\mathrm{D}i}d$. The potential energy function that describes all polarizable systems studied in this work is given by[170,202]

$$U(R) = \sum_{i=1}^{N} \frac{1}{2} k_{\mathrm{D}} |\mathbf{r}_{\mathrm{c}i} - \mathbf{r}_{\mathrm{D}i}|^2 + \sum_{\text{HSH angles}} k_\theta (\theta - \theta_0)^2$$
$$+ \sum_{\text{nonbond}} E_{\min,ij} \left[\left(\frac{R_{\min,ij}}{|\mathbf{r}_{ci} - \mathbf{r}_{cj}|} \right)^{12} - 2 \left(\frac{R_{\min,ij}}{|\mathbf{r}_{ci} - \mathbf{r}_{cj}|} \right)^{6} \right]$$
$$+ \sum_{\text{nonbond}} \left(\frac{q_{ci} q_{cj}}{|\mathbf{r}_{\mathrm{c}i} - \mathbf{r}_{\mathrm{c}j}|} + \frac{q_{ci}\, q_{\mathrm{D}j}}{|\mathbf{r}_{ci} - \mathbf{r}_{\mathrm{D}j}|} + \frac{q_{\mathrm{D}i}\, q_{cj}}{|\mathbf{r}_{\mathrm{D}i} - \mathbf{r}_{cj}|} + \frac{q_{\mathrm{D}i} q_{\mathrm{D}j}}{|\mathbf{r}_{\mathrm{D}i} - \mathbf{r}_{\mathrm{D}j}|} \right) \qquad (4.1)$$

where N is the number of interacting molecules, and $\mathbf{r}_{ci}$ and $\mathbf{r}_{Di}$ are positions of the core particle i and its Drude particle, respectively. k_θ and θ_0 are the force constant and equilibrium angle for the HSH angles θ. $E_{\min,ij}$ and $R_{\min,ij}$ are the mixed Lennard-Jones (LJ) parameters between non-bonded atoms i and j, defined by the Lorentz–Berthelot combination rules:

$$E_{\min,ij} = \sqrt{E_{\min,i} \times E_{\min,j}} \qquad \text{and} \qquad R_{\min,ij} = \frac{R_{\min,i} + R_{\min,j}}{2} \qquad (4.2)$$

Equation (4.1) does not include bond stretching energy terms since for both water and hydrogen sulfide, bonds are constrained to their equilibrium values using the RATTLE/Roll algorithm.[33] It also does not include HOH angle bending terms since the SWM4-NDP water model has a rigid molecular geometry.[113]

The polarizable model for liquid H_2S is parameterized based on the experimental properties of the gaseous monomer and the density of hydrogen sulfide in the temperature range 363–393 K and pressure range 8.023–10.013 MPa. The model is composed of three atomic sites and a Drude oscillator linked to sulfur. The equilibrium values of the SH bond length and the HSH angle are set to the gas-phase experimental values (r_{SH} = 1.328 Å and θ_{HSH} = 92.2°)[203] The bond and angle force constants, k_b and k_θ, are set to reproduce the experimental vibration frequencies of the monomer. The electrostatic parameters (partial atomic charges and polarizability) are similarly based on the experimental data of the H_2S monomer, with the partial atomic charges on S and H atoms fitted to reproduce the dipole moment, and the polarizability of the S atom set to the polarizability of gaseous H_2S. Compared to previous force fields,[197–200,201] the present model has LJ terms assigned to both sulfur and hydrogen atoms, rather than sulfur only. These parameters are optimized based on the experimental density of the fluid at temperatures 363.25, 373.25, 383.24, and 393.22 K, under pressures of 8.023, 9.344, 10.024, and 10.013 MPa, respectively.[191] Fluid densities calculated with literature models[197–200,201] deviate

from experimental data by more than 71% for at least one of these four thermodynamic conditions (see section 4.3.6.1).

Without specific LJ parameters between S and O and between S and the alkali ions, the model gives relatively poor agreement with the experimental hydration free energy of H_2S and overestimates the CCSD(T) binding energies for H_2S-alkali ion pairs. We therefore adjust the model to reproduce these values by optimizing pair-specific LJ parameters (introduced via the NBFIX[29] facility of CHARMM) between the S atom of H_2S and the O atom of H_2O, and between the S atom and each alkali ion. Optimization of the pair-specific LJ parameters between S and O is done by introducing small changes from the default mixed parameters until the experimental hydration free energy of H_2S is reproduced. Optimization of the pair-specific LJ parameters between S and the alkali ions follows an approach reported elsewhere.[18,30,31, 170,202] Briefly, optimization initially targets the ab initio PESs of the pairs. The obtained parameters are finally adjusted to reproduce the complexation energies of the fully relaxed ab initio pairs while maintaining ion-S separations within 2.0% of the ab initio CCSD(T) results.[30,202]

4.2.2.2. Molecular Dynamics

Unless otherwise stated, all MD simulations are performed with cubic periodic boundary conditions in the isothermal-isobaric ensemble (*NpT*). H_2O molecules are kept totally rigid (bonds and angles) using the RATTLE/Roll algorithm,[33] while only the bonds are kept rigid for H_2S. Simulations of pure liquid H_2S are carried out using 500 molecules at various thermodynamic conditions. To ensure a consistent comparison, all liquid H_2S simulations are repeated using the potential models of Jorgensen,[197] Forester *et al.*,[198] Kristóf and Liszi,[199] Kamath *et al.* (model c),[200] and Riahi and Rowley.[201] Except the model of Kamath *et al.*,[200] which has flexible angles, these models maintain totally rigid H_2S geometries. The solvation structure of water and alkali ions in liquid H_2S is investigated by simulating a single solute (water or alkali ion) in 500 H_2S molecules at the normal boiling point of hydrogen sulfide (T = 212.82 K, p = 0.1013 MPa = 1 atm).[192] For the purpose of comparison, the solvation structure of alkali ions in water is investigated from MD simulations of each alkali ion in 500 water molecules at same thermodynamic conditions (T = 212.82 K, p = 0.1013 MPa). The solvation structure of H_2S in water is investigated from a simulation of one H_2S molecule in 500 H_2O molecules at T = 298.15 K and p = 0.1013 MPa. Calculations of the solvation free energy of the ions in liquid hydrogen sulfide are performed by simulating each ion in 500 H_2S molecules at T

= 298.15 K and p = 2.0174 MPa = 19.91 atm (the corresponding vapor pressure of liquid H_2S). Hydrogen sulfide has a very low solubility in water,[204] and thus we investigate the preferential solvation of alkali ions in aqueous hydrogen sulfide at low mole fraction of H_2S, x_{H_2S} = 0.1. The composition of the aqueous alkali ion solutions is one alkali ion + 450 H_2O molecules + 50 H_2S molecules and the simulations are performed at the boiling point conditions of pure H_2S. It should be noted that water is in the supercooled state during the duration of simulations at 212.82 K.

Electrostatic interactions are computed using the particle-mesh Ewald method[115] with κ = 0.34 for the charge screening and a 1.0 Å grid spacing with sixth-order splines for the mesh interpolation. The real-space interactions (Lennard-Jones and electrostatic) are cut off at 20 Å and the long range contribution from the Lennard-Jones term is introduced as an average density-dependent term.[116] A dual Nosé−Hoover thermostat[205] is applied; the first is coupled to the atomic sites to keep temperature at the desired value and the second is coupled to the Drude particles to keep them at low temperature (1 K), to ensure self-consistent dipole induction.[32] The relaxation time of the atomic system is 0.1 ps, while the relaxation time of the Drude system is 0.005 ps. An Andersen−Hoover barostat[206] with a relaxation time of 0.2 ps is used to regulate the pressure. The equations of motion are integrated using a 1 fs time step. Simulations in liquid hydrogen sulfide with and without an alkali ion are run for 10 ns while those in aqueous H_2S are run for 85 ns.

4.2.2.3. Free Energy Calculations

The intrinsic free energy of solvation of each ion in liquid hydrogen sulfide is calculated at T = 298.15 K and p = 2.0174 MPa = 19.91 atm, using a free energy perturbation approach reported elsewhere.[170,202] Specifically, the solvation free energy is evaluated from the transformation of one alkali ion, M^+, into a "dummy" atom having no charge and no LJ parameters:

$$\Delta G_{\mathrm{solv}}^{\mathrm{intr}} \equiv \Delta G_{\mathrm{solv}}(\mathrm{M}^+) - \Delta G_{\mathrm{solv}}(\mathrm{dummy}) = -\Delta \mathrm{G}_{\mathrm{mut}}(\mathrm{M}^+ \rightarrow \mathrm{dummy}) \qquad (4.3)$$

where ΔG_{mut} is the relative free energy for the alchemical $\mathrm{M}^+ \rightarrow$ dummy "mutation" and $\Delta G_{\mathrm{solv}}(\mathrm{dummy}) = 0$. The transformation is controlled by a scaling parameter λ which takes the following 21 values: 0, 0.00001, 0.0001, 0.001, 0.01, 0.05, 0.1, 0.2, 0.3, 0.4, 0.5, 0.6, 0.7, 0.8, 0.9, 0.95, 0.99, 0.999, 0.9999, 0.99999, and 1.[170,202] Each λ window is equilibrated for 150 ps, and data is collected for 350 ps. Each mutation is performed in the forward and backward

directions in three independent replicates. On the basis of multiple runs, the error on the calculated values is ± 0.2 kcal/mol. Hydration free energy of H_2S is similarly calculated by mutating H_2S into a dummy molecule in a system of 500 H_2O molecules at T = 298.15 K and p = 0.1013 MPa.

4.2.2.4. Calculation of Thermodynamic and Transport Properties

Thermodynamic and transport properties are calculated for all H_2S models and compared to experimental values. The enthalpy of vaporization, ΔH_{vap}, is calculated from the net gain of potential energy $\langle \Delta u \rangle$ upon formation of the dense system.[170]

$$\Delta H_{\text{vap}} = p \times \left(\langle V \rangle_{\text{g}} - \langle V \rangle_{\text{l}} \right) + \left(\langle u \rangle_{\text{g}} - \langle u \rangle_{\text{l}} \right) \qquad (4.4)$$

where p is the pressure, $\langle V \rangle_{\text{g}}$ and $\langle V \rangle_{\text{l}}$ are the average molar volumes of gaseous and liquid H_2S, and $\langle u \rangle_{\text{g}}$ and $\langle u \rangle_{\text{l}}$ are the average potential energies of the two phases. $\langle V \rangle_{\text{l}}$ and $\langle u \rangle_{\text{l}}$ are obtained from the NpT MD simulations, $\langle V \rangle_{\text{g}}$ is taken from the NIST Chemistry webBook, and $\langle u \rangle_{\text{g}}$ is obtained from MD simulations of 500 H2S molecules in the NVT ensemble at a volume consistent with $\langle V \rangle_{\text{g}}$.

The self-diffusion coefficient of an H_2S molecule in the liquid state is obtained from the long-time limit of the mean-square displacement of the sulfur atoms:[170]

$$D_{\text{PBC}} = \lim_{t \to \infty} \frac{1}{6t} \left\langle \frac{1}{N} \sum_{i=1}^{N} \left[\mathbf{r}_{\text{S},i}(t) - \mathbf{r}_{\text{S},i}(0) \right]^2 \right\rangle \qquad (4.5)$$

The resulting diffusion coefficient, obtained from a least-square linear fit of each successive 2 ns of the last 8 ns of the trajectories, is corrected for system-size dependence using the formula of Yeh and Hummer:[124]

$$D = D_{\text{PBC}} + \frac{2.837297\ k_{\text{B}}T}{6\pi\eta L} \qquad (4.6)$$

where k_{B} is Boltzmann constant, η the shear viscosity of the solvent, and L is the average length of the cubic simulation box.[124] The viscosity values of liquid H_2S at the simulated thermodynamic conditions are taken from the NIST Chemistry webBook.[196]

The dielectric constant of the liquid, ε, was calculated using[207]

$$\varepsilon = \varepsilon_\infty + \frac{4\pi}{3\langle V \rangle k_B T} \left(\langle \boldsymbol{M}^2 \rangle - \langle \boldsymbol{M} \rangle^2 \right), \qquad (4.7)$$

where **M** is the total dipole moment of the box and ε_∞ is infinite-frequency dielectric constant, estimated from the Clausius–Mossotti equation (see, e.g., Ref. 208):

$$\frac{\varepsilon_\infty - 1}{\varepsilon_\infty + 2} = \frac{4\pi\alpha}{3v} \qquad (4.8)$$

where α is the molecular polarizability and v is the molecular volume obtained from the simulation. The convergence of ε is monitored by plotting its value as a function of time, and is averaged over the last 7 ns of 10 ns long simulations.

The specific heat capacity at constant pressure (C_p) is calculated from five simulations at different temperatures, 192.82, 197.82, 202.82, 207.82, and 212.82 K and at a constant pressure of 0.1013 MPa. The total energy $\langle U_{tot} \rangle$ and the volume $\langle V \rangle$ are averaged over time. A linear fit of the plot ($\langle U_{tot} \rangle + p\langle V \rangle$) versus T is used to calculate C_p.[170]

$$C_p = \frac{1}{N}\left(\frac{\partial(\langle U_{tot} \rangle + p\langle V \rangle)}{\partial T}\right)_{T=212.82\ \text{K},\ p=0.1013\ \text{MPa}} \qquad (4.9)$$

4.3. Results and Discussion

4.3.1. Ab initio Optimized Geometries

Due to the limited number of ab initio investigations on H_2S-containing clusters in the literature,[197,201] we report all stable conformers we have identified. To the best of our knowledge, ab initio investigations on H_2S clusters larger than the dimer and on clusters of H_2S with alkali ions (other than the Na^+-H_2S dimer[197]) have not been reported so far.

4.3.1.1. Hydrogen Sulfide Monomer

The MP2/6-311++G(d,p) calculated equilibrium geometry, dipole moment, polarizability, and vibrational frequencies of the isolated hydrogen sulfide molecule are reported in Table 4.1, together with the corresponding experimental and Drude values. The geometry of H_2S optimized at the MP2 level shows r_{SH} = 1.333 Å and θ_{HSH} = 92.0°, in agreement with the experimental data (r_{SH} = 1.328 Å, θ_{HSH} = 92.2°).[203] In comparison, the equivalent parameters for water are r_{OH} = 0.958 Å and θ_{HOH} = 104.5°,[209] showing the effect of the larger 3p orbitals on the structure of H_2S. The MP2-optimized structure possesses a dipole moment of 1.37 D, larger than the experimental gas-phase value (0.97 D).[210] Table 4.1 also shows that, compared to the experimental values,[211,212] the calculated polarizability is underestimated while the calculated frequencies are overestimated. The trend in the experimental polarizability, H_2O (1.501 $Å^3$) < NH_3 (2.103 $Å^3$) < H_2S (3.631 $Å^3$),[211] reflects the increase in molecular volume. Since MP2 calculations do not adequately reproduce the experimental values, the bonded parameters and the atomic charges of the Drude model are adjusted based on the experimental parameters.

Table 4.1. Ab initio calculated properties of the hydrogen sulfide monomer at the MP2/6-311++G(d,p) level and corresponding experimental values. Values from the optimized Drude model are also given.

Property	Ab initio	Drude	Expt.
SH bond length (Å)	1.333	1.328	1.328[a]
HSH angle (°)	92.0	92.2	92.2[a]
Dipole (D)	1.37	0.97	0.97[b]
Polarizability (α, Å^3)	2.651	3.631	3.631[c]
Vibration frequencies (cm^{-1})			
v_1	1233	1183	1183[d]
v_2	2819	2621	2615[d]
v_3	2839	2624	2626[d]

[a] Reference 203. [b] Reference 210. [c] Reference 48. [d] Reference 212.

4.3.1.2. $(H_2S)_n$ (n = 2−4) Clusters

Figure 4.1 shows structures of the $(H_2S)_n$ clusters (n = 2−4) obtained from geometry optimization at the MP2/6-311++G(d,p) level. Table 4.2 lists the interaction energies of four structures of the dimer calculated at the same level and at MP2/aug-cc-pVXZ levels (X = D, T, Q, and 5). Table 4.3 reports the MP2/6-311++G(d,p) interaction energies of the optimized structures of the trimer and tetramer clusters. Ab initio interaction energies are reported with and without correction for BSSE (E^{CP} and E, respectively). Interaction energies from the optimized Drude model are reported in Tables 4.2 and 4.3, along with energies from potential models from the literature[197–200,201] (re-calculated in this work).

Geometry optimization of the dimer reveals three stable structures (**a**–**c**) and a TS structure (**d**). Structures **a** and **b** form linear hydrogen-bonds with intermolecular distances $r_{S\cdots H}$ and angles $\theta_{S-H\cdots S}$ of 2.838 Å and 178.2° for complex **a** and of 2.833 Å and 177.0° for complex **b**. Structure **c** is cyclic, stabilized by the interaction of hydrogen atoms with electron lone pairs on sulfur, and displays $r_{S\cdots H}$ separations of 3.30 and 3.69 Å. The TS structure **d** is also cyclic, with equal $r_{S\cdots H}$ distances of 3.286 Å and $\theta_{S-H\cdots S}$ angles of 102.7°. The dihedral angle $d_{H-S-H\cdots S}$ in structure **d** is 138°. S⋯S distances are 4.172 Å for conformer **a**, 4.166 Å for **b**, 3.770 Å for **c**, and 3.808 Å for **d**. Table 4.2 shows that, while the CP-uncorrected binding energies are comparable for MP2/6-311++G(d,p) and MP2/aug-cc-pVXZ levels, they are significantly different after CP correction.

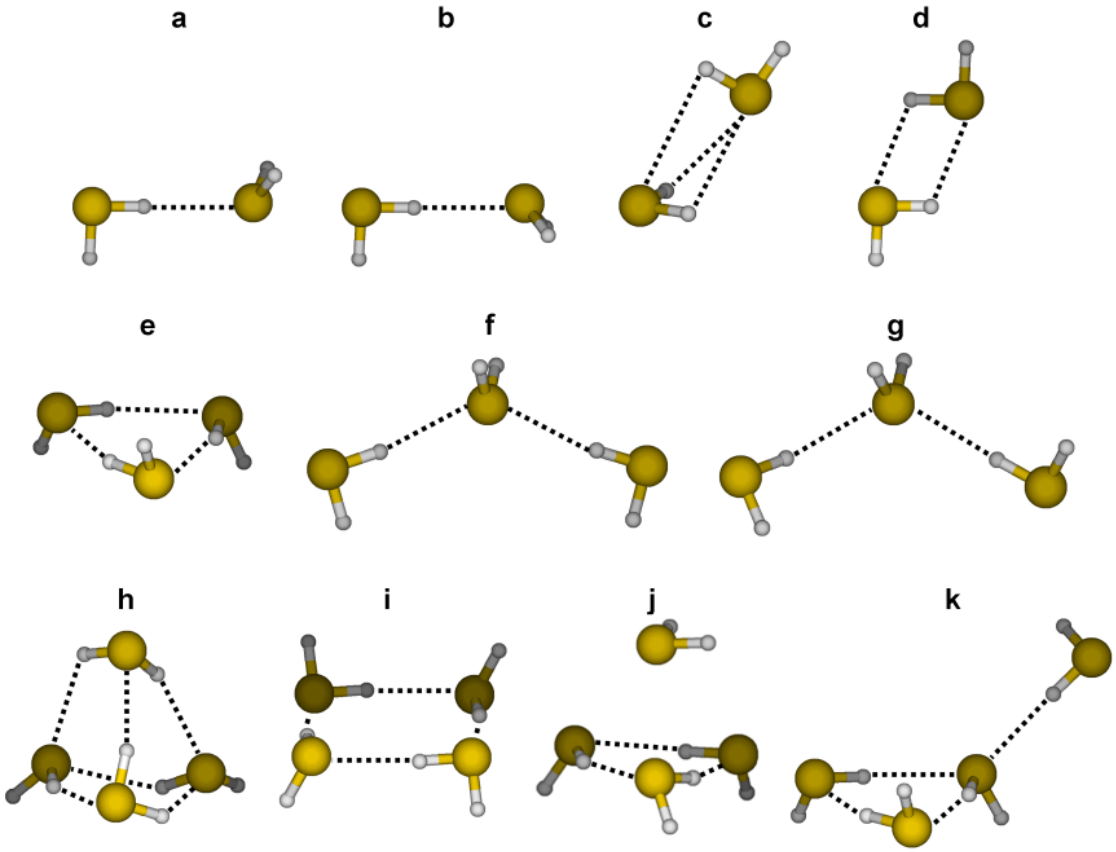

Figure 4.1. Geometries of hydrogen sulfide clusters optimized at the MP2/6-311++G(d,p) level: (a–d) dimer, (e–g) trimer, and (h–k) tetramer. Structure **d** is a transition state.

Table 4.2. Uncorrected (E) and CP-corrected (E^{CP}) binding energies of the hydrogen sulfide dimer, $(H_2S)_2$, calculated at the MP2 level at various basis sets. Binding energies calculated with potential models of H_2S are also reported. All energies are in kcal/mol.

Structure	Ab initio, MP2/										Potential models*					
	6-311++G(d,p)		aug-cc-pVDZ		aug-cc-pVTZ		aug-cc-pVQZ		aug-cc-pV5Z		$E^{MM,a}$	$E^{MM,b}$	$E^{MM,c}$	$E^{MM,d}$	$E^{MM,e}$	$E^{MM,f}$
	E	E^{CP}	E	E^{CP}	E	E^{CP}	E	E^{CP}	E	E^{CP}						
a (trans)	–2.25	–0.87	–2.73	–1.50	–2.95	–1.66	–2.26	–1.83	–2.42	–1.83	–1.79	–1.37	–1.35	–1.47	–0.95	–0.93
b (cis)	–2.17	–0.80	–2.63	–1.41	–2.87	–1.59	–2.17	–1.74	–2.35	–1.75	–1.23	–1.22	–1.16	–1.10	–0.85	–0.81
c (cyclic)	–1.99	–0.73	–2.14	–1.42	–2.33	–1.65	–2.09	–1.80	–2.21	–1.84	–1.63	–0.87	–0.82	–1.14	–0.50	–0.58
d (TS)	–1.85	–0.76	–2.15	–1.35	–2.41	–1.51	–2.00	–1.66	–2.10	–1.69	–1.41	–0.94	–0.87	–1.05	–0.57	–0.56

* Binding energies are calculated on the MP2/6-311++G(d,p) optimized geometries. [a] Jorgensen model.[197] [b] Forester *et al.* model.[198] [c] Kristóf and Liszi model.[199] [d] Model C of Kamath *et al.*[200] [e] Riahi and Rowley Drude model.[201] [f] This work.

The trimer, $(H_2S)_3$, has three stable conformations: **e**, **f**, and **g** (see Figure 4.1 and Table 4.3). Structure **e** is cyclic with two hydrogen bonds per H_2S molecule. Structures **f** and **g** differ only in the orientation of the terminal H atoms (cis in **f** and trans in **g**). The binding energies of these conformers follow the order **e** > **f** > **g** (in absolute value).

Figure 4.1 shows four conformers for the tetramer, $(H_2S)_4$. The global energy minimum is conformer **h**, in which three H_2S molecules are hydrogen-bonded in a cyclic form and each is involved in a single hydrogen bond with the fourth molecule. Conformer **i** is cyclic planar with two hydrogen bonds per H_2S molecule. Conformer **j** is structurally similar to **h**, but has no apparent hydrogen bonding between molecules in the cyclic trimer and the fourth one. Structure **k** corresponds to a cyclic trimer hydrogen-bonded to a fourth molecule through a single hydrogen bond. The binding energies of these four tetramers follow the order **h** > **i** > **j** > **k** (in absolute value).

Table 4.3. Uncorrected (E) and CP-corrected (E^{CP}) binding energies of the $(H_2S)_n$ clusters (n = 3, 4) calculated at the MP2/6-311++G(d,p) level. Binding energies calculated with the optimized Drude model and with other literature models are also reported.[a] All energies are in kcal/mol.

Conformer	Ab initio		Potential models					
	E	E^{CP}	Jorgensen[197]	Forester *et al.*[198]	Kristóf and Liszi[199]	Kamath *et al.*[200]	Riahi and Rowley[201]	This work
e	–6.22	–2.74	–4.65	–4.13	–3.92	–3.91	–2.74	–2.72
f	–4.27	–1.66	–3.16	–2.66	–2.57	–2.67	–1.82	–1.80
g	–4.23	–1.57	–2.86	–2.58	–2.47	–2.48	–1.76	–1.72
h	–10.47	–4.48	–7.67	–6.88	–6.52	–6.66	–4.91	–5.03
i	–10.09	–4.33	–7.32	–6.26	–6.00	–6.09	–4.38	–4.51
j	–10.26	–3.97	–3.79	–4.39	–3.70	–3.41	–3.83	–3.80
k	–8.71	–3.67	–6.31	–5.55	–5.28	–5.31	–3.82	–3.81

[a]Binding energies are calculated on the MP2/6-311++G(d,p) optimized geometries of the trimers and tetramers.

4.3.1.3. H_2S–H_2O Dimer

Figure 4.2 shows structures of the H_2S–H_2O pair optimized at the MP2/6-311++G(d,p) level. The corresponding ab initio binding energies (E and E^{CP}) and the Drude-calculated values (E^{MM}) are reported in Table 4.4. Structure **a** is the global energy minimum, with a linear hydrogen bond in which water is the proton acceptor. Structure **b** forms a hydrogen bond in which water is the proton donor. Conformers **c** and **d** are hydrogen-bonded TS structures in which water is the proton acceptor and donor, respectively. Intermolecular $r_{S\cdots O}$ distances for structures **a, b**, **c**, and **d** are 3.509, 3.507, 3.546, and 3.534 Å, respectively.

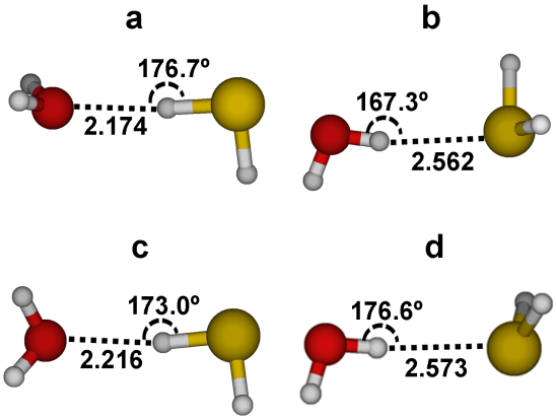

Figure 4.2. Geometries of the H_2S–H_2O pair optimized at the MP2/6-311++G(d,p) level. Structures **a** and **b** are energy minima and structures **c** and **d** are transition states. Hydrogen bond distances (in Å) and angles are reported.

Table 4.4. Uncorrected (E) and CP-corrected (E^{CP}) binding energies of the H_2S–H_2O pair, calculated at the MP2/6-311++G(d,p) level. Binding energies calculated with the optimized Drude model (E^{MM}) are also reported. All energies are in kcal/mol.

Structure	E	E^{CP}	E^{MM*}
a	–3.71	–2.33	–1.28
b	–3.40	–1.94	–1.53
c	–3.31	–2.03	–1.33
d	–3.38	–1.91	–1.58

*Binding energies are calculated on the MP2/6-311++G(d,p) optimized geometries of the dimer.

4.3.1.4. H_2S–Alkali Ion Pairs

Figure 4.3 reports the structures of the H_2S–M^+ pairs (M^+ = Li^+, Na^+, K^+, Rb^+, Cs^+) optimized at the CCSD(T) level. The structures have a C_s point-group symmetry, with both intermolecular distances $r_{S\cdots M^+}$ and angles $\theta_{M^+\cdots S\cdots Y}$ (where Y is a point on the HSH angle bisector) increasing in going from Li^+ to Cs^+. Binding energies calculated at the MP2 and CCSD(T) levels are in close agreement (see Table 4.5). The Drude model for H_2S-alkali ions interactions is optimized to reproduce binding energies at the CCSD(T) level, and energies calculated with the model (E^{MM}) are reported in Table 4.5.

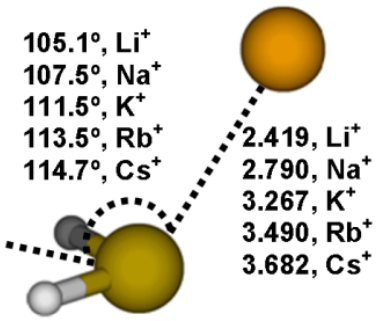

Figure 4.3. Optimized geometry of the H_2S–K^+ pair optimized at the CCSD(T) level (see Methods section for details). Bond lengths (in Å) and bond angles are reported for all ions.

Table 4.5. Uncorrected (E) and CP-corrected (E^{CP}) binding energies of the ion–H_2S pairs calculated at the MP2 and CCSD(T) levels (see Methods section for details). Binding energies calculated with the optimized Drude model (E^{MM}) are also reported. All energies are in kcal/mol.

Ion	Ab initio				Drude model
	MP2		CCSD(T)		
	E	E^{CP}	E	E^{CP}	E^{MM*}
Li^+	–25.13	–22.08	–23.57	–22.24	–22.20
Na^+	–16.17	–13.97	–16.21	–14.72	–14.70
K^+	–10.27	–9.12	–10.09	–9.47	–9.50
Rb^+	–8.50	–8.16	–8.24	–7.88	–7.90
Cs^+	–7.58	–7.23	–7.33	–6.86	–6.90

* Binding energies are calculated without geometry constraints (except for S–H bond lengths which are fixed to their equilibrium value).

4.3.2. Potential Energy Surfaces

Ab initio potential energy curves for H_2S in complex with H_2S, H_2O, and alkali ions are reported in Figure 4.4, along with the corresponding curves calculated with the Drude model. Three curves (4.4a–4.4c) are calculated for the hydrogen sulfide dimer by rigidly translating the individual molecules along the S-S axis, starting from the optimized dimer structure (structures **a**–**c** of Figure 4.1) from 2 to 10 Å. Similarly, three potential energy curves are calculated for the H_2S–H_2O pair (4.4d–4.4f) by scanning the S···O distance in three optimized structures of the pair (structures **a**, **b**, and **c** of Figure 4.2). Two curves are calculated for the H_2S-alkali ion pairs: curve 4.4g is obtained by scanning the distance between the alkali ion and the sulfur atom of H_2S from 2 to 10 Å, and curve 4.4h is calculated by scanning the M···S···Y angle from 0° to 180°. In all distance scans, H_2S and H_2O fragments are set to their optimized monomer geometries and the distance between the heavy atoms is changed.

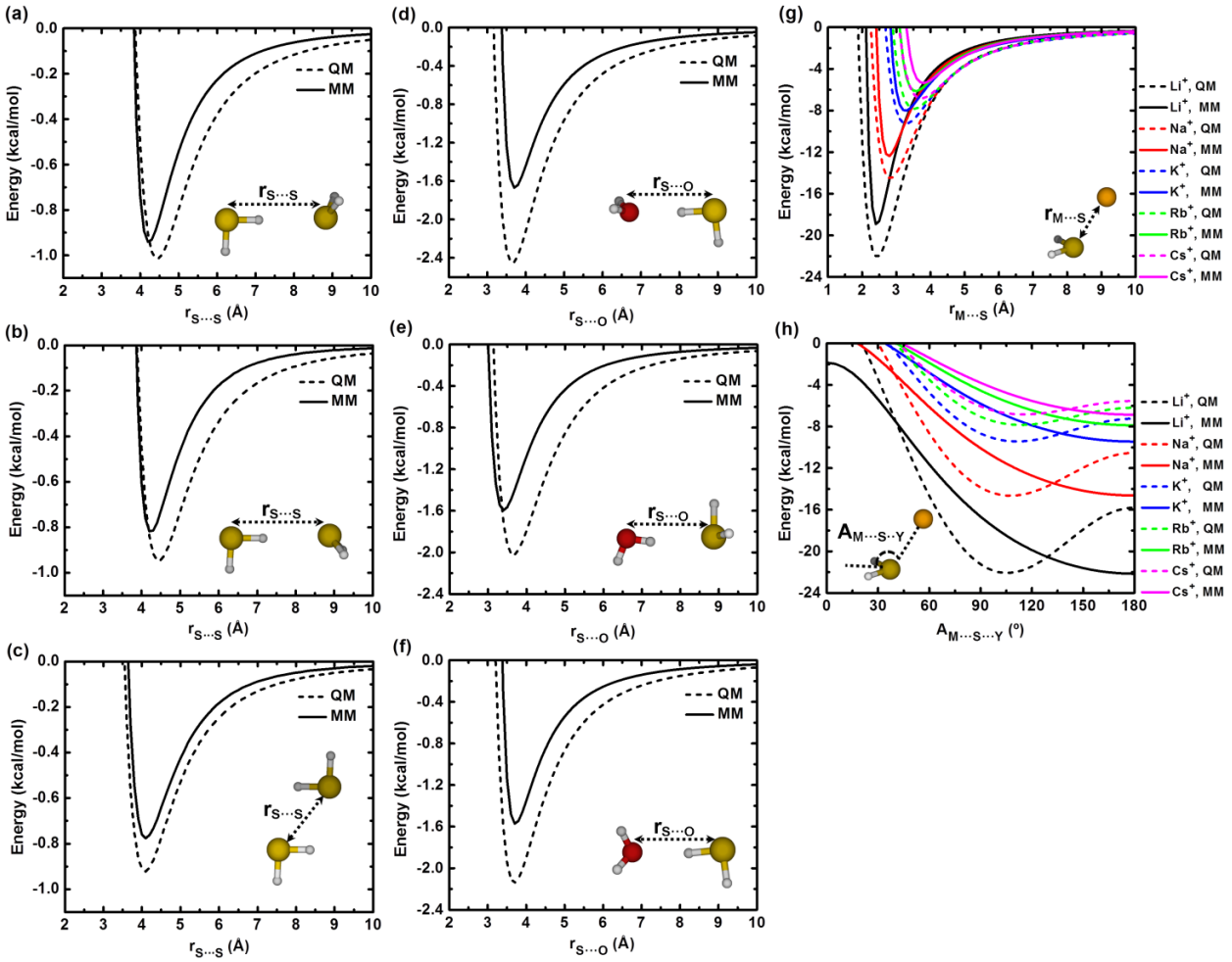

Figure 4.4. Potential energy curves for H_2S–H_2S, H_2S–H_2O, and H_2S–alkali ions complexes from ab initio calculations (dashed lines) and from the polarizable model (solid lines). Curves a–c are calculated by scanning the S···S distance in the three stable conformers of the H_2S dimer (structures **a**–**c** of Figure 4.1) from 2 to 10 Å. Curves d–f are calculated by scanning the S···O distance in three conformers of the H_2S-H_2O dimer (structures a–c of Figure 4.2) from 2 to 10 Å. Curve 4g is calculated by scanning the ion-S distance from 2 to 10 Å. Curve h is obtained by scanning the M···S···Y angle (Y is a point on the HSH angle bisector) from 0 to 180° at M···S distances of 2.4 Å for Li^+, 2.8 Å for Na^+, 3.3 Å for K^+, 3.5 Å for Rb^+, and 3.7 Å for Cs^+.

4.3.3. Optimized Force Field

The optimized parameters of the polarizable Drude model as well as parameters from previous potential models[197–200,201] are reported in Table 4.6. The equilibrium structural parameters for the H_2S model are set to the experimental data: r_{SH} = 1.328 Å and θ_{HSH} = 92.2°. The corresponding force constants, k_b = 285.0 kcal/mol/Å^2 and k_θ = 51.1 kcal/mol/rad^2, are chosen to reproduce the experimental vibration frequencies (see Table 4.1). The isotropic Drude polarizability is set to the experimental molecular polarizability and the partial atomic charges

are set to reproduce the experimental dipole moment of gaseous H_2S. The LJ parameters for S and H are optimized based on the experimental density of H_2S at four thermodynamic conditions around the critical point, in the temperature range 363–393 K and pressure range 8.023–10.013 MPa. The four LJ parameters are chosen to minimize deviations from the experimental density values at those four thermodynamic conditions.

LJ parameters for the S–O pair are optimized to reproduce the experimental hydration free energy of H_2S; for the S–alkali ion pairs, they are optimized to reproduce the CCSD(T)-calculated binding energies and the ion-S distances of the H_2S-ion pairs. Adjusted pair-specific LJ parameters are reported in Table 4.7.

Table 4.6. Parameters of the optimized H_2S model, compared to models from the literature[a]

Parameter	Jorgensen[197]	Forester *et al.*[198]	Kristóf and Liszi[199]	Kamath *et al.*[200]	Riahi and Rowley[201]	This work
r_{SH} (Å)	1.340	1.340	1.340	1.3322	1.340	1.328
θ_{HSH} (°)	92.0	92.1	92.0	92.5	92.0	92.2
r_L (Å)		0.1933	0.1862		0.2020	
q_S (e)	–0.470	0.661	0.400	–0.380	0.000	–0.220
q_H (e)	0.235	0.278	0.250	0.190	0.137	0.110
q_L (e)		–1.217	–0.900		–0.274	
α (Å^3)					2.500	3.631
$E_{min,S}$ (kcal/mol)	0.2501	0.5346	0.4969	0.4611	0.5681	0.304738
$R_{min,S}/2$ (Å)	2.0766	2.0709	2.0933	2.0878	2.088	2.174804
$E_{min,H}$ (kcal/mol)						0.157138
$R_{min,H}/2$ (Å)						0.808847

[a] r_L is the distance between the sulfur atom and the lone pair on the bisector of the HSH angle and q_L is the lone pair charge.

Table 4.7. Pair-specific LJ parameters between the S atom of H_2S and alkali ions and between S and O of water.

Parameter	Li^+	Na^+	K^+	Rb^+	Cs^+	H_2O
$E_{min,ion-S}$ (kcal/mol)	0.16186	0.18423	0.28657	0.45474	0.51518	0.27354
$R_{min,ion-S}/2$ (Å)	1.71942	1.85970	2.02462	2.09289	2.17983	1.93787

Except for the binding energies of alkali ions-H_2S pairs, which are calculated using the force field-optimized geometries, binding energies of hydrogen sulfide clusters (Figure 4.1) and of H_2S-H_2O pairs (Figure 4.2) are calculated using the MP2-optimized geometries.

Despite not being optimized to reproduce the ab initio properties of the clusters, the model shows only minor deviations from the ab initio H_2S−H_2S PESs (see Figures 4.4a–4.4c). Moreover, the Drude models for H_2S (this work and that of Riahi and Rowley[201]) give binding energies for the various hydrogen sulfide clusters in good agreement with ab initio data at the MP2/6-311++G(d,p) level (see Tables 4.2 and 4.3). In comparison the additive models of Jorgensen,[197] Forester *et al.*,[198] Kristóf and Liszi,[199] and Kamath *et al*. (model C)[200] overestimate the CP-corrected binding energies at the MP2 level.

The Drude model for the H_2S–H_2O pair, which is adjusted to reproduce the hydration free energy of H_2S and not the ab initio properties of the pair, underestimates the ab initio binding energy (see Table 4.4 and Figures 4.4d–4.4f). While MP2 results predict hydrogen-bonded structures in which H_2S is the proton donor (4.2**a**, 4.2**c**) to be slightly more stable than those in which H_2O is the proton donor (4.2**b**, 4.2**d**), the model is showing the opposite trend.

When using the Lorentz-Berthelot combination rules, the Drude models of H_2S and alkali ions[118] give binding energies for the alkali ion-H_2S pairs of –34.30 kcal/mol for Li^+, –20.14 kcal/mol for Na^+, –12.42 kcal/mol for K^+, –10.47 kcal/mol for Rb^+, and –8.50 kcal/mol for Cs^+. These values are greatly overestimated compared to the ab initio CCSD(T) binding energies (see Table 4.5). With pair-specific LJ parameters between the sulfur atom of H_2S and each alkali ion (see Table 4.7), the model reproduces the CCSD(T) binding energies of the ion-H_2S pairs and gives ion-S separations of 2.416 Å for Li^+, 2.761 Å for Na^+, 3.246 Å for K^+, 3.533 Å for Rb^+, and 3.756 Å for Cs^+, in good agreement with the ab initio data at the CCSD(T) level (see Table 4.5 and Figure 4.3). The model, however, gives a C_{2v} symmetry for all H_2S-ion pairs, with an M···S···Y angle of 180°. Reproducing the ab initio observed C_s symmetry of the pairs may require explicit description of the lone pairs of the S atom. The Drude model of Riahi and Rowley[201] possesses a "lone pair" site on the bisector of the HSH angle, yet gives a C_{2v} symmetry as well. Two lone pair sites might thus be required to mimic the tetrahedral electron-pair geometry of H_2S and reproduce the ab initio geometries of its complexes with ions.

4.3.4. Liquid Hydrogen Sulfide at the Boiling Point

The Drude model is used to calculate properties of liquid hydrogen sulfide at its normal boiling point (T = 212.82 K and p = 0.1013 MPa = 1 atm)[192]: density (ρ), heat of vaporization (ΔH_{vap}), self-diffusion coefficient (D), dielectric constant (ε), and heat capacity (C_p) (see Table 4.8). For consistent comparison, the same properties are re-calculated for all literature models.[197-200,] For non-polarizable models from the literature, the values we find are in good agreement with those reported by Riahi and Rowley.[201] The present polarizable model yields an average molecular volume of 62.04 Å^3 and a density of 0.912 ± 0.001 g/cm^3. By comparison, simulation of 500 H_2O molecules using the SWM4-NDP model[113] at the same thermodynamic conditions yields an average molecular volume of 28.70 Å^3 and a density of 1.042 g/cm^3. The densities calculated from the various models are in good agreement with the experimental value. The maximum deviation from experiment is observed for Forester *et al.*'s model,[198] which overestimates the experimental value by 7%. Enthalpies of vaporization from the various models are also in good agreement with the experimental value, with a maximum deviation of 0.59 kcal/mol for the current model.[198] The experimental value of the self-diffusion coefficient (at 206.5 K)[194] is best reproduced by our model and that of Kristóf and Liszi.[199] The models of Forester *et al.*[198] and of Riahi and Rowley[201] underestimate D by 19% and 10%, respectively, while the models of Jorgensen[197] and of Kamath *et al.*[200] overestimate it.

The dielectric constant is best reproduced by the two polarizable models. Other models[197–200] overestimate it by anywhere from 44%[198] to ~500%.[197] All models of H_2S underestimate the experimental heat capacity of the liquid, likely in part because they use H_2S molecules that are either totally rigid or that have flexible angles but rigid bonds lengths.

Table 4.8. Liquid properties of H_2S models at 212.82 K and 0.1013 MPa = 1 atm, and corresponding experimental values. All properties are calculated in this work.

Model	ρ (kg/m^3)	ΔH_{vap} (kcal/mol)	$D \times 10^{-9}$ m^2/s	ε	C_p (cal mol^{-1} K^{-1})
Jorgensen[197]	0.958 ± 0.001	4.79 ± 0.01	8.52 ± 0.1	48.8 ± 1.0	10.2 ± 0.2
Forester *et al.*[198]	1.016 ± 0.001	4.28 ± 0.01	3.01 ± 0.1	9.5 ± 0.2	9.7 ± 0.2
Kristóf and Liszi[199]	0.958 ± 0.001	4.43 ± 0.01	3.81 ± 0.1	11.6 ± 0.2	9.4 ± 0.2
Kamath *et al.*[200]	0.958 ± 0.001	4.36 ± 0.01	4.37 ± 0.1	24.5 ± 0.2	10.4 ± 0.2
Riahi and Rowley[201]	0.952 ± 0.001	4.34 ± 0.01	3.34 ± 0.1	7.6 ± 0.1	8.4 ± 0.2
This work	0.912 ± 0.001	3.87 ± 0.01	3.62 ± 0.1	8.9 ± 0.1	10.2 ± 0.2
Experiment[a]	0.949	4.46	3.7 ± 0.2	8.04	16.31

[a] Density and enthalpy of vaporization from ref 190, self-diffusion coefficient from ref 194 at 206.5 K, dielectric constant from ref 195, and heat capacity from ref 192 at 211 K.

4.3.5. Structure of Liquid H_2S

To investigate the microscopic structure of liquid hydrogen sulfide, we simulate a system of 500 H_2S molecules for all models presented.[197–200,201] Simulations are performed at T = 298 K and p = 3.1 MPa = 30.595 atm, one of the experimental thermodynamic conditions reported by Santoli *et al.*[189] The structure of the liquid is analyzed from the $g_{SS}(r)$, $g_{SH}(r)$, and $g_{HH}(r)$ radial distribution functions (RDFs), shown in Figure 4.5. The characteristic properties of the $g_{SS}(r)$ function are reported in Table 4.9.

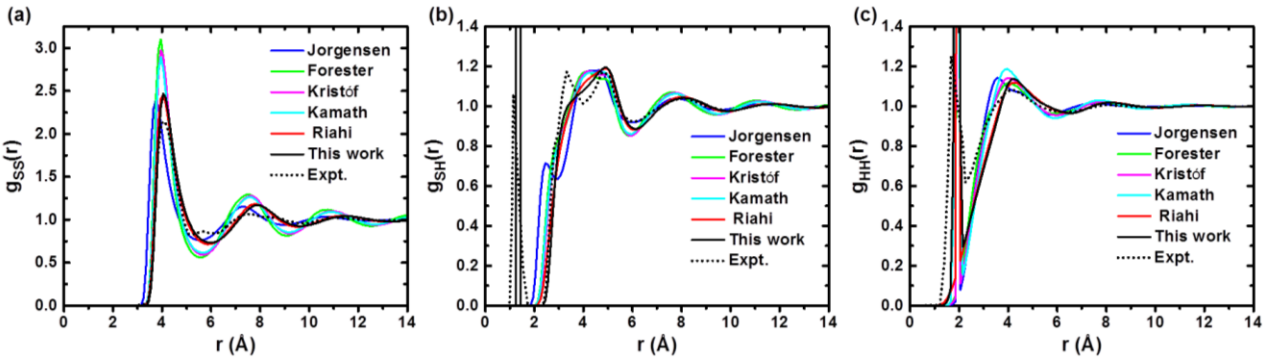

Figure 4.5. $g_{SS}(r)$, $g_{SH}(r)$, and $g_{HH}(r)$ radial distribution functions of liquid hydrogen sulfide at T = 298 K and p = 3.1 MPa calculated from D simulation using different potential models (solid lines) in comparison with NDIS experiment[189] at the same conditions (dashed lines).

Table 4.9. Characteristics of the $g_{SS}(r)$ radial distribution function of liquid hydrogen sulfide at T = 298 K and p = 3.1 MPa.[a]

Model	r_{M1} (Å)	r_{m1} (Å)	$n(r_{m1})$	r_{M2} (Å)
Jorgensen[197]	3.75	5.55	11.9	7.30
Forester *et al.*[198]	3.95	5.55	12.7	7.55
Kristóf and Liszi[199]	3.95	5.65	12.6	7.65
Kamath *et al.*[200]	3.95	5.65	12.6	7.65
Riahi and Rowley[201]	4.05	5.90	12.0	7.75
This work	4.05	5.90	11.3	7.85

[a] r_{M1} and r_{M2} are the distances at which the function has its first and second maximum, respectively. r_{m1} is the distance at which the function has its first minimum and $n(r_{m1})$ is the running integration number evaluated at r_{m1}.

Except for Jorgensen's model,[197] the position of the first peak in the g_{SS}(r) function is in good agreement with the experimental value (~4 Å).[189] Compared to experiment, the intensity of the first peak in the calculated function is overestimated, especially for models of Forester *et al.*,[198] Kristóf and Liszi,[199] and Kamath *et al.*[200] Such overestimation is likely due to the steepness of the Lennard-Jones repulsive potential.[170] The two Drude models show the first minimum in the g_{SS}(r) function at relatively longer distances compared to the pairwise-additive models. The present model predicts the lowest coordination number of all: 11.3 hydrogen sulfide molecules, compared to 12.0 for the Riahi and Rowley model.

The first peak in the $g_{SH}(r)$ function, located at r < 2 Å, corresponds to intramolecular SH pairs. Among all models, only the Jorgensen model suggests clear hydrogen bonding in liquid H_2S (evidenced by the peak centered at 2.5 Å), which is inconsistent with experiment. The present model is the most accurate in reproducing the features of the experimental $g_{SH}(r)$ function; it correctly reproduces the double peaks at ~3.2 Å and ~4.8 Å in the experimental function.[189] The peak at ~3.2 Å is consistent with the distance of 3.3 Å in structures 1**c** and 1**d** of the dimers (see section 4.3.1). It should also be noted that the very weak shoulder at ~2.8 Å in the experimental curve of Figure 4.5b is consistent with the distance found in the linearly hydrogen-bonded dimers (structures **a** and **b** of Figure 4.1). The absence of an intense peak in the $g_{SH}(r)$ function at a distance characteristic of any specific binding geometry, and hence for the observed structureless pattern might be explained by the fact that the four optimized structures of the dimer (4.1**a** to 4.1**d**) have comparable energies despite the broad $r_{S\cdots H}$ range covered (from

2.83 to 3.69 Å). However, since the four optimized structures are characterized by hydrogen bonding features, hydrogen bonding in liquid H_2S may still persist.

The $g_{HH}(r)$ function shows a first peak at 1.9 Å, due to intramolecular HH pairs. With the exception of Jorgensen's model,[197] the position of the experimental first intermolecular peak (~4.2 Å)[189] is well reproduced by the different models.

4.3.6. Liquid H_2S at Various p and T

The transferability of the optimized Drude model for H_2S is validated by calculating the density, vaporization enthalpy, and self-diffusion coefficient of H_2S at thermodynamic conditions that cover the liquid and supercritical phases of the fluid. Figure 4.6 summarizes the temperature and pressure conditions simulated.

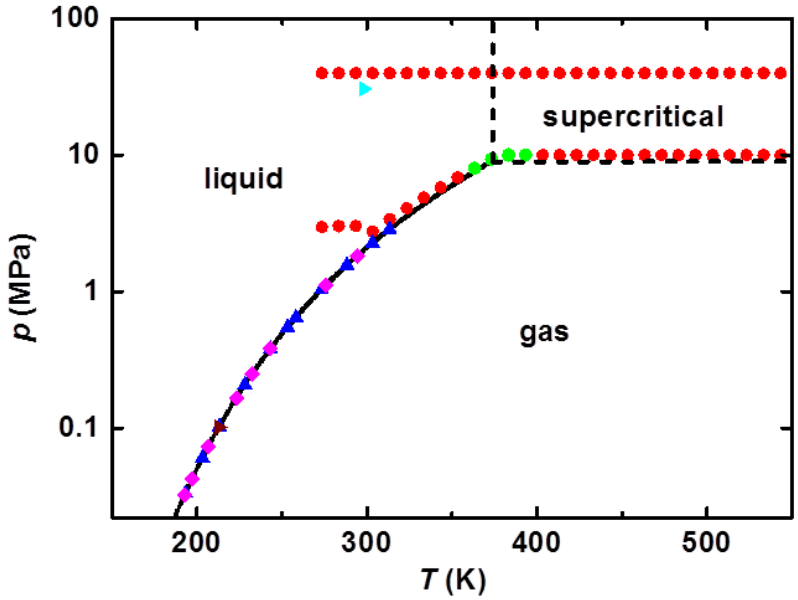

Figure 4.6. Phase diagram of H_2S. The solid and dashed lines are phase boundaries and their intersection is the critical point (T_c = 373.1 K, p_c = 9.00 MPa).[196] Green circles are the pressure and temperature conditions used to optimize the LJ parameters for H and S atoms. Red circles are the conditions at which density is investigated (see also Table 4.10). Blue triangles are conditions at which vaporization enthalpy is investigated (see also Table 4.11). Pink diamonds are conditions at which self-diffusion coefficient is investigated (see also Table 4.12). The brown triangle represents the normal boiling point of H_2S (T = 212.82 K, p = 0.1013 MPa = 1 atm)[192] and the cyan triangle represents one of Santoli *et al.*'s NDIS experimental conditions[189] (T = 298 K, p = 3.1 MPa = 30.595 atm), at which liquid structure is calculated.

4.3.6.1. Density

Ihmels and Gmehling[191] have measured the density of H_2S in the liquid and supercritical phases in the temperature range 273.39–548.30 K and in the pressure range 2.976–40.004 MPa. To validate the optimized model and to test the performance of models from the literature,[197–200,201] a system of 500 H_2S molecules is simulated for 10 ns at temperatures from ~273 K to ~543 K in 10 K increments. For each temperature, the system is simulated at two pressures that correspond to the minimum and maximum pressures used by Ihmels and Gmehling[191] (the red and green symbols on Figure 4.6). Figure 4.7 shows calculated versus experimental densities (see also table 4.10). Over the fifty-six simulated conditions, the average unsigned relative error on the density is 1.9% for the present Drude model, 13.7% for the Drude model of Riahi and Rowley,[201] and 15.0%, 23.2%, 6.1%, and 5.4% for the additive models by Jorgensen,[197] Forester *et al.*,[198] Kristóf and Liszi,[199] and Kamath *et al.*,[200] respectively. The present model, optimized at temperatures 363.25, 373.25, 383.24, and 393.22 K, under corresponding pressures of 8.023, 9.344, 10.024, and 10.013 MPa (green circles in Figure 4.6), gives the best agreement with experimental data. Throughout all simulated conditions, the only significant deviation (15.2% overestimation) between experimental and calculated densities is at T = 373.25 K and p = 9.344 MPa, near the critical point of H_2S (T = 373.2 K and p = 8.937 MPa,[191] see Figure 4.6). Figure 4.7 shows that other models deviate appreciably from experiment at certain thermodynamic conditions. The Drude model of Riahi and Rowley[201] and the pairwise-additive models of Forester *et al.*,[198] Kristóf and Liszi,[199] and Kamath *et al.*[200] largely overestimate the density at low pressure conditions, in the temperature range 353–403 K. On the other hand, the additive model of Jorgensen underestimates the density in the temperature range 313–383 K, suggesting that the liquid-vapor phase boundary has been crossed.

Table 4.10. Density of fluid H_2S calculated with different potential models and corresponding experimental values.

T (K)	p (MPa)	Jorgensen[197]	Forester *et al.*[198]	Kristóf and Liszi[199]	Kamath *et al.*[200]	Riahi and Rowley[201]	This work	Expt.[191]
273.39	2.976	0.796	0.916	0.852	0.851	0.855	0.807	0.8367
283.36	3.024	0.760	0.898	0.832	0.832	0.836	0.787	0.8140
293.33	3.024	0.718	0.879	0.811	0.810	0.818	0.763	0.7902
303.31	2.760	0.664	0.859	0.788	0.788	0.797	0.743	0.7636
313.32	3.395	0.596	0.839	0.765	0.760	0.778	0.717	0.7374
323.3	4.089	0.066	0.819	0.742	0.736	0.758	0.692	0.7089
333.29	4.892	0.084	0.798	0.717	0.710	0.737	0.666	0.6772
343.27	5.814	0.106	0.777	0.689	0.680	0.716	0.635	0.6409
353.25	6.856	0.130	0.754	0.661	0.647	0.693	0.600	0.5971
363.25	8.023	0.158	0.670	0.630	0.617	0.670	0.557	0.5391
373.25	9.344	0.184	0.706	0.596	0.569	0.645	0.506	0.4390
383.24	10.024	0.182	0.677	0.542	0.505	0.613	0.254	0.2464
393.22	10.013	0.162	0.638	0.213	0.211	0.564	0.185	0.1890
403.21	10.018	0.148	0.581	0.168	0.170	0.217	0.160	0.1650
413.2	10.023	0.137	0.174	0.150	0.152	0.165	0.148	0.1497
423.2	10.022	0.128	0.151	0.138	0.138	0.149	0.136	0.1384
433.2	10.023	0.120	0.137	0.128	0.128	0.138	0.128	0.1296
443.2	10.024	0.114	0.128	0.121	0.121	0.127	0.121	0.1224
453.2	10.021	0.108	0.120	0.114	0.114	0.120	0.115	0.1162
463.2	10.014	0.103	0.113	0.108	0.110	0.114	0.110	0.1109
473.2	10.022	0.099	0.108	0.104	0.105	0.109	0.106	0.1062
483.2	10.023	0.095	0.103	0.100	0.100	0.104	0.101	0.1020
493.2	10.021	0.092	0.099	0.096	0.097	0.101	0.098	0.0982
503.2	9.998	0.088	0.094	0.093	0.091	0.097	0.094	0.0944
513.2	10.003	0.086	0.091	0.089	0.089	0.093	0.091	0.0912
523.2	10.022	0.083	0.089	0.087	0.087	0.091	0.089	0.0883
533.2	10.021	0.081	0.086	0.084	0.084	0.088	0.086	0.0853
543.2	10.021	0.079	0.083	0.083	0.082	0.086	0.083	0.0825
273.39	40.000	0.899	0.955	0.899	0.903	0.898	0.858	0.8895
283.36	39.986	0.878	0.940	0.884	0.888	0.884	0.842	0.8733
293.33	39.993	0.857	0.925	0.868	0.872	0.870	0.828	0.8569
303.31	39.995	0.837	0.909	0.853	0.855	0.855	0.813	0.8403
313.32	39.992	0.814	0.894	0.837	0.838	0.840	0.797	0.8233
323.3	39.992	0.793	0.878	0.821	0.822	0.825	0.781	0.8063
333.29	39.992	0.770	0.862	0.804	0.806	0.811	0.766	0.7888
343.27	39.993	0.747	0.846	0.787	0.789	0.795	0.749	0.7709
353.25	39.988	0.724	0.829	0.770	0.770	0.779	0.733	0.7526
363.25	39.999	0.701	0.812	0.752	0.750	0.764	0.716	0.7337

Table 4.10. Continued

373.25	39.999	0.677	0.795	0.734	0.732	0.747	0.699	0.7146
383.24	39.991	0.654	0.777	0.716	0.714	0.731	0.680	0.6947
393.22	39.995	0.630	0.760	0.697	0.695	0.713	0.662	0.6747
403.21	39.995	0.605	0.740	0.677	0.673	0.697	0.643	0.6543
413.2	39.993	0.581	0.721	0.657	0.654	0.679	0.624	0.6336
423.2	39.995	0.559	0.702	0.638	0.633	0.660	0.609	0.6125
433.2	39.980	0.536	0.681	0.617	0.613	0.642	0.585	0.5912
443.2	39.985	0.514	0.660	0.596	0.592	0.622	0.568	0.5698
453.2	39.988	0.494	0.639	0.573	0.570	0.604	0.547	0.5484
463.2	39.999	0.473	0.616	0.553	0.547	0.584	0.526	0.5272
473.2	39.990	0.453	0.594	0.532	0.528	0.564	0.506	0.5063
483.2	39.995	0.436	0.572	0.510	0.505	0.542	0.488	0.4860
493.2	39.981	0.419	0.549	0.488	0.483	0.523	0.470	0.4663
503.2	39.986	0.403	0.525	0.469	0.465	0.503	0.450	0.4475
513.2	39.985	0.388	0.503	0.449	0.445	0.484	0.434	0.4295
523.2	39.984	0.374	0.481	0.431	0.427	0.464	0.417	0.4125
533.2	39.993	0.361	0.461	0.414	0.409	0.446	0.400	0.3963
543.2	39.982	0.349	0.441	0.397	0.394	0.428	0.386	0.3810

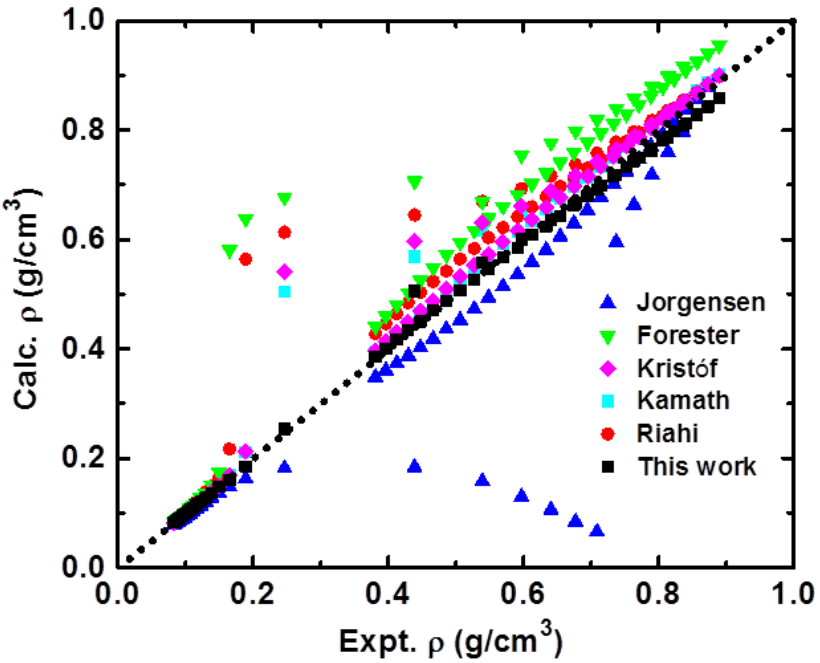

Figure 4.7. Calculated versus experimental[191] densities of fluid hydrogen sulfide under the thermodynamic conditions shown in red in Figure 4.6 (also reported in Table 4.10). The dotted line represents the equation Calc. ρ = Expt. ρ.

4.3.6.2. Vaporization Enthalpy

Figure 4.8 shows the temperature dependence of the vaporization enthalpy of liquid H_2S in the temperature range 193–313 K of the vapor-liquid coexistence curve (see Table 4.11 for tabulated data). The potential models of Kristóf and Liszi,[199] and of Kamath *et al.*[200] show the best agreement with experiment. While the current model systematically underestimates the calculated vaporization enthalpies by ~0.5 kcal/mol, Jorgensen's model[197] overestimates it by ~0.3 kcal/mol. The Drude model of Riahi and Rowley[201] shows good agreement with experiment at high temperature. The model of Forester *et al.*[198] underestimates the vaporization enthalpies by an amount that increases with temperature.

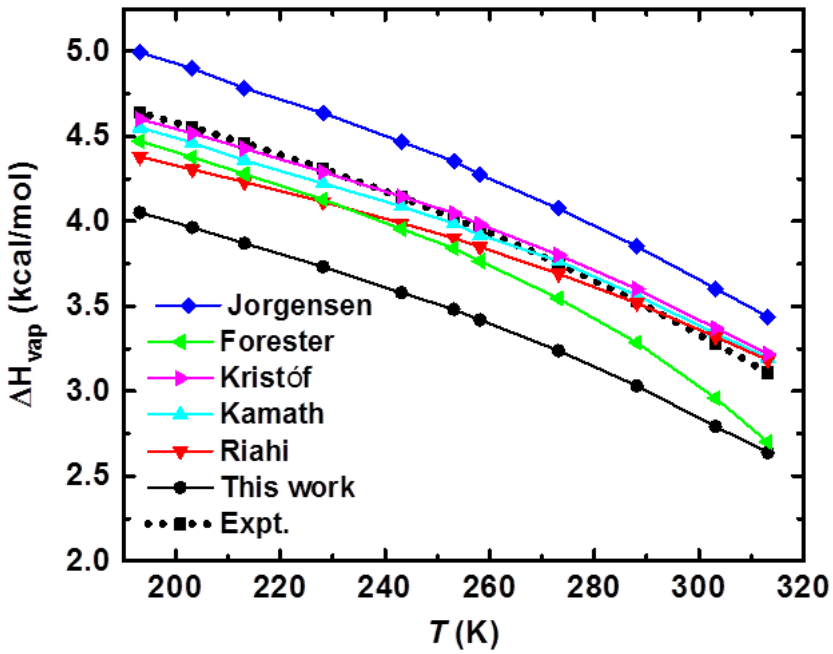

Figure 4.8. Enthalpy of vaporization of H_2S calculated with the present model and with models from the literature[197–200,201] in the temperature range 193.15−313.15 K, along the liquid-vapor coexistence curve. Experimental values are from ref 190.

Table 4.11. Vaporization enthalpy of liquid H_2S calculated with different potential models and corresponding experimental values.

T (K)	p (MPa)	Jorgensen[197]	Forester *et al.*[198]	Kristóf and Liszi[199]	Kamath *et al.*[200]	Riahi and Rowley[201]	This work	Expt.[190]
193.15	0.033	4.993	4.471	4.601	4.551	4.381	4.051	4.640
203.15	0.060	4.900	4.378	4.518	4.462	4.304	3.964	4.552
213.15	0.103	4.783	4.278	4.428	4.358	4.231	3.870	4.461
228.15	0.207	4.638	4.128	4.290	4.223	4.114	3.732	4.310
243.15	0.381	4.467	3.955	4.145	4.088	3.988	3.580	4.140
253.15	0.546	4.354	3.841	4.048	3.986	3.902	3.482	4.020
258.15	0.647	4.274	3.766	3.982	3.918	3.848	3.419	3.957
273.15	1.032	4.074	3.546	3.802	3.767	3.692	3.239	3.753
288.15	1.565	3.852	3.286	3.601	3.563	3.518	3.032	3.528
303.15	2.275	3.604	2.959	3.371	3.339	3.320	2.792	3.282
313.15	2.861	3.438	2.701	3.219	3.196	3.184	2.638	3.109

4.3.6.3. Self-Diffusion Coefficient

Self-diffusion coefficients are calculated along the liquid-vapor coexistence curve, in the temperature range 192.8–294.1 K, using a system of 500 H_2S molecules. Figure 4.9 shows the temperature dependence of the calculated and experimental[194] values (see also Table 4.12). Results are consistent with those reported by Riahi and Rowley.[201] The Jorgensen model overestimates the diffusivity of H_2S over the entire temperature range (likely due to low density), while the Forester model underestimates it. The best agreement with experiment corresponds to the Kamath *et al.* model.[200] Results from the present Drude model and from the model of Kristóf and Liszi[199] are comparable and in good agreement with experiment. While self-diffusion coefficients from both Drude models (this work and that of Riahi and Rowley[201]) are comparable at low temperature, the present model remains closer to experimental data at high temperatures.

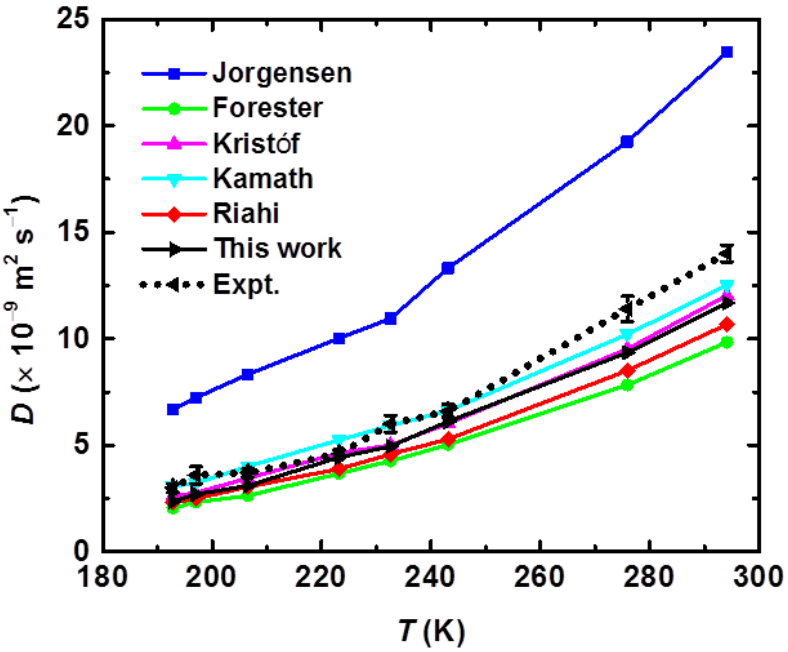

Figure 4.9. Self-diffusion coefficient of H_2S calculated with the present model and with models from the literature[197–200,201] in the temperature range 192.8−294.1 K, along the experimental liquid-vapor coexistence curve. Experimental values (with error bars) are from ref 194.

Table 4.12. Self-diffusion coefficient of liquid H_2S calculated with different potential models and corresponding experimental values.

T (K)	*p* (MPa)	Jorgensen[197]	Forester *et al.*[198]	Kristóf and Liszi[199]	Kamath *et al.*[200]	Riahi and Rowley[201]	This work	Expt.[194]
192.8	0.032	6.7	2.1	2.6	3.1	2.3	2.4	3 ± 0.2
197.0	0.042	7.2	2.3	2.8	3.2	2.5	2.7	3.6 ± 0.4
206.5	0.073	8.3	2.6	3.5	3.9	3.0	3.1	3.7 ± 0.2
223.2	0.166	10.0	3.7	4.6	5.0	3.9	4.4	4.6 ± 0.2
232.6	0.249	10.9	4.3	5.0	6.0	4.6	5.0	6 ± 0.4
243.1	0.380	13.3	5.0	6.0	6.7	5.3	6.1	6.6 ± 0.3
275.9	1.118	19.3	7.8	9.5	10.0	8.5	9.4	11.4 ± 0.6
294.1	1.824	23.4	9.8	12.0	12.6	10.7	11.7	14 ± 0.4

4.3.7. Hydration of H_2S

Using the regular Lorentz-Berthelot mixing rules, the Drude models of H_2S and H_2O yield a hydration free energy (ΔG_{hyd}) of H_2S of –0.1 ± 0.1 kcal/mol at 298.15 K and 0.1013 MPa (1 atm), in poor agreement with the experimental value (–0.54 kcal/mol).[213,214] In comparison, using the regular Lorentz-Berthelot mixing rules, the Drude model of Riahi and Rowley[201] gives a hydration free energy of 0.24 kcal/mol.[215] To better reproduce the experimental value, pair-specific LJ parameters are optimized between the sulfur atom of H_2S and the oxygen atom of H_2O (see Table 4.7). These parameters yield ΔG_{hyd} = –0.5 ± 0.1 kcal/mol.

The hydration structure of H_2S is investigated from the simulation of one hydrogen sulfide molecule in 500 water molecules at 298.15 K and 0.1013 MPa. The $g_{SO}(r)$, $g_{SH}(r)$, $g_{HO}(r)$, and $g_{HH}(r)$ RDFs between the hydrogen sulfide solute and its water solvent are reported in Figure 4.10. For comparison, we also report the $g_{SO}(r)$ and $g_{SH}(r)$ functions calculated by Riahi and Rowley, who have also calibrated their model to reproduce the hydration free energy of H_2S at 298 K.[215] Remarkably, the $g_{SO}(r)$ function calculated with the present model is almost identical to that from Riahi and Rowley model.[215]. It exhibits a first peak with a maximum at 3.64 Å and a minimum at 5.35 Å. Integration up to this minimum shows 20.5 water molecules in the first solvation shell of H_2S, comparable to what is found around an isolated NH_3 (~23 water molecules[170]) and markedly more than around H_2O (4.6 water molecules[113]). The $g_{SH}(r)$ function shows a small shoulder at ~2.4 Å that corresponds to S···H–O hydrogen-bonded pairs. Integration up to the shallow minimum at 2.6 Å yields a coordination number of 0.5. The function also shows a broad peak centered at 3.65 Å with a minimum at ~5.7 Å. Except for the shoulder at ~2.4 Å, the $g_{SH}(r)$ function is in close agreement with that from the Drude model of Riahi and Rowley.[215] The current model shows a higher intensity of the shoulder at ~2.4 Å, in agreement with ab initio MD simulation results.[215] Taking in consideration that both simulations use the same water model, this suggests that the details of the H_2S model have a minimal influence on the hydration structure. Both $g_{HO}(r)$ and $g_{HH}(r)$ RDFs (Figure 4.10b) show a peak with a maximum at 4.25 Å and a minimum at ~5.7 Å. The absence of a clear peak in the distance range 2–3 Å of $g_{HO}(r)$ indicates that O···H–S hydrogen bonds are weak and transient. Moreover, functions $g_{HO}(r)$ and $g_{HH}(r)$ have the same overall shape, which indicates that the water molecules around the H_2S solute have no significant directionality.

The RDFs are consistent with a picture of H_2S hydration in which the molecule is solvated by 20.5 water molecules with minimal hydrogen bonding between solute and solvent molecules.

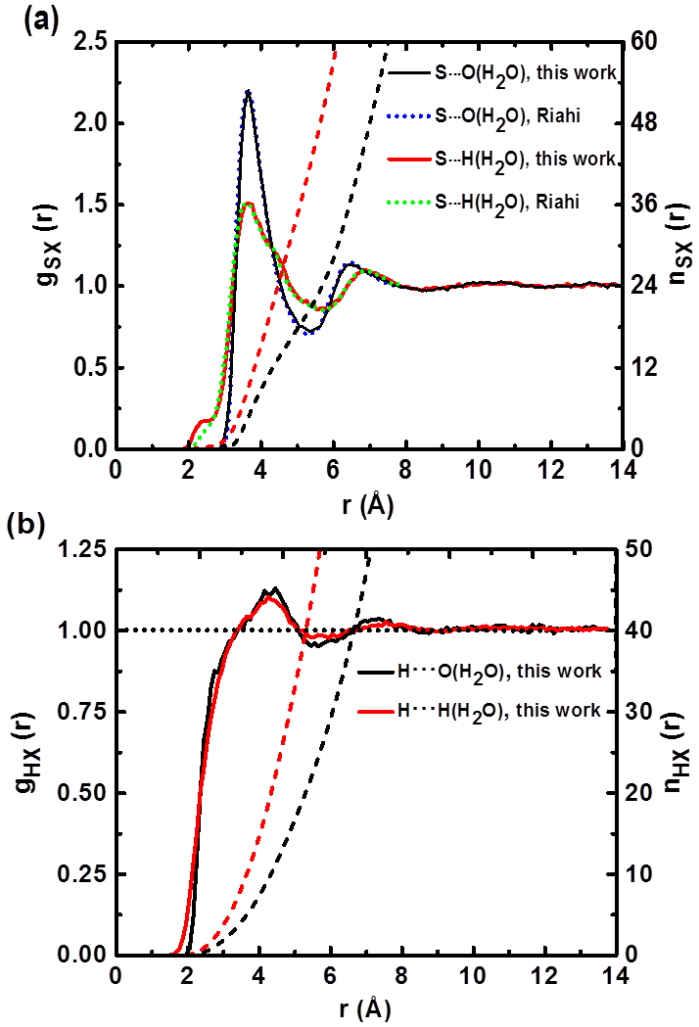

Figure 4.10. Radial distribution functions, $g(r)$, between a single hydrogen sulfide molecule solvated by 500 water molecules at T = 298.15 K and p = 0.1013 MPa = 1 atm. Panel a shows sulfur-oxygen (black) and sulfur-hydrogen (red) RDFs. Panel b shows hydrogen-oxygen (black) and hydrogen-hydrogen (red) RDFs. Dashed lines represent running coordination numbers, $n(r)$. The green and blue dotted curves in panel a are sulfur-oxygen (blue) and sulfur-hydrogen (green) RDFs produced from reference 215.

4.3.8. Water Solvated in H_2S

Figure 4.11 reports the $g_{\mathrm{OS}}(r)$, $g_{\mathrm{OH}}(r)$, $g_{\mathrm{HS}}(r)$, and $g_{\mathrm{HH}}(r)$ RDFs obtained from the simulation of one water molecule in 500 hydrogen sulfide molecules at 212.82 K and 0.1013 MPa. The $g_{\mathrm{OS}}(r)$ function exhibits a first peak at 3.55 Å and a second peak at 7.18 Å. Integration up to the first minimum (at 5.24 Å) shows 9.9 H_2S molecules in the first solvation shell of H_2O and integration up to the second minimum (at 8.9 Å) shows 48 H_2S molecules in the first and second solvation shells combined. The $g_{\mathrm{OH}}(r)$ function exhibits a first peak at 2.55 Å

(corresponding to O···H–S hydrogen-bonded pairs) and a second peak at 4.33 Å. Integration up to the first minimum (at 3.25 Å) shows an average of 4.0 hydrogen atoms coordinating the H_2O molecule, most certainly not all forming O···H–S hydrogen bonds. Integration up to the second minimum (at 5.40 Å) gives 21.5 hydrogen atoms, consistent with the ~10 H_2S molecules in the first solvation shell. The $g_{HS}(r)$ function shows a peak at 2.45 Å corresponding to O–H···S hydrogen-bonded pairs. Integration up to the minimum at 2.96 Å yields a coordination number of 0.9, which suggests that O–H···S contacts are less frequent than O···H–S contacts. Since the force field underestimates the stability of H_2O-H_2S dimer structure 4.2**a** (forming an O···H–S bond) relative to that of 4.2**b** (forming an O–H···S bond) (see Figure 4.2 and Table 4.2), this preference for O···H–S contacts can be expected to be even greater than what the simulation suggests.

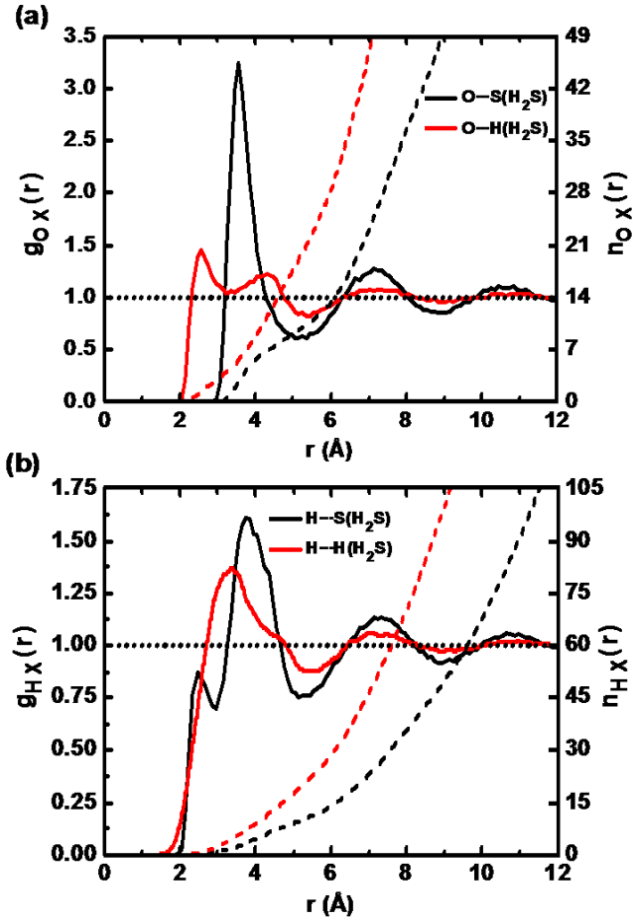

Figure 4.11. Radial distribution functions, $g(r)$, between a single water molecule solvated by 500 hydrogen sulfide molecules at T = 212.82 K and p = 0.1013 MPa = 1 atm. Panel a shows oxygen-sulfur (black) and oxygen-hydrogen (red) RDFs and panel b shows hydrogen-sulfur (black) and hydrogen-hydrogen (red) RDFs. Dashed lines represent the corresponding running coordination numbers, $n(r)$.

4.3.9. Solvation of Alkali Ions in H_2S

The model is used to explore the solvation of alkali ions in liquid H_2S. Table 4.13 shows the calculated absolute solvation free energies of the different alkali ions in liquid H_2S at T = 298.25 K and p = 2.0174 MPa = 19.91 atm. For comparison, the solvation free energies of the alkali ions in liquid water (at T = 298.15 K and p = 0.1013 MPa = 1 atm[118]) and in liquid ammonia (at T = 298.15 K and p = 1.0031 MPa = 9.9 atm)[202] are also reported in Table 4.13. To the best of our knowledge, no experimental data are available for the solvation thermodynamics of alkali ions in H_2S. Table 4.13 shows that, while solvation free energies in water and ammonia are comparable[202], those in hydrogen sulfide are much lower (in absolute value). It is noted however that the difference between the solvation free energy of a given ion in water and in hydrogen sulfide decreases on going from Li^+ to Cs^+; it is 33.4 kcal/mol for Li^+, 20.9 kcal/mol for Na^+, 13.5 kcal/mol for K^+, 11.4 kcal/mol for Rb^+, and 6.5 kcal/mol for Cs^+. This reflects the fact that the ion gets softer on going from the smaller Li^+ to the larger Cs^+ and thus its affinity to the hard water relative to the soft hydrogen sulfide decreases.

Table 4.13. Calculated absolute ($\Delta G_{\text{solv}}^{\text{intr}}$) solvation free energies of alkali ions in liquid water (at T = 298.15 K and p = 0.1013 MPa), liquid ammonia (at T = 298.15 K and p = 1.0031 MPa), and liquid hydrogen sulfide (at T = 298.15 K and p = 2.0174 MPa). All values are in kcal/mol.

Ion	Solvent		
	H_2O[a]	NH_3[b]	H_2S[c]
Li^+	–109.8	–109.5	–76.4
Na^+	–85.6	–85.0	–64.7
K^+	–67.9	–68.5	–54.4
Rb^+	–63.0	–61.2	–51.6
Cs^+	–55.8	–55.4	–49.3

[a] Reference 118. [b] Reference 202. [c] This work

The structure of alkali ions in liquid H_2S is investigated from MD simulations of each alkali ion in 500 H_2S molecules at 212.82 K and 0.1013 MPa for 10 ns. The structure of H_2S molecules around each ion is analyzed from the distribution functions $g_{\mathrm{ion-S}}(r)$ and $g_{\mathrm{ion-H}}(r)$. The functions are calculated from the last 8 ns of each MD simulation, and shown in Figure 4.12. Their characteristics are summarized in Table 4.14.

The first peak of the $g_{\mathrm{ion-S}}(r)$ function decreases in amplitude and shifts away from the ion on going from Li^+ to Cs^+. The coordination number up to the minimum following the first peak is 4.5 for Li^+, 6.0 for Na^+, 8.3 for K^+, 9.6 for Rb^+, and 11.0 for Cs^+ (see Table 4.14). By comparison, alkali ions in SWM4-NDP water at 212.82 K and 0.1013 MPa display coordination numbers of 4.0 for Li^+, 5.7 for Na^+, 6.6 for K^+, 8.0 for Rb^+, and 9.9 for Cs^+. These numbers are obtained from MD simulations of one alkali ion in 500 water molecules, by integrating the $g_{\mathrm{ion-O}}(r)$ function up to its first minimum (at 2.55 Å for Li^+, 3.05 Å for Na^+, 3.35 Å for K^+, 3.65 Å for Rb^+, and 4.05 Å for Cs^+). This is showing that, in its first solvation shell, each alkali ion is surrounded by a larger number of hydrogen sulfide molecules compared to water molecules. While the molecular volume of H_2S is larger than that of H_2O, the observed higher coordination number might be attributed to the larger intermolecular separation between the ions and H_2S. To our knowledge, no experimental data are available for the solvation structure of alkali ions in H_2S.

Table 4.14. Characteristics of the radial distribution functions, $g_{\mathrm{ion-S}}(r)$ and $g_{\mathrm{ion-H}}(r)$, for a single ion in liquid hydrogen sulfide at T = 212.82 K and p = 0.1013 MPa.[a]

Ion	$g_{\mathrm{ion-S}}(r)$						$g_{\mathrm{ion-H}}(r)$					
	r_{M1}	r_{m1}	$n(r_{\mathrm{m1}})$	r_{M2}	r_{m2}	$n(r_{\mathrm{m2}})$	r_{M1}	r_{m1}	$n(r_{\mathrm{m1}})$	r_{M2}	r_{m2}	$n(r_{\mathrm{m2}})$
Li^+	2.55	3.56	4.5	6.3	7.4	29.0	3.64	4.30	10.3	6.7	8.10	70.4
Na^+	2.95	4.00	6.0	6.7	7.8	34.3	3.96	4.82	14.1	6.8	8.55	82.7
K^+	3.42	4.72	8.3	7.2	8.5	42.4	4.45	5.35	19.0	7.3	9.11	99.9
Rb^+	3.65	4.98	9.6	7.4	8.8	46.7	4.70	5.73	22.9	7.6	9.45	111.4
Cs^+	3.87	5.31	11.0	7.6	9.1	51.2	4.90	5.90	25.0	7.8	9.65	118.7

[a] r_{M1} and r_{M2} are the distances (in Å) where the function has its first and second maximum, respectively. At r_{m1} and r_{m2} (in Å), the function has its first and second minimum. $n(r)$ is the running integration numbers evaluated at $r = r_{\mathrm{m1}}$ and r_{m2}.

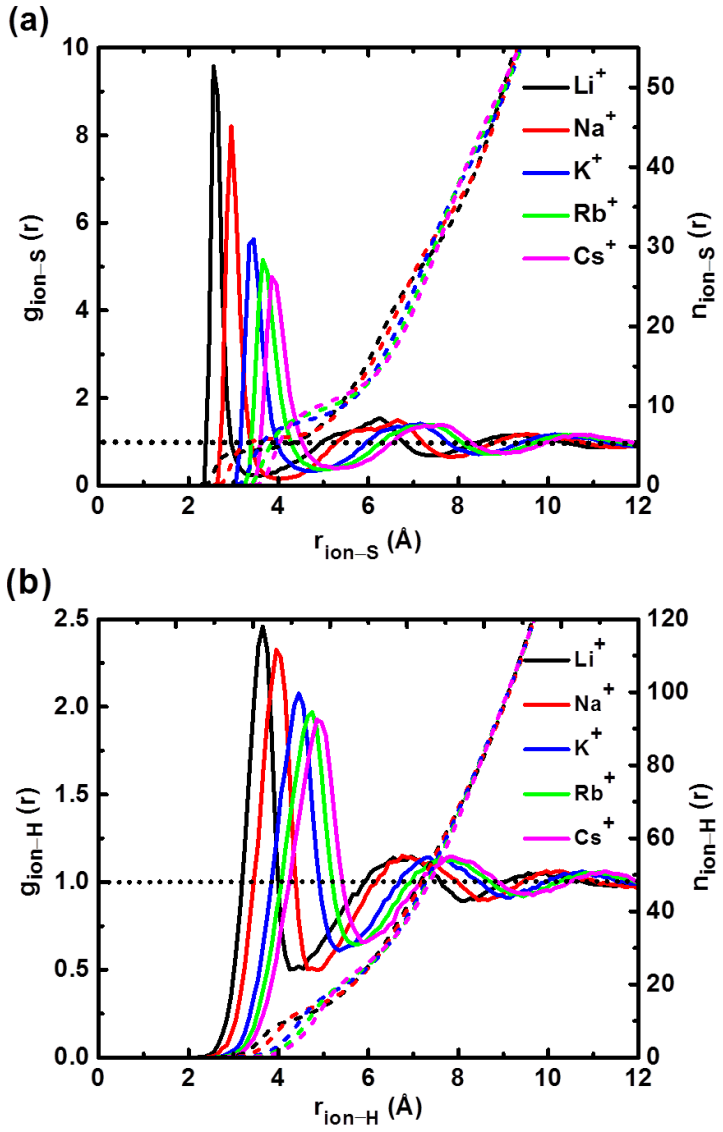

Figure 4.12. Ion−S (a) and ion−H (b) radial distribution functions (solid curves) and running integration numbers (dashed lines) from molecular dynamics simulations of Li^+ (black), Na^+ (red), K^+ (blue), Rb^+ (green), or Cs^+ (pink) in 500 H_2S molecules at 212.82 K and 0.1013 MPa.

4.3.10. Preferential Solvation of Alkali Ions in Aqueous H_2S

The preferential solvation of the alkali ions in aqueous H_2S is investigated from 85-ns long simulations of each ion in aqueous H_2S solution at molar fraction $x_{H_2S} = 0.1$ (450 H_2O molecules and 50 H_2S molecules), at T = 212.82 K and p = 0.1013 MPa. We simulate a dilute H_2S mixture because of the low solubility of H_2S in water[204] and to avoid phase separation. Simulations show that the number of H_2S/H_2O molecules in the first solvation shell is 0.00/4.0 for Li^+, 0.02/5.4 for Na^+, 0.02/6.4 for K^+, 0.02/7.4 for Rb^+, and 0.08/7.8 for Cs^+. For the second

solvation shell, the number of H_2S/H_2O molecules is 1.4/14.4 for Li^+, 1.7/15.9 for Na^+, 2.1/17.1 for K^+, 2.3/18.5 for Rb^+, and 2.4/18.1 for Cs^+. These coordination numbers are calculated by integrating $g_{\mathrm{ion-S}}(r)$ and $g_{\mathrm{ion-O}}(r)$ up to the minimum following the first (or second) peak of $g_{\mathrm{ion-(S+O)}}(r)$, the total RDF. (The first minimum of $g_{\mathrm{ion-(S+O)}}(r)$ is at 2.55 Å for Li^+, 3.05 Å for Na^+, 3.35 Å for K^+, 3.55 Å for Rb^+, and 3.75 Å for Cs^+; the second minimum is at 5.05 Å for Li^+, 5.35 Å for Na^+, 5.65 Å for K^+, 5.75 Å for Rb^+, and 5.95 for Cs^+). These coordination numbers indicate that H_2S molecules are almost totally expelled from the first shell of all ions except Cs^+, whose first shell shows very low occupancy by H_2S. The numbers of H_2S and H_2O molecules in the second shell of each ion are close to their bulk distributions at $x_{\mathrm{H_2S}} = 0.1$ and indicate that the second solvation shells possess no marked selectivity to either ligands.

The results provide insight on the influence of salts on the solubility of H_2S in water. For instance, experiments show that NaCl causes a so-called "salting out" of H_2S, that is, decreases its solubility in water.[216] Based on the binding selectivity of the ions toward water molecules, we suggest that this salting-out effect results from the expulsion of H_2S molecules from the first hydration shells of the ions. This decreases the volume of solution available to H_2S and leads to aggregation and, ultimately, to phase separation. Although not considered in the present work, anions are expected to have a similar selectivity towards water and to further increase the salting-out effect.

4.4. Conclusion

A polarizable potential model for hydrogen sulfide is optimized based on the experimental properties of the H_2S monomer and the density of hydrogen sulfide. The model gives binding energies for hydrogen sulfide clusters in very good agreement with ab initio results. It also yields density, self-diffusion coefficient, and dielectric constant of the liquid at the boiling point in agreement with experiments. Compared to previous models from the literature, the model is showing the best agreement with the experimental structure of liquid H_2S. It is also the most accurate at reproducing the experimental density in the liquid and supercritical phases. It yields self-diffusion coefficient for H_2S in the temperature range 193–294 of the liquid-vapor coexistence curve in good agreement with experiment. The model underestimates the experimental vaporization enthalpy in the temperature range 193–313 of the coexistence curve. This underestimation is however systematic (by ~0.5 kcal/mol), which allows for a simple post-correction.

The model is calibrated to reproduce the hydration free energy of H_2S, by adjusting pair-specific LJ parameters between S and O, and used to investigate the solvation structure of a single H_2S molecule in liquid H_2O and of a single H_2O molecule in liquid H_2S. Simulations show weak hydrogen bonding and lower number of hydrogen bonds compared to these between water molecules.

The model is also calibrated to reproduce the ab initio (CCSD(T)) complexation energy of the alkali ion-H_2S pairs, by adjusting pair-specific LJ parameters between S and each alkali ion. While ab initio calculations suggest C_s symmetry for the alkali ions-H_2S pairs, the model gives C_{2v} symmetry. Reproducing the ab initio-observed C_s symmetry of the pairs may require explicit description of the lone pairs of S and mimic the tetrahedral electron-pair geometry of H_2S.

The model was used to investigate the solvation structure and solvation free energy of alkali ions in liquid H_2S, and the preferential solvation of alkali ions in aqueous H_2S. Simulations show that the ions are almost totally solvated by water in their first solvation shells. This is giving insight in the salting-out effect of salts on the solubility of H_2S in water; solvation of the ions by water lower the volume of water available to H_2S molecules and thus decreases their solubility.

In combination with models for hydrocarbons, the present model for H_2S can be used to investigate the properties of binary and complex mixtures between hydrocarbons and H_2S. Such investigations are useful to devise possible separation strategies of H_2S-containing oils and natural gases. The model can also be used to investigate the selectivity of ions toward ligands of different hardness and study their coordination geometry and dynamics around the ions.

5. Optimization of AM1-based Semiempirical Models for Mg^{2+} and Ca^{2+} Metalloproteins

Abstract

Magnesium and calcium play important roles in biological system. For instance, magnesium stabilizes polyphosphate compounds in the cell and calcium is important for proper bone formation. The two metal ions act as cofactors in numerous enzymatic reactions. Although the two ions have similar physical and chemical characteristics, the activity of enzymes that require one ion as a cofactor can be inhibited by the other. Understanding the mechanism of action of the two ions in these enzymes requires investigations at the molecular level. As a compromise between the computationally expensive ab initio quantum mechanics and the limitations of molecular mechanics in describing chemical reactions, semiempirical models seem the most appropriate for this purpose. We optimize semiempirical models for Mg^{2+} and Ca^{2+} based on the AM1 approach. Two models are optimized for each ion. One model (labeled AM1/Mg, AM1/Ca) is optimized using the original AM1 parameters for H, C, N, O, and S and the other (labeled RM1/Mg, RM1/Ca) is optimized using the RM1 parameters of these elements. Parameters are optimized using the ab initio binding energies and structural geometries of 26 binary complexes of Mg and 30 binary complexes of Ca as training set. These are complexes of the metal ions with one and six (or five) molecules of ligands that are chosen to mimic protein groups that bind metal ions (water, methanol, hydrogen sulfide, methanethiol, ammonia, methylamine, formaldehyde, acetaldehyde, formamide, acetamide, imidazole, 4-methylimidazole, 5-methylimidazole, formate ion, and acetate ion). Optimized models are then tested on the ab initio properties of 169 ion-ligand binary and ion-ligand-water ternary complexes of the two ions. The optimized AM1/Mg model yields an average error in binding energy of 5.2 kcal/mol for the training set and of 6.9 kcal/mol for the testing set, compared to 7.8 and 7.9 kcal/mol for the RM1/Mg model. For Ca, the optimized AM1/Ca model shows an average error in binding energy of 5.0 kcal/mol for the training set and of 7.7 kcal/mol for the testing set. The corresponding errors for the RM1/Ca model are 7.0 and 7.9 kcal/mol. The models of both metal ions give structures of the various complexes in good agreement with those from ab initio MP2 calculations.

5.1. Introduction

Magnesium is the eighth most abundant element in the earth's crust.[217,218] Following calcium, potassium, and sodium, magnesium is the fourth most abundant cation in vertebrates.[219,220] After K^+, Mg^{2+} is the second most abundant intracellular cation and is crucial for various physiological functions.[220–223] Inside the cell, it mainly acts as a counter ion for ATP, DNA, and RNA.[221,224] It stabilizes enzymes and many enzymes require the presence of magnesium for their catalytic action.[222,225] In plants, magnesium is necessary for synthesis of chlorophyll. Magnesium is important for ATP metabolism, muscle contraction and relaxation, release of neurotransmitters, regulation of vascular tone, heart rhythm, and for bone formation.[224,226] It also plays a role in the structural function of proteins and mitochondria. The imbalance in the level of magnesium results in neuromuscular, cardiac, or nervous disorder.[224]

Calcium is the fifth most abundant element on earth[217,218,224,227–230] and the first most abundant metal in vertebrates.[227–230] In an adult human body (average 70 kg mass), the total calcium content is ~1000 g, compared to ~24 g of magnesium.[224,230] 99% of body calcium exists in bones in the form of calcium phosphate.[230] Ca^{2+} plays crucial roles in the physiology and biochemistry of organisms and cells. Through interacting with various proteins, Ca^{2+} functions as a signaling agent and modulates the activity of these proteins. It is also involved in a number of biological processes such as contraction of all muscle cell types, cell division and growth, enzyme activity, hormonal secretion, neurotransmission, and many enzymes require calcium ions as a cofactor.[227–230] Extracellular calcium is also important for maintaining the potential difference across excitable cell membranes, as well as proper bone formation. In plants, Ca^{2+} often forms links between individual cells and is required to maintain plant rigidity.[227] It is also believed that binding of Ca^{2+} to proteins increases their thermal stability.[227] Intercellular Ca^{2+} is maintained at concentration around 100 nM. High intracellular Ca^{2+} is incompatible with life due to aggregation of proteins and nucleic acids and precipitation of phosphates.[227–230]

Magnesium and calcium are Group 2 (alkaline earth) elements and thus share similar physical and chemical characteristics. For example, both metals are hard solids, highly reactive, and possess a charge of +2 in their compounds. Both metals are hard acids and thus prefer oxygen ligands over nitrogen and sulfur ligands. Several differences between the two metals are however critical for their biological function. The ionic radius of Ca^{2+} is larger than that of Mg^{2+} which results in coordination numbers (CN) between 6 and 8 for the first, compared to the

regular octahedral structures (CN = 6) of magnesium complexes.[227,228,231] For a given CN, the ionic radius of Ca^{2+} is always larger than that of Mg^{2+}, which results in complexes of Ca^{2+} with large multidentate ligands being more stable.[227,228] For example complexes of Ca^{2+} with proteins containing the "EF-hand" binding sites are about 10^4 times stronger than Mg^{2+} complexes.[227] In aqueous solutions, magnesium binds water tighter than calcium and is thus harder to dehydrate.[224] This results in ligands exchanging water molecules in the inner coordination shell of Ca^{2+} faster than in Mg^{2+} which results in Ca^{2+} being faster binding agent (10^3 times faster than Mg^{2+}).[227,228] Magnesium salts are more soluble than the respective calcium salts, which makes the first more readily available to organisms.[219,224] The low solubility of calcium salts results in calcium forming insoluble salts with organic and inorganic anions (such as carbonate and phosphate).[224,228–230] Intracellular Ca^{2+} is thus typically maintained at low concentration to prevent protein aggregation and insoluble salt formation.[228–230] While Ca^{2+} ions react readily with biological molecules due to their flexible coordination geometry and rapid binding kinetics, the chemical similarity with Mg^{2+} still allows for interference between the two ions. For example the magnesium-dependent enzyme human phosphoserine phosphatase, an enzyme that catalyses the last step in the synthesis of L-serine, is inhibited by Ca^{2+}.[232]

The hardness of Mg^{2+} and Ca^{2+} ions results in large affinity of the ions toward oxygen-containing ligands. Glusker *et al.*[231] surveyed the Cambridge Structural Database (CSD) for the coordination structure around the two ions. Results showed that oxygen is the most dominant around the ions and that sulfur is almost totally excluded from the ion's first solvation shell. For complexes of Mg^{2+}, the composition of nitrogen ligands around the ions ranges between 9 and 56%. For Ca^{2+} the nitrogen composition ranges between 0 and 16 %. Since the coordination geometry and rate of ligand exchange are important in determining the readability of metal binding to proteins, it is important to measure the rate of exchange of water with various ligands and to study the ion complexation geometry as a function of ligand structure and composition of the solvation shell.

Due to their numerous biological functions, understanding the mechanism of action of Mg^{2+} and Ca^{2+} at the molecular level is required. Given the large size of biological systems, ab initio quantum mechanical calculations seem inappropriate, due to their computational demanding nature. Even for simple systems in which an ion is solvated in a mixture of ligands, ab initio calculations might not be suitable. This is because ion-ligand interactions are strong and the rate of ligand exchange will require very long simulations for reliable sampling. While force

fields (FFs) can be used in studying ion selectivity, complexation geometry, and rate of ligand exchange, they cannot be used to study the mechanism of function of enzymatic reactions. Alternatively semiempirical (SE) quantum mechanical models can be used. SE models are computationally less expensive than ab initio calculations yet allow for studying chemical reactions.

SE methods are based on the Hartree–Fock formalism, but use approximations to avoid computationally expensive steps and obtain some parameters from empirical data. The use of empirical parameters allows for implicit inclusion of electron correlation effects. One of the popular families of such methods is the neglect of diatomic differential overlap (NDDO) method, developed by Pople.[233,234] In attempts to increase accuracy and generality, several modifications were made to the NDDO formalism, among which are AM1,[28] PM3,[235–237] PM6,[238] PM7,[239] and RM1[240] methods.

Except for the latest PM7 model,[239] which aimed at improving the description of noncovalent interactions, SE methods are traditionally optimized on the geometry, heat of formation, dipole moment, and ionization energies of elements and small organic molecules. Optimized models are mostly reliable for molecular systems similar to those used in the parameterization. For example while popular models may be reliable in studying small organic molecules, they may not perform well when applied to biological systems.[241] None of the SE models have considered the binding affinity between metal ions and ligands in binary and ternary clusters and might thus be unsuitable in studying metalloproteins and even small ion-ligand clusters. Despite their limited transferability, SE models can be re-parameterized for specific systems or classes of reactions.[242–246]

The focus of this work is to optimize reliable models for Mg and Ca that can be used to study metalloproteins. We optimize SE models for Mg^{2+} and Ca^{2+} interacting with various O, N, and S ligands, some of which mimic protein fragments that can complex the metal ion. Two models are optimized for each ion, one is compatible with the AM1 parameters for H, C, N, O, and S and the other is compatible with the RM1 parameters of these elements. Optimization of the model is done on the complexation energy and geometry of the dimers (with one ligand molecule) and binary heptamers or hexamers (with six or five ligand molecules) of the two ions with different ligands calculated at high ab initio levels. The transferability of each model is then tested on the ab initio properties of 169 different binary and ternary complexes of each ion.

5.2. Methods

5.2.1. Ligand and Complex Selection

Since the primary aim of this study is to parameterize SE models for magnesium and calcium that can be used in metalloproteins, ligands are mostly selected to mimic protein backbones and amino acid side chains that can bind the two metals. Ligands include water (H_2O), methanol (CH_3OH, model for Ser and Thr), hydrogen sulfide and methanethiol (H_2S, CH_3SH, models for Cys and Met), ammonia and methylamine (NH_3, CH_3NH_2, models for Lys), formamide and acetamide ($HCONH_2$, CH_3CONH_2, models for Asn, Gln, and peptide backbone), imidazole, 4-methylimidazole, and 5-methylimidazole ($C_3H_4N_2$, $C_4H_6N_2$, models for His), and formate and acetate ions (HCO_2^-, $CH_3CO_2^-$, models for Asp and Glu). 4-methylimidazole and 5-methylimidazole are considered to mimic His when it is protonated on N_δ and N_ε. In addition formaldehyde (HCHO) and acetaldehyde (CH_3CHO) are also considered, resulting in a total of fifteen ligands considered. The optimized geometries of the various ligands are presented in Figure 5.1. Binary complexes containing 1–6 ligands with Mg^{2+} ($Mg^{2+}L_{1-6}$) and Ca^{2+} ($Ca^{2+}L_{1-6}$) are studied to investigate the influence of successive ligand addition on complex stability and to compare stability of the various complexes. Ternary complexes that are composed of a cation and a total of five or six (water + ligand) molecules are also considered to study the impact of subsequent substitution of water molecules in the cation's first solvation shell on the geometry and stability of the complex.

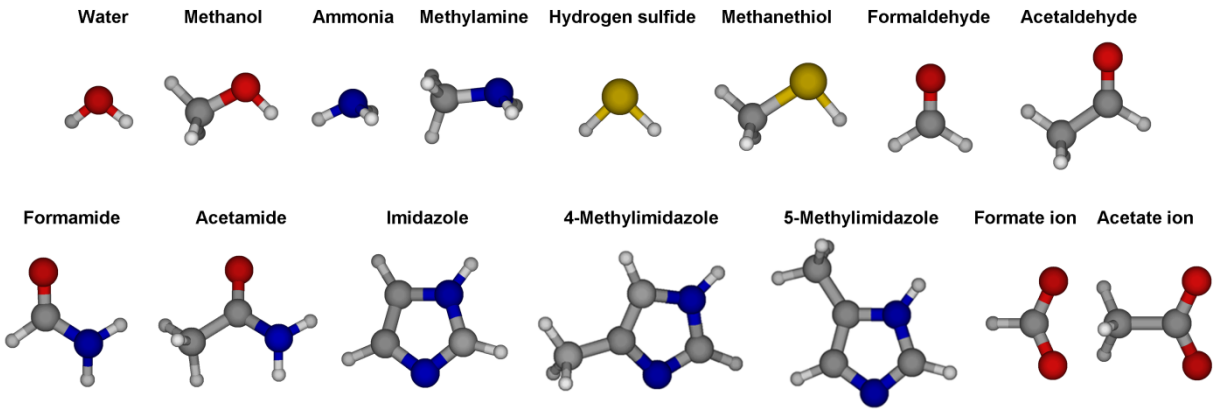

Figure 5.1. Optimized structures of the various ligands used to form the binary and ternary complexes with Mg^{2+} and Ca^{2+}. Except for the formate and acetate ions which are electrically negative, all ligands are neutral. Structures are optimized at the MP2(FC)/6-311++G(d,p) level.

5.2.2. Ab initio and Semiempirical Calculations

Except for the largest clusters, ab initio calculations on isolated ligands (L) and on $M^{2+}L_m$ and $M^{2+}L_m(H_2O)_{6-m}$ clusters (L = ligand, M = Mg or Ca, m = 1–6) are carried out at the MP2/6-311++G(d,p) level with frozen-core (FC) electrons, using Gaussian 09 program.[26] Due to their large size, binary complexes of the ions with six molecules of imidazole, 4-methylimidazole, or 5-methylimidazole are not considered (accordingly, for these complexes m = 1–5). Binary heptamers of the ions with acetamide, binary hexamers of the ion with 4-methylimidazole and 5-methylimidazole, and ternary hexamer complexes containing four molecules of the last two ligands are optimized at the B3LYP/6-311++G(d,p) level. In all complexes, interaction energies are calculated at the MP2(FC)/6-311++G(d,p) level and corrected for basis set superposition error (BSSE) using the counterpoise (CP) procedure proposed by Boys and Bernardi.[111] Parameterization of the SE models for Mg and Ca are performed using an in-house version of MOPAC7.[247] Except for complexes of Mg containing sulfur (S) ligands (hydrogen sulfide and methanethiol), SE geometry optimization is performed without any constraints, using the ab initio-optimized structures as initial guesses. Optimization of binary and ternary complexes containing more than three S ligands around Mg^{2+} showed an unrealistic formation of disulfide bond between some of the ligands. We thus do not optimize the geometry of S-containing Mg^{2+} complexes and calculate their binding energies at the MP2 optimized geometries. In comparison, Ca^{2+} stabilizes the S-containing ligands in its first shell and no bond formation between the ligands is observed. This is likely due to the large size of the ion. We consequently optimize S-containing complexes of Ca^{2+} with the optimized SE models without any constraints.

5.2.3. Parameterization of Semiempirical Models

The AM1 SE model was first reported for four elements; H, C, N, and O.[28] The model was then extended for twenty other main group elements, mostly metals.[248] In that latter extension, the AM1 scheme was modified by introducing two bond-specific parameters in the core-core repulsion term. These two parameters are added for alkali and alkaline earth elements with various specific elements. The model was then reparameterized using a training set composed of 1736 molecules and the new parameters were referred to as the RM1 SE model.[240] It should be noted that AM1 and RM1 have the exact formalism but different parameters. Hutter *et al*. parameterized an AM1 model for magnesium using a genetic algorithm approach.[249] This model is based on the original AM1 scheme (i.e. no bond specific parameters are included) and

is optimized to describe diverse chemical environments, with emphasis on structural features of biologically relevant systems.[249] To the best of our knowledge no parameters have been reported for calcium that use the original[28] AM1 functional form. Due to the popularity of AM1 and RM1, we optimize new SE models for Mg and Ca that are compatible with parameters of the two methods. For each metal, a model (labeled AM1) is optimized to be compatible with the AM1 parameters for H, C, N, O, and S and another model (labeled RM1) is optimized to be compatible with the RM1 parameters of these atoms.

5.2.3.1. Preparation of Training and Testing Sets

The training set contains the minimum-energy conformers of some binary metal ion complexes. For Mg^{2+}, the training set is composed of: 1) Thirteen dimer complexes ($Mg^{2+}L$, L = H_2O, CH_3OH, NH_3, CH_3NH_2, HCHO, CH_3CHO, $HCONH_2$, CH_3CONH_2, HCO_2^-, $CH_3CO_2^-$, $C_3H_4N_2$, $C_4H_6N_2$), 2) Three binary hexamer complexes of the ion with imidazole, $Mg^{2+}(C_3H_4N_2)_5$, and 4-methylimidazole and 5-methylimidazole, $Mg^{2+}(C_4H_6N_2)_5$, and 3) Ten binary heptamer complexes ($Mg^{2+}L_6$, L = H_2O, CH_3OH, NH_3, CH_3NH_2, HCHO, CH_3CHO, $HCONH_2$, CH_3CONH_2, HCO_2^-, $CH_3CO_2^-$). In addition to these types of complexes, the training set of Ca included binary dimer and heptamer complexes of the metal ion with hydrogen sulfide and methanethiol. This results in a total of 26 complexes for Mg and 30 complexes for Ca.

The testing set contains: a) The minimum-energy conformers for trimer, tetramer, and pentamer complexes of each ion with imidazole, 4-methylimidazole, and 5-methylimidazole, b) The minimum-energy conformers for the trimer to hexamer complexes of each ion with each of the twelve other ligands, and c) various minimum-energy structures of ternary ion complexes. These ternary structures possess the general structural formula $M^{2+}L_m(H_2O)_n$, where M = Mg or Ca, L = ligand (other than water), m = 1–5 (m = 1–4 for imidazole, 4-methylimidazole, and 5-methylimidazole) and n = 6–m (n = 5–m for imidazole, 4-methylimidazole, and 5-methylimidazole). This resulted in a total of 169 structures being included. For both training and testing sets, the ab initio calculated structures and binding energies of the complexes are used as reference data.

5.2.3.2. Error Function

The overall error function that is minimized during parameterization is as follows:

$$\chi = \sum_i \left| E^{\mathrm{SE}}(i) - E^{\mathrm{QM}}(i) \right| + W_s \sum_i \mathrm{MSD}(i) \qquad 5.1$$

where $E^{\mathrm{SE}}(i)$ is the SE-calculated binding energy of complex and $E^{\mathrm{QM}}(i)$ is its ab initio binding energy calculated at the MP2/6-311++G(d,p) and corrected for BSSE. SE binding energies are calculated as the difference in heat of formation between the complex and the sum of the heat of formations of the isolated fragments forming the complex. MSD is the mean square deviation of the model (SE) structure relative to the reference ab initio structure. To calculate MSD, the optimized structure from the SE model is aligned with the corresponding reference ab initio structure and MSD is calculated as follows:[246]

$$\mathrm{MSD} = \frac{1}{n}\sum_{a=1}^{n}\left|\boldsymbol{r}_a^{\mathrm{SE}} - \boldsymbol{r}_a^{\mathrm{QM}}\right|^2 \qquad 5.2$$

Where n is the number of atoms in the complex and $\left|\boldsymbol{r}_a^{\mathrm{SE}} - \boldsymbol{r}_a^{\mathrm{QM}}\right|$ is the difference in position of atom a between the model and reference structures. W_s is a weighting factor set to 33 kcal/mol.Å^2.[246] The error function χ is composed of one MSD term and one E term for each complex.

5.2.3.3. Parameterization Procedure

Parameterization is performed following Wang *et al*'s procedure for optimizing a SE model for proton transfer reactions in water.[246] In particular, parameterization is performed using a genetic algorithm approach that is commonly used in model parameterization.[249–259] We use a parallel version of the PIKAIA program[260] for this purpose. For parameterization of both Mg and Ca, the AM1 parameters of Mg reported by Hutter *et al*.[249] are used as initial guess. Parameters of other elements (H, N, C, O, and S) are set to their AM1[28] or RM1[240] values and kept unchanged. To ensure a faster search and speed up the convergence, parameters of Mg and Ca are initially allowed to change by up to ±50% of the original values of Mg.[249] Optimized parameters are then used as a new guess and are allowed to change by up to ±40%. This process is repeated allowing optimized parameters to change by ±30%, then by ±20%, then by ±10% and finally by ±5%. This procedure allows parameters for an overall change by more than 100% of their original values. Each full round of optimization consists of a PIKAIA run to optimize the 21 parameters for magnesium or calcium. Each PIKAIA run simulates the evolution of 100 individuals for 300 generations. The 100 individuals are initially randomly distributed inside the search space and each represents a set of SE model parameters different from the original values. Each new generation is obtained by genetic recombination (crossover) of pairs of individuals

selected from the previous generation, followed by random mutation.[246] The individual that yields the lowest value for the error function during any of the 300 generations is chosen as the final parameter set for the run.

5.3. Results and Discussion

5.3.1. Optimized Semiempirical Models

Optimized parameters for the new SE models for Mg and Ca, together with parameters for the AM1 model of Mg by Hutter *et al*.[249] are reported in Table 5.1. Optimized AM1 parameters for Mg deviate from the original parameters of Hutter *et al*.[249] by 49% on average, with a maximum deviation of ~200%. The performance of each model on the properties of binary and ternary complexes is presented in Figures 5.2 and 5.3 and Table 5.2. As expected, the properties of the training set for Mg are better described with the new models (see Figure 5.2a). The AM1/Mg model yields an average unsigned error in binding energies of 5.2 kcal/mol, compared to 13.5 kcal/mol for Hutter *et al*.'s model.[249] The optimized RM1/Mg model yields an average error of 7.8 kcal/mol. Except for the clusters involving H_2S, the performance of the new AM1 model of Mg for properties of the complexes in the testing set is better than the original[249] AM1 model (see Figure 5.2b and Table 5.2). For complexes containing S ligands, the model underestimates their binding energies in proportion to the number of ligands (see Tables 5.7, 5.8, 5.21, 5.22). Excluding these complexes, the model gives an average error for binding energy of 6.9 kcal/mol compared to 14.8 kcal/mol for original AM1 model.[249] The RM1/Mg model gives an average error of 7.9 kcal/mol.

Compared to the original AM1 model of Mg,[249] The present models are also better in reproducing the structural properties of the various complexes (see Figures 5.2a and b and Table 5.2). Excluding H_2S complexes (which are not optimized with the models), the average MSD for the training set is 0.09 $Å^2$ for the optimized AM1/Mg and RM1/Mg models and 0.08 $Å^2$ for Hutter *et al*. model.[249] For testing set, the average MSD is 0.22 $Å^2$ for the AM1/Mg model, 0.15 $Å^2$ for the RM1/Mg model and 0.31 $Å^2$ for Hutter *et al*. model.[249]

Table 5.1. Parameters of the optimized AM1 and RM1 models for Mg and Ca. parameters of Hutter *et al*.'s AM1 model of Mg^{249} are also reported.

Parameter	Mg^{2+}			Ca^{2+}	
	AM1[a]	AM1[b]	RM1[b]	AM1[b]	RM1[b]
U_{ss} (eV)	–14.96959313	–17.37339030	–17.93701124	–2.01361382	–4.65542363
U_{pp} (eV)	–11.56229248	–8.99555614	–8.10066682	–2.88964802	–1.92608182
Z_s (au)	1.22339270	0.69945341	0.62524860	2.54946775	2.29741399
Z_p (au)	1.02030798	1.58814500	1.59776906	1.47571692	0.10638759
B_s (eV)	–1.25974355	–1.02135312	–0.69284439	–0.31873930	–0.15001026
B_p (eV)	–0.77836604	–0.99101850	–0.37311667	–0.12340900	–0.13867718
G_{ss} (eV)	7.50132277	8.80764247	8.89044736	13.04907958	11.09384366
G_{sp} (eV)	6.34591536	16.27489807	9.24317081	8.85551027	9.60324795
G_{pp} (eV)	4.77534467	2.14230435	4.08337806	2.97236549	2.52723151
G_{p2} (eV)	4.34017279	13.05343791	6.43473532	9.26527581	2.24406784
H_{sp} (eV)	0.48930466	0.58966014	0.34889385	0.73830671	0.17785199
α ($Å^{-1}$)	1.67049799	2.11078387	2.15298579	1.96384479	4.17035391
K_1 (eV)	2.55017735	2.16457775	3.57572156	2.10714013	3.13919064
L_1 ($Å^{-1}$)	4.29397225	5.71101784	6.55869823	2.70453602	3.26336657
M_1 (Å)	0.79989601	0.99041533	0.36143871	0.91021047	0.92596778
K_2 (eV)	–0.00565806	–0.01039500	–0.00725925	–0.00616428	–0.01360585
L_2 ($Å^{-1}$)	2.96053910	2.71389603	4.05249865	0.80220473	4.24837362
M_2 (Å)	1.47499983	2.64496738	1.03583115	2.30667513	2.40752019
K_3 (eV)	–0.00610286	–0.00950647	–0.00529425	–0.01019293	–0.01512304
L_3 ($Å^{-1}$)	2.61416919	1.53718136	3.01223977	2.05711612	4.41649621
M_3 (Å)	2.42604040	3.09969618	1.20946206	3.84564737	2.24399036

[a] Parameters of the original AM1 model by Hutter *et al*.[249] [b] This work.

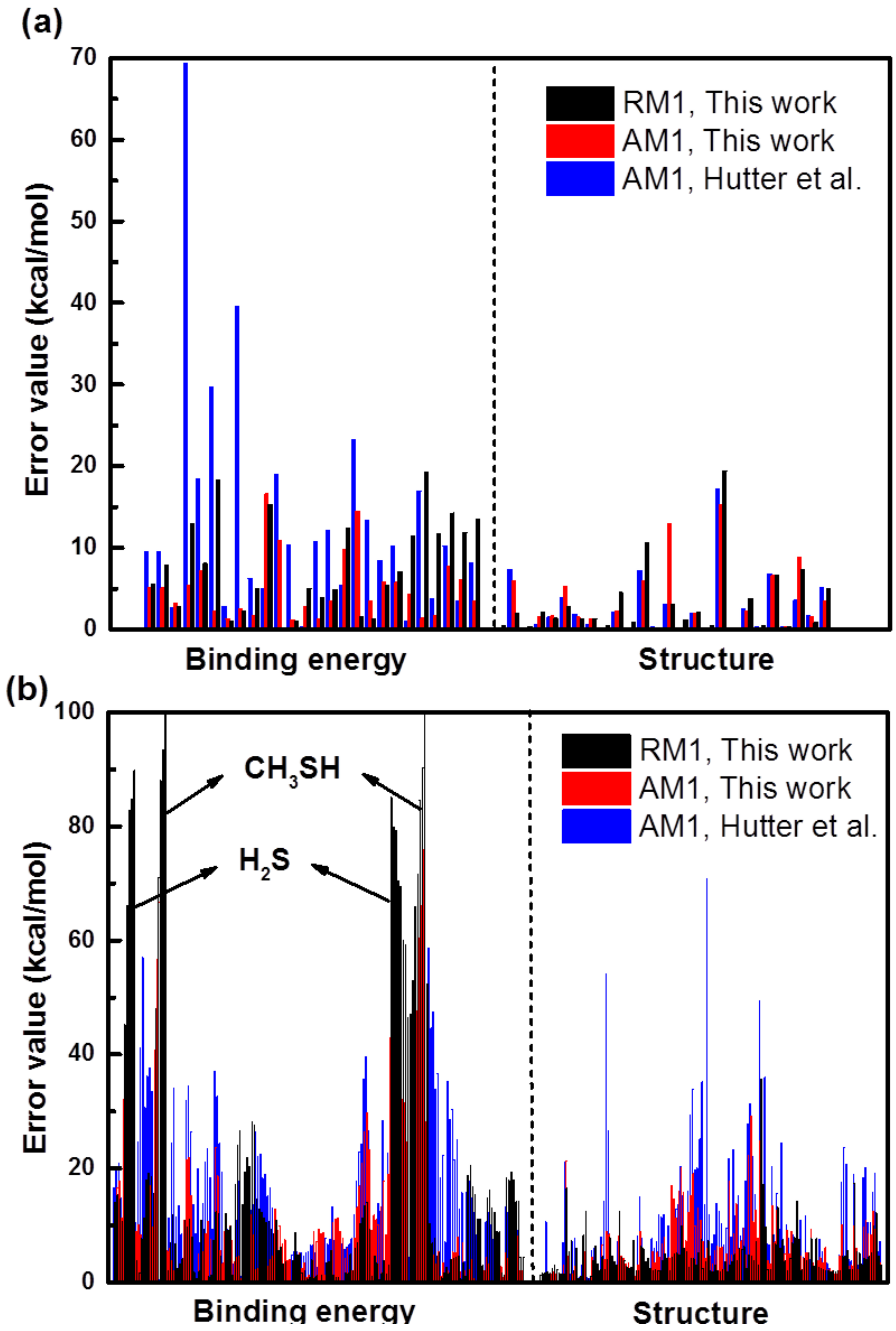

Figure 5.2. Panel a shows the performance of optimized AM1/Mg and RM1/Mg models on the binding energies and structures of the training set and panel b gives their performance on the testing set. For comparison, the performance of the original AM1 model of Mg by Hutter *et al.*[249] is shown in blue. Large errors (> 30 kcal/mol) in binding energies from optimized models in panel b correspond to binary and ternary complexes containing S. these binding energies are calculated at the MP2 optimized geometries. Structures of binary and ternary complexes containing H_2S are not shown in panel b because they are not optimized with the models. Errors in structure are defined in *Eq* 5.2 (A structure error of 5 kcal/mol corresponds to an MSD of 0.17 $Å^2$).

The optimized AM1/Ca and RM1/Ca models reproduce the ab initio properties of both training and testing sets (see Figures 5.3 a and b and Table 5.2). The AM1 model gives an average error in binding energy of 5.0 kcal/mol for the training set and of 7.7 kcal/mol for the testing set. It shows an average MSD of 0.07 $Å^2$ for training set and 0.23 $Å^2$ for testing set. The RM1 model shows comparable behavior. It yields an average error in binding energy of 7.0 kcal/mol for training set and of 7.9 kcal/mol for testing set. It gives average MSD of 0.09 $Å^2$ for training set and of 0.18 $Å^2$ for testing set.

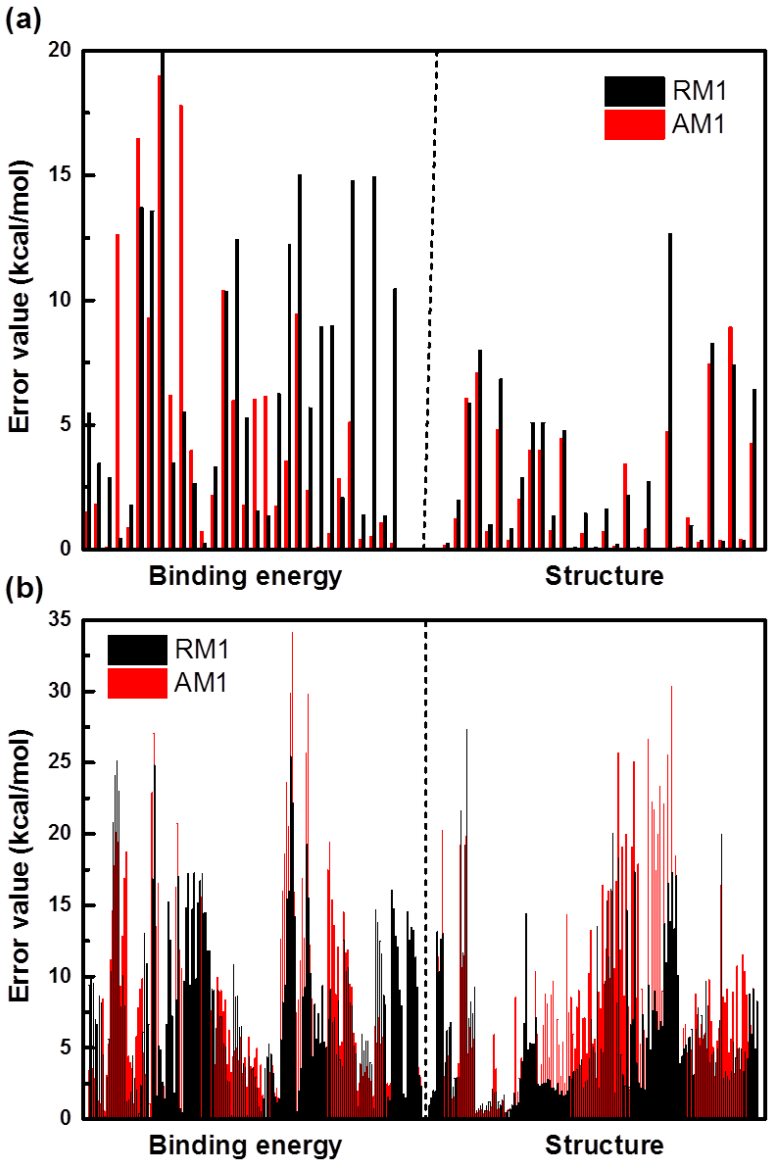

Figure 5.3. Performance of optimized AM1/Ca model (in red) and RM1/Ca model (in black) on the properties of the training set (panel a) and on the properties of the testing sets (panel b).

Table 5.2. Mean absolute error in binding energies (in kcal/mol) and average MSD (in $Å^2$) of the different binary and ternary complexes of Mg^{2+} and Ca^{2+} for the optimized models of the two metals and for the original AM1 model of Mg.[249]

System	Mg^{2+}						Ca^{2+}			
	Binding energy			MSD			Binding energy		MSD	
	AM1*	AM1	RM1	AM1*	AM1	RM1	AM1	RM1	AM1	RM1
Binary complexes										
$M(H_2O)_m$	15.3	11.4	11.4	0.09	0.04	0.05	2.7	7.5	0.03	0.04
$M(CH_3OH)_m$	31.1	11.7	16.3	0.10	0.12	0.14	16.7	21.0	0.06	0.07
$M(NH_3)_m$	34.3	6.3	6.7	0.08	0.04	0.06	6.3	5.8	0.11	0.16
$M(CH_3NH_2)_m$	19.1	3.6	5.2	0.06	0.09	0.08	3.0	2.2	0.14	0.19
$M(H_2S)_m$	14.7	38.5	64.4	–	–	–	3.9	5.2	0.26	0.32
$M(CH_3SH)_m$	7.3	51.4	69.5	–	–	–	13.6	6.0	0.33	0.40
$M(HCHO)_m$	7.5	5.4	6.9	0.16	0.13	0.13	7.5	4.1	0.01	0.02
$M(CH_3CHO)_m$	15.0	7.1	4.6	0.10	0.06	0.12	2.0	5.7	0.02	0.04
$M(HCONH_2)_m$	22.6	12.0	5.3	0.10	0.08	0.13	3.0	8.1	0.01	0.03
$M(CH_3CONH_2)_m$	25.0	11.6	5.4	0.68	0.22	0.21	6.0	9.6	0.04	0.09
$M(imidazole)_m$	10.0	3.7	19.7	0.05	0.07	0.12	7.4	11.7	0.12	0.13
$M(4\text{-methylimidazole})_m$	10.1	7.9	20.3	0.23	0.12	0.12	5.3	10.7	0.12	0.15
$M(5\text{-methylimidazole})_m$	6.4	2.6	16.2	0.03	0.10	0.11	3.2	11.5	0.13	0.19
$M(HCHOO^-)_m$	10.1	2.6	5.3	0.06	0.11	0.13	15.4	8.6	0.07	0.05
$M(CH_3COO^-)_m$	6.8	6.7	7.5	0.08	0.06	0.08	10.0	7.4	0.07	0.03
Ternary complexes										
$M(CH_3OH)_m(H_2O)_n$	19.1	3.1	11.3	0.23	0.19	0.19	9.8	11.8	0.18	0.08
$M(NH_3)_m(H_2O)_n$	33.6	3.3	5.0	0.07	0.09	0.06	8.7	7.5	0.14	0.15
$M(CH_3NH_2)_m(H_2O)_n$	21.6	4.4	3.0	0.13	0.14	0.14	2.9	4.3	0.21	0.20
$M(H_2S)_m(H_2O)_n$	7.9	36.1	68.7	–	–	–	3.7	6.3	0.33	0.21
$M(CH_3SH)_m(H_2O)_n$	19.1	41.0	70.6	–	–	–	12.2	6.3	0.44	0.42
$M(HCHO)_m(H_2O)_n$	1.8	6.8	4.2	0.30	0.15	0.07	7.1	4.9	0.18	0.06
$M(CH_3CHO)_m(H_2O)_n$	5.3	3.2	3.5	0.26	0.15	0.09	4.2	6.1	0.21	0.10
$M(HCONH_2)_m(H_2O)_n$	4.9	5.9	2.1	0.44	0.46	0.14	3.7	2.4	0.22	0.16
$M(CH_3CONH_2)_m(H_2O)_n$	7.6	7.6	1.5	0.43	0.43	0.17	2.6	3.1	0.37	0.32
$M(imidazole)_m(H_2O)_n$	9.9	2.0	12.3	0.41	0.20	0.19	5.1	9.0	0.23	0.19
$M(4\text{-methylimidazole})_m(H_2O)_n$	9.2	5.8	13.9	0.41	0.19	0.18	5.3	10.0	0.23	0.19
$M(5\text{-methylimidazole})_m(H_2O)_n$	6.9	2.5	9.6	0.31	0.14	0.17	2.1	9.5	0.15	0.13
$M(HCHOO^-)_m(H_2O)_n$	23.3	17.6	9.2	0.73	0.35	0.33	21.4	14.6	0.31	0.23
$M(CH_3COO^-)_m(H_2O)_n$	12.1	12.6	2.5	0.94	0.31	0.14	15.5	8.6	0.35	0.18

* Using the AM1 model of Hutter *et al*.[249]

5.3.2. Ab initio Optimized Geometries of Binary Complexes

The geometry of binary complexes formed between Mg^{2+} or Ca^{2+} and up to 6 molecules of the different ligands, $M^{2+}L_m$ (M = Mg or Ca, L= ligand, m = 1–6), are optimized starting from various plausible initial conformations and only structures of the most stable complexes are reported. Except for M^{2+}(acetamide)$_6$, M^{2+}(4-methylimidazole)$_5$, and M^{2+}(5-methylimidazole)$_5$ complexes, which are optimized at the B3LYP/6-311++G(d,p), all complexes are optimized at the MP2(FC)/6-311++G(d,p) level. When described, the geometry specifies the arrangement of atoms in direct contact with the metal ion. In most complexes, binary trimers of Mg^{2+} are linear while those of Ca^{2+} are bent. All ion tetramers, $M^{2+}L_3$, are characterized by trigonal planar geometry except for Ca^{2+} tetramers with hydrogen sulfide and methanethiol, which are characterized by trigonal pyramidal geometries (see Figures 5.8e and 5.9e). All pentamer complexes, $M^{2+}L_4$, are tetrahedral in geometry and all heptamer complexes, $M^{2+}L_6$, are octahedral. Hexamer complexes, $M^{2+}L_5$, are either trigonal bipyramidal or tetragonal pyramidal.

For all complexes, binding energies without and with correction for BSSE (E and E^{CP}, respectively) are calculated at the MP2(FC)/6-311++G(d,p) level of theory. The notation MP2(FC)/6-311++G(d,p)//B3LYP/6-311++G(d,p) indicates that binding energy is calculated at the MP2(FC)/6-311++G(d,p) level using the B3LYP/6-311++G(d,p) optimized geometry. It is generally found that Mg^{2+} complexes are more stable (binding energies are more negative) and possess shorter ion-ligand separations compared to corresponding Ca^{2+} complexes (see Figures 5.4–5.18 and Tables 5.3–5.17). This is due to the small size of Mg^{2+} relative to Ca^{2+}. Results also show that in most complexes, subsequent addition of up to four ligands around Mg^{2+} results in increasing the binding energy of the complex more than the increase in binding energy when same ligands are added to Ca^{2+}. The increase in binding energy upon addition of the fifth or sixth ligand is almost equal for both ions. For small clusters, the small size Mg^{2+} stabilizes ligands more than the relatively larger Ca^{2+} however in large clusters ligands will be better accommodated by the larger Ca^{2+}. It is also observed that in complexes of each ion with a particular ligand, the separation between the ion and the ligand increases as the number of ligands increases (see Figures 5.4–5.18). This is due to the steric crowding imposed by large number of ligands. Results show that the degree of complex stabilization decreases as subsequent ligands are introduced. For example the increase in binding energy on going from the trimer to the tetramer is lower than that when going from the dimer to the trimer. It is also found that ion-

ligand separation decreases and the binding energy increases when the ligand is methylated. For example, the ion···O distances in a given ion-methanol complex (see Figure 5.5) is shorter than that in the corresponding ion-water complex (see Figure 5.4). Binding energies of ion-methanol complexes (see Table 5.4) are higher (more negative) than those of corresponding ion-water clusters (see Table 5.3). This is attributed to the electron donating nature of the methyl group which increases the electron density of the atom coordinating the metal ion and results in shorter ion-ligand distances and in more stable complex.

5.3.2.1. $M^{2+}(H_2O)_m$ Clusters

The geometry of complexes formed between Mg^{2+} or Ca^{2+} with one up to six water molecules are optimized at the MP2(FC)/6-311++G(d,p) level. Figure 5.4 shows the geometry of the global minimum conformers together with some of their structural features. The pentamer complex of each ion displays a tetragonal pyramidal geometry (Figure 5.4e). Table 5.3 lists the binding energies of these complexes without and with correction for BSSE (E and E^{CP}, respectively) together with binding energies calculated with SE models. It should be noted that our calculations at the MP2(full)/6-311++G(d,p) level shows $E = –79.2$ kcal/mol and $E^{CP} = –76.5$ for the Mg^{2+}–water pair and shows $E = –55.9$ kcal/mol and $E^{CP} = –53.9$ kcal/mol for the Ca^{2+}–water pair, in close agreement with results using frozen core approximation (see Table 5.3). All semiempirical models underestimate the E^{CP} values for both ions complexes, with the new optimized models being better in describing the binding energy and the geometry (see Tables 5.2 and 5.3).

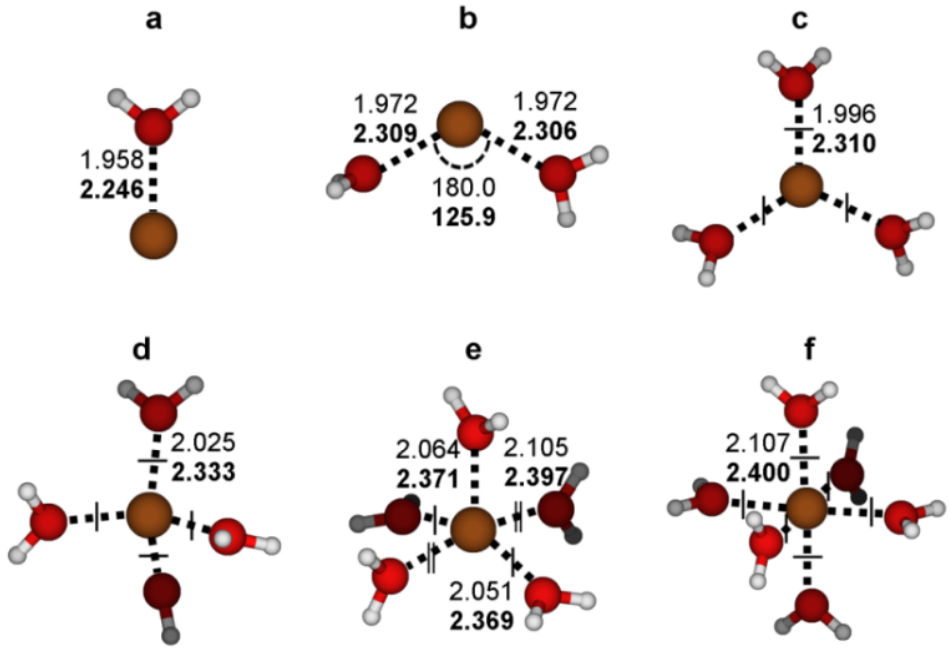

Figure 5.4. Optimized geometries of the binary complexes of Mg^{2+} and Ca^{2+} with water along with important geometrical parameters as computed at the MP2(FC)/6-311++G(d,p) level of theory. The single and double dashes indicate equal ion-water separations. Illustrated structures and the parameters in bold are for Ca^{2+}. All distances are in Å.

Table 5.3. Binding energies for $M^{2+}(H_2O)_m$ complexes (M = Mg or Ca, and m = 1–6) calculated at the MP2(FC)/6-311++G(d,p) level without and with correction for BSSE (E, E^{CP}, respectively). Binding energies calculated with different SE models are also reported. All energies are in kcal/mol.

m	Mg^{2+}					Ca^{2+}			
	Ab initio		SE			Ab initio		SE	
	E	E^{CP}	AM1*	AM1	RM1	E	E^{CP}	AM1	RM1
1	–78.8	–76.2	–66.6	–71.1	–70.7	–55.6	–53.0	–51.5	–47.5
2	–150.5	–144.8	–128.1	–132.2	–130.7	–105.4	–101.6	–98.2	–92.2
3	–208.9	–200.5	–180.5	–183.9	–185.1	–149.9	–143.9	–140.6	–134.0
4	–257.6	–245.6	–224.7	–227.8	–230.9	–189.7	–181.2	–177.7	–171.7
5	–292.7	–276.7	–261.9	–265.4	–266.0	–223.2	–211.9	–209.1	–204.9
6	–325.9	–305.1	–295.5	–300.0	–297.3	–254.3	–238.9	–237.1	–235.4

* Using the AM1 model of Hutter *et al*.[249]

5.3.2.2. $M^{2+}(CH_3OH)_m$ Clusters

Optimized geometries for the minimum-energy conformers in the complexes of Mg^{2+} and Ca^{2+} with methanol molecules are reported in Figure 5.5. These structures are similar to those for the ion-water complexes but with shorter ion···O distances. Ab initio and SE binding energies of these various clusters are given in Table 5.4. As seen in Tables 5.2 and 5.4, the binding nergies of Mg^{2+} complexes are better reproduced by the new SE models. The new models for Ca underestimate the binding energies but reproduce the structure of the different clusters.

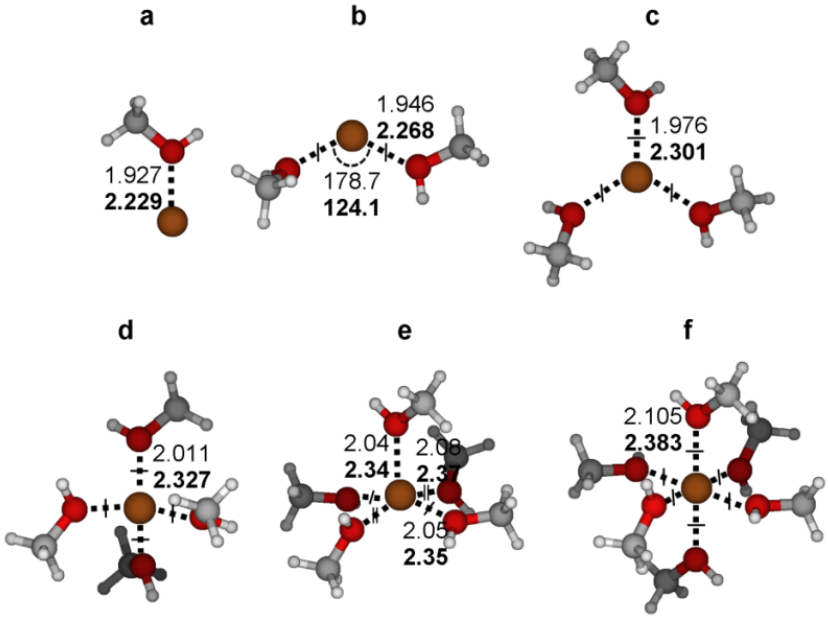

Figure 5.5. Optimized geometries of the binary complexes of Mg^{2+} and Ca^{2+} with methanol along with important geometrical parameters as computed at the MP2(FC)/6-311++G(d,p) level of theory. Illustrated structures and the parameters in bold are for Ca^{2+}. All distances are in Å.

Table 5.4. Binding energies for $M^{2+}(CH_3OH)_m$ complexes (M = Mg or Ca, and m = 1–6) calculated at the MP2(FC)/6-311++G(d,p) level without and with correction for BSSE (E, E^{CP}, respectively). Binding energies calculated with different SE models are also reported. All energies are in kcal/mol.

m	Mg^{2+}					Ca^{2+}			
	Ab initio		SE			Ab initio		SE	
	E	E^{CP}	AM1*	AM1	RM1	E	E^{CP}	AM1	RM1
1	–94.2	–91.7	–73.2	–84.5	–83.6	–66.0	–64.0	–54.7	–50.4
2	–175.4	–169.6	–138.9	–154.0	–151.6	–121.7	–117.9	–103.3	–97.1
3	–237.1	–228.6	–192.4	–210.2	–209.4	–170.2	–164.3	–146.5	–140.2
4	–286.5	–274.2	–236.5	–257.2	–255.6	–212.0	–203.5	–183.4	–178.3
5	–320.7	–303.3	–269.7	–293.5	–287.7	–245.9	–233.6	–214.1	–210.6
6	–352.4	–329.6	–299.8	–327.3	–311.2	–277.5	–260.4	–241.4	–240.5

* Using the AM1 model of Hutter *et al.*[249]

5.3.2.3. $M^{2+}(NH_3)_m$ Clusters

Figure 5.6 shows the structures of optimized stable conformers of ammonia complexes with Mg^{2+} and Ca^{2+}. The pentamer complex of each ion is characterized by trigonal bipyramidal geometry. Binding energies calculated at the MP2(FC)/6-311++G(d,p) level and with different SE models are reported in Table 5.5. Figure 5.6 shows ion···N distances that are larger than ion···O distances in the corresponding ion-water clusters. Table 5.5 shows however binding energies that are relatively larger than for corresponding ion-water complexes. The fact that gaseous ammonia possesses a dipole moment of 1.470 D,[261] smaller than that of gaseous water (1.850 D),[261] indicates that ion-dipole interaction is not the determinant factor of the relative complex stability. The larger polarizability of NH_3 (2.103 $Å^3$)[211] compared to H_2O (1.501 $Å^3$)[211] results in a larger induced dipole moment in NH_3 when binding the ion and hence strengthens the complex. The original AM1 model of Mg[249] largely overestimates the binding energy of the clusters (see Tables 5.2 and 5.5). The optimized AM1/Mg and RM1/Mg models show error in binding energies that are only 6.3 and 6.7 kcal/mol, respectively. The optimized models for Ca similarly show low errors in binding energies, valued at an average of 6.3 kcal/mol for the AM1/Ca model and 5.8 for the RM1/Ca model.

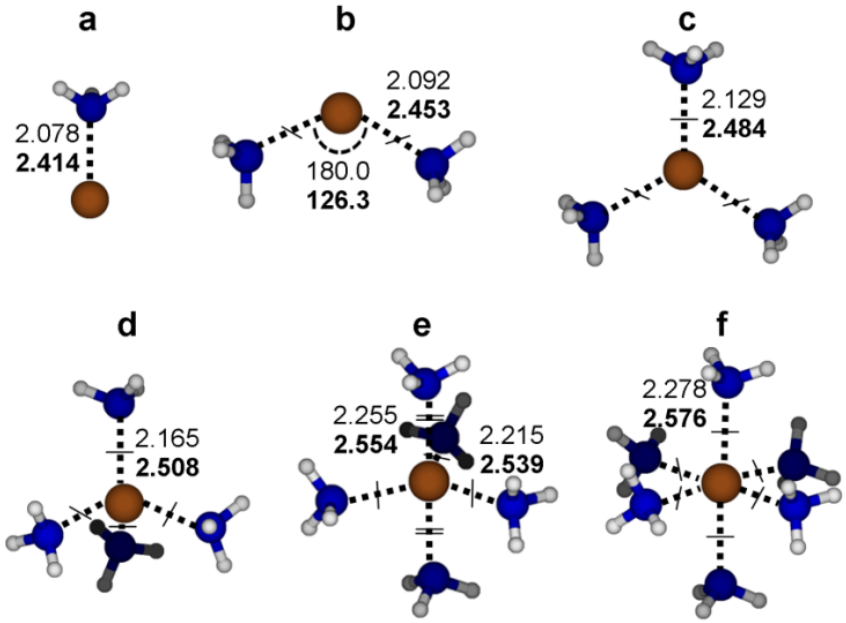

Figure 5.6. Optimized geometries of the binary complexes of Mg^{2+} and Ca^{2+} with ammonia along with important geometrical parameters as computed at the MP2(FC)/6-311++G(d,p) level of theory. Illustrated structures and the parameters in bold are for Ca^{2+}. All distances are in Å.

Table 5.5. Binding energies (in kcal/mol) for $M^{2+}(NH_3)_m$ complexes (M = Mg or Ca, and m = 1–6) calculated at the MP2(FC)/6-311++G(d,p) level (E and E^{CP}) and with SE models.

m	Mg^{2+}					Ca^{2+}			
	Ab initio		SE			Ab initio		SE	
	E	E^{CP}	AM1*	AM1	RM1	E	E^{CP}	AM1	RM1
1	–95.3	–92.6	–95.3	–89.4	–89.7	–64.1	–62.0	–61.1	–60.2
2	–178.4	–172.6	–183.1	–163.6	–168.7	–119.5	–115.4	–116.0	–115.2
3	–241.0	–232.6	–257.3	–222.4	–234.3	–168.2	–161.9	–165.0	–164.8
4	–291.2	–279.6	–320.8	–271.2	–287.3	–210.2	–201.8	–207.1	–207.4
5	–321.1	–306.2	–363.2	–304.5	–317.4	–242.1	–231.1	–242.3	–241.5
6	–348.6	–329.8	–399.2	–335.2	–342.8	–270.4	–256.7	–273.2	–270.4

* Using the AM1 model of Hutter *et al*.[249]

5.3.2.4. $M^{2+}(CH_3NH_2)_m$ Clusters

Geometries of the most stable complexes of Mg^{2+} and Ca^{2+} with up to six methylamine molecules together with important structural properties are reported in Figure 5.7. The complexes are structurally similar to corresponding ion-ammonia complexes but possess shorter ion···N distances and higher binding energies. The binding energies of these clusters calculated from ab initio and SE models are reported in Table 5.6. Similar to what is observed for NH_3, the AM1 model of Mg by Hutter *et al*.[249] overestimates the binding energy of the complexes with an average error of 19.1 kcal/mol. The optimized models of Mg and Ca show a maximum average error in binding energy of 5.2 kcal/mol (see Tables 5.2 and 5.6).

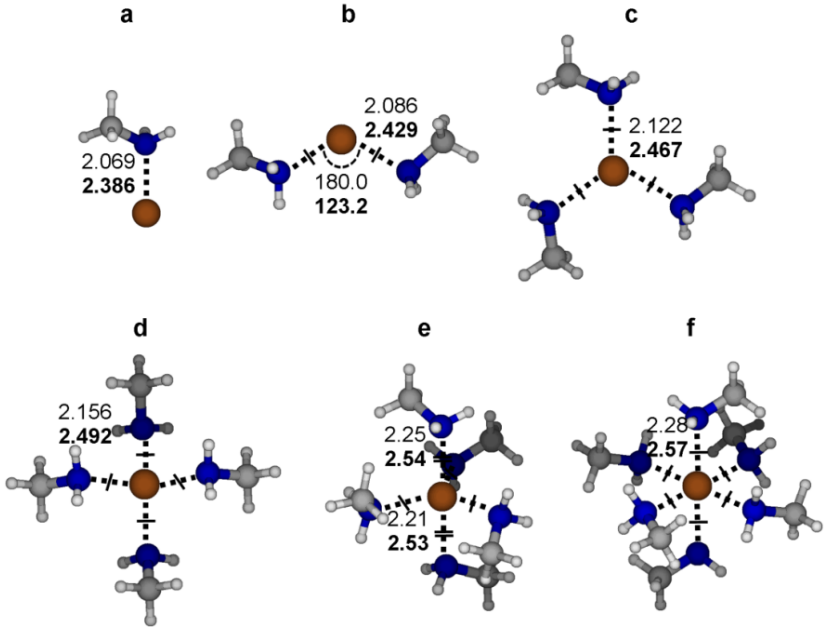

Figure 5.7. Optimized geometries of the binary complexes of Mg^{2+} and Ca^{2+} with methylammine along with important geometrical parameters as computed at the MP2(FC)/6-311++G(d,p) level of theory. Equal separations are indicated with single or double dashes. Illustrated structures and the parameters in bold are for Ca^{2+}. All distances are in Å.

Table 5.6. Binding energies (in kcal/mol) for $M^{2+}(CH_3NH_2)_m$ complexes (M = Mg or Ca, and m = 1–6) calculated at the MP2(FC)/6-311++G(d,p) level (E and E^{CP}) and with SE models.

m	Mg^{2+}					Ca^{2+}			
	Ab initio		SE			Ab initio		SE	
	E	E^{CP}	AM1*	AM1	RM1	E	E^{CP}	AM1	RM1
1	–105.1	–102.7	–99.8	–101.4	–103.7	–70.1	–68.1	–64.1	–65.4
2	–193.2	–187.8	–190.1	–182.2	–189.9	–128.7	–124.8	–120.4	–123.5
3	–257.2	–249.1	–260.5	–243.0	–256.2	–179.1	–173.2	–169.3	–175.1
4	–308.2	–296.6	–321.0	–292.7	–308.4	–222.2	–213.9	–210.3	–218.3
5	–338.2	–322.7	–356.7	–320.5	–329.5	–255.1	–243.6	–242.5	–246.5
6	–366.1	–346.3	–385.9	–343.8	–344.1	–284.1	–269.4	–270.1	–269.1

* Using the AM1 model of Hutter *et al*.[249]

5.3.2.5. $M^{2+}(H_2S)_m$ Clusters

The calculated optimized geometries for complexes of Mg^{2+} and Ca^{2+} with up to six H_2S molecules are given in Figure 5.8. Compared to water, which shows a planar dimer, the dimer of H_2S is characterized by an M···S···Y angle (Y is a point on the bisector of the HSH angle) of 100.5° for Mg^{2+} and of 110.5° for Ca^{2+}. This is likely a consequence of the larger 3p orbitals of sulphur.[262] While $Mg^{2+}(H_2S)_3$ is trigonal planar (Figure 5.8d) and $Mg^{2+}(H_2S)_5$ is trigonal

bipyramidal (Figure 5.8g), $Ca^{2+}(H_2S)_3$ is trigonal pyramidal (Figure 5.8e) and $Ca^{2+}(H_2S)_5$ is tetragonal pyramidal. Binding energies from ab initio and SE calculations are reported in Table 5.7. Compared to water and ammonia, binding energies of H_2S clusters are much lower. H_2S possesses a dipole moment of 0.970 D[261] (smaller than H_2O, 1.850 D, and NH_3, 1.470 D) and a polarizability[211] of 3.631 $Å^3$ (larger than H_2O, 1.501 $Å^3$, and NH_3, 2.103 $Å^3$). This shows that electrostatic (ion-dipole) rather than polarization (ion-induced dipole) forces being the dominant contributor to the ion-ligand interactions. The optimized models for Mg significantly underestimate the ab initio calculated binding energies of all ion-H_2S complexes (see Tables 5.2 and 5.7). Given the fact that Mg^{2+} does not bind S in biological or chemical systems, this likely is not a significant limitation of the model. In comparison the original AM1 model shows a better performance with an average error in binding energy of 14.7 kcal/mol. It should be noted that no S-containing complexes were included in the training set because of the observed formation of disulfide bonds between ligands in large clusters. Optimized models for Ca show however binding energies in very good agreement with MP2 results (see Table 5.7).

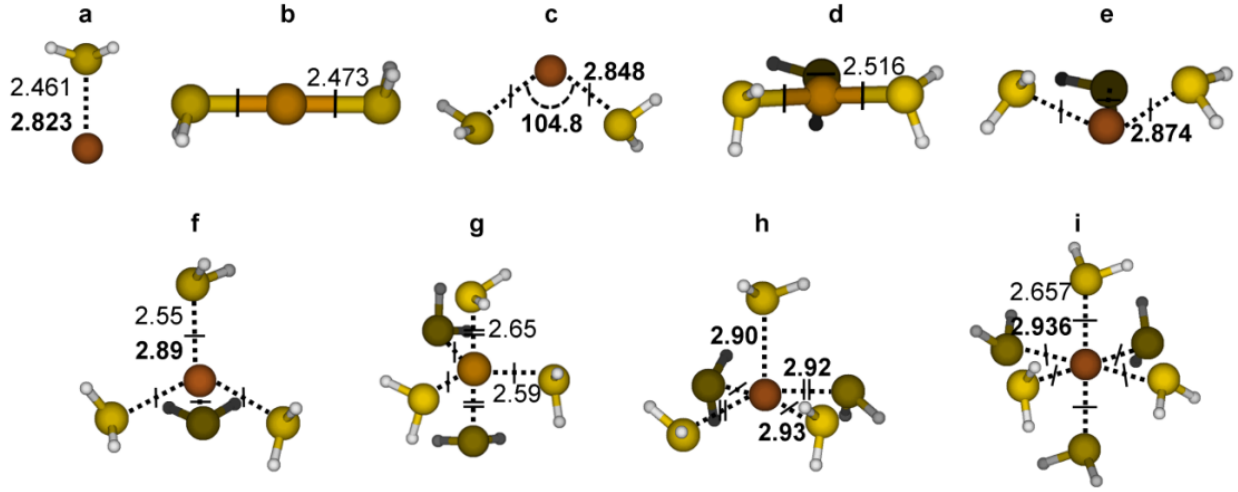

Figure 5.8. Optimized geometries of the binary complexes of Mg^{2+} and Ca^{2+} with hydrogen sulfide along with important geometrical parameters as computed at the MP2(FC)/6-311++G(d,p) level of theory. Structures b, d, and g are for Mg^{2+} and structures c, e, and h are for Ca^{2+}. Structures a, f, and i are reported for Ca^{2+} with parameters of both ions displayed (in bold are parameters of Ca^{2+}). All distances are in Å.

Table 5.7. Binding energies (in kcal/mol) for $M^{2+}(H_2S)_m$ complexes (M = Mg or Ca, and m = 1–6) calculated at the MP2(FC)/6-311++G(d,p) level (E and E^{CP}) and with SE models.

m	Mg^{2+}					Ca^{2+}			
	Ab initio		SE			Ab initio		SE	
	E	E^{CP}	AM1*	AM1	RM1	E	E^{CP}	AM1	RM1
1	–75.3	–72.1	–68.4	–62.4	–54.7	–41.4	–39.4	–39.3	–42.3
2	–137.2	–130.4	–129.5	–98.2	–85.2	–77.3	–73.3	–73.5	–79.9
3	–180.8	–170.5	–177.7	–125.3	–104.4	–109.3	–102.7	–103.9	–111.3
4	–216.4	–201.7	–222.0	–147.8	–118.9	–137.9	–128.3	–129.4	–136.4
5	–237.7	–217.6	–243.7	–171.3	–132.8	–161.7	–148.2	–156.7	–152.7
6	–261.0	–234.3	–264.2	–190.8	–144.5	–185.3	–167.0	–179.6	–166.5

* Using the AM1 model of Hutter *et al*.[249]

5.3.2.6. $M^{2+}(CH_3SH)_m$ Clusters

The optimized geometries for methanethiol complexes with Mg^{2+} and Ca^{2+} (Figure 5.9) are structuraly similar to those of H_2S. Calculated binding energies are shown in Table 5.8. The methyl group results in shorter ion···S distances and in higher binding energies for methanethiol complexes. Similar to H_2S complexes of Mg, the original AM1 model for Mg is superior to the new models in reproducing the binding energies of Mg-CH_3SH complexes (see Tables 5.2 and 5.8). Optimized models for Ca show binding energies in good agreement with MP2 results with the RM1/Ca model being relatively better.

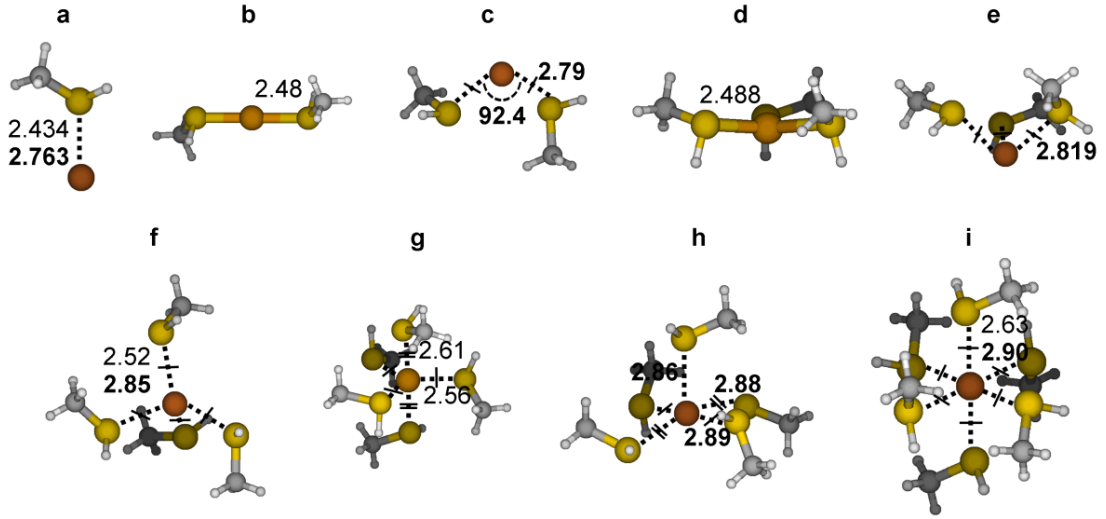

Figure 5.9. Optimized geometries of the binary complexes of Mg^{2+} and Ca^{2+} with methanethiol along with important geometrical parameters as computed at the MP2(FC)/6-311++G(d,p) level. Structures b, d, and g are for Mg^{2+} and structures c, e, and h are for Ca^{2+}. Structures a, f, and i are reported for Ca^{2+} with parameters of both ions displayed (in bold for Ca^{2+}). Distances are in Å.

Table 5.8. Binding energies (in kcal/mol) for $M^{2+}(CH_3SH)_m$ complexes (M = Mg or Ca, and m = 1–6) calculated at the MP2(FC)/6-311++G(d,p) level (E and E^{CP}) and with SE models.[a]

m	Mg^{2+}					Ca^{2+}			
	Ab initio		SE			Ab initio		SE	
	E	E^{CP}	AM1*	AM1	RM1	E	E^{CP}	AM1	RM1
1	–90.6	–87.6	–75.7	–74.4	–71.4	–52.5	–50.6	–44.4	–54.1
2	–161.5	–154.9	–139.0	–114.1	–106.9	–96.4	–92.0	–82.7	–99.9
3	–210.9	–200.6	–188.0	–143.8	–129.6	–135.0	–127.4	–114.6	–137.5
4	–250.8	–235.3	–235.7	–168.6	–147.3	–168.0	–157.7	–140.8	–165.6
5	–277.2	–254.8	–254.2	–190.3	–161.3	–196.7	–181.5	–162.7	–182.7
6	–303.0	–273.9	–271.4	–207.6	–173.9	–223.7	–203.1	–185.3	–197.6

[a] Binding energies for Mg^{2+} complexes are calculated at the ab initio geometries. * Using the AM1 model of Hutter *et al*.[249]

5.3.2.7. $M^{2+}(CH_2O)_m$ Clusters

Optimized geometries for $M^{2+}(CH_2O)_m$ complexes (M = Mg or Ca, m = 1–6) are reported in Figure 5.10. The hexamer complex of both ions is characterized by trigonal bipyramidal geometry (Figure 5.10e). Binding energies calculated at the MP2(FC)/6-311++G(d,p) level and with SE models are given in Table 5.9. These complexes are generally more stable than the corresponding water complexes (see Table 5.3). The performance of the three models of Mg are similar but the new models are slightly better in describing the energy and structure of the complexes (see Tables 5.2 and 5.9). The optimized models for Ca show good agreement in calculated structures and binding energies.

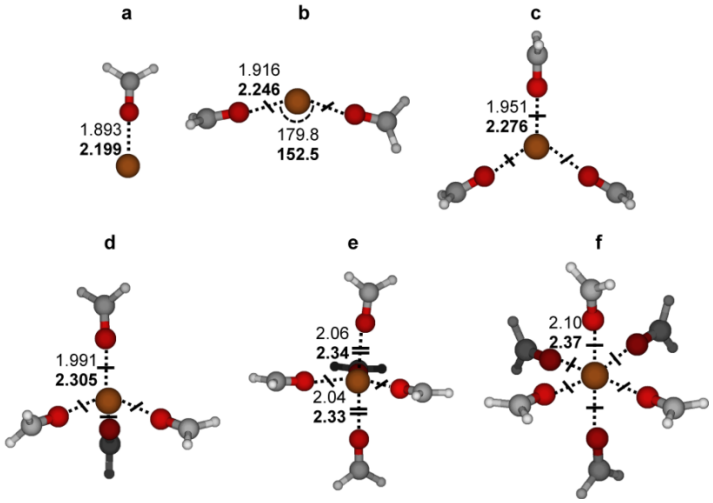

Figure 5.10. Optimized geometries of the binary complexes of Mg^{2+} and Ca^{2+} with formaldehyde along with important geometrical parameters as computed at the MP2(FC)/6-311++G(d,p) level of theory. Structures and parameters in bold are for Ca^{2+}. Distances are in Å.

Table 5.9. Binding energies (in kcal/mol) for $M^{2+}(HCHO)_m$ complexes (M = Mg or Ca, and m = 1–6) calculated at the MP2(FC)/6-311++G(d,p) level (E and E^{CP}) and with SE models.

m	Mg^{2+}					Ca^{2+}			
	Ab initio		SE			Ab initio		SE	
	E	E^{CP}	AM1*	AM1	RM1	E	E^{CP}	AM1	RM1
1	–86.5	–85.3	–79.0	–87.0	–90.2	–62.8	–61.5	–63.7	–58.2
2	–161.4	–158.4	–147.0	–157.8	–161.0	–115.7	–113.3	–119.1	–111.2
3	–218.2	–213.9	–200.5	–212.9	–217.2	–161.3	–157.7	–165.5	–157.3
4	–262.3	–255.8	–247.3	–257.4	–260.0	–199.2	–194.4	–203.5	–196.8
5	–293.7	–283.1	–283.5	–294.0	–293.9	–229.7	–222.5	–232.4	–228.6
6	–325.0	–307.9	–312.9	–324.5	–323.3	–255.5	–245.7	–256.1	–256.1

* Using the AM1 model of Hutter *et al*.[249]

5.3.2.8. $M^{2+}(CH_3CHO)_m$ Clusters

Optimized structures for ion-acetaldehyde complexes are reported in Figure 5.11 and their binding energies from ab initio and SE calculations are shown in Table 5.10. These complexes are characterized by similar structural geometries and higher binding energies compared to corresponding formaldehyde complexes. The original AM1 model of Mg underestimates the binding energies of these complexes with an average error in binding energy of 15.0 kcal/mol. In comparison the new AM1/Mg and RM1/Mg models show only average errors in binding energies of 7.1 and 4.6 kcal/mol. Optimized models for Ca are also accurate in descriping the properties of these complexes (see Tables 5.2 and 5.10).

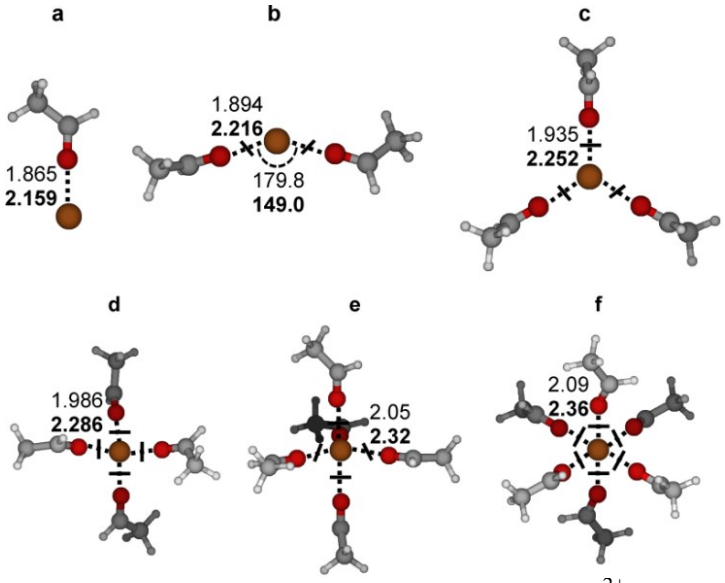

Figure 5.11. Optimized geometries of the binary complexes of Mg^{2+} and Ca^{2+} with acetaldehyde along with important geometrical parameters as computed at the MP2(FC)/6-311++G(d,p) level of theory. Structures and parameters in bold are for Ca^{2+}. All distances are in Å.

Table 5.10. Binding energies (in kcal/mol) for $M^{2+}(CH_3CHO)_m$ complexes (M = Mg or Ca, and m = 1–6) calculated at the MP2(FC)/6-311++G(d,p) level (E and E^{CP}) and with SE models.

m	Mg^{2+}					Ca^{2+}			
	Ab initio		SE			Ab initio		SE	
	E	E^{CP}	AM1*	AM1	RM1	E	E^{CP}	AM1	RM1
1	–102.7	–101.2	–89.1	–97.8	–106.1	–75.3	–73.8	–72.1	–67.5
2	–187.8	–184.1	–163.0	–175.5	–184.5	–135.9	–133.1	–133.4	–128.2
3	–248.8	–243.5	–220.0	–232.7	–244.5	–186.3	–182.1	–183.4	–179.5
4	–295.7	–286.9	–268.5	–279.4	–288.2	–227.0	–221.0	–223.3	–222.4
5	–329.6	–315.2	–305.8	–317.8	–322.7	–258.6	–249.6	–252.6	–256.3
6	–362.0	–341.0	–335.6	–350.8	–353.4	–285.5	–272.3	–275.9	–284.5

* Using the AM1 model of Hutter *et al*.[249]

5.3.2.9. $M^{2+}(HCONH_2)_m$ Clusters

Optimized geometries for Mg^{2+} and Ca^{2+} complexes with formamide together with their characteristic structural properties are provided in Figure 5.12. The hexamer complex of each ion has trigonal bipyramidal geometry (Figure 5.12e). Binding energies from both ab initio and SE calculations are reported in Table 5.11. These complexes are more stable than the corresponding complexes of water and formaldehyde. This is due to resonance in formamide which results in a negative charge on oxygen and hence a strong binding to the metal ions. Hutter *et al*.[249] AM1 model for Mg underestimates the binding energies of the complexes and possesses an average error value of 22.6 kcal/mol. In comparison the new AM1/Mg and RM1/Mg models give average errors of 12.0 and 5.3 kcal/mol. AM1/Ca and RM1/Ca models give binding energies and structures in good agreement with MP2 results (see Table 5.2 and 5.11).

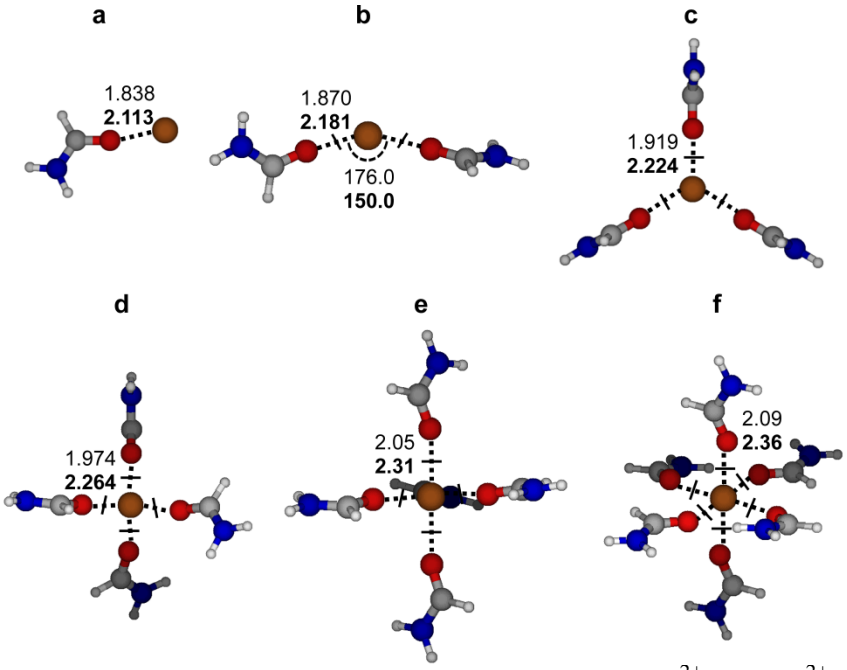

Figure 5.12. Optimized geometries of the binary complexes of Mg^{2+} and Ca^{2+} with formamide along with important geometrical parameters as computed at the MP2(FC)/6-311++G(d,p) level of theory. Structures and parameters in bold are for Ca^{2+}. All distances are in Å.

Table 5.11. Binding energies (in kcal/mol) for $M^{2+}(HCONH_2)_m$ complexes (M = Mg or Ca, and m = 1–6) calculated at the MP2(FC)/6-311++G(d,p) level (E and E^{CP}) and with SE models

m	Mg^{2+}					Ca^{2+}			
	Ab initio		SE			Ab initio		SE	
	E	E^{CP}	AM1*	AM1	RM1	E	E^{CP}	AM1	RM1
1	–125.5	–123.8	–104.8	–112.9	–123.8	–94.3	–92.7	–86.7	–80.3
2	–226.0	–221.8	–189.9	–200.3	–212.1	–166.9	–163.9	–159.2	–150.9
3	–293.3	–287.2	–252.8	–265.3	–276.1	–224.1	–219.6	–216.4	–208.7
4	–343.9	–333.9	–307.4	–318.6	–326.0	–268.4	–262.1	–260.6	–255.5
5	–376.7	–360.6	–346.9	–361.5	–358.8	–299.5	–289.9	–291.0	–290.0
6	–411.2	–387.9	–377.5	–389.1	–386.9	–328.9	–313.4	–315.2	–318.7

* Using the AM1 model of Hutter *et al*.[249]

5.3.2.10. $M^{2+}(CH_3CONH_2)_m$ Clusters

Minimum-energy conformers for clusters formed between Mg^{2+} and Ca^{2+} and up to six acetamide molecules are shown in Figure 5.13 and their binding energies are given in Table 5.12. The AM1 model of Hutter *et al*.[249] results in an average error in binding energy of 25.0 kcal/mol, compared to average values of 11.6 and 5.4 kcal/mol for the AM1/Mg and RM1/Mg models optimized in this work. AM1/Ca and RM1/Ca models give average error in binding energies of 6.0 and 9.6 kcal/mol

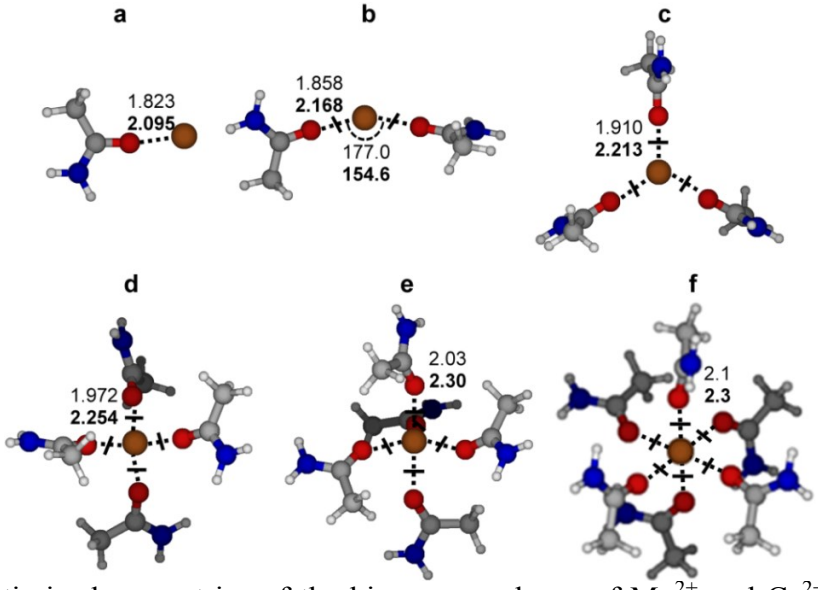

Figure 5.13. Optimized geometries of the binary complexes of Mg^{2+} and Ca^{2+} with acetamide along with important geometrical parameters as computed at the MP2(FC)/6-311++G(d,p) level. For the heptamer complex, the geometry is optimized at the B3LYP/6-311++G(d,p) level. Structures and parameters in bold are for Ca^{2+}. Distances are in Å.

Table 5.12. Binding energies (in kcal/mol) for $M^{2+}(CH_3CONH_2)_m$ complexes (M = Mg or Ca, and m = 1–6) calculated at the MP2(FC)/6-311++G(d,p) level (E and E^{CP}) and with SE models. For the heptamer complexes, binding energies are calculated at the MP2(FC)/6-311++G(d,p)//B3LYP/6-311++G(d,p) level.

m	Mg^{2+}					Ca^{2+}			
	Ab initio		SE			Ab initio		SE	
	E	E^{CP}	AM1*	AM1	RM1	E	E^{CP}	AM1	RM1
1	–134.5	–132.8	–109.5	–118.3	–131.2	–101.9	–100.2	–90.8	–85.2
2	–240.0	–235.9	–198.8	–212.2	–223.5	–178.2	–175.0	–166.2	–159.8
3	–308.7	–302.4	–269.8	–283.7	–290.4	–237.4	–232.6	–224.8	–220.1
4	–360.5	–348.6	–324.2	–342.9	–344.0	–282.7	–275.6	–269.3	–268.4
5	–393.4	–373.7	–354.3	–377.1	–374.1	–315.4	–302.4	–301.2	–304.2
6	–432.7	–407.1	–393.7	–410.6	–408.4	–346.0	–328.1	–330.5	–333.8

* Using the AM1 model of Hutter *et al*.[249]

5.3.2.11. $M^{2+}(imidazole)_m$ Clusters

Optimized structures of the complexes of the two ions with up to five imidazole molecules are reported in Figure 5.14. The binding energies of the various complexes from ab initio and SE calculations are shown in Table 5.13. The data shows that all complexes are more stable than the corresponding ion-water clusters. While the AM1 model of Mg optimized in this work shows the pest performance in reproducing the binding energies of the different complexes (average error = 3.7 kcal/mol), the optimized RM1 model overestimate the binding energies with an average error of 19.7 kcal/mol. In comparison the original AM1 model shows a reasonable performance with an average error of 10.0 kcal/mol. Models for Ca show results in agreement with ab initio calculations (see Tables 5.2 and 5.13).

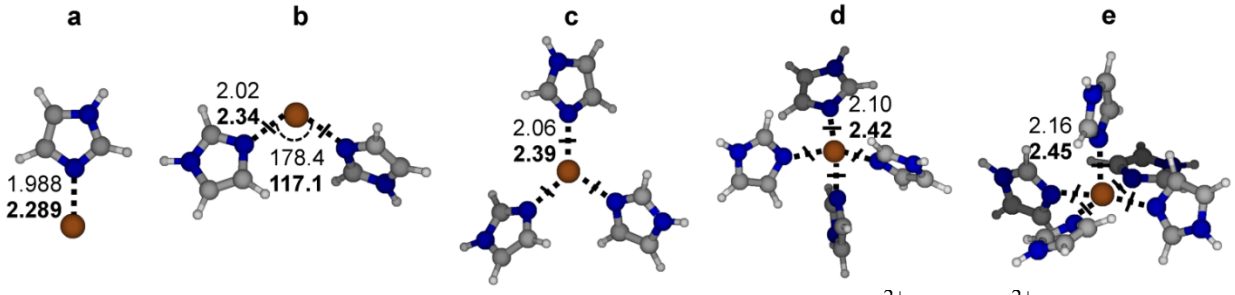

Figure 5.14. Optimized geometries of the binary complexes of Mg^{2+} and Ca^{2+} with imidazole along with important geometrical parameters as computed at the MP2(FC)/6-311++G(d,p) level of theory. Structures and parameters in bold are for Ca^{2+}. Distances are in Å.

Table 5.13. Binding energies (in kcal/mol) for $M^{2+}(imidazole)_m$ complexes (M = Mg or Ca, and m = 1–6) calculated at the MP2(FC)/6-311++G(d,p) level (E and E^{CP}) and with SE models.

m	Mg^{2+}					Ca^{2+}			
	Ab initio		SE			Ab initio		SE	
	E	E^{CP}	AM1*	AM1	RM1	E	E^{CP}	AM1	RM1
1	–131.3	–129.5	–128.5	–133.9	–140.9	–92.7	–90.9	–93.8	–93.0
2	–235.7	–231.3	–234.7	–234.9	–248.4	–166.0	–162.3	–170.5	–172.0
3	–309.5	–302.4	–313.2	–306.8	–326.5	–227.4	–221.3	–232.0	–236.1
4	–367.5	–355.5	–373.3	–360.1	–382.2	–279.0	–269.1	–279.1	–286.3
5	–408.5	–388.6	–405.5	–387.2	–407.9	–321.6	–305.7	–310.8	–320.5

* Using the AM1 model of Hutter *et al.*[249]

5.3.2.12. M^{2+}(4-methylimidazole)$_m$ Clusters

Complexes of Mg^{2+} and Ca^{2+} with up to four 4-methylimidazole molecules are optimized at the MP2(FC)/6-311++G(d,p) level. Complexes of each ion with five ligand molecules are optimized at the B3LYP/6-311++G(d,p) level. Global minimum structures are reported in Figure 5.15 and their binding energies are given in Table 5.14. The performance of the SE models of Mg follow the same trend observed for complexes of imidazole. Optimized AM1 and RM1 models of Ca give average errors in binding energies of 5.3 and 10.7 kcal/mol.

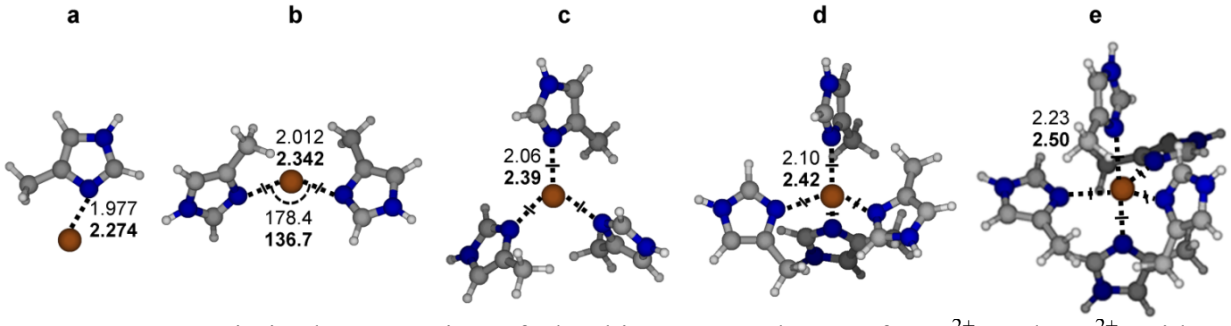

Figure 5.15. Optimized geometries of the binary complexes of Mg^{2+} and Ca^{2+} with 4-methylimidazole along with important geometrical parameters as computed at the MP2(FC)/6-311++G(d,p) level of theory. The hexamer complex of each ion is optimized at the B3LYP/6-311++G(d,p) level. Structures and parameters in bold are for Ca^{2+}.

Table 5.14. Binding energies (in kcal/mol) for M^{2+}(4-methylimidazole)$_m$ complexes (M = Mg or Ca, and m = 1–6) calculated at the MP2(FC)/6-311++G(d,p) level (E and E^{CP}) and with SE models. For the hexamer complexes, binding energies are calculated at the MP2(FC)/6-311++G(d,p)//B3LYP/6-311++G(d,p) level.

m	Mg^{2+}					Ca^{2+}			
	Ab initio		SE			Ab initio		SE	
	E	E^{CP}	AM1*	AM1	RM1	E	E^{CP}	AM1	RM1
1	–139.7	–137.6	–141.1	–143.7	–149.5	–98.9	–96.7	–97.8	–98.0
2	–244.1	–239.2	–251.5	–248.9	–259.6	–174.0	–169.5	–176.6	–179.3
3	–318.3	–309.2	–321.9	–321.1	–337.4	–236.2	–227.8	–237.5	–243.0
4	–377.4	–360.9	–374.5	–369.3	–388.5	–287.8	–274.8	–283.3	–291.5
5	–416.8	–392.7	–400.9	–389.2	–406.2	–331.2	–312.1	–311.8	–322.6

* Using the AM1 model of Hutter *et al*.[249]

5.3.2.13. M^{2+}(5-methylimidazole)$_m$ Clusters

Similar to complexes of 4-methylimidazole, complexes of the ions with 1–4 molecules of 5-methylimidazole are optimized at the MP2(FC)/6-311++G(d,p) level while complexes with 5 molecules of the ligand are optimized at B3LYP/6-311++G(d,p) level. Optimized geometries are given in Figure 5.16 and their binding energies are shown in Table 5.15. Ab initio calculations show that with the exception of the dimer, ion-complexes with 5-methylimidazole are more stable than with 4-methylimidazole. This is due to steric crowding imposed by the methyl groups in large clusters of 4-methylimidazole. Again the optimized AM1 model for Mg is the best among the three models and optimized models of Ca show good agreement with MP2 results.

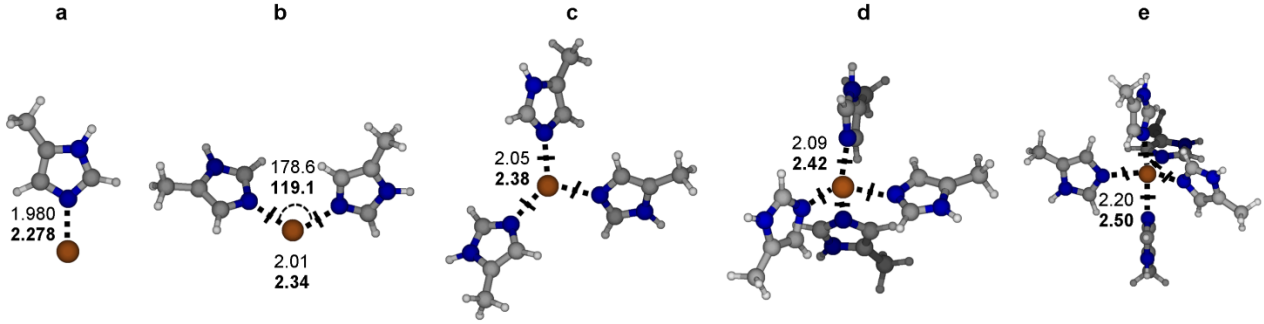

Figure 5.16. Optimized geometries of complexes of Mg^{2+} and Ca^{2+} with 5-methylimidazole along with important geometrical parameters as computed at the MP2(FC)/6-311++G(d,p) level of theory. The hexamer complex of each ion is optimized at the B3LYP/6-311++G(d,p) level. Structures and parameters in bold are for Ca^{2+}. Distances are in Å.

Table 5.15. Binding energies (in kcal/mol) for M^{2+}(5-methylimidazole)$_m$ complexes (M = Mg or Ca, and m = 1–6) calculated at the MP2(FC)/6-311++G(d,p) level (E and E^{CP}) and with SE models. For the hexamer complexes, binding energies are calculated at the MP2(FC)/6-311++G(d,p)//B3LYP/6-311++G(d,p) level.

m	Mg^{2+}					Ca^{2+}			
	Ab initio		SE			Ab initio		SE	
	E	E^{CP}	AM1*	AM1	RM1	E	E^{CP}	AM1	RM1
1	–137.6	–135.8	–132.0	–137.5	–147.5	–98.0	–96.2	–96.6	–97.6
2	–245.6	–241.1	–240.0	–240.2	–254.9	–174.3	–170.6	–175.2	–180.0
3	–321.2	–314.0	–319.1	–312.7	–333.3	–237.7	–231.4	–237.3	–246.1
4	–380.3	–367.9	–379.4	–366.4	–389.8	–290.5	–279.8	–284.3	–297.1
5	–420.4	–401.1	–411.3	–393.3	–415.4	–332.8	–317.6	–317.1	–332.5

* Using the AM1 model of Hutter *et al*.[249]

5.3.2.14. $M^{2+}(HCOO^{-})_m$ Clusters

Optimized geometries for the complexes between Mg^{2+} and Ca^{2+} and the formate ion are shown in Figure 5.17 and their binding energies are given in Table 5.16. While the formate ion binds the metal ions in the dimer, trimer, and tetramer complexes in a bidentate fashion, it binds them in unidentate geometry in larger clusters. Table 5.15 shows that while adding the second and third formate ion increases the stability of the complex, further addition of the ion destabilizes the complex. For example while going from the dimer to the tetramer increases the binding energy by 209.5 kcal/mol for Mg^{2+} and by 178.6 kcal/mol for Ca^{2+}, going from the tetramer to the pentamer decreases the binding energy by 30.4 kcal/mol for Mg^{2+} and by 33.0 kcal/mol for Ca^{2+}. The binding energy of the heptamer is lower even than the dimer. Beyond the second formate ion, a net negative charge develops and electrostatic repulsion between the ligand and the negatively charged complex destabilizes the complex. The new AM1 and RM1 models of Mg and the original AM1 model of Hutter *et al*.[249] give average errors in binding energies of 2.6, 5.3, and 10.4 kcal/mol, respectively. The average error in binding energies for optimized Ca models is 15.4 kcal/mol for the AM1/Ca model and 8.6 kcal/mol for the RM1Ca model.

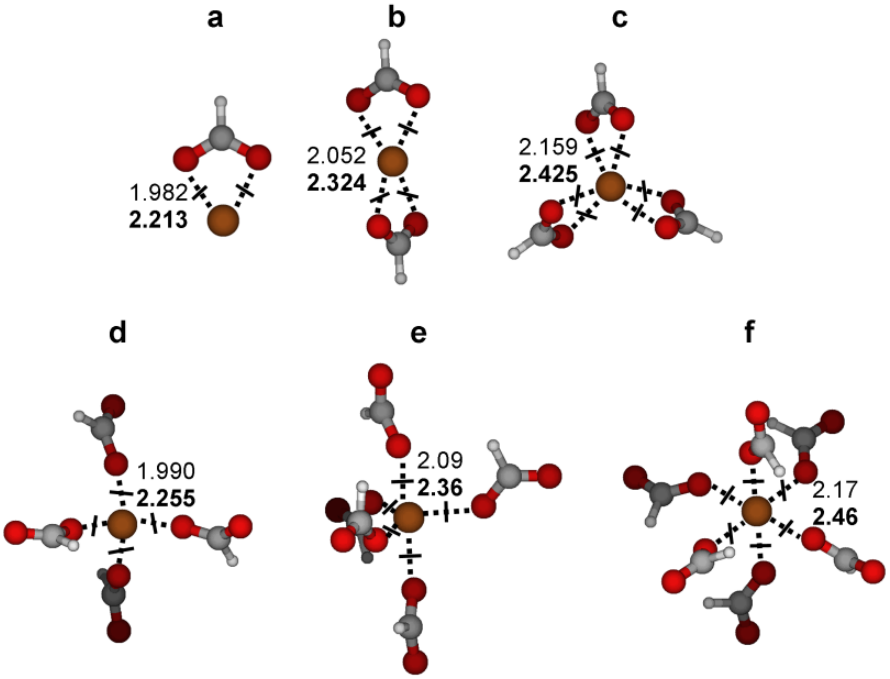

Figure 5.17. Optimized geometries of the binary complexes of Mg^{2+} and Ca^{2+} with formate ion along with important geometrical parameters as computed at the MP2(FC)/6-311++G(d,p) level of theory. Structures and parameters in bold are for Ca^{2+}. All distances are in Å.

Table 5.16. Binding energies (in kcal/mol) for $M^{2+}(HCOO^{-})_m$ complexes (M = Mg or Ca, and m = 1–6) calculated at the MP2(FC)/6-311++G(d,p) level (E and E^{CP}) and with SE models.

m	Mg^{2+}					Ca^{2+}			
	Ab initio		SE			Ab initio		SE	
	E	E^{CP}	AM1*	AM1	RM1	E	E^{CP}	AM1	RM1
1	–361.6	–356.8	–356.5	–359.6	–361.8	–308.1	–304.1	–310.1	–302.5
2	–576.7	–566.3	–574.8	–566.6	–567.0	–489.9	–482.7	–505.6	–499.6
3	–639.8	–623.9	–643.9	–629.0	–625.9	–557.0	–546.1	–573.2	–570.9
4	–606.7	–593.5	–600.5	–592.9	–604.5	–520.8	–513.1	–526.6	–514.7
5	–515.7	–497.6	–511.4	–503.0	–507.0	–440.4	–428.4	–444.9	–433.5
6	–368.0	–344.8	–355.6	–346.1	–340.9	–303.8	–288.5	–294.6	–287.1

* Using the AM1 model of Hutter *et al*.[249]

5.3.2.15. $M^{2+}(CH_3COO^{-})_m$ Clusters

Minimum-energy structures for the complexes of Mg^{2+} and Ca^{2+} with up to six acetate ions are given in Figure 5.18 and their binding energies from ab initio and SE calculations are reported in Table 5.17. The three SE models for Mg and the two models of Ca have similar performance on energies and structures of the clusters (see Tables 5.2 and 5.17).

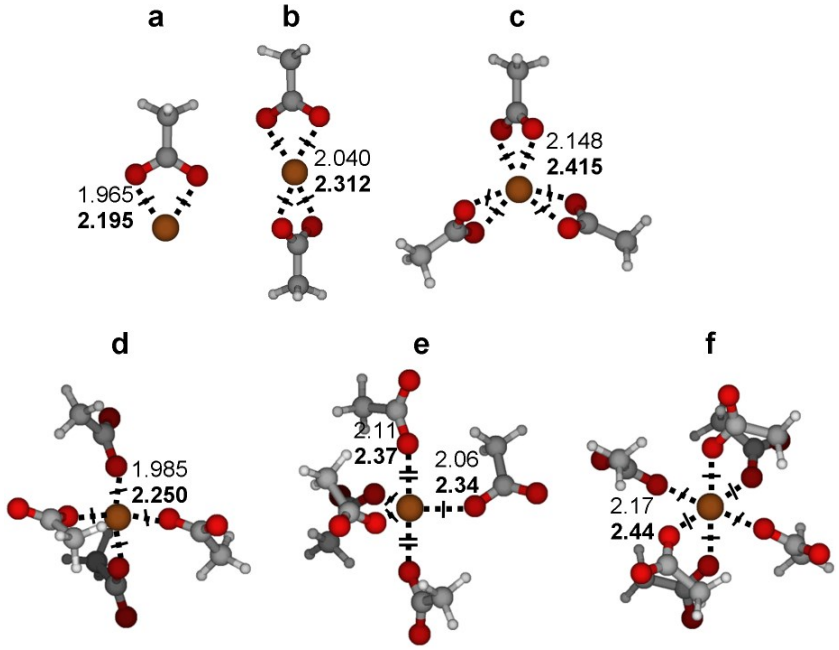

Figure 5.18. Optimized geometries of the binary complexes of Mg^{2+} and Ca^{2+} with acetate ion along with important geometrical parameters as computed at the MP2(FC)/6-311++G(d,p) level of theory. Structures and parameters in bold are for Ca^{2+}. All distances are in Å.

Table 5.17. Binding energies (in kcal/mol) for $M^{2+}(CH_3COO^-)_m$ complexes (M = Mg or Ca, and m = 1–6) calculated at the MP2(FC)/6-311++G(d,p) level (E and E^{CP}) and with SE models.

m	Mg^{2+}					Ca^{2+}			
	Ab initio		SE			Ab initio		SE	
	E	E^{CP}	AM1*	AM1	RM1	E	E^{CP}	AM1	RM1
1	–372.4	–367.4	–358.9	–361.6	–362.0	–317.3	–313.1	–313.2	–304.2
2	–587.5	–576.7	–574.4	–567.7	–564.6	–499.0	–491.6	–507.9	–499.9
3	–647.7	–630.8	–640.2	–628.6	–621.6	–564.0	–552.7	–573.4	–569.7
4	–615.5	–599.3	–606.9	–609.3	–609.2	–526.8	–517.4	–529.2	–516.7
5	–525.7	–502.9	–505.4	–510.2	–504.2	–452.0	–435.9	–446.4	–436.4
6	–387.2	–357.2	–346.9	–351.4	–350.1	–324.8	–302.3	–301.6	–293.3

* Using the AM1 model of Hutter *et al*.[249]

The ab initio calculated binding energies of the different ion-ligand pairs are in good agreement with reported data. Suárez *et al*.[263] calculated the binding energy of some Ca^{2+} dimers at the CCSD(T)(FC)/aug-cc-pVTZ//MP2(FC)/aug-cc-pVTZ level and reported BSSE-uncorrected binding energies of E = –57.0 kcal/mol for Ca^{2+}–water dimer, E = –67.6 kcal/mol for the Ca^{2+}–methanol pair, E = –65.9 kcal/mol for the Ca^{2+}–ammonia pair, E = –73.3 kcal/mol for the Ca^{2+}-–methylamine dimer, E = –45.6 for Ca^{2+}–hydrogen sulfide dimer, E = –57.6 kcal/mol for Ca–methanethiol dimer, E = –67.6 kcal/mol for Ca^{2+}–formaldehyde dimer, E = –96.6 kcal/mol for Ca–formamide dimer, E = –104.3 kcal/mol for the Ca–acetamide dimer, E = –98.1 kcal/mol for the Ca^{2+}–imidazole dimer, E = –316.1 for Ca^{2+}–formate dimer, and a value of E = –324.2 for Ca^{2+}–acetate dimer. These values are generally in good agreement with the calculated binding energies at the MP2(FC)/6-311++G(d,p) in this work.

5.3.3. Optimized Geometries of Ternary Complexes

The geometry of ternary complexes having the general composition $M^{2+}L_m(H_2O)_n$ (M = Mg or Ca, L = ligand other than water, imidazole, 4-methylimidazole, and 5-methylimidazole, *m* = 1–5, and *n* = 6–*m*) are optimized at the MP2(FC)/6-311++G(d,p) level of theory. These complexes are generated by subsequent substitution of ligands in the heptamer complex ($M^{2+}L_6$) with water molecules. Two structures are optimized for the $M^{2+}L_4(H_2O)_2$ complex with water molecules arranged in a linear or bent conformation. Water molecules in $M^{2+}L_3(H_2O)_3$ complexes are oriented around the ion in either T-shaped or triangular configurations. Two conformations are optimized for $M^{2+}L_2(H_2O)_4$ complexes, with water molecules arranged in a square planar or seesaw geometries. For ternary complexes involving imidazole, 4-methylimidazole, and 5-methylimidazole, the hexamer complex $M^{2+}L_m(H_2O)_n$ (*m* = 1–4, and *n* = 5–*m*) are considered. Again structures are generated by replacing the ligand by water molecules and two structures that differ in the position of water molecules around the ion are optimized for each complex. Ternary hexamer clusters containing four molecules of 4-methylimidazole or of 5-methylimidazole are optimized at the B3LYP/6-311++G(d,p). Other ternary complexes are optimized at the MP2(FC)/6-311++G(d,p) level.

In all complexes, binding energies without and with correction for BSSE are calculated at the MP2(FC)/6-311++G(d,p) level. Like observed for the binary clusters, ternary clusters of Mg^{2+} are more stable and possess shorter cation···ligand separations than the corresponding Ca^{2+} complexes. Results are also showing that the changes in binding energies when ligands are replaced by water molecules are similar for Mg^{2+} and Ca^{2+} complexes. For example while replacing a single methanol molecule in the $Mg^{2+}(CH_3OH)_6$ complex by water reduces the binding energy by 3.9 kcal/mol, it reduces it by 3.4 kcal/mol for the $Ca^{2+}(CH_3OH)_6$ complex. This is attributed to the comparable affinity of both ions toward a given ligand at high ion's coordination numbers. Similar to binary complexes, ternary complexes containing the methylated ligands are more stable than their corresponding "simple" ligands. Results are also showing that for a given complex composition, the binding energy of the cluster is almost independent on ligand arrangements. For example while the $Mg^{2+}(CH_3OH)_4(H_2O)_2$ complex display a binding energy of E^{CP}= –321.6 kcal/mol for the conformer with linear arrangements of water molecules arround the metal ion, it displays E^{CP}= –321.8 kcal/mol for the structure with bent arrangement.

5.3.3.1. $M^{2+}(CH_3OH)_m(H_2O)_n$ Clusters

The optimized geometries of the ternary complexes of Mg^{2+} and Ca^{2+} with water and methanol are reported in Figure 5.19 and their calculated binding energies are given in Table 5.18. For comparison, the structures and binding energies of the binary heptamers are also presented. In all Mg^{2+} complexes, $Mg^{2+}\cdots$O(methanol) distance is ~2.10 Å and $Mg^{2+}\cdots$O(water) distance is ~2.12 Å. For Ca^{2+} complexes, $Ca^{2+}\cdots$O(methanol) distance is ~2.38 and $Ca^{2+}\cdots$O(water) distance is ~2.42 Å. It is shown that the binding energy decreases (become less negative) as methanol molecules are replaced by water molecules. It is also shown that complexes that only differ in conformation are almost isoenergetic (i.e. possess similar binding energies). The properties of Mg complexes are best reproduces by the new models optimized in this work (see Tables 5.2 and 5.18). The original AM1 model shows binding energies for the complexes that are almost unaffected by the composition and gives an average error of 19.1 kcal/mol. Table 5.2 is showing that while the AM1 model of Ca shows slightly lower average error in binding energy compared to the RM1 model, the latter better reproduce the geometry of the clusters.

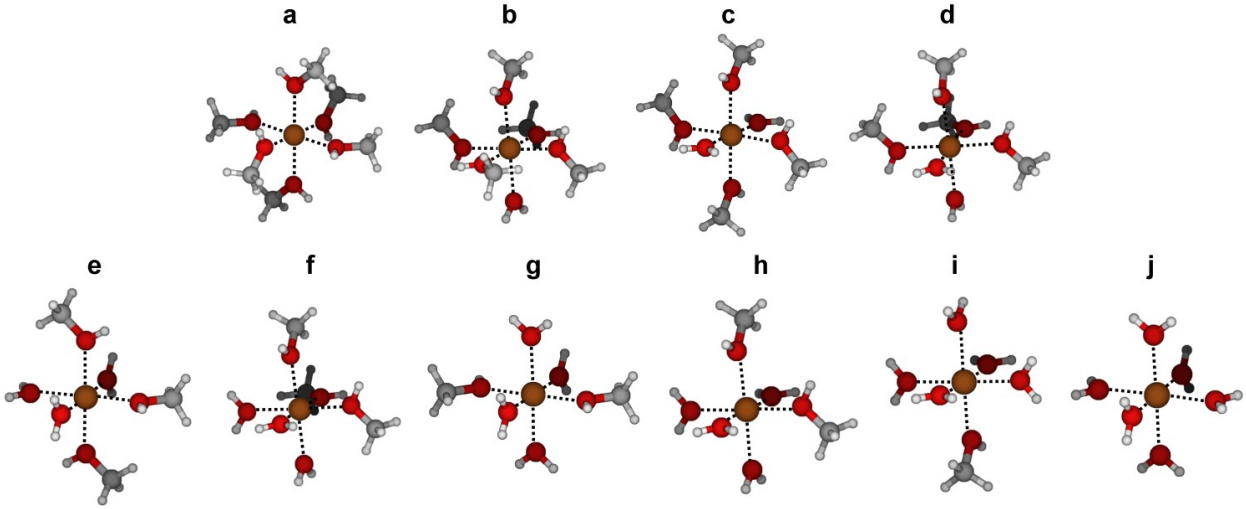

Figure 5.19. Optimized geometries of the ternary complexes of Mg^{2+} and Ca^{2+} with water and methanol as computed at the MP2(FC)/6-311++G(d,p) level of theory. Structures of the binary heptamers (panels a and j) are also shown. Structures are illustrated with Ca^{2+} complexes.

Table 5.18. Binding energies (in kcal/mol) for $M^{2+}(CH_3OH)_m(H_2O)_n$ complexes (M = Mg or Ca, m = 0–6, and n = 6–m) calculated at the MP2(FC)/6-311++G(d,p) level (E and E^{CP}) and with SE models.

structure	m	n	Mg^{2+}					Ca^{2+}			
			Ab initio		SE			Ab initio		SE	
			E	E^{CP}	AM1*	AM1	RM1	E	E^{CP}	AM1	RM1
a	6	0	–352.4	–329.6	–299.8	–327.3	–311.2	–277.5	–260.4	–241.4	–240.5
b	5	1	–347.9	–325.7	–299.3	–323.3	–311.0	–273.7	–257.0	–241.4	–239.8
c	4	2	–343.4	–321.6	–299.5	–319.0	–308.7	–269.7	–253.4	–241.4	–238.9
d	4	2	–343.7	–321.8	–299.3	–319.3	–309.5	–270.0	–253.5	–241.0	–239.0
e	3	3	–339.1	–317.6	–299.3	–315.3	–306.3	–266.0	–249.9	–240.3	–238.1
f	3	3	–339.3	–317.8	–298.7	–314.7	–307.2	–266.1	–250.0	–239.7	–238.2
g	2	4	–334.6	–313.5	–298.3	–310.6	–302.7	–262.0	–246.3	–238.7	–237.2
h	2	4	–334.8	–313.6	–297.1	–309.5	–304.2	–262.1	–246.3	–239.4	–237.3
i	1	5	–330.4	–309.4	–296.3	–304.8	–300.8	–258.3	–242.7	–238.9	–236.4
j	0	6	–325.9	–305.1	–295.5	–300.0	–297.3	–254.3	–238.9	–237.1	–235.4

* Using the AM1 model of Hutter *et al*.[249]

5.3.3.2. $M^{2+}(NH_3)_m(H_2O)_n$ Clusters

Figure 5.20 shows the optimized geometries of ternary complexes formed between each metal ion with ammonia and water molecules. In all Mg^{2+} complexes, the $Mg^{2+}\cdots N$ distances are 2.20–2.28 Å and the $Mg^{2+}\cdots O$ distances are between 2.11–2.21 Å. For Ca^{2+} complexes, $Ca^{2+}\cdots N$ distances are 2.53–2.58 Å and $Ca^{2+}\cdots O$ distances are 2.40–2.45 Å. Calculated binding energies of the various structures are reported in Table 5.19. Again the binding energy decreases as ammonia molecules are replaced with water. Properties of the different complexes are reproduced by the new models of Mg and Ca (see Table 5.2 and 5.19). In comparison the AM1 model of Hutter *et al*.[249] shows an average error in binding energy of 33.6 kcal/mol.

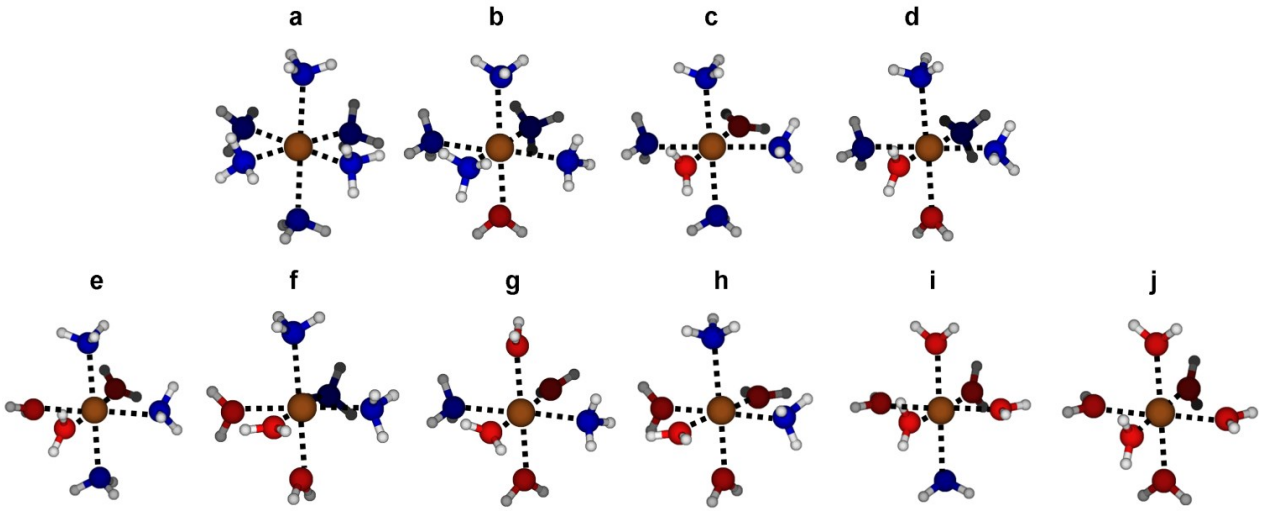

Figure 5.20. Optimized geometries of the $M^{2+}(NH_3)_m(H_2O)_n$ complexes (M = Mg or Ca, m = 0–6, and n = 6–m) calculated at the MP2(FC)/6-311++G(d,p) level. Structures are illustrated with Ca^{2+} complexes.

Table 5.19. Binding energies (in kcal/mol) for $M^{2+}(NH_3)_m(H_2O)_n$ complexes (M = Mg or Ca, m = 0–6, and n = 6–m) calculated at the MP2(FC)/6-311++G(d,p) level (E and E^{CP}) and with SE models.

structure	m	n	Mg^{2+}					Ca^{2+}			
			Ab initio		SE			Ab initio		SE	
			E	E^{CP}	AM1*	AM1	RM1	E	E^{CP}	AM1	RM1
a	6	0	–348.6	–329.8	–399.2	–335.2	–342.8	–270.4	–256.7	–273.2	–270.4
b	5	1	–344.6	–325.8	–384.4	–330.8	–336.2	–267.4	–253.7	–268.2	–266.3
c	4	2	–340.7	–321.8	–366.4	–325.1	–328.7	–264.5	–250.8	–262.5	–261.1
d	4	2	–341.0	–321.9	–369.4	–326.8	–329.6	–264.7	–250.9	–262.8	–261.5
e	3	3	–336.5	–317.1	–351.0	–320.3	–321.7	–261.6	–247.7	–257.2	–255.8
f	3	3	–337.8	–318.3	–354.9	–323.8	–323.4	–262.4	–248.2	–257.5	–256.1
g	2	4	–332.0	–312.2	–330.6	–313.4	–313.0	–258.6	–244.4	–250.4	–249.5
h	2	4	–333.5	–313.6	–335.9	–317.1	–315.3	–259.4	–245.0	–250.3	–249.6
i	1	5	–329.6	–309.2	–316.3	–309.1	–306.6	–256.7	–241.9	–243.8	–242.8
j	0	6	–325.9	–305.1	–295.5	–300.0	–297.3	–254.3	–238.9	–237.1	–235.4

* Using the AM1 model of Hutter *et al*.[249]

5.3.3.3. $M^{2+}(CH_3NH_2)_m(H_2O)_n$ Clusters

Figure 5.21 shows the optimized geometries of ternary complexes formed between Mg^{2+} and Ca^{2+} with methylamine and water molecules. In all complexes, the $Mg^{2+}\cdots N$, $Mg^{2+}\cdots O$, $Ca^{2+}\cdots N$, and $Ca^{2+}\cdots O$ distances fall in same range listed for ternary complexes of ammonia. Binding energies of the various structures from both ab initio and SE calculations are reported in Table 5.20. Tables 5.2 and 5.20 show that the optimized models for Mg and Ca yield binding energies and structures in agreement with ab initio data. The original AM1 model of Mg overestimates the binding energies of the ternary clusters with an average error of 21.6 kcal/mol.

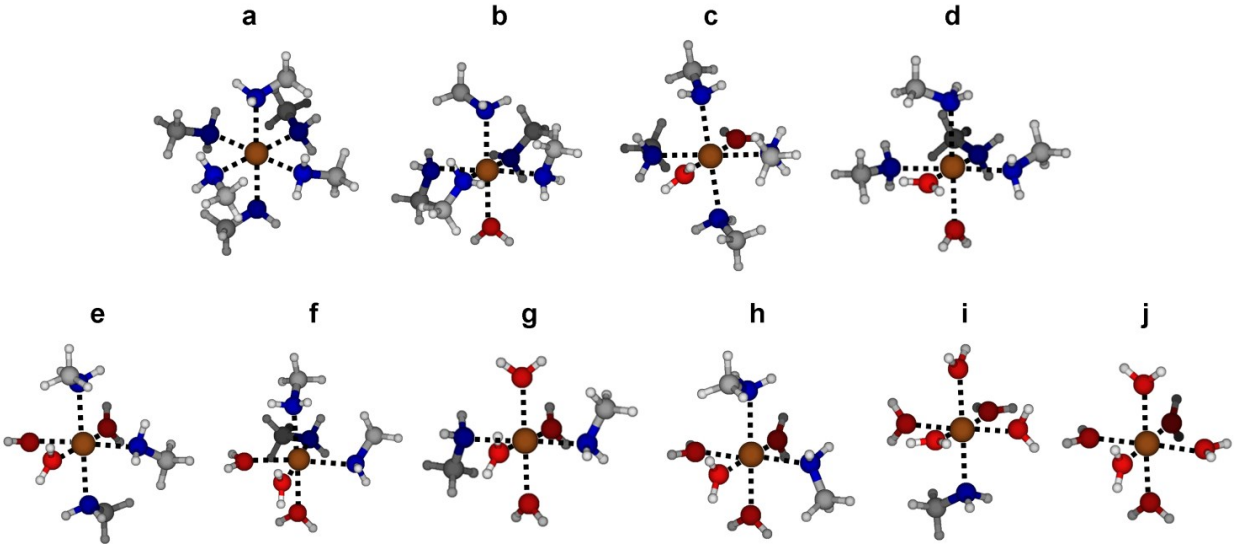

Figure 5.21. Optimized geometries of the $M^{2+}(CH_3NH_2)_m(H_2O)_n$ ternary complexes (M = Mg or Ca, m = 0–6, and n = 6–m) calculated at the MP2(FC)/6-311++G(d,p) level. Structures are illustrated with Ca^{2+} complexes.

Table 5.20. Binding energies (in kcal/mol) for $M^{2+}(CH_3NH_2)_m(H_2O)_n$ complexes (M = Mg or Ca, m = 0–6, and n = 6–m) calculated at the MP2(FC)/6-311++G(d,p) level (E and E^{CP}) and with SE models.

structure	m	n	Mg^{2+}					Ca^{2+}			
			Ab initio		SE			Ab initio		SE	
			E	E^{CP}	AM1*	AM1	RM1	E	E^{CP}	AM1	RM1
a	6	0	–366.1	–346.3	–385.9	–343.8	–344.1	–284.1	–269.4	–270.1	–269.1
b	5	1	–359.4	–339.6	–375.0	–341.8	–341.2	–278.9	–264.4	–266.9	–268.3
c	4	2	–351.7	–332.0	–360.6	–335.6	–336.0	–273.3	–258.8	–262.6	–264.7
d	4	2	–353.3	–333.5	–363.9	–338.9	–337.7	–274.0	–259.4	–262.4	–264.2
e	3	3	–345.8	–325.8	–347.3	–331.0	–330.3	–268.7	–254.2	–257.5	–259.7
f	3	3	–347.1	–327.2	–352.2	–335.2	–331.9	–269.6	–254.9	–258.6	–260.3
g	2	4	–338.7	–318.4	–331.2	–320.3	–319.0	–263.4	–248.8	–251.7	–252.8
h	2	4	–339.7	–319.6	–335.3	–326.5	–323.0	–264.2	–249.5	–252.2	–253.3
i	1	5	–332.6	–312.2	–315.9	–314.3	–311.1	–259.2	–244.2	–245.8	–244.9
j	0	6	–325.9	–305.1	–295.5	–300.0	–297.3	–254.3	–238.9	–237.1	–235.4

* Using the AM1 model of Hutter *et al*.[249]

5.3.3.4. $M^{2+}(H_2S)_m(H_2O)_n$ Clusters

Optimized geometries of heptamer complexes formed between Mg^{2+} or Ca^{2+} and hydrogen sulfide and water are presented in Figure 5.22 and their binding energies are listed in Table 5.21. The structures are characterized by separations of ~2.66 Å for $Mg^{2+}\cdots S$, ~2.11 Å for $Mg^{2+}\cdots O$, ~2.96 Å for $Ca^{2+}\cdots S$, and ~2.38 Å for $Ca^{2+}\cdots O$. The weak binding affinity between the ions and H_2S compared to H_2O, results in increase of binding energy as H_2S moelcules get replaced by H_2O. As observed for binary complexes of H_2S, the original AM1 model of Mg is relatively better in describing the binding energies of these ternary complexes. Optimized SE models for Ca give low average errors in binding energies of the ternary complexes (see Tables 5.2 and 5.21).

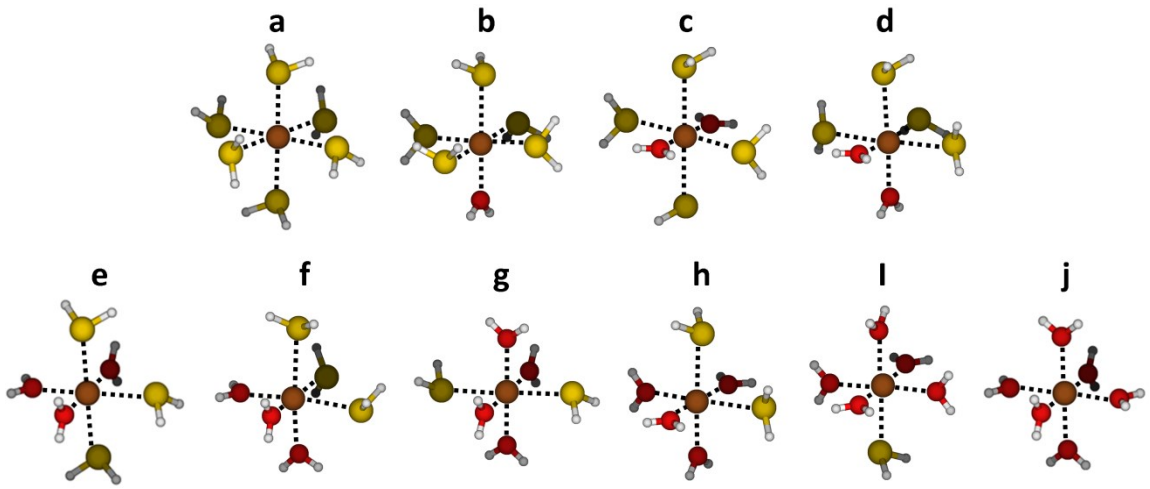

Figure 5.22. Optimized geometries of the $M^{2+}(H_2S)_m(H_2O)_n$ ternary complexes (M = Mg or Ca, m = 0–6, and n = 6–m) calculated at the MP2(FC)/6-311++G(d,p) level. Structures are illustrated with Ca^{2+} complexes.

Table 5.21. Binding energies (in kcal/mol) for $M^{2+}(H_2S)_m(H_2O)_n$ complexes (M = Mg or Ca, m = 0–6, and n = 6–m) calculated at the MP2(FC)/6-311++G(d,p) level (E and E^{CP}) and with SE models.

structure	m	n	Mg^{2+}					Ca^{2+}			
			Ab initio		SE			Ab initio		SE	
			E	E^{CP}	AM1*	AM1	RM1	E	E^{CP}	AM1	RM1
a	6	0	–261.0	–234.3	–264.2	–190.8	–144.5	–185.3	–167.0	–179.6	–166.5
b	5	1	–271.5	–245.7	–260.2	–202.7	–160.6	–197.4	–179.5	–187.9	–175.1
c	4	2	–281.9	–257.0	–259.6	–215.3	–177.1	–209.4	–191.9	–192.2	–183.9
d	4	2	–282.7	–257.7	–260.6	–216.2	–178.5	–209.2	–191.8	–197.4	–186.2
e	3	3	–293.0	–269.0	–264.2	–231.6	–198.6	–221.1	–204.1	–205.3	–196.7
f	3	3	–293.6	–269.5	–265.6	–232.8	–200.0	–221.0	–204.0	–208.7	–198.7
g	2	4	–303.7	–280.8	–269.6	–248.6	–220.9	–232.5	–216.2	–211.3	–206.8
h	2	4	–304.2	–281.2	–271.4	–249.6	–222.1	–232.5	–216.0	–218.6	–210.6
i	1	5	–314.9	–293.0	–279.8	–268.4	–246.6	–243.7	–227.7	–225.6	–222.7
j	0	6	–325.9	–305.1	–295.5	–300.0	–297.3	–254.3	–238.9	–237.1	–235.4

* Using the AM1 model of Hutter *et al*.[249]

5.3.3.5. $M^{2+}(CH_3SH)_m(H_2O)_n$ Clusters

Optimized geometries of heptamer complexes formed between Mg^{2+} or Ca^{2+} and methanethiol and water are presented in Figure 5.23 and their binding energies from ab initio and SE calculations are given in Table 5.22. The ab initio structures are characterized by separations of ~2.62 Å for $Mg^{2+}\cdots S$, ~2.12 Å for $Mg^{2+}\cdots O$, ~2.92 Å for $Ca^{2+}\cdots S$, and ~2.39 Å for $Ca^{2+}\cdots O$.

Similar to H_2S, binding energy increases when water substitutes methanethiol molecules. Again, the original AM1 model of Mg is superior in describing the binding energies of Mg complexes containing methanethiol. Optimized SE models for Ca give results in good agreement with ab initio calculations.

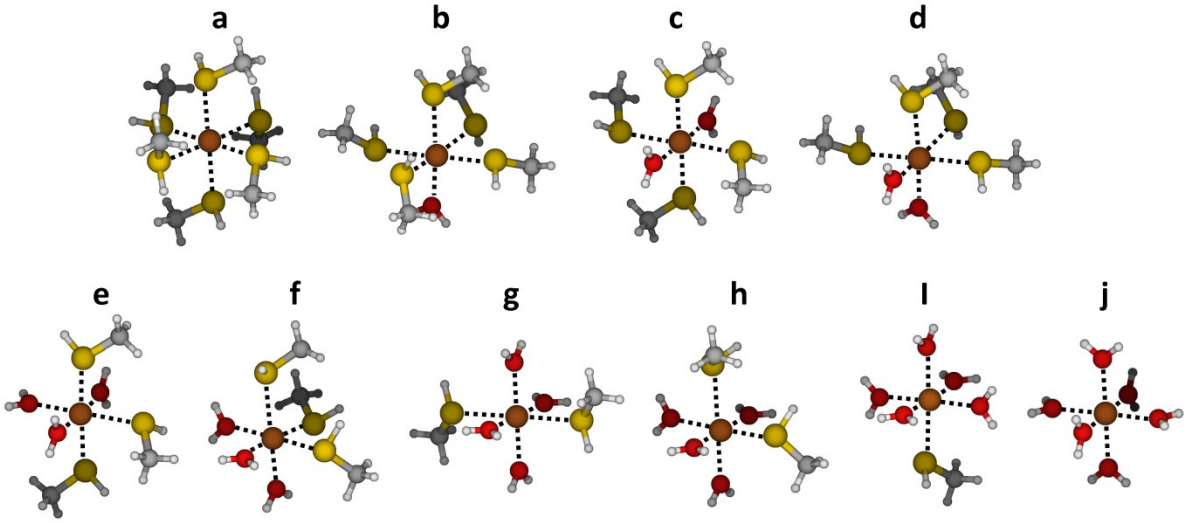

Figure 5.23. Optimized geometries of the $M^{2+}(CH_3SH)_m(H_2O)_n$ ternary complexes (M = Mg or Ca, m = 0–6, and n = 6–m) calculated at the MP2(FC)/6-311++G(d,p) level. Structures are illustrated with Ca^{2+} complexes.

Table 5.22. Binding energies (in kcal/mol) for $M^{2+}(CH_3SH)_m(H_2O)_n$ complexes (M = Mg or Ca, m = 0–6, and n = 6–m) calculated at the MP2(FC)/6-311++G(d,p) level (E and E^{CP}) and with SE models.

structure	m	n	Mg^{2+}					Ca^{2+}			
			Ab initio		SE			Ab initio		SE	
			E	E^{CP}	AM1*	AM1	RM1	E	E^{CP}	AM1	RM1
a	6	0	–303.0	–273.9	–271.4	–207.6	–173.9	–223.7	–203.1	–185.3	–197.6
b	5	1	–305.9	–278.9	–274.4	–286.1	–231.9	–228.4	–209.1	–191.6	–202.2
c	4	2	–308.1	–283.0	–270.9	–284.1	–230.0	–232.9	–215.3	–195.9	–206.2
d	4	2	–309.3	–283.8	–269.3	–242.0	–217.9	–233.5	–215.2	–199.8	–208.4
e	3	3	–312.0	–288.3	–267.0	–240.8	–216.7	–238.1	–221.2	–207.6	–214.1
f	3	3	–312.9	–289.0	–264.9	–228.6	–204.5	–238.4	–221.1	–212.4	–216.6
g	2	4	–315.6	–293.2	–263.2	–227.1	–202.9	–243.0	–227.1	–215.0	–218.8
h	2	4	–316.0	–293.5	–265.9	–217.6	–193.5	–243.6	–227.2	–222.0	–223.0
i	1	5	–320.9	–299.3	–280.7	–271.0	–246.9	–248.6	–233.1	–227.7	–229.4
j	0	6	–325.9	–305.1	–295.5	–300.0	–297.3	–254.3	–238.9	–237.1	–235.4

* Using the AM1 model of Hutter *et al*.[249]

5.3.3.6. $M^{2+}(HCHO)_m(H_2O)_n$ Clusters

Minimum-energy structures for ternary heptamer complexes containing formaldehyde are reported in Figure 5.24. These structures are characterized by $Mg^{2+}\cdots O(HCHO)$ separation of ~2.11 Å, $Mg^{2+}\cdots O(H_2O)$ of ~2.10 Å, $Ca^{2+}\cdots O(HCHO)$ of ~2.37 Å, and $Ca^{2+}\cdots O(H_2O)$ of ~2.40 Å. Binding energies of the various structures from both ab initio and SE calculations are reported in Table 5.23. The three SE models for Mg and the two models for Ca perform reasonably well on the ab initio calculated properties of the clusters (see Tables 5.2 and 5.23).

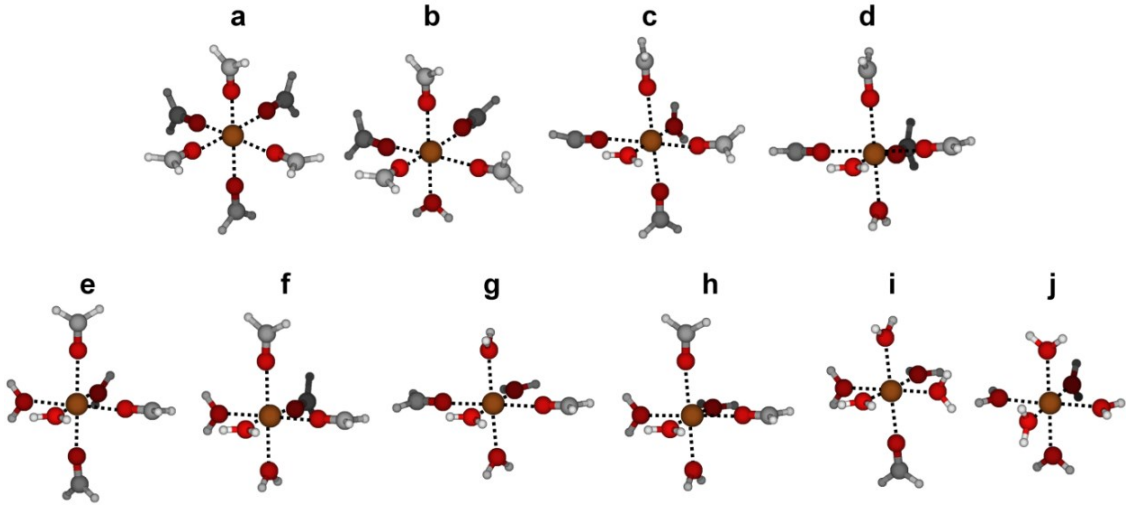

Figure 5.24. Optimized geometries of the $M(HCHO)_m(H_2O)_n$ ternary complexes (M = Mg or Ca, m = 0–6, and n = 6–m) calculated at the MP2(FC)/6-311++G(d,p) level. Structures are illustrated with Ca^{2+} complexes.

Table 5.23. Binding energies (in kcal/mol) for $M^{2+}(HCHO)_m(H_2O)_n$ complexes (M = Mg or Ca, m = 0–6, and n = 6–m) calculated at the MP2(FC)/6-311++G(d,p) level (E and E^{CP}) and with SE models.

structure	m	n	Mg^{2+}					Ca^{2+}			
			Ab initio		SE			Ab initio		SE	
			E	E^{CP}	AM1*	AM1	RM1	E	E^{CP}	AM1	RM1
a	6	0	–325.0	–307.9	–312.9	–324.5	–323.3	–255.5	–245.7	–256.1	–256.1
b	5	1	–324.5	–307.4	–310.5	–320.3	–318.3	–255.5	–244.7	–254.7	–253.7
c	4	2	–325.8	–308.3	–309.5	–317.5	–314.0	–255.5	–243.7	–252.6	–250.9
d	4	2	–325.2	–307.6	–309.3	–317.5	–313.8	–255.4	–243.8	–252.8	–251.0
e	3	3	–325.0	–306.6	–306.4	–313.4	–309.9	–254.8	–242.2	–249.7	–247.5
f	3	3	–325.9	–307.3	–307.4	–314.8	–310.9	–255.3	–242.8	–251.2	–247.8
g	2	4	–323.7	–304.7	–303.2	–308.5	–305.0	–254.4	–241.2	–245.0	–243.8
h	2	4	–324.9	–305.7	–304.0	–309.7	–305.7	–254.9	–241.5	–247.7	–244.1
i	1	5	–324.8	–305.2	–300.3	–305.2	–301.4	–254.6	–240.2	–243.5	–240.0
j	0	6	–325.9	–305.1	–295.5	–300.0	–297.3	–254.3	–238.9	–237.1	–235.4

* Using the AM1 model of Hutter *et al.*[249]

5.3.3.7. $M^{2+}(CH_3CHO)_m(H_2O)_n$ Clusters

Optimized geometries for ternary heptamer complexes of the metal ions with water and acetaldehyde are reported in Figure 5.25. These structures are characterized by $Mg^{2+}\cdots O(CH_3CHO)$ separation of ~2.09 Å, $Mg^{2+}\cdots O(H_2O)$ of ~2.11 Å, $Ca^{2+}\cdots O(HCHO)$ of ~2.35 Å, and $Ca^{2+}\cdots O(H_2O)$ of ~2.40 Å. Binding energies of the various structures from both ab initio and SE calculations are reported in Table 5.24. All SE models reasonably reproduce the ab initio properties of the ternary complexes (see Tables 5.2 and 5.24).

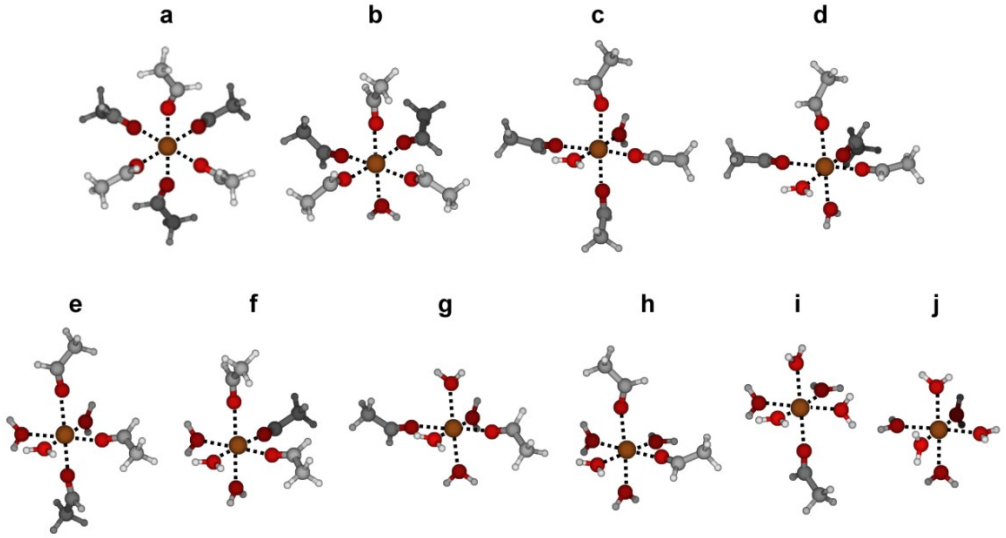

Figure 5.25. Optimized geometries of the $M^{2+}(CH_3CHO)_m(H_2O)_n$ ternary complexes (M = Mg or Ca, m = 0–6, and n = 6–m) calculated at the MP2(FC)/6-311++G(d,p) level. Structures are illustrated with Ca^{2+} complexes.

Table 5.24. Binding energies (in kcal/mol) for $M^{2+}(CH_3CHO)_m(H_2O)_n$ complexes (M = Mg or Ca, m = 0–6, and n = 6–m) calculated at the MP2(FC)/6-311++G(d,p) level (E and E^{CP}) and with SE models.

structure	m	n	Mg^{2+}					Ca^{2+}			
			Ab initio		SE			Ab initio		SE	
			E	E^{CP}	AM1*	AM1	RM1	E	E^{CP}	AM1	RM1
a	6	0	–362.0	–341.0	–335.6	–350.8	–353.4	–285.5	–272.3	–275.9	–284.5
b	5	1	–356.6	–336.0	–330.5	–342.7	–344.7	–281.3	–268.0	–272.4	–278.8
c	4	2	–352.0	–332.2	–326.6	–336.3	–337.1	–277.2	–263.7	–268.5	–272.3
d	4	2	–351.3	–331.2	–327.0	–336.4	–336.1	–277.0	–263.5	–268.5	–272.1
e	3	3	–345.8	–325.7	–320.5	–328.2	–327.4	–272.1	–258.1	–262.2	–264.5
f	3	3	–346.5	–326.1	–321.5	–329.6	–328.1	–272.0	–258.1	–263.9	–264.6
g	2	4	–338.0	–317.9	–312.8	–318.8	–317.2	–266.2	–251.9	–255.1	–255.8
h	2	4	–338.9	–318.7	–313.4	–320.0	–317.7	–266.6	–252.3	–256.6	–255.9
i	1	5	–331.9	–311.6	–305.1	–310.4	–307.6	–260.6	–245.9	–248.2	–246.1
j	0	6	–325.9	–305.1	–295.5	–300.0	–297.3	–254.3	–238.9	–237.1	–235.4

* Using the AM1 model of Hutter *et al*.[249]

5.3.3.8. $M^{2+}(HCONH_2)_m(H_2O)_n$ Clusters

Figure 5.26 lists the structures of the ion-water-formamide heptamer complexes optimized at the MP2(FC)/6-311++G(d,p) level of theory. Mg^{2+} complexes are characterized by $Mg^{2+}\cdots O(HCONH_2)$ distances of 2.03–2.11 Å and $Mg^{2+}\cdots O(H_2O)$ distances of 2.11–2.18 Å and Ca^{2+} complexes are characterized by corresponding distances of 2.29–2.39 Å and 2.40–2.44 Å. Table 5.25 shows binding energies from ab initio and SE calculations. While the three SE models of Mg perform reasonably well, the new AM1 model shows the best agreement with ab initio binding energies and structures of the ternary complexes (see Tables 5.2 and 5.25). The AM1 and RM1 models for Ca yield average error in binding energy of the ternary complexes valued at 3.7 kcal/mol for AM1 and 2.4 kcal/mol for RM1.

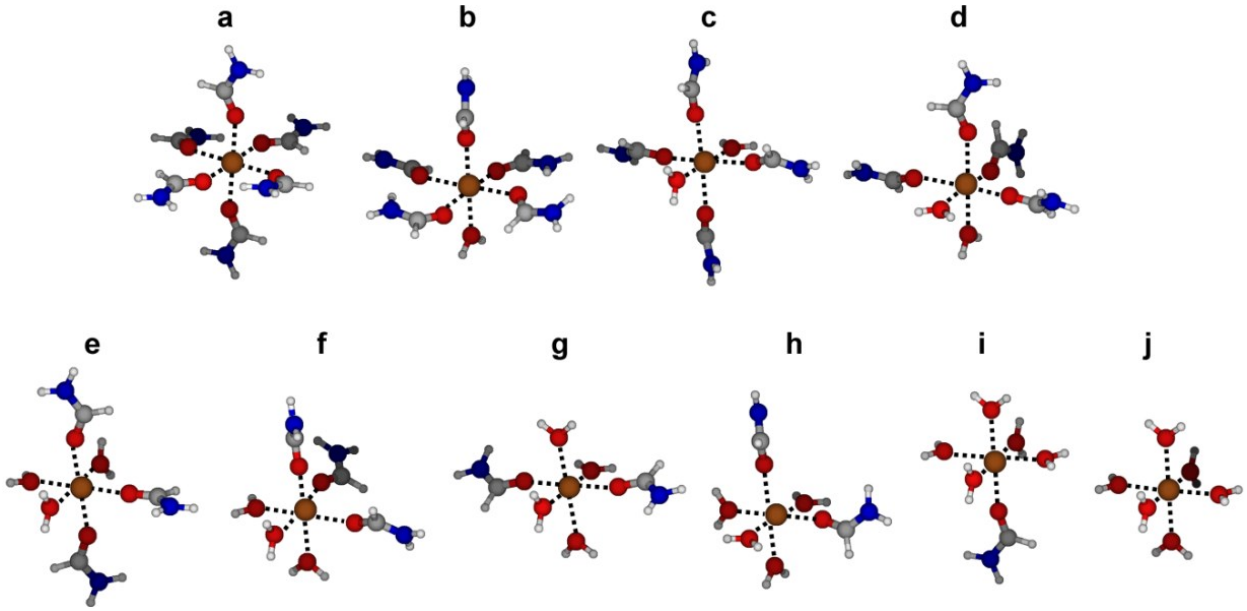

Figure 5.26. Optimized geometries of the $M^{2+}(HCONH_2)_m(H_2O)_n$ ternary complexes (M = Mg or Ca, m = 0–6, and n = 6–m) calculated at the MP2(FC)/6-311++G(d,p) level. Structures are illustrated with Ca^{2+} complexes.

Table 5.25. Binding energies (in kcal/mol) for $M^{2+}(HCONH_2)_m(H_2O)_n$ complexes (M = Mg or Ca, m = 0–6, and n = 6–m) calculated at the MP2(FC)/6-311++G(d,p) level (E and E^{CP}) and with SE models.

structure	m	n	Mg^{2+}					Ca^{2+}			
			Ab initio		SE			Ab initio		SE	
			E	E^{CP}	AM1*	AM1	RM1	E	E^{CP}	AM1	RM1
a	6	0	–411.2	–387.9	–377.5	–389.1	–386.9	–328.9	–313.4	–315.2	–318.7
b	5	1	–398.9	–376.5	–369.9	–385.5	–377.4	–319.0	–303.8	–309.5	–308.1
c	4	2	–387.4	–365.9	–360.5	–373.1	–364.7	–309.3	–295.1	–298.8	–298.6
d	4	2	–385.5	–364.2	–361.5	–373.5	–364.5	–309.4	–295.1	–298.7	–298.7
e	3	3	–371.1	–350.3	–348.6	–358.8	–349.1	–297.0	–282.9	–287.2	–285.8
f	3	3	–371.1	–349.7	–349.0	–358.5	–349.7	–298.7	–284.2	–289.2	–286.3
g	2	4	–358.8	–338.4	–330.6	–337.0	–334.9	–285.1	–270.6	–272.8	–271.5
h	2	4	–359.7	–339.1	–332.4	–339.4	–335.4	–285.5	–271.0	–274.8	–271.5
i	1	5	–343.3	–322.7	–315.1	–320.0	–317.0	–270.9	–256.1	–257.8	–254.7
j	0	6	–325.9	–305.1	–295.5	–300.0	–297.3	–254.3	–238.9	–237.1	–235.4

* Using the AM1 model of Hutter *et al*.[249]

5.3.3.9. $M^{2+}(CH_3CONH_2)_m(H_2O)_n$ Clusters

Binary and ternary heptamer complexes of both ions with water and acetamide are optimized at the MP2(FC)/6-311++G(d,p) level and obtained structures are given in Figure 5.27. Mg^{2+} and Ca^{2+} complexes are characterized by $M^{2+}\cdots O$ separations similar to those for formamide. Table 5.26 lists binding energies from both ab initio and SE calculations. Among the three models of Mg, the new RM1 model gives the best agreement with ab intio binding energies and structures. The new and original AM1 models for Mg have similar performance. AM1 and RM1 models for Ca show very good agreement with ab initio properties of the complexes (see Tables 5.2 and 5.26).

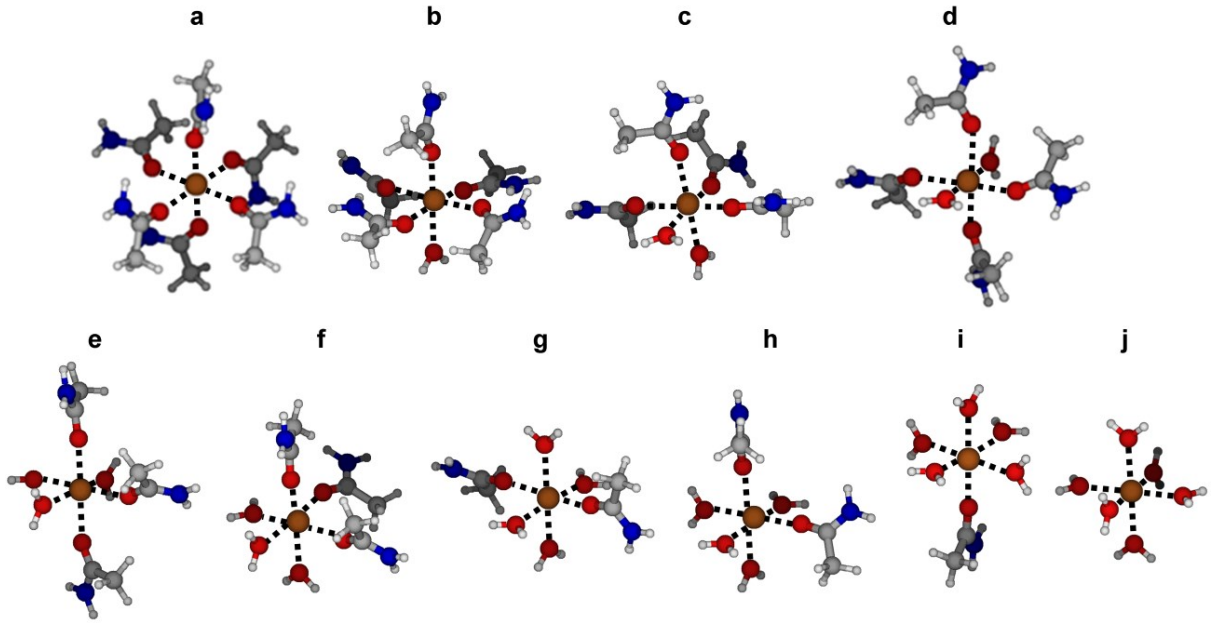

Figure 5.27. Optimized geometries of the $M^{2+}(CH_3CONH_2)_m(H_2O)_n$ ternary complexes (M = Mg or Ca, m = 0–6, and n = 6–m) calculated at the MP2(FC)/6-311++G(d,p) level. The binary ion-acetamide heptamer complexes (panel a) are optimized at the B3LYP/6-311++G(d,p) level of theory. Structures are illustrated with Ca^{2+} complexes.

Table 5.26. Binding energies (in kcal/mol) for $M^{2+}(CH_3CONH_2)_m(H_2O)_n$ complexes (M = Mg or Ca, m = 0–6, and n = 6–m) calculated at the MP2(FC)/6-311++G(d,p) level (E and E^{CP}) and with SE models.

structure	m	n	Mg^{2+}					Ca^{2+}			
			Ab initio		SE			Ab initio		SE	
			E	E^{CP}	AM1*	AM1	RM1	E	E^{CP}	AM1	RM1
a	6	0	–432.7	–407.1	–393.7	–410.6	–408.4	–346.0	–328.1	–330.5	–333.8
b	5	1	–412.2	–386.3	–373.1	–396.8	–387.6	–336.6	–317.8	–319.2	–321.3
c	4	2	–398.7	–375.3	–367.8	–386.4	–374.4	–322.6	–305.5	–308.4	–309.8
d	4	2	–398.0	–374.0	–365.6	–385.4	–375.0	–321.5	–304.8	–308.4	–310.0
e	3	3	–381.9	–359.7	–353.4	–368.6	–360.0	–306.5	–290.6	–293.9	–295.2
f	3	3	–384.0	–361.3	–354.6	–369.1	–360.9	–308.5	–292.2	–296.0	–295.4
g	2	4	–364.9	–343.8	–338.0	–348.0	–342.1	–291.9	–276.9	–278.7	–278.5
h	2	4	–366.4	–344.8	–338.6	–350.8	–343.2	–292.2	–277.2	–279.3	–278.3
i	1	5	–346.8	–326.1	–319.4	–326.8	–321.2	–274.6	–259.6	–261.1	–258.2
j	0	6	–325.9	–305.1	–295.5	–300.0	–297.3	–254.3	–238.9	–237.1	–235.4

* Using the AM1 model of Hutter *et al*.[249]

5.3.3.10. $M^{2+}(imidazole)_m(H_2O)_n$ Clusters

Minimum-energy structures in $M(imidazole)_m(H_2O)_n$ (m = 1–5 and n = 5–m) complexes reported in Figure 5.28. Mg^{2+} complexes are characterized by $Mg^{2+}\cdots N$ distances of 2.11–2.16 Å and $Mg^{2+}\cdots O$ distances of 2.07–2.15 Å. Corresponding separations in Ca^{2+} complexes are 2.41–2.46 Å and ~2.39 Å, respectively. Calculated binding energies for these complexes are presented in Table 5.27. The properties of Mg^{2+} complexes are best reproduced by the new AM1 model. The new SE models of Ca show low average errors in binding energies of the ternary clusters (see Tables 5.2 and 5.27).

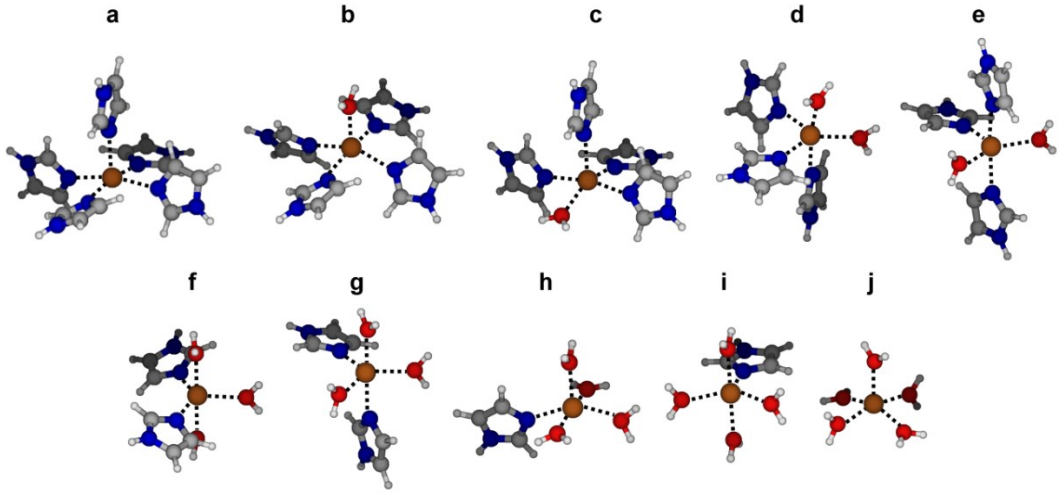

Figure 5.28. Optimized geometries of the $M^{2+}(imidazole)_m(H_2O)_n$ ternary complexes (M = Mg or Ca, m = 0–5, and n = 5–m) calculated at the MP2(FC)/6-311++G(d,p) level. Structures are illustrated with Ca^{2+} complexes.

Table 5.27. Binding energies (in kcal/mol) for $M^{2+}(imidazole)_m(H_2O)_n$ complexes (M = Mg or Ca, m = 0–5, and n = 5–m) calculated at the MP2(FC)/6-311++G(d,p) level (E and E^{CP}) and with SE models.

structure	m	n	Mg^{2+}					Ca^{2+}			
			Ab initio		SE			Ab initio		SE	
			E	E^{CP}	AM1*	AM1	RM1	E	E^{CP}	AM1	RM1
a	5	0	–408.5	–388.6	–405.5	–387.2	–407.9	–321.6	–305.7	–310.8	–320.5
b	4	1	–387.0	–369.3	–385.2	–370.2	–388.1	–303.2	–289.0	–295.5	–303.7
c	4	1	–387.7	–369.9	–387.6	–372.1	–390.4	–304.5	–290.1	–295.4	–303.8
d	3	2	–367.0	–350.2	–365.0	–354.2	–367.1	–285.9	–272.7	–279.8	–285.2
e	3	2	–368.3	–351.7	–364.1	–352.4	–367.0	–286.0	–273.4	–278.7	–285.0
f	2	3	–345.2	–329.3	–337.7	–331.5	–340.5	–266.2	–254.2	–260.0	–262.9
g	2	3	–345.2	–329.3	–337.7	–331.6	–340.4	–266.8	–254.9	–260.7	–262.9
h	1	4	–319.9	–304.0	–305.1	–302.4	–307.0	–245.6	–234.1	–236.6	–235.7
i	1	4	–321.0	–305.2	–305.0	–303.2	–307.2	–246.0	–234.5	–236.9	–235.8
j	0	5	–292.7	–276.7	–261.9	–265.4	–266.0	–223.2	–211.9	–209.1	–204.9

* Using the AM1 model of Hutter *et al.*[249]

5.3.3.11. M^{2+}(4-methylimidazole)$_m$(H_2O)$_n$ Clusters

Ternary complexes of the composition M(4-methylimidazole)$_m$(H_2O)$_n$ (m = 1–5 and n = 5–m) are optimized the MP2(FC)/6-311++G(d,p) level except for complexes with m = 4, which are optimized at the B3LYP/6-311++G(d,p) level. The complexes are characterized by geometries (Figure 5.29) similar to those involving imidazole. Mg^{2+} complexes are characterized by Mg^{2+}···N distances of 2.09–2.23 Å and Mg^{2+}···O distances of 2.07–2.17 Å. Corresponding separations in Ca^{2+} complexes are 2.41–2.50 Å and 2.38–2.45 Å. Table 5.28 lists binding energies from both ab initio and SE calculations. Similar to complexes of imidazole, the new AM1 model for Mg and both models for Ca show the good agreement with ab initio properties of the ternary systems (see Tables 5.2 and 5.28).

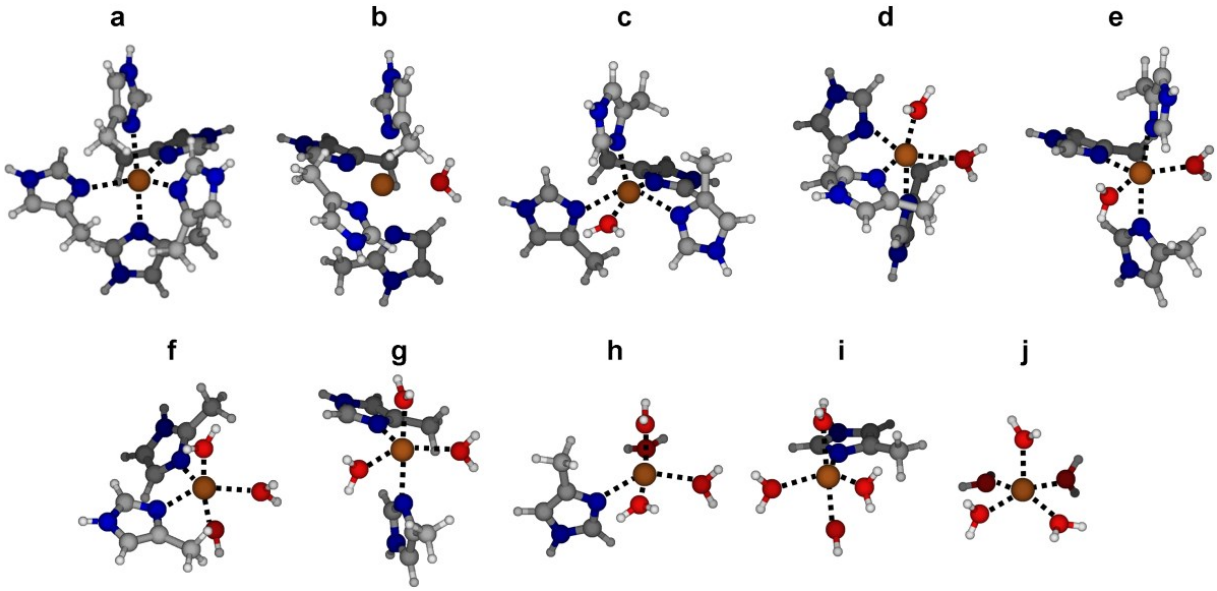

Figure 5.29. Optimized geometries of the M^{2+}(4-methylimidazole)$_m$(H_2O)$_n$ ternary complexes (M = Mg or Ca, m = 0–5, and n = 5–m) calculated at the MP2(FC)/6-311++G(d,p) level. Complexes with four or five 4-methylimidazole molecules are optimized at the B3LYP/6-311++G(d,p) level. Structures are illustrated with Ca^{2+} complexes.

Table 5.28. Binding energies (in kcal/mol) for M^{2+}(4-methylimidazole)$_m$(H_2O)$_n$ complexes (M = Mg or Ca, m = 0–6, and n = 6–m) calculated at the MP2(FC)/6-311++G(d,p) level (E and E^{CP}) and with SE models.

structure	m	n	Mg^{2+}					Ca^{2+}			
			Ab initio		SE			Ab initio		SE	
			E	E^{CP}	AM1*	AM1	RM1	E	E^{CP}	AM1	RM1
a	5	0	–416.8	–392.7	–400.9	–389.2	–406.2	–331.2	–312.1	–311.8	–322.6
b	4	1	–393.5	–372.9	–386.2	–378.2	–391.4	–311.2	–294.9	–299.9	–309.4
c	4	1	–394.5	–373.6	–385.9	–377.9	–391.5	–311.2	–295.0	–298.2	–307.6
d	3	2	–373.7	–354.1	–368.6	–364.0	–373.5	–292.6	–276.5	–283.5	–290.0
e	3	2	–374.1	–354.7	–366.1	–360.7	–372.7	–291.8	–276.9	–283.5	–290.2
f	2	3	–349.5	–332.3	–341.5	–340.5	–346.5	–270.4	–257.3	–264.1	–268.7
g	2	3	–349.5	–332.3	–341.5	–340.4	–346.5	–270.5	–257.3	–264.6	–266.5
h	1	4	–323.1	–306.8	–308.3	–309.0	–311.2	–247.6	–235.4	–239.0	–238.5
i	1	4	–323.1	–306.8	–308.6	–308.9	–311.2	–248.3	–235.9	–238.8	–238.2
j	0	5	–292.7	–276.7	–261.9	–265.4	–266.0	–223.2	–211.9	–209.1	–204.9

* Using the AM1 model of Hutter *et al*.[249]

5.3.3.12. M^{2+}(5-methylimidazole)$_m$(H_2O)$_n$ Clusters

The optimized geometries of ternary hexamer complexes containing 5-methylimidazole are given in Figure 5.30. The complexes are characterized by ion···N and ion···O distances similar to those for 4-methylimidazole. Table 5.29 lists binding energies from both ab initio and SE calculations. Tables 5.2 and 5.29 are showing that the new AM1 model for Mg and Ca have the best performance over the binding energies and structures of these complexes.

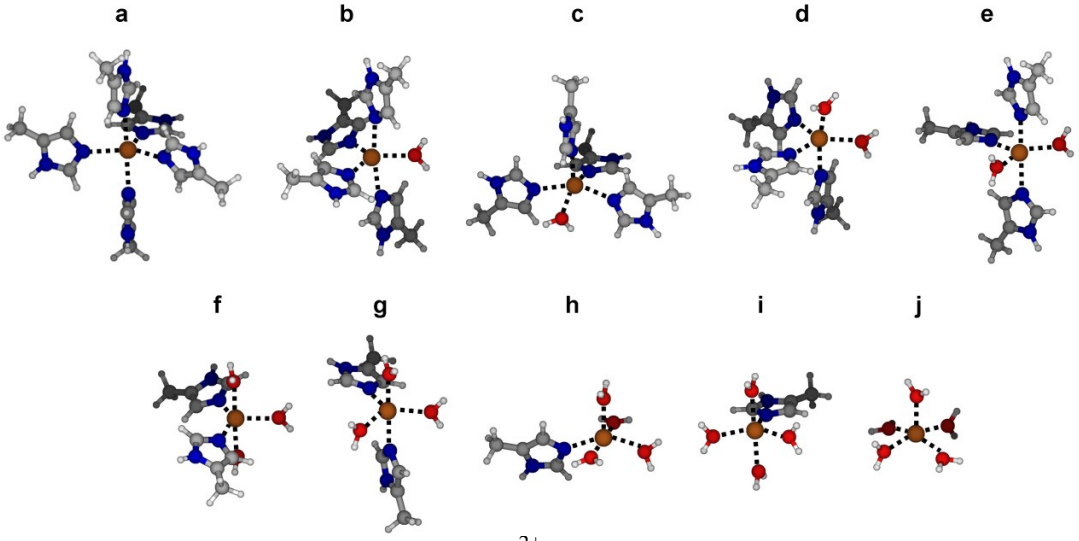

Figure 5.30. Optimized geometries of the M^{2+}(5-methylimidazole)$_m$(H_2O)$_n$ ternary complexes (M = Mg or Ca, m = 0–5, and n = 5–m) calculated at the MP2(FC)/6-311++G(d,p) level. Complexes with four or five 5-methylimidazole molecules are optimized at the B3LYP/6-311++G(d,p) level. Structures are illustrated with Ca^{2+} complexes.

Table 5.29. Binding energies (in kcal/mol) for M^{2+}(5-methylimidazole)$_m$(H_2O)$_n$ complexes (M = Mg or Ca, m = 0–5, and n = 5–m) calculated at the MP2(FC)/6-311++G(d,p) level (E and E^{CP}) and with SE models.

structure	m	n	Mg^{2+}					Ca^{2+}			
			Ab initio		SE			Ab initio		SE	
			E	E^{CP}	AM1*	AM1	RM1	E	E^{CP}	AM1	RM1
a	5	0	–420.4	–401.1	–411.3	–393.3	–415.4	–332.8	–317.6	–317.1	–332.5
b	4	1	–397.8	–380.4	–391.0	–376.0	–395.2	–312.6	–299.0	–301.5	–315.1
c	4	1	–398.5	–381.1	–393.4	–377.9	–397.2	–314.2	–300.4	–301.5	–315.1
d	3	2	–376.9	–359.8	–370.0	–359.3	–372.9	–294.8	–281.2	–284.6	–294.0
e	3	2	–378.0	–361.1	–368.7	–357.3	–373.4	–294.8	–281.9	–283.5	–294.0
f	2	3	–352.6	–336.4	–341.6	–335.5	–345.3	–272.7	–260.5	–264.0	–269.6
g	2	3	–352.6	–336.4	–341.7	–335.5	–345.3	–273.3	–261.2	–264.1	–269.2
h	1	4	–323.9	–308.0	–307.4	–305.2	–309.6	–249.1	–237.5	–238.2	–239.3
i	1	4	–325.0	–309.1	–305.6	–305.4	–310.0	–249.5	–238.0	–238.9	–239.5
j	0	5	–292.7	–276.7	–261.9	–265.4	–266.0	–223.2	–211.9	–209.1	–204.9

* Using the AM1 model of Hutter *et al*.[249]

5.3.3.13. $M^{2+}(HCOO^-)_m(H_2O)_n$ Clusters

Ternary cation-formate-water complexes are optimized at the MP2(FC)/6-311++G(d,p) level and the obtained structures are reported in Figure 5.31. Only structures in which the six ligands are in direct binding to the metal ion were initially considered for optimization and only structure 5.31c has ligands (a single water molecule) not coordinating the metal ion. Calculated binding energies of these complexes are reported in Table 5.30. The original AM1 model of Mg gives binding energies and structures of the ternary complexes in poor agreement with MP2 calculations. It has an average error in binding energy of 23.3 kcal/mol and an average MSD of 0.73 Å^2. In comparison, the new AM1 model for Mg yields average error in binding energy of 17.6 kcal/mol and average MSD of 0.35 Å^2. The optimized RM1 model gives the best agreement with ab initio data with average error in binding energy = 9.2 kcal/mol and average MSD = 0.33 Å^2. Optimized AM1 and RM1 models for Ca show average error in binding energy of 21.4 and 14.6 kcal/mol and average MSD of 0.31 Å^2 and 0.23 Å^2, respectively.

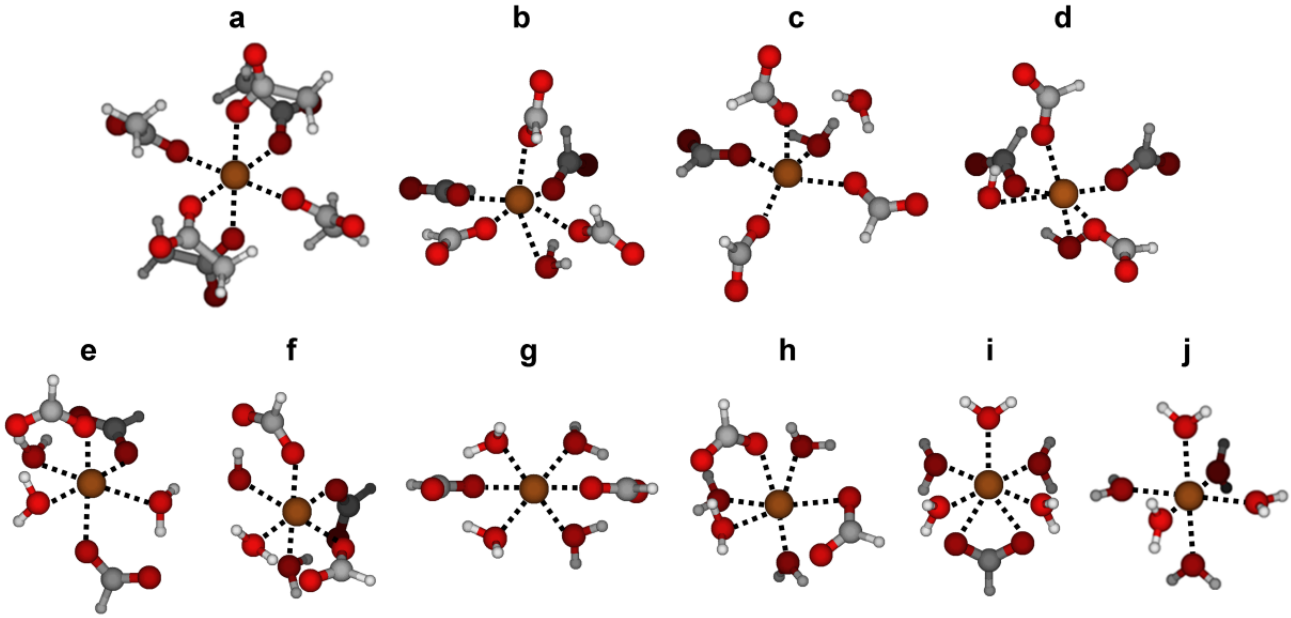

Figure 5.31. Optimized geometries of the $M^{2+}(HCOO^{-})_m(H_2O)_n$ ternary complexes (M = Mg or Ca, m = 0–6, and n = 6–m) calculated at the MP2(FC)/6-311++G(d,p) level. Structures are illustrated with Ca^{2+} complexes.

Table 5.30. Binding energies (in kcal/mol) for $M^{2+}(HCO_2^{-})_m(H_2O)_n$ complexes (M = Mg or Ca, m = 0–6, and n = 6–m) calculated at the MP2(FC)/6-311++G(d,p) level (E and E^{CP}) and with SE models.

structure	m	n	Mg^{2+}					Ca^{2+}			
			Ab initio		SE			Ab initio		SE	
			E	E^{CP}	AM1*	AM1	RM1	E	E^{CP}	AM1	RM1
a	6	0	–368.0	–344.8	–355.6	–346.1	–340.9	–303.8	–288.5	–294.6	–287.1
b	5	1	–541.0	–520.0	–527.8	–522.0	–522.0	–461.0	–445.0	–457.6	–450.6
c	4	2	–638.7	–617.0	–629.0	–624.8	–623.0	–556.3	–540.6	–556.6	–548.8
d	4	2	–632.3	–609.6	–627.5	–622.8	–616.6	–554.5	–538.1	–556.7	–547.5
e	3	3	–686.0	–659.0	–681.9	–676.0	–669.4	–603.3	–582.5	–606.1	–597.9
f	3	3	–684.7	–657.5	–681.8	–678.5	–668.9	–603.5	–582.5	–603.0	–598.5
g	2	4	–648.8	–622.6	–658.3	–649.0	–636.0	–564.7	–544.6	–574.5	–570.0
h	2	4	–647.4	–621.1	–660.7	–650.9	–635.2	–562.6	–542.5	–576.6	–564.6
i	1	5	–524.7	–500.7	–527.3	–524.0	–510.0	–449.9	–432.6	–448.6	–446.8
j	0	6	–325.9	–305.1	–295.5	–300.0	–297.3	–254.3	–238.9	–237.1	–235.4

* Using the AM1 model of Hutter *et al*.[249]

5.3.3.14. $M^{2+}(CH_3COO^-)_m(H_2O)_n$ Clusters

Optimized ternary cation-acetate-water complexes are reported in Figure 5.32. Structure 5.32c is similar to structure 5.31c for the formate ion. Calculated binding energies of the different complexes are reported in Table 5.31. Similar to what is observed for the formate ion, the new SE models for Mg are yield structures in better agreement with MP2 results compared to the original AM1 model. Models of Ca are reasonably reproducing the structures of the complexes and the RM1 model is characterized by a small average error in binding energies (see Table 5.2).

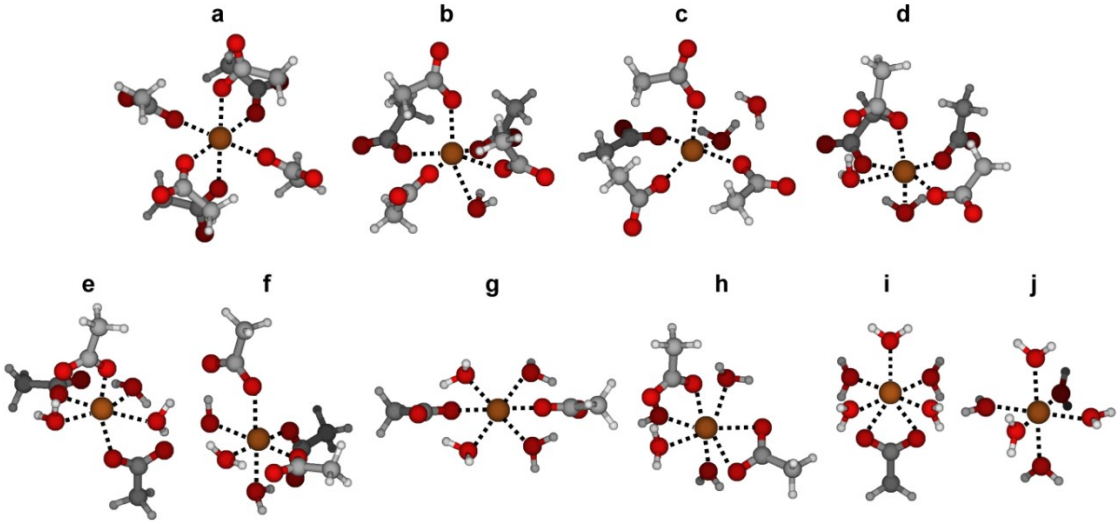

Figure 5.32. Optimized geometries of the $M^{2+}(CH_3COO^-)_m(H_2O)_n$ complexes calculated at the MP2(FC)/6-311++G(d,p) level. Structures are illustrated with Ca^{2+} complexes.

Table 5.31. Binding energies (in kcal/mol) for $M^{2+}(CH_3CO_2^-)_m(H_2O)_n$ complexes (M = Mg or Ca, m = 0–6, and n = 6–m) calculated at the MP2(FC)/6-311++G(d,p) level (E and E^{CP}) and with SE models.

structure	m	n	Mg^{2+}					Ca^{2+}			
			Ab initio		SE			Ab initio		SE	
			E	E^{CP}	AM1*	AM1	RM1	E	E^{CP}	AM1	RM1
a	6	0	–387.2	–357.2	–346.9	–351.4	–350.1	–324.8	–302.3	–301.6	–293.3
b	5	1	–551.8	–524.4	–527.2	–533.6	–523.3	–475.8	–453.9	–461.4	–453.4
c	4	2	–647.5	–619.7	–625.0	–631.5	–615.1	–565.1	–545.9	–554.3	–547.9
d	4	2	–645.1	–617.8	–624.2	–628.9	–614.4	–568.1	–546.9	–558.0	–550.5
e	3	3	–693.1	–664.6	–678.5	–674.7	–665.2	–610.2	–588.1	–605.0	–596.7
f	3	3	–692.4	–663.6	–676.2	–676.8	–665.2	–620.4	–588.2	–600.9	–597.4
g	2	4	–655.7	–628.6	–657.0	–646.4	–632.5	–572.3	–550.8	–576.5	–570.1
h	2	4	–627.4	–654.6	–659.5	–646.2	–653.1	–569.8	–548.9	–578.7	–564.4
i	1	5	–530.6	–506.5	–529.2	–525.5	–509.6	–455.3	–437.8	–450.0	–448.0
j	0	6	–325.9	–305.1	–295.5	–300.0	–297.3	–254.3	–238.9	–237.1	–235.4

* Using the AM1 model of Hutter *et al*.[249]

5.4. Conclusion

Semiempirical quantum mechanical models are optimized for Mg and Ca based on the ab initio properties of binary complexes of the two metal ions with various ligands. Two models are optimized for each metal. Both models are based on the original AM1 scheme, with one optimized to be compatible with the AM1 parameters of H, C, N, O, and S and the other optimized to be compatible with the RM1 parameters of these elements. The optimized models have been tested on the properties of a large testing set containing about 170 binary and ternary complexes of each metal. The optimized models for Mg underestimate the binding energies of binary and ternary complexes containing hydrogen sulfide and methanethiol. The models however show low average error in binding energies (6–8 kcal/mol) of other binary and ternary complexes compared to the original AM1 model[249] of Hutter *et al*. (14 kcal/mol). The optimized models of Ca are showing very good agreement with ab initio data for all complexes, including those containing S. The average error in binding energy of all Ca complexes is 6.3 kcal/mol for the AM1/Ca model and 7.8 kcal/mol for the RM1/Ca model.

The models can be used in MD simulations to investigate the selectivity of the two metal ions toward various ligands in complex mixture solutions. MD simulations can also be performed to elucidate the coordination number and geometry of each metal in different pure and mixed ligand systems. The dynamics of ligand exchange in the ion's first solvation shell can also be investigated. These investigations are important toward identifying protein binding sites for the two metal ions and to understand the geometrical and structural requirements for selective binding of proteins toward either of the two metal ions. The models can also be used to measure the binding affinity between the two metal ions and different ligands in aqueous solutions and between the two ions and different metalloproteins. The models are also important for SE QM/MM MD simulations on metalloproteins because they are much faster than ab initio QM/MM MD. In addition the reported ab initio properties of the various binary and ternary complexes of the two metals are useful benchmark data for optimization of different semiempirical and force field models for the two cations.

6. Complexation of Rb^+, Cs^+, and Tl^+ with Aromatics, Alcohols, and Amides in Gas Phase and in Aqueous Solution

Abstract

Cation–π interactions are important non-covalent interactions in biological systems. They play key roles in stabilizing protein structures and protein-ligand and protein-DNA complexes. While extensively studied in gas phase, little is known about their strength in aqueous solution, and accurate molecular models for these interactions are scarce. In this work we present ab initio quantum mechanical calculations on the interaction of Rb^+, Cs^+, and Tl^+ with eight aromatic compounds (benzene, toluene, phenol, 4-methylphenol, indole, 3-methylindole, imidazole, and 5-methylimidazole) at the MP2 level of theory. The interaction of the three cations with ethanol, acetamide, and N-methylacetamide is also studied to compare cation–π with charge-dipole affinities. Different possible conformers of the complexes of the three cations with the benzene dimer are studied and the cooperativity or anti-cooperativity between cation–π and π–π interactions in these complexes is analyzed. Similar to reported models for Rb^+ and Cs^+, a polarizable potential model for Tl^+ is optimized based on the hydration free energy of the ion. Polarizable potential models for the interaction of the three cations with the different ligands are parameterized based on ab initio calculations of the ion-ligand complexes. The models are used to investigate the stability of these complexes in aqueous solution by calculating the potential of mean force between each cation and each ligand and by analyzing the organization of the solvent as a function of the cation-ligand separation. The results show that cation–π complexes are more stable than charge-dipole complexes in water. The increase in binding affinity between alkali ions and aromatic compounds as the size of the ion increases indicates that cation–π interactions play a role in the increased solubility of aromatic compounds in aqueous alkali metal salts on going from Li to Cs. Molecular dynamics simulations of each cation in presence of two benzene molecules in water show that π–cation–π binding motifs are the most stable structural arrangement. Among the three cations, Tl^+–π complexes are found to be the most stable in aqueous solution.

6.1. Introduction

Non-covalent interactions play crucial roles in chemical and biological systems.[264] For example, hydrogen bonding stabilizes the double helical structure of DNA[265,266] and hydrophobic and π–π interactions stabilize protein structures.[264,267] Recently the interaction between cations and aromatic compounds has been viewed as a novel non-covalent interaction force.[268] This interaction is due to the attractive binding of cations to the π electrons in organic compounds and is referred to as cation–π interaction.[6,268–270]

These interactions are dominated by electrostatic forces between the ion and the dipole or quadrupole moments of the aromatic compounds.[6,13,271,272] In addition, upon complexation, the strong electric filed of the ion generates an induced dipole moment in the π system and further stabilizes the complex.[14–16,30,31,274–276] The polarizability of the interacting dimer is thus a key factor in modeling cation–π complexation.[31] In particular, polarizable models are critical in describing the cooperative and anti-cooperative interplay between cation–π and π–π interactions.[31,31]

Cation–π interactions in protein structures are due to association of the cationic moieties of lysine (Lys) and arginine (Arg) with the aromatic moieties or phenylalanine (Phe), tyrosine (Tyr), and tryptophan (Trp).[6,269] These interactions are found to be common among protein structures[269,277–279] and are believed to play key roles in their stability.[8,280–284] In addition, proteins can interact with ligands through cation–π interactions with the ligand providing the cationic or aromatic component of the interacting pair.[285]

Cation–π interactions involving alkali metal ions have been the subject of extensive theoretical and experimental investigations in gas phase.[13,15,16,169,272,286–294] The majority of these however have been focused on the light hard atoms (Li^+, Na^+, and K^+), due to their biological relevance. Investigating the properties of cation–π interactions of the heavier ions (Rb^+ and Cs^+) and of soft ions (such as Tl^+) is required to understand the trend in binding strength as a function of the ion properties. In addition, the majority of studies have been focused on the prototypical π system benzene.[2169,286,287,294,295] Studying the influence of the aromatic moieties and of their substituents is also important for accurate understanding of the strength and directionality of these interactions, which is a requirement for proper design of cation-selective receptors.

Calculations reveal that cation–π interactions are among the strongest noncovalent interactions in gas phase. Although cation–π complexes become less stable as they get progressively hydrated,[296] they persist even in bulk aqueous solution.[30,31,297] Interestingly, while cations bind anions much stronger than aromatics in gas phase, the trend is reversed in water.[297]

Calculating the stability of cation–π interactions in water is an important step toward understanding their stability in protein structures and their roles in biological systems in general (which are commonly solvent exposed). To the best of our knowledge, the strength of cation–π interactions involving Rb^+, Cs^+, and Tl^+ in aqueous media has not been reported so far.

The interplay between non-covalent interactions may not be simply additive and can be cooperative or anti-cooperative.[30,31] Cooperative interactions strengthen one another and result in net stabilization energy higher than the sum of the individual isolated interactions. On the other hand anti-cooperative interactions are weaker when combined and hence the overall complexation energy is lower than the sum of the individual energies. While cation–π and π–π interactions are cooperative in complexes with cation–π–π patterns,[30,298–300] they are anti-cooperative in π–cation–π motifs.[30,300]

While quantum mechanical (QM) calculations are feasible for cation–π interactions in small complexes in gas phase,[286,289,290,294,295] they are computationally prohibitive for large systems (such as water-solvated complexes and biological systems). Alternatively, force fields are commonly used. Studying cation–π interactions with force fields requires however specific calibration[18,30,31] because they are commonly not calibrated for ion-protein interactions.[31]

Due to having similar chemistry, thallium (Tl) is commonly regarded as a relativistic alkali metal.[301–303] Compared to the rest of group 13 elements, which favor the +3 oxidation state, Tl has a higher preference to the +1 oxidation state. This is attributed to the effect of the inert pair of electrons in the 6s orbital.[302,303] Like alkali metal hydroxides, TlOH is water soluble and reacts with carbon dioxide to form water-soluble thallium carbonate.[302] The hydrated ionic radius of Tl^+ is close to that of K^+ and Rb^+.[304] Tl is able to replace K in biological systems with up to 10 times higher binding affinity.[302] Thallium is however much softer than alkali ions, which results in high affinity for sulfur functional groups.[303] This high affinity and the non-reversibility of its complexation reactions, due to high binding affinities, is the reason for toxicity of thallium salts.[301,303] Tl is however proposed as a useful radioisotope for medical applications such as myocardial visualization, renal medullary imaging, and in tumor detection.[301] Development of a molecular model for Tl^+ is thus important to compare its solvation structure and solvation free energy to those of alkali ions (especially K^+) and to investigate the influence of the ion's polarizability on ion-ligand interactions in gas phase and in aqueous solution. This model is also useful for understanding the high affinity of the ion, compared to K^+, toward proteins.

In previous work,[18,30] we have optimized polarizable force field (FF) models for the interaction of Na^+, K^+, and NH_4^+ with ethanol, N-methylacetamide (NMA), and with model compounds to aromatic amino acid side chains; benzene, toluene, phenol, 4-methylphenol, indole, 3-methylindole, imidazole, and 5-methlimidazole based on the ab initio properties of these complexes at the MP2 level. In this work, we optimize a polarizable model for Tl^+ and report polarizable models for Rb^+, Cs^+, and Tl^+ interacting with the above ligands and with acetamide. The optimized models are then used in molecular dynamics simulations to determine the binding free energy between each pair in water. We also investigate the interplay between cation–π and π–π interactions in both gas phase and in aqueous solutions.

6.2. Methods

6.2.1. Ab initio Calculations

Ab initio QM calculations are performed using Gaussian 09.[26] The structures of the twelve ligands considered in this work are shown in Figure 6.1. The geometry of these ligands and of the benzene dimer and of their complexes with Rb^+, Cs^+, and Tl^+ are optimized at the full-electron MP2 level with the 6-311+G(3df,2p) basis set for H, C, N, and O and with effective core potentials (ECPs) and valence basis sets for the metal ions. We use the Stuttgart RSC 1997 (ECP) basis set[168] to which d and f polarization functions are added with exponents 0.39 and 0.55 for Rb^+, and 0.29 and 0.44 for Cs^+.[31,169] For Tl^+, the relativistic ECP and double-ζ valence basis set developed by Stevens, Basch, Krauss, Jasien, and Cundari (SBKJC VDZ ECP)[305] is used. The basis set used to study Rb^+ and Cs^+ clusters was shown to give binding energies for the benzene-ion, and ammonia-ion complexes in good agreement with experimental results.[31,169,202] The basis set of Tl^+ has been used by Vchirawongkwin *et al.*[306] in a QM/MM simulation of one Tl^+ ion in bulk water and by Mudring and Rieger in studying macrocyclic compounds of Tl^+.[301] All calculations are done without symmetry constraints and frequency calculations are performed on the resulting structures to confirm that they are energy minima. Interaction energies are corrected for basis set superposition error (BSSE) using the counterpoise (CP) procedure of Boys and Bernardi.[111] Potential energy surfaces (PESs) for ions in complex with the twelve ligands are generated by scanning the distance between the ion and a certain site on the ligand from 2 to 10 Å. That site represents the center of the six membered aromatic rings of benzene, toluene, phenol, 4-methylphenol, indole, and 3-methylindole, the O atom of water, ethanol, acetamide, and NMA, and the nitrogen atom (N_3, see Figure 6.1) of imidazole and 5-methylimidazole.

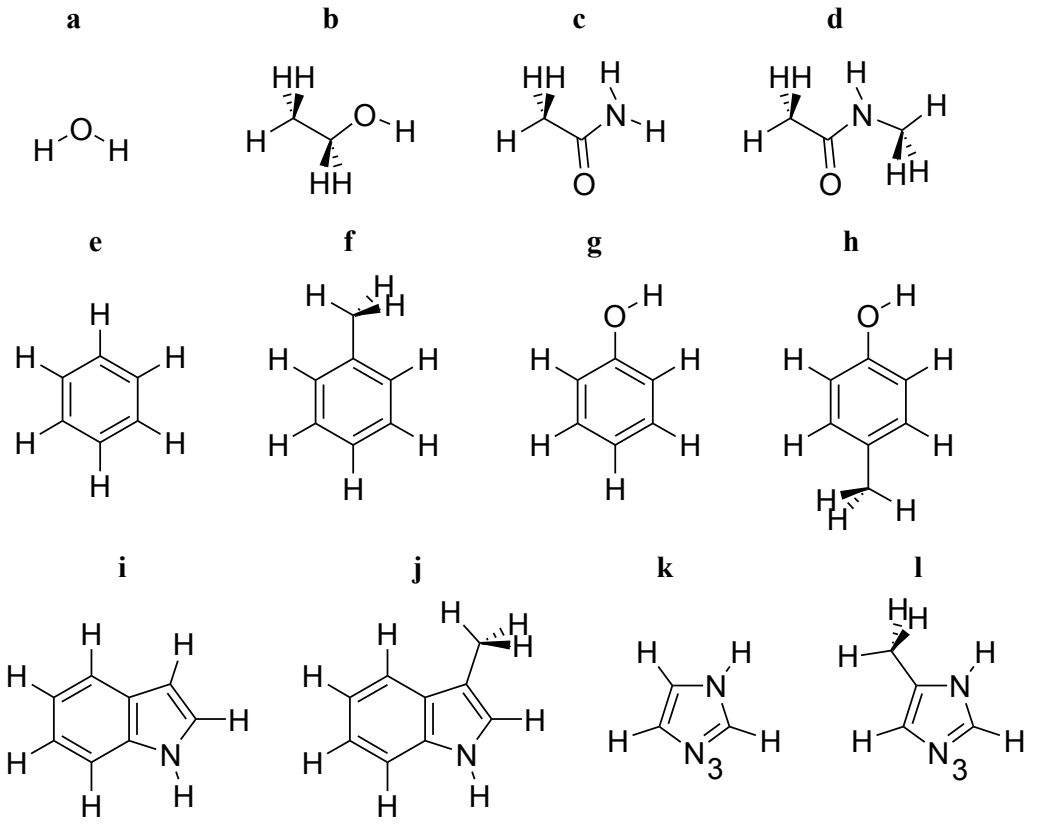

Figure 6.1. Structural formula of compounds interacting with Rb^+, Cs^+, and Tl^+: a, water; b, ethanol, c, acetamide; d, NMA; e, benzene; f, toluene; g, phenol; h, 4-methylphenol; i, indole; j, 3-methylindole; k, imidazole; l, 5-methylimidazole. To facilitate the discussion, we assign the number 3 to one nitrogen atom in imidazole and 5-methylimidazole.

6.2.2. Molecular Mechanics Calculations

Molecular mechanics (MM) calculations are performed with the program CHARMM.[29] Polarizable potential models based on classical Drude oscillators[32] have been reported for H_2O,[113] alcohols,[307] aromatic compounds,[125] amides,[308] alkali ions,[118] and Tl^+.[309] The SWM4-NDP water model was calibrated to reproduce the main properties of liquid water. The alcohol[307] and aromatic models[125] yield good agreement with pure solvent properties, and the amide model[308] reproduce the anomalously large dielectric constant of liquid amides. The alkali cation model[118] reproduces the experimental solvation structure and hydration free energies of the ions. We optimize a polarizable model Tl^+ based on the the experimental hydration free energy of the ion. Following previous work,[18,30,125,170,262] polarizable models for Rb^+, Cs^+, and Tl^+ interactions with the different ligands are optimized based on the ab initio properties of the interacting dimers.

6.2.2.1. Parameterization Strategy

A polarizable model of Tl^+ is optimized to yield the experimental hydration free energy of the ion via optimizing the generic Lennard-Jones (LJ) parameters of the ion (E_{min} and R_{min}). The parameters are first optimized on the PES of the Tl^+–H_2O dimer. While maintaining the R_{min} parameter at the value obtained from the previous step, we then adjust the E_{min} parameter to yield the experimental hydration free energy. Following our previous approach,[18,30,170,202,262] polarizable models for ion-ligand interactions are optimized via adjusting pair-specific LJ parameters between each ion and certain atoms in the interacting ligands based on the ab initio PESs of the dimers. The Drude models of the three ions are optimized to reproduce the hydration free energy and no pair-specific LJ are adjusted for their interactions with water. We initially optimize parameters for ion interactions with the simple ligands. These parameters are usually transferable to the methylated derivative, otherwise they are readjusted.

6.2.2.2. Molecular Dynamics

All molecular dynamics (MD) simulations are performed with cubic periodic boundary conditions in the isothermal-isobaric ensemble (*NpT*) at T = 298.15 K and p = 1 atm. Systems composed of ion-ligand dimers solvated in 600 water molecules are simulated to calculate the binding affinity in these dimers in aqueous solutions. A system of one thallium ion and 250 water molecules is simulated to calculate the hydration structure and hydration free energy of the ion. In addition, systems composed of one ion, 2 benzene molecules, and 600 water molecules are simulated to investigate the interplay between cation–π and π–π interactions in aqueous solutions. We use the same simulation protocol as reported previously.[30,170,202] Electrostatic interactions are computed using the particle-mesh Ewald method[115] with κ = 0.34 for the charge screening and a 1.0 Å grid spacing with fourth-order splines for the mesh interpolation. The real-space interactions (Lennard-Jones and electrostatic) are cut off at 15 Å and the long range contribution from the Lennard-Jones term is introduced as an average density-dependent term.[116] The temperature of the system is controlled with a two-thermostats algorithm, where atoms are kept at the desired temperature and oscillations of the Drude particles are kept at low temperature (1 K) to ensure self-consistent dipole induction.[32] The equations of motion are integrated using a 1 fs time step, with all bonds involving hydrogen atoms kept at their reference lengths using the SHAKE/Roll and RATTLE/Roll algorithms.[33]

6.2.2.3. Free Energy Calculations

The intrinsic free energy of hydration of Tl^+ is calculated using the free energy perturbation (FEP) protocol reported previously.[202,262] Specifically, the solvation free energy is evaluated from the transformation of Tl^+ into a "dummy" atom having no charge and no LJ parameters:

$$\Delta G_{\mathrm{solv}}^{\mathrm{intr}} \equiv \Delta G_{\mathrm{solv}}(\mathrm{Tl}^+) - \Delta G_{\mathrm{solv}}(\mathrm{dummy}) = -\Delta \mathrm{G}_{\mathrm{mut}}(\mathrm{Tl}^+ \rightarrow \mathrm{dummy}) \qquad (6.1)$$

where $\Delta \mathrm{G}_{\mathrm{mut}}$ is the relative free energy for the alchemical $\mathrm{Tl}^+ \rightarrow$ dummy "mutation" and $\Delta G_{\mathrm{solv}}(\mathrm{dummy}) = 0$. The transformation in performed in 21 steps, controlled by a scaling parameter λ which takes the following values: 0, 0.00001, 0.0001, 0.001, 0.01, 0.05, 0.1, 0.2, 0.3, 0.4, 0.5, 0.6, 0.7, 0.8, 0.9, 0.95, 0.99, 0.999, 0.9999, 0.99999, and 1.[202,262] Each λ window is equilibrated for 150 ps, followed by subsequent data collection for 350 ps. Each mutation is performed in the forward and backward directions in three independent replicates, in order to confirm the convergence and estimate the error on the calculated values.

6.2.2.4. Potential of Mean Force Calculations

Potentials of mean force (PMFs) between each ion (Rb^+, Cs^+, or Tl^+) and all ligands, except water, in pure water are calculated using umbrella sampling, according to a previously reported procedure.[30] For these simulations, each system is composed of one ion and one ligand solvated in 600 water molecules. The distances between the ion and the center of the six membered ring (designated X) of benzene, toluene, phenol, 4-methylphenol, indole, and 3-methylindole, between the ion and the oxygen atom of ethanol, acetamide and NMA, and between the ion and the N_3 nitrogen atom of imidazole and 5-methylimidazole are used as reaction coordinate, and are sampled from 1 to 10 Å using 0.5-Å separated windows. A harmonic potential of force constant 10 kcal/mol/Å^2 is applied to bias the sampling. Each window is simulated for 2.5 ns and the last 2 ns are used to construct the unbiased PMF using WHAM.[173]

6.3 Results and Discussion

6.3.1. Optimized Dimers

The optimized geometries for Rb^+, Cs^+, and Tl^+ complexes with the twelve ligands considered in this work and some of their characteristic structural parameters are reported in Figure 6.2. Binding energies calculated without and with correction for BSSE (E and E^{CP}, respectively) and using the optimized Drude models (E^{MM}) are reported in Table 6.1. Figure 6.2

shows that the ion-ligand separation increases with the size of the ion ($Tl^+ < Rb^+ < Cs^+$), which is accompanied by a decrease (less negative) in the binding energy (see Table 6.1). Methyl (and ethyl in case of water) substituents result in higher binding energy and shorter distances between the ion and the ligand.

The three ions bind water, ethanol, acetamide, NMA, through the oxygen atom and bin imidazole, and 5-methylimidazole through the N_3 nitrogen atom. The minimum-energy structures in the cation–π complexes between the ions and benzene, toluene, phenol, 4-methylphenol, indole, and 3-methylindole are characterized by an ion on top of the six membered ring. Complexation of Rb^+ with phenol and 4-methylphenol stabilizes an additional conformer in which the ion is displaced toward oxygen. The binding energies of the latter conformers are slightly lower than those for cation–π complexes (see Table 6.1). No stable cation–π complexes are found for imidazole or 5-methylimidazole.

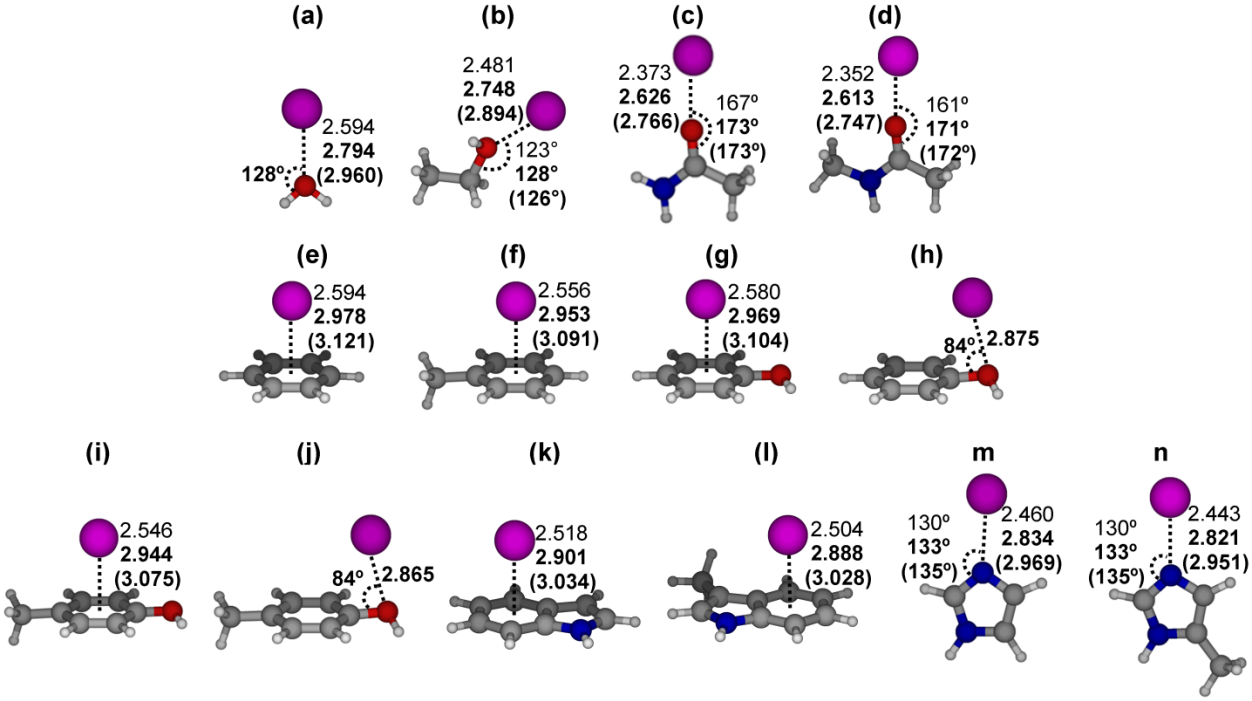

Figure 6.2. Optimized geometries at MP2 level of theory (see methods sections for details) for the complexes of Rb^+, Cs^+, and Tl^+ with: (a) water, (b) ethanol, (c) acetamide, (d) NMA (e) benzene, (f) toluene, (g and h) phenol, (i and j) 4-methylphenol, (k) indole, (l) 3-methylindole, (m) imidazole, and (n) 5-methylimidazole. The structures are illustrated with Rb^+. Structural parameters (bond length in Å and bond angles in degrees) are reported in normal for Tl^+, bold for Rb^+, and between brackets for Cs^+. Conformers h and j are reported for Rb^+ only since the corresponding Cs^+ and Tl^+ structures are not stable.

The data in Table 6.1 are in good agreement with reported ab initio data on some of the complexes considered in this work.[169,286–289,291–294] The calculated interaction energies of Rb^+ with monomers of benzene (–16.78 kcal/mol), toluene (–18.20 kcal/mol), phenol (–17.49 kcal/mol), and indole (–22.44 kcal/mol), are comparable to the corresponding experimental gas-phase binding enthalpies (at 298 K) of −16.4 ± 0.9,[287] −17.3 ± 1.1,[293] −16.8 ± 0.9,[288] and −21.6 ± 0.7 kcal/mol,[291] respectively. Interactions energies of Cs^+ with benzene, toluene, phenol, and indole monomers are, in respective, –16.21, –17.67, –17.06, and –22.23 kcal/mol and are also in good agreement with the corresponding experimental gas-phase binding enthalpies (at 298 K) of −15.4 ± 1.1,[287] −15.5 ± 1.1,[293] −15.8 ± 0.9,[288] and −20.9 ± 0.7 kcal/mol.[291] To the best of our knowledge, no experimental data are available for the studied Tl^+ complexes.

Table 6.1. BSSE-uncorrected and corrected binding energies (E and E^{CP}, respectively) of energy minima structures for complexes of Rb^+, Cs^+, and Tl^+ with various ligands. Binding energies calculated with the optimized Drude models (E^{MM}) are also shown. All energies are in kcal/mol.

Ligand	Rb^+			Cs^+			Tl^+		
	E	E^{CP}	E^{MM}	E	E^{CP}	E^{MM}	E	E^{CP}	E^{MM}
Water	–15.68	–15.24	–15.87	–13.73	–14.33	–13.54	–19.17	–17.15	–19.61
Ethanol	–18.18	–17.65	–18.02	–16.93	–16.08	–16.44	–25.39	–21.62	–22.30
Acetamide	–27.42	–26.71	–26.75	–25.82	–24.77	–24.82	–37.19	–32.35	–33.22
NMA	–28.67	–27.91	–27.74	–27.11	–25.98	–25.82	–39.77	–34.56	–34.60
Benzene	–17.96	–16.78	–16.86	–18.00	–16.21	–16.26	–33.68	–25.40	–26.55
Toluene	–19.52	–18.20	–18.10	–19.72	–17.67	–17.50	–37.72	–27.92	–28.83
Phenol	–18.76	–17.49	–17.81	–19.03	–17.06	–17.31	–35.60	–26.72	–27.74
	(–18.66)[a]	(–17.30)[a]	(–14.78)[a]						
4-Methylphenol	–20.20	–18.78	–19.26	–20.64	–18.39	–18.75	–39.45	–29.06	–30.22
	(–20.16)[b]	(–18.75)[b]	(–15.34)[b]						
Indole	–24.16	–22.44	–23.04	–24.93	–22.23	–22.71	–44.31	–33.15	–34.60
3-Methylindole	–25.04	–23.23	–23.35	–25.98	–23.08	–23.07	–46.22	–34.56	–35.61
Imidazole	–25.08	–24.36	–24.17	–23.69	–22.56	–22.46	–39.48	–33.53	–33.48
5-Methylimidazole	–26.88	–26.12	–26.08	–25.48	–24.27	–24.27	–42.50	–36.14	–35.81

[a] Data for structure 1h. [b] Data for structure 1j.

While K^+ is slightly smaller than Tl^+, thallium complexes with water, ethanol, NMA, imidazole, and 5-methylimidazole have binding energies larger (more negative) than the corresponding K^+ complexes, calculated at the MP2/6-311++G(d,p) level of theory.[18,30] Complexes of Tl^+ with the aromatic compounds (benzene, toluene, phenol, 4-methylphenol, indole, and 3-methylindole) are more stable even than the corresponding Na^+ complexes, optimized at MP2/6-311++G(d,p).[18] The markedly observed high binding energies in Tl^+ complexes are likely due to the high polarizability of the ion.

6.3.2. Interplay between Cation–π and π–π Interactions

To investigate the interplay between cation–π and π–π interactions, we optimize the structure of the $M^+(benzene)_2$ trimer (M = Rb, Cs, or Tl) in four different conformations (see Figure 6.3). Two of these possess the cation–π–π structural motif with the benzene dimer in an exact parallel (Figure 6.3a) or displaced parallel orientation (Figure 6.3b). The other two conformers are characterized by a π–cation–π arrangement in sandwiched (Figure 6.3c) or triangular (Figure 6.3d) geometry. The stability of these conformers follow the order triangular > sandwiched > displaced parallel > exact parallel. Similar to what is observed for the ion-aromatic dimers, complexes of Tl^+ with the benzene dimer are more stable than the corresponding Na^+ complexes that are calculated at MP2/6-311++G(d,p) level.[30] Figure 6.3 shows that cation–π–π structural motifs display separations between the ions and the center of the nearest benzene molecule that are shorter than those in the corresponding ion-benzene dimers (see Figure 6.2e). These motifs are also displaying a distance between benzene molecules that is also shorter in presence of the cation. That is indicating that cation–π and π–π interactions in these complexes are cooperative.[30,298,299] On the other hand, π–cation–π arrangements show ion-benzene separations that are longer than those in the ion-benzene dimers, showing that the two interactions are competitive.[30,300]

We evaluate the cooperativity of a complex, E_{coop}, as the difference between the total energy of the complex (E_{tot}) and the sum of all pairwise interaction energies in the complex:[30]

$$E_{\mathrm{coop}} = E_{\mathrm{tot}} - E_{\mathrm{M-B_1}} - E_{\mathrm{M-B_2}} - E_{\mathrm{B_1-B_2}} \qquad (6.2)$$

where $E_{\mathrm{M-B_1}}$ is the complexation energy of the ion with the closest benzene molecule, $E_{\mathrm{M-B_2}}$ is the ion's complexation energy with the other benzene molecule, and $E_{\mathrm{B_1-B_2}}$ is the complexation

energy of the benzene pair. These energies are calculated at the geometry obtained from the optimization of the whole complex, and corrected for BSSE (see Table 6.2).

Table 6.2 shows a negative E_{coop} for cation–π–π complexes, indicating that the two interactions strengthens one another.[30,298,299] The positive E_{coop} observed in π–cation–π complexes indicates on the other hand that the two interactions are competitive.[30,300] Table 6.2 shows that the E_{coop} term is greatest for Tl^+ complexes and is similar for Rb^+ and Cs^+ complexes.

The cooperative or anti-cooperative behavior depends on the orientation of induced dipoles in benzene molecules.[30] Parallel induced dipoles are produced in cation–π–π complexes and result in a stabilization of the complex. Induced dipoles in benzene molecules of π–cation–π complexes are antiparallel, which destabilizes the complex. Reproducing the cooperative or anti-cooperative interplay between cation–π and π–π interactions requires explicit description of polarization and hence represents a shortcoming of conventional, non-polarizable force field.

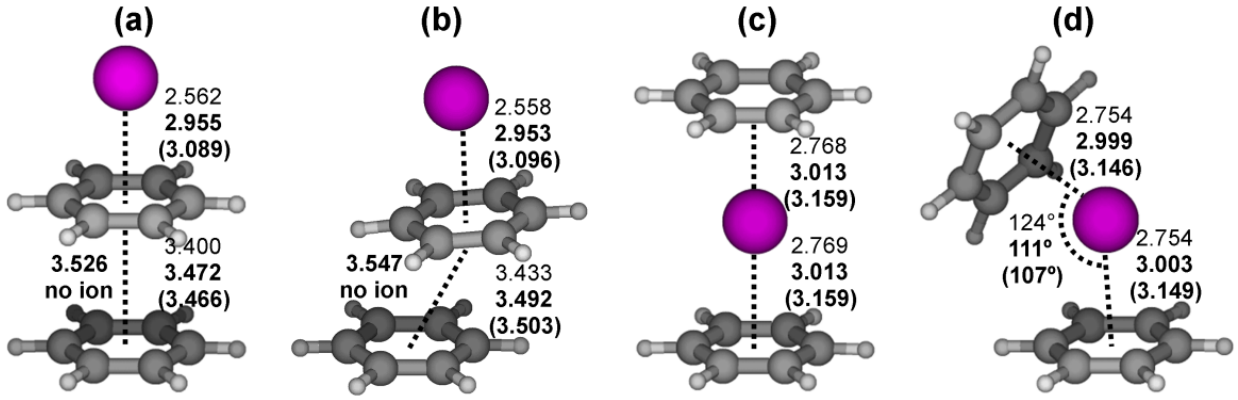

Figure 6.3. Optimized geometries at MP2 level of theory (see method section for details) for the complexes of each ion with two benzene molecules. The geometry of the complexes is exact parallel (panel a), parallel displaced (panel b), sandwiched (panel c), and triangular (panel d). Structures are illustrated with Rb^+ complexes (data in bold) but corresponding parameters for the Cs^+ (bold between brackets) and Tl^+ (not bold) complexes are reported.

Table 6.2. BSSE-corrected complexation energies calculated at the MP2 level, and corresponding interaction energies calculated using the polarizable models (in brackets). E_{tot} is the total complexation energy, E_{A-B} are complexation energies of the different fragment pairs, and E_{coop} is the cooperativity [see Equation (6.2)]. All energies are in kcal/mol.

Complex	Ion	E_{tot}	E_{M-B_1}	E_{M-B_2}	$E_{B_1-B_2}$	E_{coop}
	Tl^+	–32.64	–24.92	–3.31	–2.06	–2.35
		(–27.37)	(–24.56)	(–2.45)	(1.01)	(–1.37)
4(a)	Rb^+	–22.58	–16.73	–2.55	–2.58	–0.72
		(–19.51)	(–16.72)	(–1.85)	(–0.11)	(–0.83)
	Cs^+	–21.94	–16.17	–2.43	–2.55	–0.79
		(–18.75)	(–16.12)	(–1.80)	(–0.04)	(–0.79)
	Tl^+	–34.05	–24.85	–3.56	–3.26	–2.38
		(–21.93)	(–24.40)	(–2.66)	(6.63)	(–1.5)
4(b)	Rb^+	–24.00	–16.73	–2.73	–3.82	–0.72
		(–15.23)	(–16.71)	(–2.00)	(4.34)	(–0.86)
	Cs^+	–23.31	–16.14	–2.61	–3.78	–0.78
		(–14.29)	(–16.08)	(–1.96)	(4.57)	(–0.82)
	Tl^+	–42.91	–26.16	–26.16	–0.39	9.80
		(–48.37)	(–26.20)	(–26.20)	(–0.54)	(4.57)
4(c)	Rb^+	–31.45	–16.80	–16.80	–0.18	2.33
		(–32.30)	(–16.80)	(–16.80)	(–0.33)	(1.63)
	Cs^+	–30.13	–16.27	–16.27	–0.11	2.52
		(–31.08)	(–16.21)	(–16.21)	(–0.25)	(1.59)
	Tl^+	–43.40	–26.06	–26.05	–1.42	10.13
		(–49.41)	(–26.14)	(–26.13)	(–1.11)	(3.97)
4(d)	Rb^+	–32.05	–16.79	–16.78	–1.33	2.85
		(–32.52)	(–16.80)	(–16.79)	(–1.06)	(2.13)
	Cs^+	–31.10	–16.26	–16.24	–1.25	2.65
		(–31.57)	(–16.21)	(–16.19)	(–1.02)	(1.85)

[a] data for structure 3a [b] data for structure 3b [c] data for structure 3c [d] data for structure 3d

6.3.3. Potential Energy Surfaces

PESs calculated for Rb^+, Cs^+, and Tl^+ in complex with the various ligands are reported in Figure 6.4. For water, ethanol, acetamide, and NMA, curves are calculated by scanning the $O\cdots M^+$ distance (Figures 6.4a–d). For benzene, toluene, phenol, 4-methylphenol, indole, and 3-methylindole, curves are generated by scanning the distance between the ion and the center of the six membered ring (labeled X) (Figures 6.4e–j). For complexes of the ions with imidazole and 5-methylimidazole, curves are generated by scanning the distance between the ions and the N_3 nitrogen (Figures 6.4k and 6.4l).

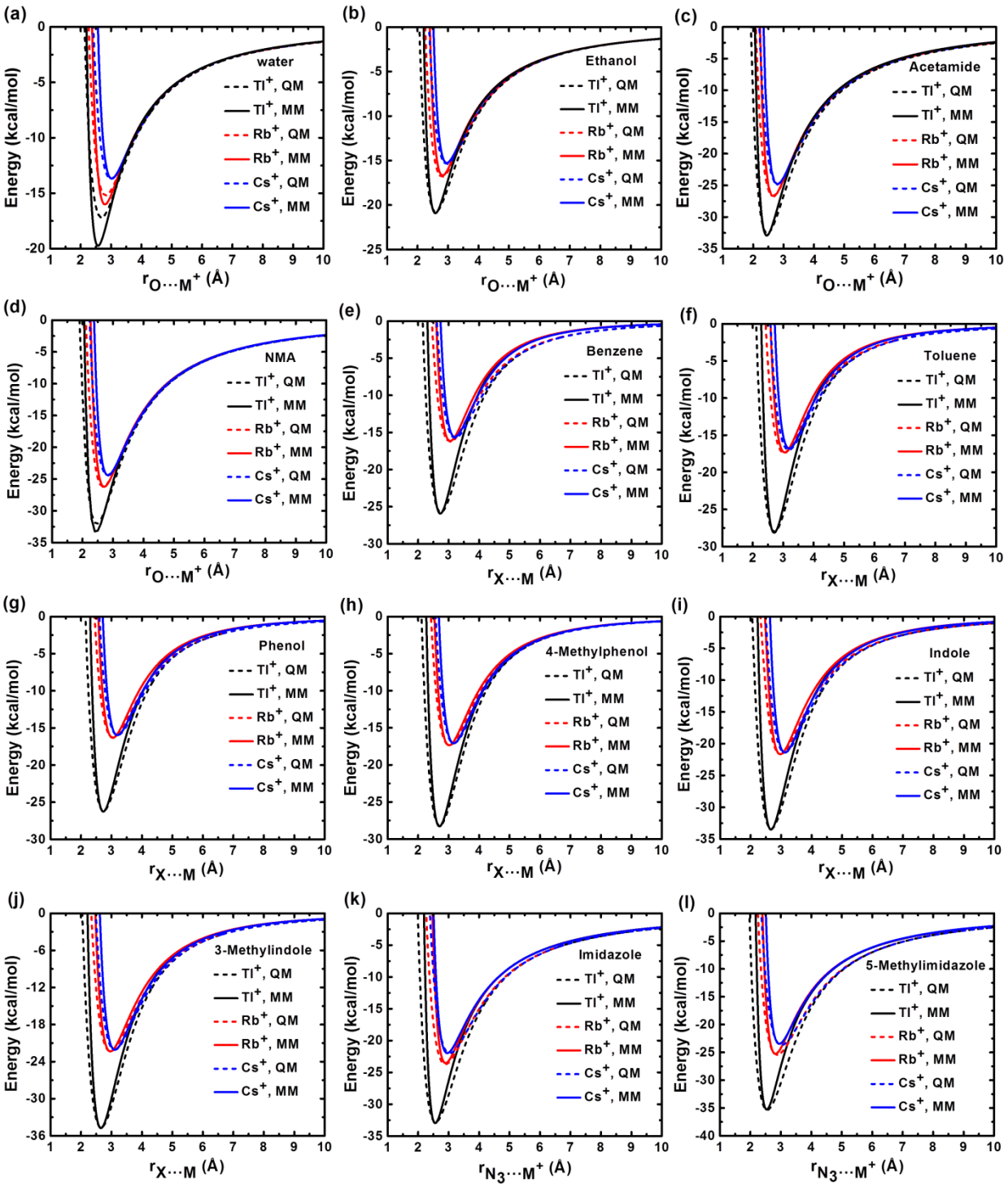

Figure 6.4. Potential energy curves from ab initio MP2 calculations (dashed lines) and from polarizable models (solid lines) for Tl^+ (in black), Rb^+ (in red), and Cs^+ (in blue) interactions. The $M^+\cdots O$ distance is scanned for ion complexes with water, ethanol, acetamide, NMA (panels a–d). The $M^+\cdots X$ distance is scanned for benzene, toluene, phenol, 4-methylphenol, indole, and 3-methylindole complexes (panels e–j) and the $M^+\cdots N_3$ distance is scanned for imidazole (panel k) and 5-methylimidazole (panel l). In all scans the ion and the ligand possess relative orientation as found in the global minimum structures (see Figure 6.3).

6.3.4. Optimized Force Fields

A new Drude model is optimized for Tl^+. The generic LJ parameters of Tl^+ are optimized to reproduce the experimental hydration free energy of the ion. The optimized values are E_{min} = 0.24 kcal/mol and $R_{min}/2$ = 1.61 Å. In addition, the Drude model of Tl^+ is characterized by a charge of +1 and a polarizability of 3.5 $Å^3$.[309] Similar to Tl^+, the Drude model for alkali ions[118] were optimized on the ion's hydration free energies. The optimized pair-specific LJ parameters for Rb^+, Cs^+, and Tl^+ interactions with the different ligands are reported in Table 6.3. Models of Cs^+ and imidazole give binding energies for the Cs^+–imidazole pair in good agreement with ab initio results and thus no pair-specific LJ parameters are adjusted for the pair. Optimized parameters for ion-acetamide interactions are transferable to the corresponding ion-NMA interactions. Optimized parameters for Rb^+ and Cs^+ interactions with benzene are transferable to toluene. Adjusted parameters for Rb^+, Cs^+, and Tl^+ interactions with phenol, indole, and imidazole and for Tl^+-benzene complex are readjusted for the ion interactions with the corresponding methyl derivatives of these ligands. These parameters are optimized to reproduce the PESs of the interacting dimers (see Figure 6.4). Without further adjustments, the parameters yield ion-ligand binding energies in the relaxed complexes (keeping only bonds to hydrogen atoms at their equilibrium values) in very good agreement with ab initio results (see Table 6.1). The Drude model for Tl^+, optimized on the ion's hydration free energy, slightly overestimates the ab initio calculated binding energy of Tl^+-water dimer (See Table 6.1). The optimized model for Rb^+-phenol and Rb^+-4-methylphenol slightly underestimates the binding energy of the local minima structures in these complexes (see Figure 6.2h for phenol and 6.2j for 4-methylphenol). Drude models for ion-benzene interactions predict the cooperativity in the ion-benzene-benzene complexes and anti-cooperativity in the benzene-ion-benzene complexes, which is again an advantage over non-polarizable FFs. Except for underestimating the anti-cooperativity in benzne-Tl^+-benzene complexes, the models yield E_{coop} in good agreement with ab initio results (see Table 6.2).

Table 6.3. Pair-specific LJ parameters between Rb^+, Cs^+, and Tl^+ and atom sites (i) in the interacting ligands.[a]

Molecule	Atom, i	Pair-specific LJ parameters					
		Rb^+		Cs^+		Tl^+	
		$Emin_{iRb}{}^+$ (kcal/mol)	$Rmin_{iRb}{}^+$ (Å)	$Emin_{iCs}{}^+$ (kcal/mol)	$Rmin_{iCs}{}^+$ (Å)	$Emin_{iTl}{}^+$ (kcal/mol)	$Rmin_{iTl}{}^+$ (Å)
Ethanol	O	0.36393	3.45035	0.34892	3.61366	0.48589	3.21373
	C[b]	0.11022	4.50428	0.10095	4.59408	0.09305	4.47685
NMA	O	0.02483	4.10902	0.04981	4.06701	0.03440	3.85742
	C[c]	0.29896	4.76008	0.32948	4.84531	0.09691	4.82440
NMA	O	0.02483	4.10902	0.04981	4.06701	0.03440	3.85742
	C[c]	0.29896	4.76008	0.32948	4.84531	0.09691	4.82440
Benzene	C[d]	0.60104	3.62409	0.71806	3.72491	1.29609	3.27746
Toluene	C[d]	0.60104	3.62409	0.71806	3.72491	1.38705	3.2477
Phenol	O	0.40945	3.69463	0.55338	3.77118	1.11134	3.30617
4-Methylphenol	O	0.35381	3.71000	0.50913	3.77142	1.12516	3.28371
Indole	C[d]	0.39408	3.68541	0.59130	3.73889	1.12556	3.28432
3-Methylindole	C[d]	0.3109	3.74110	0.50368	3.77205	1.02934	3.29772
Imidazole	N[e]	0.59933	3.51047	–	–	1.35264	3.06296
5-Methylimidazole	N[e]	0.69996	3.36015	0.79997	3.46572	2.27016	2.92798
	C[f]	0.16110	4.58099	0.11606	4.83354	0.06205	4.57728

[a] For ion-water and Tl^+-imidazole interactions, no pair-specific LJ parameters are optimized, instead the default mixed LJ parameters are used. [b] Methylene carbon atom. [c] Carbonyl carbon atom. [d] Carbon atoms of the six membered rings. [e] The N_3 nitrogen atom (see Figure 6.1). [f] Carbon atom between the two nitrogen atoms.

6.3.5. Hydration of Tl^+

The Drude model of Tl^+ is adjusted to reproduce the experimental hydration free energy of the ion and yields a value of –70.7 kcal/ mol, in agreement with the experimental value of –71.65 kcal/mol.[304] In comparison the Drude model of Tl^+ reported by Lev *et al.*[309] is found (this work) to show a hydration free energy of –67.7 kcal/mol. In comparison, Vchirawongkwin *et al*. have calculated hydration free energies of –84 ± 16 and –222 ± 7 kcal/mol using QM/MM and classical MD simulations, respectively.[306] The hydration free energy of Tl^+ is close to that of K^+. The Drude model for K^+ yield a hydration free energy of –67.9 kcal/mol[118] and the experimental value is –70.5 kcal/mol.[304]

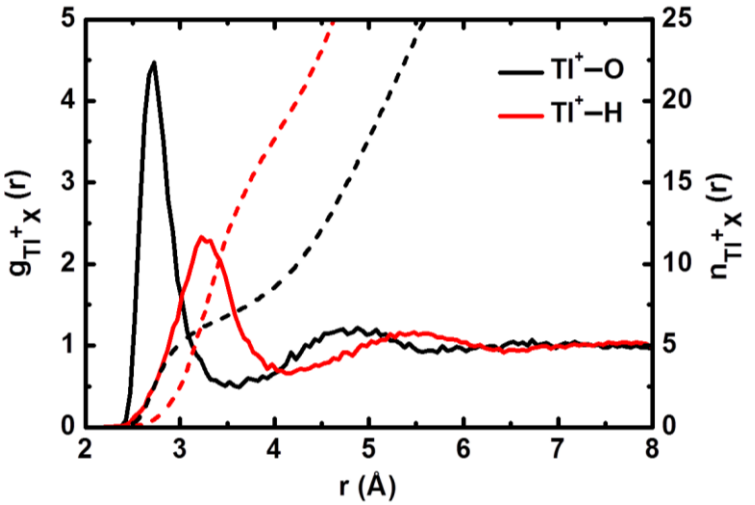

Figure 6.5. Tl^+–O and Tl^+–H radial distribution functions (solid lines, scale on left) and running integration numbers (dashed lines, scale on right) of Tl^+ in water at 298.15 K.

The hydration structure of Tl^+ is investigated from the analysis of a 5 ns MD simulation of one Tl^+ ion solvated in 250 SWM4-NDP water molecules. Correlation functions $g_{Tl^+O}(r)$ and $g_{Tl^+H}(r)$ are reported in Figure 6.5. Function $g_{Tl^+O}(r)$ shows a maximum at 2.71 Å and a minimum at 3.60 Å. Integration up to this minimum yields a coordination number of 7.1 water molecules in the first solvation shell of the ion. By comparison, the Drude model of Tl^+ of Lev *et al.* shows a first peak centered within 2.77–2.82 Å with a coordination number of 7.[309] Using QM/MM MD simulations, Vchirawongkwin *et al*. reported a first peak of the $g_{Tl^+O}(r)$ function at 2.79 Å with a coordination number of 5.9[306] and Lev *et al.* calculated a first peak centered in the range 2.66–2.80 Å with a coordination number of 7.[309] Function $g_{Tl^+H}(r)$ shows a first peak at 3.24 Å and a minimum at 4.15 Å (see Figure 6.5). Like the hydration free energy, the hydration structure of Tl^+ is very similar to that of K^+. The Drude model of K^+ yields[118] $g_{K^+O}(r)$function with a first peak centered at 2.74 Å with its minimum at 3.56 Å and with a first shell coordination number of 6.9.

6.3.6. Ion-Ligand Interactions in Aqueous Solution

In aqueous solutions, water competes with the ligands for binding an ion. Compared to gas phase, complexes of the three ions and the different ligands are thus expected to be weaker in aqueous solution.[30,31,296,297] The binding affinity of Rb^+, Cs^+, and Tl^+ with the ligands in liquid water is estimated from PMF calculations (see Figure 6.6). Binding of a ligand to a hydrated metal ion results in expulsion of a number of water molecules from the ion's first solvation shell.

Figure 6.6 also shows the number of water molecules in the first solvation shell of Rb^+, Cs^+, and Tl^+ as a function of the ion-ligand separation. These coordination numbers are calculated from the pair distribution function g_{MO} up to the first minimum (3.80 Å for Rb^+, 4.10 Å for Cs^+, and 3.60 Å Tl^+). Table 6.4 reports separations at which the PMFs are minima and the value of the PMFs, the number of water molecules coordinating each ion, and the number of water molecules expulsed from the ion's first shell (Δn) at these minima. The PMF minima correspond to directly coordinated ions and no solvent-separated complex is observed.

While Rb^+ complexes are more stable in gas phase, those of Cs^+ are more stable in aqueous solution. This is in line with our finding for binding affinity of benzene with Li^+, Na^+, and K^+.[30,31] Except for its complexes with ethanol, acetamide, and NMA, complexes of Tl^+ are more stable in water than the corresponding Rb^+ and Cs^+ complexes. Ethanol, acetamide, NMA, imidazole, and 5-methylimidazole bind the metal ions via a single atom (O or N) which results in the expulsion of about one water molecule from the first solvation shell of the ion. Binding of the aromatic ligands (benzene, toluene, phenol, 4-methylphenol, indole, and 3-methylindole) through their large hydrophobic phases results in the expulsion of 2–2.5 water molecules from the ion's first solvation shell.

It is observed that complexes of the three ions with ethanol, acetamide, NMA, imidazole, and 5-methylimidazole are weaker than cation–π complexes. This is likely due to the hydrophilicity of these ligands which results in the ligand being preferably hydrated and hence weakens their affinity toward the cations. This is in line with the finding from Gallivan and Dougherty[297] from studying complexes of methylammonium with benzene and acetate in gas phase and in water. These authors found that, contrary to gas phase, methylammonium binds benzene more strongly than acetate in water.[297]

In a previous work, we found that benzene does not bind the first shell of Li^+ and Na^+ in water and binds K^+ with an affinity of –1.2 kcal/mol. Table 6.4 reports a binding free energy of –2.9 kcal/mol for the Rb^+–benzene complex and –4.3 kcal/mol for the Cs^+–benzene complex. This trend in binding affinity between alkali ions and benzene is the reverse of gas phase affinities.

The solubility of benzene in water can be enhanced or reduced by salts, a phenomenon known as salting-in and salting-out.[310] For alkali chloride solutions, it follows the trend CsCl > RbCl > KCl > NaCl.[310] Interestingly, this is the same trend observed for binding affinity of benzene with the cations of these salts in water. This is suggesting that cation–π interactions are playing a role in the extent of benzene solubility in water; the larger the affinity between the cation and benzene, the higher the solubility.[30]

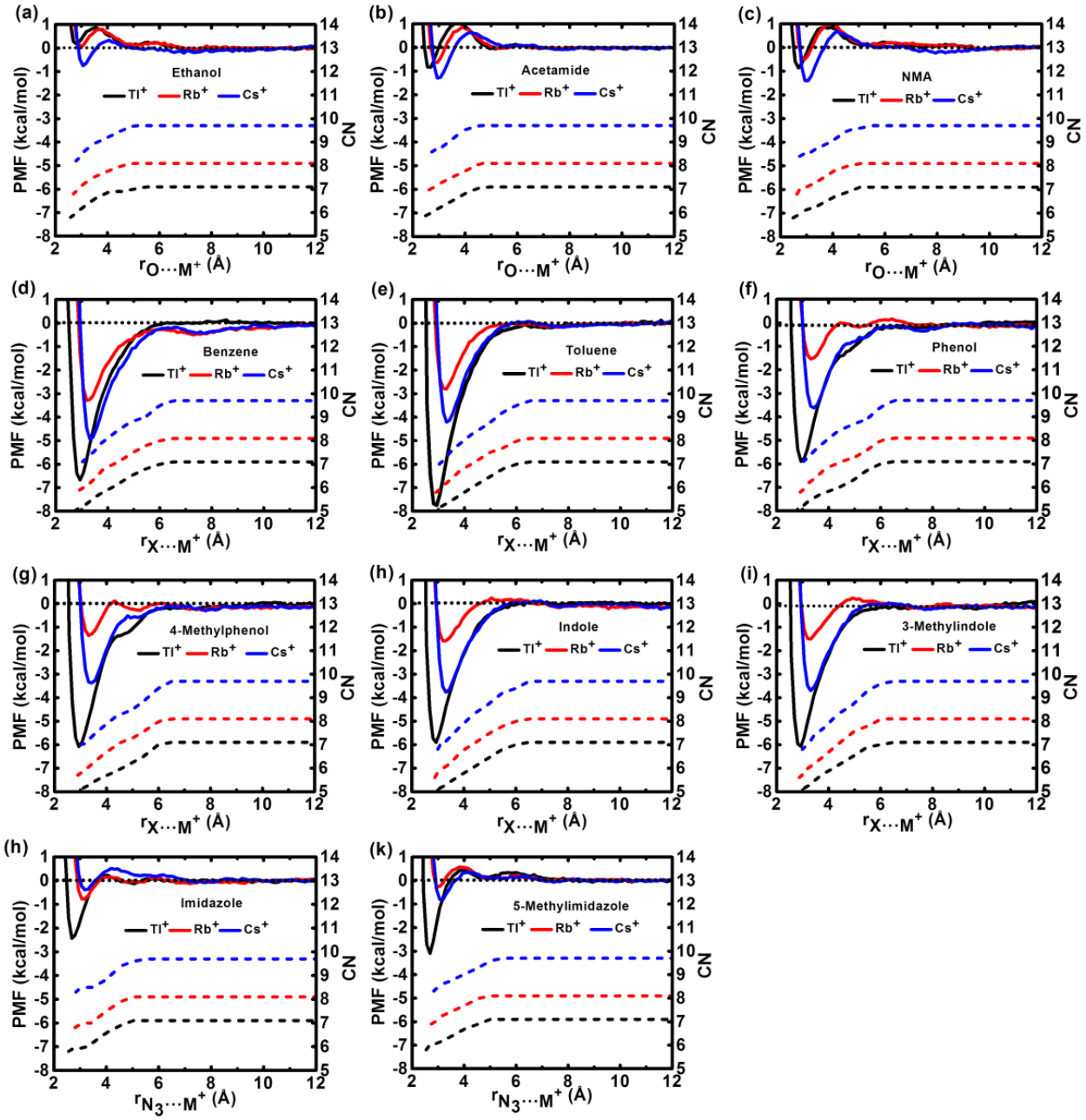

Figure 6.6. Potentials of mean force (PMFs) between Rb^+, Cs^+, and Tl^+ and the different ligands (solid lines) and water-coordination number (CN) of the three ions as a function of their separation from each ligand (dotted lines, scale on the left).

Table 6.4. Characteristic properties of the ion-ligand PMFs[a]

Ligand	Rb^+			Cs^+			Tl^+		
	ΔG_{bind}	r (Å)	Δn	ΔG_{bind}	r (Å)	Δn	ΔG_{bind}	r (Å)	Δn
Ethanol	0.06	3.00	1.0	–0.8	3.07	1.1	0.17	2.81	1.1
Acetamide	–0.6	2.92	0.9	–1.3	3.00	1.0	–0.8	2.63	1.1
NMA	–0.5	2.91	1.0	–1.4	3.01	1.2	–0.9	2.70	1.2
Benzene	–2.9	3.25	2.0	–4.3	3.37	2.3	–6.7	2.94	1.9
Toluene	–2.8	3.25	2.0	–4.3	3.37	2.3	–7.7	2.90	2.0
Phenol	–1.3	3.33	1.8	–3.1	3.43	2.2	–5.9	2.96	1.9
4-Methylphenol	–1.1	3.33	2.0	–2.8	3.43	2.4	–6.1	2.94	2.0
Indole	–1.3	3.25	2.1	–3.2	3.33	2.5	–5.9	2.94	2.0
3-Methylindole	–1.3	3.25	2.1	–3.2	3.32	2.5	–6.1	2.92	2.0
Imidazole	–0.4	3.13	1.1	–0.8	3.19	1.2	–2.4	2.74	1.2
5-Methylimidazole	–0.3	3.00	1.0	–0.8	3.13	1.1	–3.1	2.69	1.1

[a] r is the ion-ligand separation at which the PMF is minimum. E and Δn are the binding free energy (in kcal/mol) and the number of water molecules lost from the ion's first solvation shell calculated at an ion-ligand separation = r.

6.3.7. Cation–π and π–π Interactions in Water

Ab initio calculations on complexes between one ion and two benzene molecules show that π–cation–π complexes are more stable than cation–π–π ones (see Table 6.2). The interplay between cation–π and π–π interactions in aqueous medium is investigated via MD simulations of two benzene molecules and one ion (Rb^+, Cs^+, or Tl^+) in 600 water molecules. The arrangement of the two benzene molecules relative to the cation is investigated using 105-ns simulations. To avoid unproductive sampling, an energy restraint is applied to prevent the centers of the two benzene molecules from separating by more than 7 Å in one simulation and to prevent the cation and one benzene molecule from separating by more than 6 Å in a different simulation. These biased simulations represent the interaction of the ion with a pre-formed benzene dimer and the interaction of the second benzene molecule with a pre-formed cation–benzene pair.[30] A harmonic force constant of 5 kcal/mol/Å^2 is used for the restraints.

Figures 6.7a,c,e present the distribution of the ion as the *conditional* free energy surface – $k_B T \ln[\rho_M(z_M, r_M)/2\pi r_M]$, where $\rho_M(z_M, r_M)$ is the ion density relative to the restrained benzene

dimer, in cylindrical coordinates. Figures 6.7b,d,f show the distribution of one benzene molecule as the conditional free energy surface $-k_B T \ln[\rho_X(z_X, r_X)/2\pi r_X]$, where $\rho_X(z_X, r_X)$ is the benzene density relative to the restrained ion-benzene complex, in cylindrical coordinates.

Figure 7a shows a maximum density of Rb^+ at z = 0 Å and r = 0.0 or ~2.0 Å, where the ion is coordinating both benzene molecules (located at $z \sim \pm$ 2.6 Å and r = 0 Å) and forming a sandwiched or triangular conformation. An intermediate Rb^+ density is found at $z \sim$ 6.0 Å and r < 1 Å, where the system is forming a Rb^+–benzene–benzene stacked conformation.

Figure 6.7b shows three markedly populated regions. The most populated regions corresponds to triangular conformation at $z \sim$ –0.5 Å and r ~ 3.5 Å and benzene–Rb^+–benzene sandwich conformation at $z \sim$ –3.5 Å and r < 1 Å, with the first being slightly more populated. The Rb^+–benzene–benzene stacked conformation at $z \sim$ 8 Å and r < 2 Å is on the other hand less populated. The simulations involving Cs^+ and Tl^+ display similar features (see Figures 6.7c,d,e,f).

Simulations are thus showing that, like gas phase, π–cation–π arrangements are more stable in aqueous solutions than cation–π–π structures, in agreement with our previous finding for K^+ and NH_4^+ complexes with a benzene dimer in water.[30]

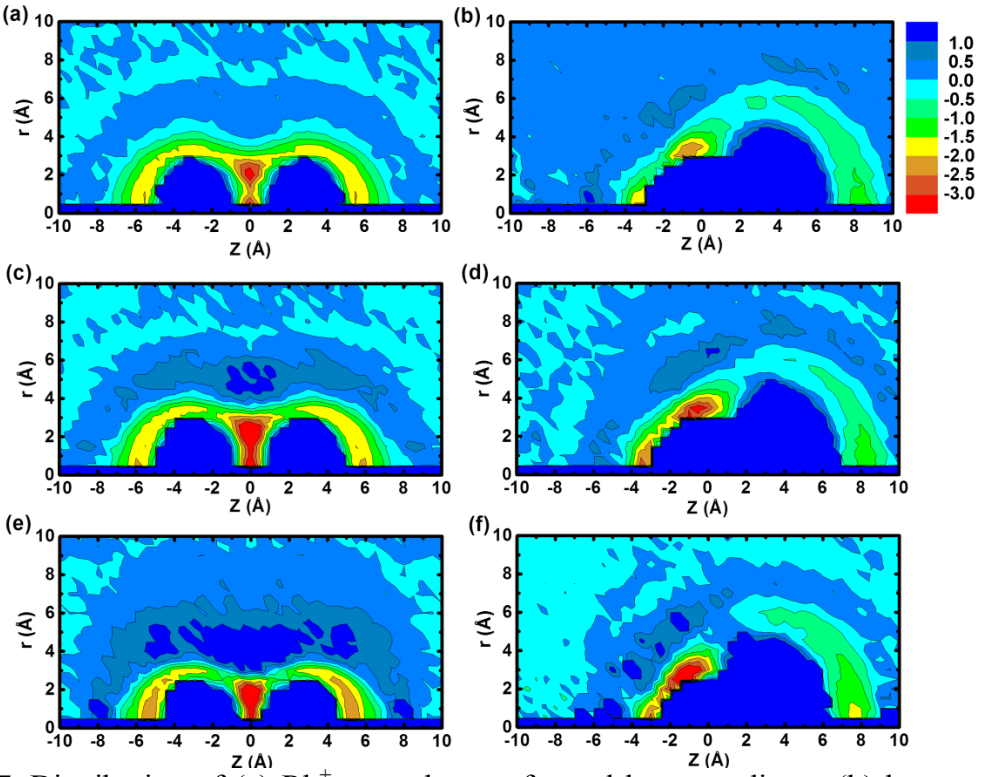

Figure 6.7. Distribution of (a) Rb^+ around a pre-formed benzene dimer. (b) benzene around a pre-formed Rb^+–benzene pair. (c) Cs^+ around a pre-formed benzene dimer, (d) benzene around a pre-formed Cs^+–benzene pair, (e) Tl^+ around a pre-formed benzene dimer, (f) benzene around a pre-formed Tl^+–benzene pair. Densities are presented as the free energy surfaces $-k_BT \ln[\rho(z,r)/2\pi r]$, where $\rho(z,r)$ is the distribution relative to the restrained solutes, in cylindrical coordinates. Benzene molecules are at $z \sim \pm 2.6$ Å and $r = 0$ Å in panels (a), (c), and (e). In panels (b), (d), and (f) the ion is at $z = r = 0$ Å and the benzene molecule is at $r = 0$ Å and $z \sim 3.3$ Å for Rb^+ and Cs^+, and ~3.0 for Tl^+.

6.3.8. Tl^+–π Interactions in Proteins

The observed higher stability of Tl^+–π complexes in aqueous solutions (see Table 6.4) is suggesting that these complexes are common among chemical and biological systems. Recently, Caracelli *et al*. surveyed the Cambridge Structural Database for M–π(arene) interactions for M = gallium, indium and thallium and found that Tl–π(arene) interactions are found in nearly 14% of thallium(I)-containing structures with at least one arene ring.[311] To examine the existence of Tl^+–π complexes in proteins, we investigated Tl^+-bound protein structures in the Protein Data Bank (PDB)[312] for binding of Tl^+ with the side chains of Phe, Tyr, Trp, and His.

We searched the PDB for structures containing thallium as a ligand (TL). Of the 40 revealed structures, 25 are proteins and the rest are DNA and RNA structures. These 25 protein structures correspond to 7 distinct protein families; the sodium proton antiporter PaNhaP (PDB

ID: 4CZA), the human TRAAK K^+ channel (PDB IDs: 4WFG and 4WFH), the bacterial KcsA K^+ channel (PDB IDs: 1R3J, 1R3K, 2BOB, 2BOC, 2DWD), Fructose-1,6-Bisphosphatase (PDB IDs: 1FPJ, 1FPK, 1FPL, 1NV0, 1NV1, 1NV2, 1NV3, 1NV4, 1NV5, 1NV6, 1NV7), the glutamate transporter homologue GltPh (PDB IDS: 4P1A, 4P6H), the bacterial chaperone protein GroEL (PDB IDS: 2YNJ, 3E76), Glutamine synthetase (PDB ID: 1F1H), and Fosfomycin resistance protein A (FosA) (PDB ID: 1LQO). Of these seven protein families, structures of the last three families show Tl^+–π complexes (see Figure 6.8).

GroEL is a bacterial chaperone protein that assembles into a homotetradecameric complex and uses Mg^{2+} and K^+ as cofactors to bind and hydrolyze ATP. Using Tl^+ to identify monovalent cation binding sites, the structure of GroEL (PDB ID: 3E76) is crystalized at 3.94 Å resolution and show four Tl^+-binding sites.[313] One of these sites (Figure 6.8a) shows a cation–π complex between Tl^+ and Phe 219. This binding site is however located far from the nucleotide-binding pocket and from the interface between monomers which makes its functional significance unresolved.[313]

Glutamine synthetase (GS) catalyzes the ATP-dependent condensation of ammonium and glutamate to form glutamine, ADP, and free phosphate. The structure of GS complexed with thallium, used as analogue to determine ammonium binding sites, is determined at 2.67 Å resolution (PDB ID: 1F1H).[314] The crystallographic identified binding site for ammonium is showing Tl^+ forming a cation–π–π motif with Tyr179 and Phe180 (Figure 6.8b).

The fosfomycin resistance protein (FosA) is a Mn(II)-dependent metalloenzyme that catalyzes the addition of glutathione (GSH) to the broad-spectrum antibiotic fosfomycin rendering it inactive.[315] The crystal structure of thallium-bound FosA is resolved at 2.0 Å resolution. The structure reveals three cation–π complexes (see Figure 6.8). The first is between Tl^+ and Tyr62, the second is between Tl^+ and Tyr100 and His112, and the third shows Tl^+ complexing the side chains of Tyr39, Trp46 and His7.

While is is hard to draw a quantitative conclusion about the occurrence of Tl^+–π interactions in proteins, due to the lack of sufficient data, the calculated strong binding affinity between the ion and aromatic compounds and the observed complexes in available protein structures are suggesting that these interactions are significant in protein structures.

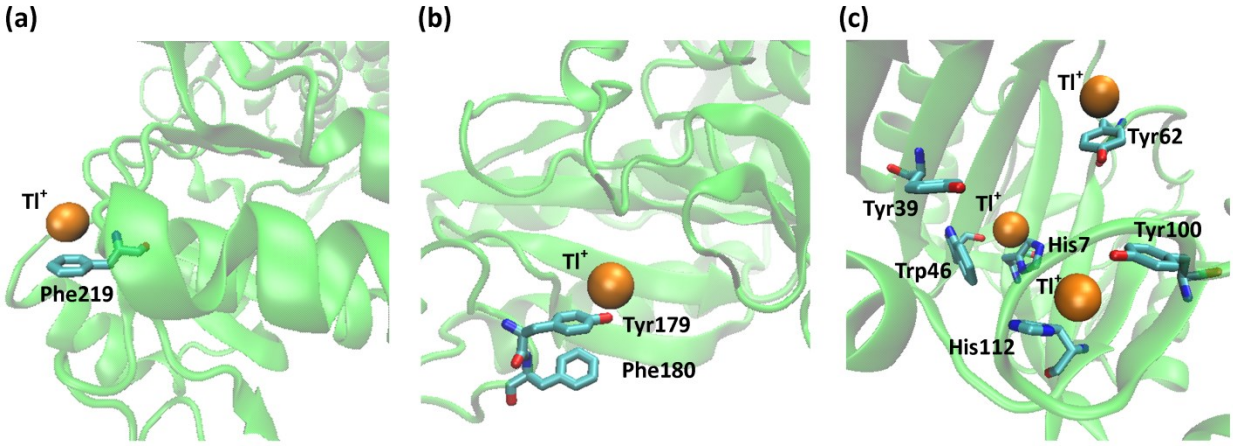

Figure 6.8. Tl^+–π interactions found in protein structures. Panel (a) shows binding of Tl^+ to Phe219 in the bacterial chaperone protein GroEL (PDB ID: 3E76). Panel (b) shows cation–π interactions between Tl^+ and Tyr179 and Phe180 in the crystal structure of glutamine synthetase (PDB ID: 1F1H). Panel (c) shows three cation–π complexes (between Tl^+ and Tyr62, between Tl^+ and both Tyr100 and His112, and between Tl^+ and Tyr39, Trp46, and His7) in the crystal structure of FosA (PDB ID: 1LQO).

6.4. Conclusion

Ab initio calculations on the complexes of Rb^+, Cs^+, and Tl^+ with monomer ligands (water, acetamide, N-methylacetamide, benzene, toluene, phenol, 4-methylphenol, indole, 3-methylindole, imidazole, and 5-methylimidazole) are performed at the MP2 level of theory. It is found that complexes of Tl^+ are more stable than those of Rb^+ and Cs^+. Tl^+ complexes with aromatic compounds are even more stable than the corresponding complexes of the much smaller Na^+ ion. Calculations on the ion–$(benzene)_2$ systems show that cation–π and π–π interactions cooperate in cation–π–π motifs but compete in π–cation–π motifs.

A polarizable model for Tl^+ is optimized to reproduce the ion's hydration free energy. The model predicts a hydration structure and hydration free energy of the ion that closely resembles those of K^+. This is likely a reason for the ability of Tl^+ to replace K^+ in biological systems.[302,303] Polarizable of models for the interaction Rb^+, Cs^+, and Tl^+ with the various ligands are parameterized to reproduce ab initio calculated PESs of the ion-ligand dimers. These models reproduce the ab initio calculated binding energies of the dimers and the interplay between cation–π and π–π interactions.

Potentials of mean force between cation–ligand pairs in aqueous solution show that cation–π complexes are more stable than electrostatic interactions in aqueous solution. Especially with aromatic compounds, the complexes of Tl^+ are more stable than those of Rb^+ and Cs^+ in

water. That large stability is likely a reason for the higher affinity of biological system toward Tl^+, compared to K^+.[302,303] While Rb^+ complexes are more stable than Cs^+ complexes in gas phase, the reversed trend is observed in water. The trend of binding affinity between alkali ions and benzene in water is suggesting a role of cation–π interactions on the influence of salts on benzene solubility in water; ions with high binding affinity to benzene results in benzene being more soluble in aqueous solutions of their salts.

Simulations of one ion and two benzene molecules in water show that, similar to gas phase, complexes with π–cation–π motifs are more stable than those with cation–π–π arrangements.

A survey of the PDB for cation–π complexes involving Tl^+ suggests that these complexes exist in protein structures.

7. Cation–π Interactions between Quaternary Ammonium Ions and Aromatic Amino Acids Side Chains in Aqueous Solution

Abstract

Cation–π interactions are known to play important roles in stabilization of protein structures, in molecular recognition, and in protein-ligand interactions. They contribute to the binding of quaternary ammonium ligands (mainly RNH_3^+ and $RN(CH_3)_3^+$) to various protein receptors and are also likely involved in the blockage of potassium channels by tetramethylammonium (TMA^+) and tetraethylammonium (TEA^+). Polarizable molecular models are developed for NH_4^+, TMA^+, and TEA^+ interacting with benzene, toluene, 4-methylphenol, and 3-methylindole (aromatic compounds used as models for side chains of phenylalanine, tyrosine, and tryptophan). The models are adjusted based on the ab initio properties of the complexes calculated at the MP2(full)/6-311++G(d,p) level of theory. They are used in molecular dynamics simulations to investigate the stability of cation–π pairs in aqueous solution, and the directionality of their interaction. While the gas-phase affinity with a given aromatic compound follows the trend $NH_4^+ > TMA^+ > TEA^+$, simulation results show a reversed trend in aqueous solutions, likely due to a contribution from the hydrophobic effect. Both gas phase and aqueous solution studies are showing that the ions preferably binds the aromatic moiety "en face" rather than "edge-on".

7.1. Introduction

Cation–π interactions refer to the non-covalent association between an inorganic cation or the cationic moiety of an organic molecule and π electrons of alkenes, alkynes, or aromatics.[268] In proteins, cation–π interactions usually involve one of the following combinations: (1) the ammonium group of lysine (Lys) or the guanidinium group of arginine (Arg) and the aromatic side chains of phenylalanine (Phe), tyrosine (Tyr), or tryptophan (Trp);[6,269] (2) aromatic amino acids and inorganic cations (such as K^+ and NH_4^+) or organic cations; or (3) cationic side chains of Lys and Arg and aromatic ligands.

Cation–π interactions between amino acids side chains of protein structures are found more commonly than expected from chance alone.[269,274,277−279] They are also commonly found at protein-protein[316] and protein-DNA interfaces.[7,10] Cation–π interactions contribute to protein stability,[8,280−282] protein-ligand interactions,[6,11] and to molecular recognition in general.[317]

Electrostatics and polarization forces represent the dominant contributions to cation–π interactions.[6,273,276] Contributions from other forces such as dispersion and charge transfer are much smaller. The strong electric field produced by the cation, especially a small and/or multivalent ion, results in electronic polarization being a determining factor in the stability of the complex.[30,31,273] For these interactions, polarizable force fields are thus believed to be more accurate than pairwise-additive ones.[30,31,273,276]

Ab initio investigations on cation−π interactions involving quaternary ammonium ions have not received as much attention as those involving metal ions.[30,31,289,290,294,295,318–324] Ammonium (NH_4^+) can be viewed as a minimal model compound for the side chain of Lys (RNH_3^+). Tetramethylammonium (TMA^+) is a model for ligands with a $RN(CH_3)_3^+$ cationic moiety, such as trimethyllysine (one of the methylation products of lysine by methyltransferases)[325,326] or acetylcholine (known to bind through its quaternary ammonium head to the π electrons of a Tyr residue in acetylcholinesterase).[317] TMA^+ inhibits the activity of most potassium channels, and so does the larger tetraethylammonium (TEA^+).[327,328] Ab initio calculations on the complexation of quaternary ammonium ions and model compounds to the side chains of Phe, Tyr, and Trp are thus important for understanding the strength and directionality of these interactions and for calibrating potential models of cation−π interactions in proteins and protein-ligand complexes.

While cation−π interactions are strong in gas phase,[30,31,329] their strength is reduced by the successive addition of water molecules to the complex.[296] The strength of these interactions are significantly reduced in aqueous solutions.[30,31,297,330–332,334] Although cation−π interactions interactions are typically not as strong as cation-anion interactions in the gas phase, they are less destabilized by the successive addition of water molecules and retain their attractive character even in aqueous solutions. Calculation of the binding affinity between cations and aromatic systems in aqueous solutions is an important step toward understanding their strength and directionality in proteins. Given the computational costs of ab initio simulations,[334] force fields are often used for such purpose.[30,31,297,330–333] It is however required that these force fields correctly describe the various interactions in the system (ion-water, ion-aromatic, and water-aromatic).

The aim of this work is to computationally investigate the binding affinity and the binding directionality between quaternary ammonium ions (NH_4^+, TMA^+, and TEA^+) and aromatic amino acids side chains (modeled by benzene, toluene, 4-methylphenol, and 3-methylindole) in aqueous solution. The results are also useful in understanding the phenomenon of salting-in of aromatic hydrocarbons by quaternary ammonium salts.

7.2. Methods

7.2.1. Ab initio Calculations

The geometries of NH_4^+, TMA^+, and TEA^+ in complex with water, benzene, toluene, 4-methylphenol, and 3-methylindole are optimized (without symmetry constraints) at the MP2(full)/6-311++G(d,p) level using Gaussian 09.[26] The interaction energies are corrected for basis set superposition error (BSSE) by the counterpoise method[111] (and referred to as E^{CP}). Frequency calculations are performed on all reported optimized structures to confirm that they are energy minima. The optimization of each pair involves various initial structures, with different binding modes of the ion (uni, bi, and tridentate) and different orientations of the ion with respect to the plane of the aromatic moiety, and only the global minimum structures are considered. Potential energy surfaces (PESs) of all interacting pairs are calculated at the same level and all interaction energies are corrected for BSSE. The surfaces are calculated by scanning the distance between the nitrogen atom of the ion and the center of the six-membered ring of the aromatic compound or the oxygen atom of water from 2.0 Å to 8.0 Å. During the scan, the geometry of each fragment is kept at the gas-phase MP2(full)/6-311++G(d,p) optimized

geometry and the relative orientation of the two fragments is kept at the orientation found in the optimized pair.

7.2.2. Molecular Mechanics Calculations

Molecular mechanics (MM) calculations are performed with the program CHARMM.[29] Polarizable potential models based on classical Drude oscillators[32] have been reported for H_2O,[113] NH_4^+,[30] and aromatic compounds.[125,335] Following our previous work,[18,30,31,170,202] a polarizable model for interaction of NH_4^+, TMA^+, and TEA^+ with water, benzene, toluene, 4-methylphenol, and 3-methylindole is optimized based on the ab initio properties of their cation–π pairs. Unpublished force field parameters for the studied ions and ligands were obtained from the MacKerell group (Pedro Lopes and Alexander MacKerell, personal communication).

7.2.2.1. Parameterization Strategy

Optimization of potential models for the various cation–π and cation–water pairs follows our previously reported approach.[18,30,31,170,202] In particular, the optimization is based on adjusting pair-specific Lennard-Jones (LJ) parameters between atom *i* in the ion and atom *j* in the aromatic compound, $E_{\min,ij}$ and $R_{\min,ij}$, defined by the Lorentz–Berthelot combination rules:

$$E_{\min,ij} = \sqrt{E_{\min,i} \times E_{\min,j}} \qquad \text{and} \qquad R_{\min,ij} = \frac{R_{\min,i} + R_{\min,j}}{2} \qquad (7.1)$$

Optimization initially targets the ab initio PESs of the interacting pair. Each point of the energy surfaces contributes to the error function χ^2 to be minimized by a Boltzmann-weighted error term.[30] Since the PESs are computed using the rigid monomer geometries, parameters obtained from the minimization of χ^2 are further refined to reproduce the complexation energies of the fully relaxed ab initio pairs.[30] Optimization of pair-specific LJ parameters for NH_4^+ interactions have been reported previously.[18,30] No optimization of pair-specific LJ parameters was found necessary for TMA^+-water interaction. For the interaction of TMA^+ with the aromatic ligands (benzene, toluene, 4-methylphenol, and 3-methylindole), pair specific LJ parameters are optimized between the nitrogen atom of the ion and the carbon atoms of the six-membered ring. For TEA^+ interactions, pair-specific LJ parameters are optimized between the methylene carbon atoms of the ion and the oxygen atom of water or the carbon atoms of the six-membered rings of the aromatic ligands. Models for TMA^+-benzene and TEA^+-benzene are optimized first. The transferability of the optimized parameters to the other ion-aromatic complexes is then tested. For complexes where the ion-benzene parameters are considered nontransferable (if the

complexation energies of the complexes are deviating by more than 3% from ab initio data), the parameters are re-adjusted. For TEA^+ complexes, the E_{min} parameter between the methylene carbon atoms of the ion and the carbon atoms of the six-membered aromatic ring of the ligand is found to be not very sensitive and is set to the ion-benzene optimized value. All other mixed LJ parameters are derived from the Lorentz-Berthelot combination rules.

7.2.2.2. Molecular Dynamics

All MD simulations are performed with cubic periodic boundary conditions in the isothermal-isobaric ensemble (*NpT*). Water molecules are described with the polarizable SWM4-NDP water model model.[113] In all simulations, water molecules are totally rigid (OH bonds and HOH angles) and all covalent bonds to hydrogen atoms are made rigid using the SHAKE/Roll-RATTLE/Roll algorithm.[33] All simulations are carried out using one ion, one aromatic compound, and 500 water molecules at T = 298.15 and p = 1 atm. Electrostatic interactions are computed using the particle-mesh Ewald method[115] with κ = 0.34 for the charge screening and a 1.0 Å grid spacing with sixth-order splines for the mesh interpolation. The real-space interactions (Lennard-Jones and electrostatic) are cut off at 15 Å and the long range contribution from the Lennard-Jones term is introduced as an average density-dependent term.[116] A dual Nosé−Hoover thermostat[205] is applied; the first is coupled to the atomic motions to keep temperature at 298.15 K and the second is coupled to the Drude oscillators to keep them at low temperature (1 K) and ensure self-consistent dipole induction.[325] The relaxation time of the atomic thermostat is 0.1 ps, while the relaxation time of the Drude thermostat is 0.005 ps. The Andersen−Hoover barostat[206] with a relaxation time of 0.2 ps is used to regulate the pressure. The equations of motion are integrated using a 1-fs time step.

7.2.2.3. Potential of Mean Force Calculations

Potentials of mean force (PMFs) between each cation (NH_4^+, TMA^+, or TEA^+) and each aromatic compound (benzene, toluene, 4-methylphenol, or 3-methylindole) are calculated using umbrella sampling. The distance r between the nitrogen atom of the ion and the center of the six-membered ring of the aromatic compound is used as a reaction coordinate and a harmonic potential of force constant 10 kcal/mol/Å^2 is applied to bias the sampling. The reaction coordinate is sampled between 2.0 Å and 12.0 Å using 0.5-Å separated windows, and each window is simulated for 2.5 ns, the first 0.5 ns of which is used as equilibration and discarded. Simulations are performed either without constraining the geometry of the pair, or with

constraining it to the so-called "en face" and "edge-on" orientations. The en face geometry is enforced by constraining all six C···X···N angles to 90° (where C is a carbon atom of the aromatic six-membered ring, X is the center of the ring, and N is the nitrogen atom of the ligand) using a force constant of 100 kcal/mol/rad^2. The edge-on binding is enforced by constraining the center of the ion to be in the plane of the aromatic moiety of the ligand, using a force constant of 100 kcal/mol/rad^2. In all simulations, the ligand is constrained to the center of the simulation box using a 2 kcal/mol/Å^2 harmonic force constant. While the ligand is set free to rotate in the unconstrained and the en face-constrained simulations, it is kept at a fixed plane through all edge-on constrained simulation. The unbiased PMF is reconstructed using the weighted histogram analysis method (WHAM)[172,173] and the radial variation in the entropy of the solute pairs is taken into account by adding a $2RT$ ln(r) correction term to the PMFs from the unconstrained and en face-constrained simulations, and by adding a RT ln(r) correction term to the PMF from the edge-on constrained simulations.

7.3. Results and Discussion

7.3.1. Ab initio Interaction Energies

TEA^+ is reported[336] to possess two main conformers (Figure 7.1). The nitrogen and methyl carbon atoms form a quasi-planar configuration in conformer **a** (termed "planar"), while the methyl carbon atoms form an asymmetric pyramid in conformer **b** (termed "pyramidal").[336] Optimization of the two structures at the MP2(full)/6-311++G(d,p) level shows that conformer **a** is 1.17 kcal/mol more stable than conformer **b**. Complexation of both conformers with benzene in gas phase and in aqueous solution is found to give similar binding affinities (see below), and thus only conformer **a** is considered for complexes of TEA^+.

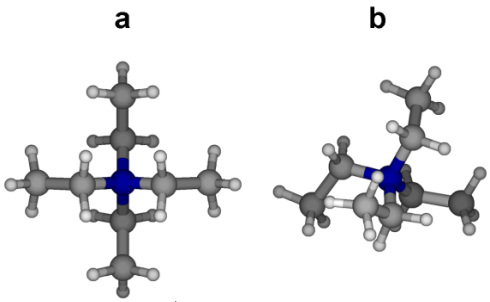

Figure 7.1. Optimized geometries of TEA^+ at the MP2(full)/6-311++G(d,p) level of theory. The methyl carbon atoms are in a quasi-planar configuration in conformer **a** and form an asymmetric pyramid in conformer **b**. Conformer **a** possesses a C_{2v} point symmetry while conformer **b** has a C_1 symmetry.

The optimized geometries of all studied complexes are presented in Figure 7.2. BSSE-corrected and uncorrected complexation energies (E^{CP} and E, respectively), as well as binding energies from the optimized Drude model (E^{Drude}) are reported in Table 7.1. Equilibrium separations between the nitrogen atom of the ion and the oxygen atom of water or the center of the six-membered ring of the aromatic compounds from both ab initio (r_{eq}^{QM}) and Drude (r_{eq}^{Drude}) calculations are also reported in Table 7.1. For the NH_4^+-4-methylphenol pair, the distance is between the nitrogen atom of the ion and the oxygen atom of the ligand. The MP2(full)/6-311++G(d,p) results for NH_4^+-containing pairs are in close agreement with our previous results obtained at the MP2(FC)/6-311++G(d,p) level.[18,30] For each of the five ligands, the binding energies across the ion series follow the trend $NH_4^+ >> TMA^+ > TEA^+$.

NH_4^+ binds water in a unidentate fashion.[30] Except for 4-methylphenol complex (2**d**), in which NH_4^+ interacts with oxygen, complexes of NH_4^+ with the aromatic compounds (2**b**, 2**c**, and 2**e**) are characterized by cation–π geometries, with the ion located on top of the six-membered ring.[18,30] In addition to structure 2**d**, complexation of NH_4^+ with 4-methylphenol yields another stable structure (not shown) in which the ion is interacting with the π electrons, with E^{CP} = –19.74 kcal/mol, E = –22.55 kcal/mol, and r_{eq}^{QM} = 2.904 Å. In the global minimum conformer, TMA^+ binds water in a tridentate conformation. Complexes of TMA^+ (2**f** to 2**j**) display cation–π geometries but with the ion displaced from the center of the six-membered ring. Complexes of TEA^+ (2**l** to 2**o**) possess binding energies close to the corresponding TMA^+ complexes (see Table 7.1). Complexation of the pyramidal conformer (1**b**) of TEA^+ with benzene results in a slightly more stable complex (structure not shown) compared to complex 2**l**. The complex is characterized by E^{CP} = –8.98 kcal/mol, E = –14.79 kcal/mol, and r_{eq}^{QM} = 4.313 Å. The BSSE-corrected binding energy between NH_4^+ and benzene (E^{CP} = −17.55 kcal/mol) and between TMA^+ and benzene (E^{CP} = −8.97 kcal/mol) are in agreement with the experimental heats of formation of the complexes in gas phase (–17.1 kcal/mol[319,329] and –9.4 kcal/mol[337], respectively).

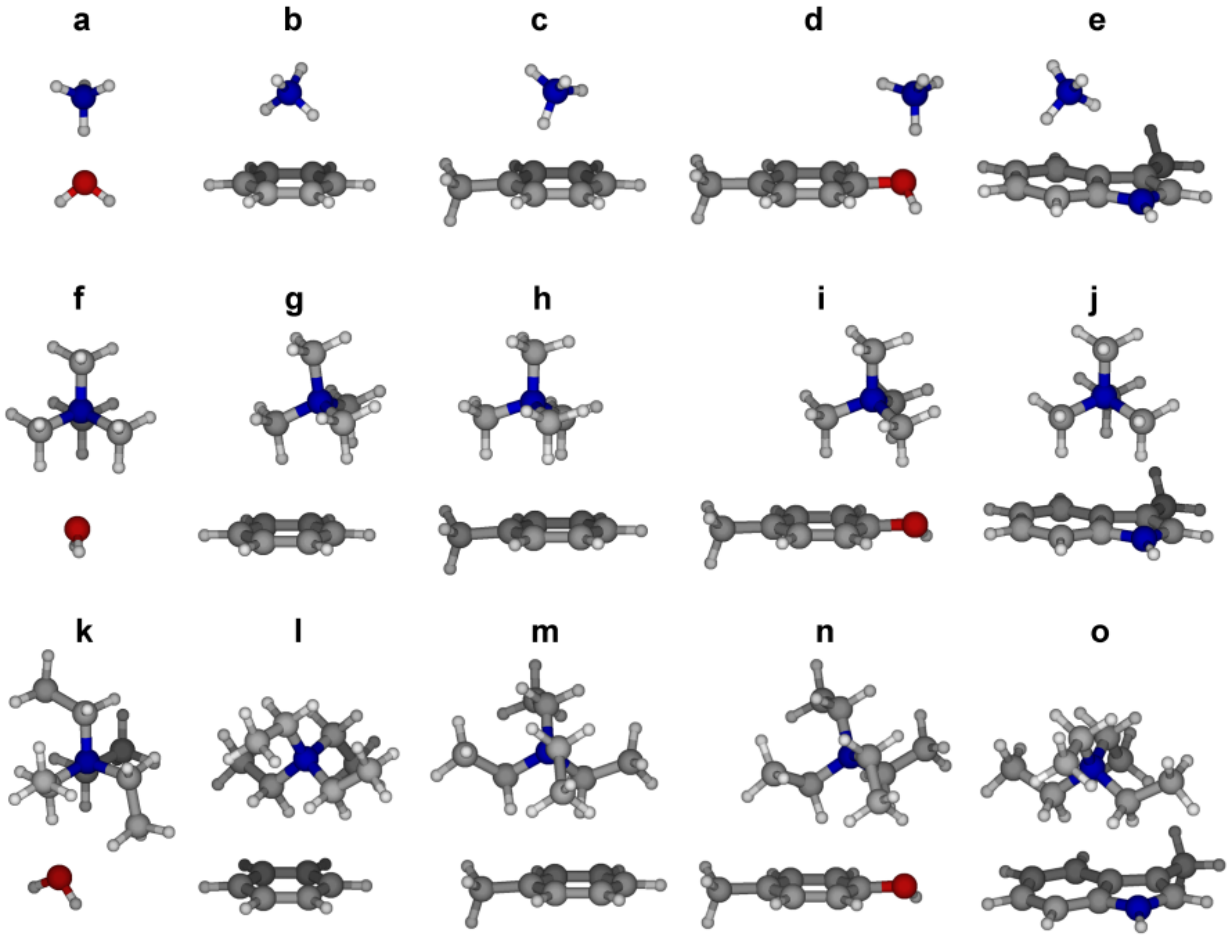

Figure 7.2. Optimized geometries at the MP2(full)/6-311++G(d,p) level of theory for the complexes of NH_4^+ with water (a), benzene (b), toluene (c), 4-methylphenol (d), and 3-methylindole (e), complexes of TMA^+ with water (f), benzene (g), toluene (h), 4-methylphenol (i), and 3-methylindole (j), and complexes of TEA^+ with water (k), benzene (l), toluene (m), 4-methylphenol (n), and 3-methylindole (o).

Table 7.1. Ab initio complexation energies (E: uncorrected; E^{CP}: BSSE-corrected) and equilibrium distances (r_{eq}^{QM}) calculated at the MP2(full)/6-311++G(d,p) level of theory, and corresponding energies (E^{Drude}) and distances (r_{eq}^{Drude}) calculated using the polarizable models. Energies are in kcal/mol and distances are in Å.[a]

Ligand	Ion	Conformer	E	E^{CP}	E^{Drude}	r_{eq}^{QM}	r_{eq}^{Drude}
H_2O	NH_4^+	a	−22.25	−20.29	−20.28	2.703	2.805
	TMA^+	f	−11.65	−9.78	−9.87	3.632	3.560
	TEA^+	k	−10.34	−7.97	−8.25	3.882	3.801
Benzene	NH_4^+	b	−19.89	−17.55	−17.56	2.917	2.892
	TMA^+	g	−12.90	−8.97	−8.93	4.204	4.301
	TEA^+	l	−13.90	−8.49	−8.77	4.325	4.373
Toluene	NH_4^+	c	−21.59	−18.90	−19.06	2.920	2.901
	TMA^+	h	−14.15	−9.99	−10.02	4.166	4.283
	TEA^+	m	−15.44	−9.53	−9.76	4.273	4.431
4-Methylphenol	NH_4^+	d	−26.38	−23.80	−20.24	2.641	2.742
	TMA^+	i	−16.95	−12.62	−13.00	4.177	4.138
	TEA^+	n	−18.17	−11.70	−11.76	4.276	4.451
3-Methylindole	NH_4^+	e	−28.07	−25.04	−24.60	2.822	3.016
	TMA^+	j	−21.28	−15.38	−15.48	4.088	4.152
	TEA^+	o	−22.98	−14.88	−14.98	4.199	4.366

[a] For water and 4-methylphenol, r_{eq} refers to the distance between the N atom of the ion and the O atom of the ligand. For all other ligands, it refers to the distance between the N atom and the center of the six-membered ring.

7.3.2. Ab initio Potential Energy Surfaces

Ab initio potential energy curves for NH_4^+, TMA^+, and TEA^+ in complex with water, benzene, toluene, 4-methylphenol, and 3-methylindole are reported in Figure 7.3 (dashed lines), along with the corresponding curves obtained from the optimized Drude models (see Section 7.3.3).

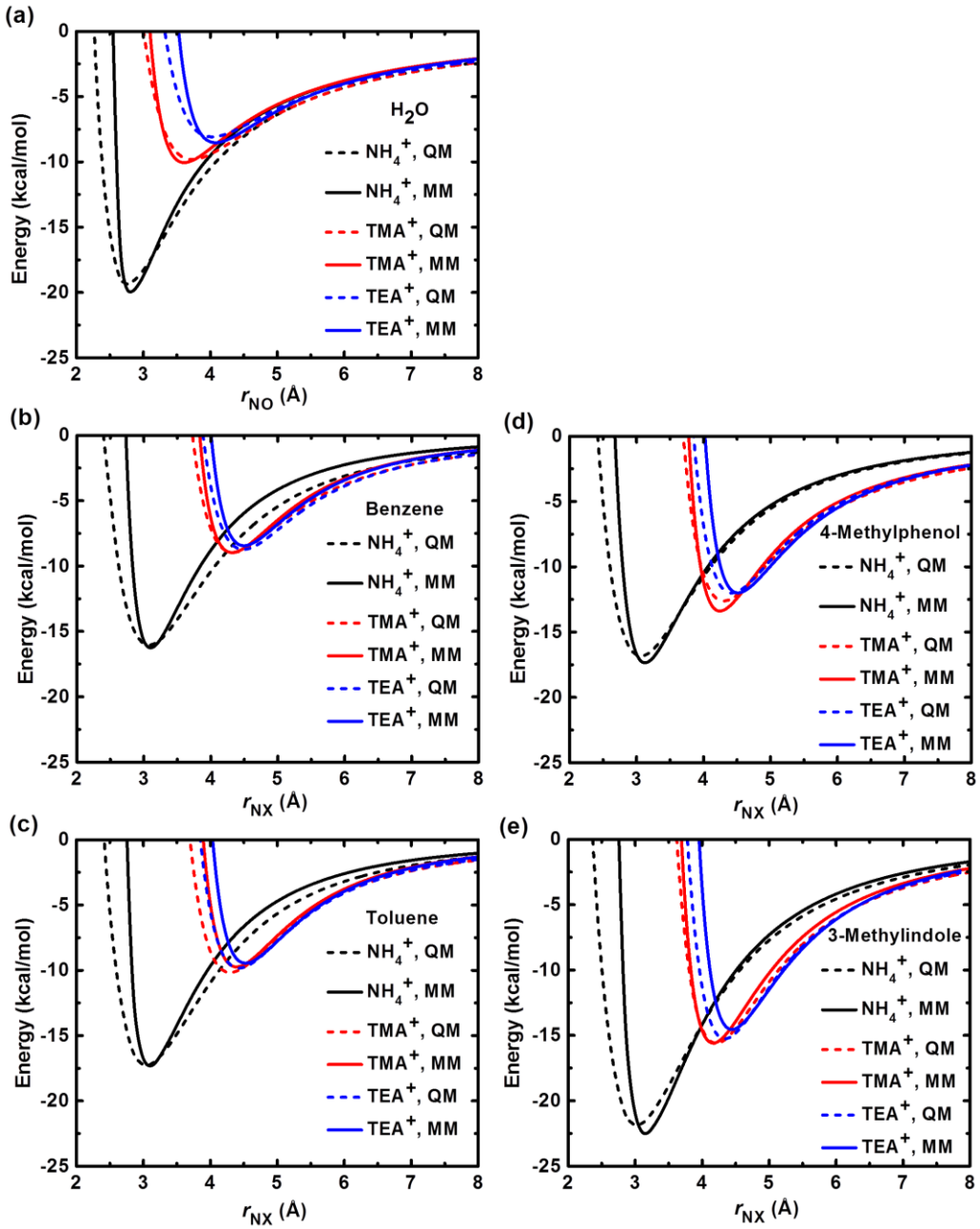

Figure 7.3. Potential energy curves for NH_4^+, TMA^+, and TEA^+ in complex with (a) water, (b) benzene, (c) toluene, (d) 4-methylphenol, and (e) 3-methylindole. For complexes between the ions and water, the distance between the nitrogen atom of the ion and the O atom of water is scanned between 2 and 8 Å. For complexes between the ions and the aromatic ligands, the distance between the nitrogen atom of the ligand and the center of the six-membered ring of the ligand is scanned between 2 and 8 Å. In all curves, the monomers are kept in their gas-phase internal geometries and the distance is scanned in 0.1 Å increments, keeping the relative orientations of the monomers as in the optimized complex.

7.3.3. Optimized Force Field

Pair-specific LJ parameters for the interaction of NH_4^+ with water, benzene, toluene, 4-methylphenol, and 3-methylindole have been optimized previously.[18,30] These, together with the optimized pair-specific LJ parameters for the interaction of TMA^+ and TEA^+ with the five ligands, are reported in Table 7.2. These parameters are first optimized based on the ab initio PESs and then refined to reproduce the ab initio geometry and interaction energy in the global minimum complex (see columns "E^{CP}" and "E^{Drude}" of Table 7.1). Similar to ab initio results, the optimized model for the interaction between NH_4^+ and 4-methylphenol predicts a second stable structure of cation-π binding geometry with E^{Drude} = –21.52 kcal/mol and r_{eq}^{Drude} = 3.237 Å. In line with ab initio results, complexation of benzene with the pyramidal conformer (1**b**) of TEA^+ gives a more stable complex than with the planar conformer (1**a**). The model predicts a complexation energy of –9.93 kcal/mol and r_{eq}^{Drude} = 4.411 Å. The models also reproduce the ab initio PESs, as shown in Figure 7.3. The properties of the TMA^+-water complex are adequately described by the LJ parameters obtained from the combination rule. The optimized pair-specific LJ parameters for the interaction of TMA^+ with benzene are transferable to the interaction of the ion with toluene and 3-methylindole. For complexes of TEA^+, the methylene carbons rather than the N atom of the ion are used to adjust the pair specific LJ parameters (see Table 7.2). The optimized parameters for TEA^+-toluene interaction are transferred to the interaction of the ion with 4-methylphenol.

Table 7.2. Optimized pair-specific Lennard-Jones parameters for the interactions of NH_4^+, TMA^+, and TEA^+ with water, benzene, toluene, 4-methylphenol, and 3-methylindole.[a]

Molecule	i	Pair-specific LJ parameters							
		$N(NH_4^+)$		$H(NH_4^+)$		$N(TMA^+)$		$C(TEA^+)$[d]	
		$Emin_{i,N}$ (kcal/mol)	$Rmin_{i,N}$ (Å)	$Emin_{i,H}$ (kcal/mol)	$Rmin_{i,H}$ (Å)	$Emin_{i,N}$ (kcal/mol)	$Rmin_{i,N}$ (Å)	$Emin_{i,C}$ (kcal/mol)	$Rmin_{i,C}$ (Å)
H_2O	O	0.10185	3.75920	0.00924	2.88481	–	–	0.01349	5.01795
Benzene	X[b]	0.14706	3.50006	0.00602	3.28084	0.0	0.0	0.0	0.0
	C[c]	–	–	–	–	0.30971	4.80186	0.06216	4.30961
Toluene	X[b]	0.14706	3.50006	0.00602	3.28084	0.0	0.0	0.0	0.0
	C[c]	–	–	–	–	0.30971	4.80186	0.0621	4.42961
4-Methylphenol	X[b]	0.01872	4.69984	0.0	0.0	0.0	0.0	0.0	0.0
	O	0.39753	3.33581	0.01844	2.56374	–	–	–	–
	C[c]	–	–	–	–	0.36967	4.18721	0.06216	4.42961
3-Methylindole	X[b]	0.66323	2.99080	0.02714	2.77158	0.0	0.0	0.0	0.0
	C[c]	0.31052	3.73231	0.00836	3.49493	0.30971	4.80186	0.06216	4.62561

[a] Parameters for NH_4^+ are reproduced from references 30 and 18. [b] Refers to a non-atomic site at the center of the six-membered ring (see references 18,30,31 for details). [c] Refers to the carbon atoms of the six-membered ring. [d] Refers to the methylene carbon atoms in TEA^+. The dashes in the table indicate that no pair-specific LJ parameters are optimized and that the corresponding LJ parameters are obtained using the Lorenz–Berthelot combination rules.

7.3.4. Cation–π Interactions in Aqueous Solution

The binding affinity of NH_4^+, TMA^+, and TEA^+ with the four aromatic ligands in water is estimated from PMF calculations. The PMFs from the unconstrained and from both the en face and edge-on constrained orientations are shown in Figure 7.4 (the positions and depths of the PMF minima are reported in Table 7.3). Results show that, for a given aromatic ligand, the binding free energy from the unconstrained and the en face constrained simulations follows the trend $TEA^+ > TMA^+ > NH_4^+$, which is the reverse trend to the gas-phase binding energies (see Table 7.1). For a given ligand, binding free energies from the edge-on constrained simulations are comparable across the ion series, and no systematic trend is observed. The equilibrium separations between the ion and the center of the six-membered ring are similar for both the unconstrained and en face simulations. These distances are slightly larger than the equilibrium separations in the gaseous pairs (by about 0.4 Å; see Table 7.1), yet consistent with contact complexes. The complex of NH_4^+ with 3-methylindole displays a broad free energy well between ~3 and ~6 Å. Solvent-separated complexes correspond to weak shoulders or peaks in Figure

7.4a-h. Unconstrained simulations (Figure 7.4a-d) show these shoulders/peaks at about 8.5 Å for complexes of TMA^+ and at about 9.5 Å for complexes of TEA^+. For en face simulations, these occur at about 6.0 Å for complexes of NH_4^+, at about 7.5 Å for complexes of TMA^+, and at about 8.8 for complexes of TEA^+. For edge-on PMFs these shoulders are located at about 9.5 Å in some of the of TMA^+ and TEA^+ complexes.

Binding free energies of these solvent separated pairs are always weaker than those of contact complexes. Figure 7.4a indicates that the two conformers of TEA^+ (see Figure 7.1) possess similar binding affinities for benzene, especially at the minimum of the PMF. In comparison to unconstrained and en face simulations, equilibrium separations from the edge-on simulations are much larger, to avoid steric clashes and electrostatic repulsion between the cations and the aromatic hydrogens.

The PMFs from the unconstrained and en face simulations show that among all complexes of TEA^+, the complex with 3-methylindole is the most stable. In comparison, complexes of NH_4^+ and TMA^+ with toluene are the most stable among the complexes of the two ions with the four ligands. In nonpolar or water-poor environments, binding affinities might be larger and the trend in binding affinity between an ion and different aromatic ligands will likely follows the trend of gas-phase binding affinity.

The values of –3.3 and –0.9 kcal/mol for en face and edge-on binding affinities between benzene and NH_4^+ are within statistical errors with the values of –3.2 and –0.8 kcal/mol obtained from a two dimensional PMF and reported elsewhere.[31] Compared to results in Figure 7.4 and Table 7.3, Sa *et al.*[334] performed a fully quantum mechanical simulation on the NH_4^+-benzene pair in water and calculated an en face binding free energy of –5.75 kcal/mol (at 3.25 Å) and an edge-on binding free energy of –0.33 kcal/mol. Using a corrected additive force field, Chipot *et al.*[332] reported an en face binding free energy of –5.47 kcal/mol at 3.05 Å separation and an average PMF of –2.99 kcal/mol at 3.16 Å separation for the NH_4^+–toluene pair. Using a hybrid QM/MM approach, Gao *et al.*[330] have calculated "average" binding free energies of –0.6 kcal/mol and –1.8 kcal/mol for the contact and solvent separated TMA^+-benzene complex at distances of 4.7 Å and 7.5 Å, respectively. Using Monte Carlo simulations, Duffy *et al.*[331] reported a –3.3 kcal/mol "average" free energy minimum at contact distance (4.75 Å), and no free energy minimum at solvent-separated distances of the TMA^+-benzene complex. Using the solvent reaction field method, Gaberšček and Mavri have estimated a free energy of association between phenol and TMA^+ in water of –11.06 kcal/mol.[333] This value is most likely

overestimated, given that an optimization of the gaseous TMA^+-phenol complex at the MP2(full)/6-311++G(d,p) level yields $E^{CP} = -11.36$ kcal/mol.

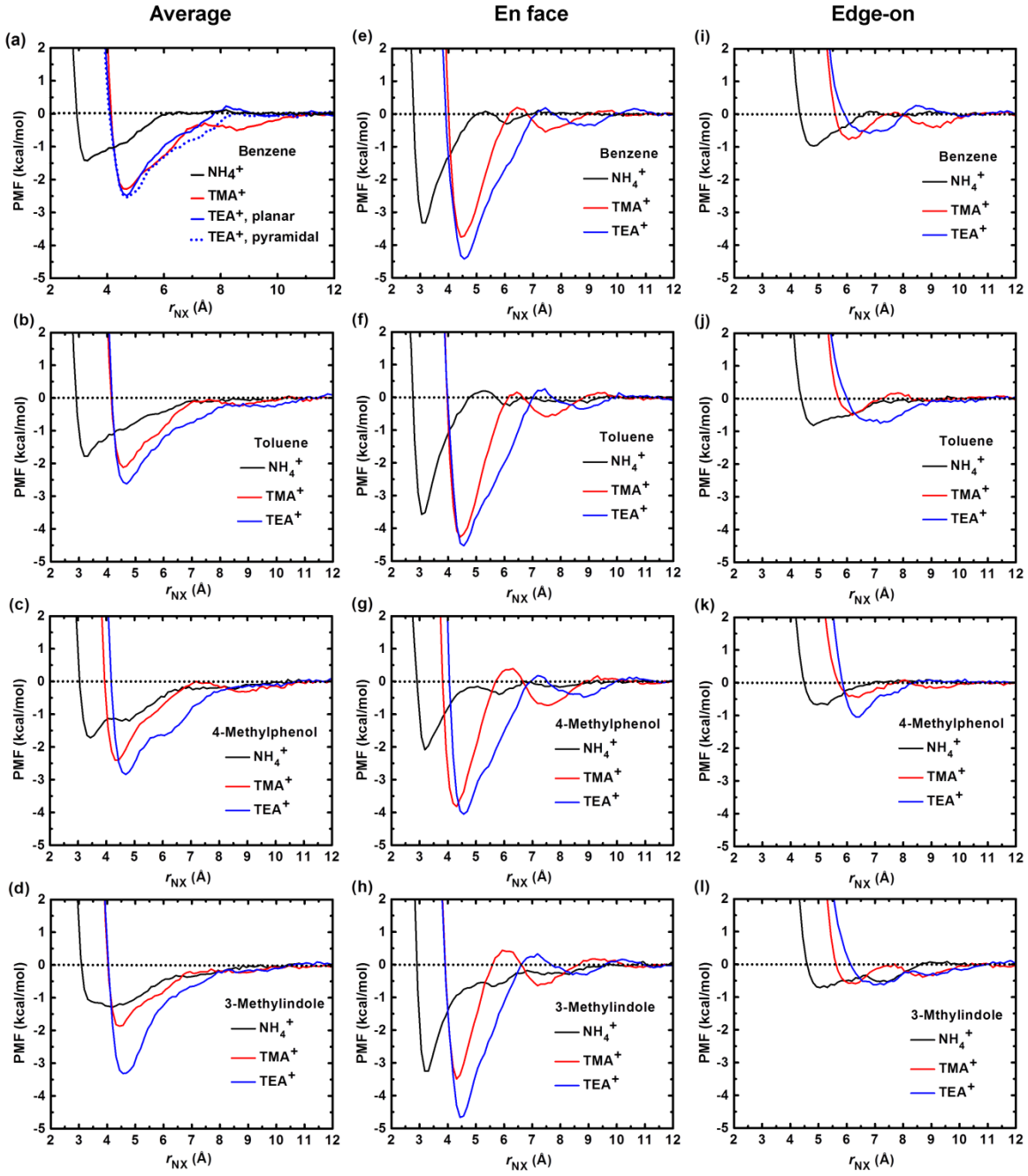

Figure 7.4. Potentials of mean force between the centers of ions (NH_4^+, TMA^+, and TEA^+) and the center of the six-membered ring of (a,e,i) benzene, (b,f,j) toluene, (c,g,k) 4-methylphenol, and (d,h,l) 3-methylindole. Panels a–d are obtained from the unconstrained simulations, panels e–h are obtained from the en face constrained simulations, and panels i–l are obtained from the edge-on constrained simulations. The dashed line in panel a represents the PMF obtained with conformer 1b of TEA^+; all other PMFs involving TEA^+ are calculated with conformer 1a only.

Table 7.3. Binding free energy (in kcal/mol) and equilibrium distance (in Å) of the PMF between the center of the ion and the center of the six-membered ring of the aromatic ligand, obtained with and without geometry constraints.[a]

Ligand	Ion	Unconstrained				En face				Edge-on			
		r_1	PMF (r_1)	r_2	PMF (r_2)	r_1	PMF (r_1)	r_2	PMF (r_2)	r_1	PMF (r_1)	r_2	PMF (r_2)
Benzene	NH_4^+	3.3	–1.4[b]	–	–	3.2	–3.3[b]	6.0	–0.3[c]	4.8	–0.9[d]	–	–
	TMA^+	4.7	–2.3[b]	8.5	–0.5[c]	4.4	–3.8[b]	7.4	–0.5[c]	6.1	–0.8[d]	9.0	–0.4[e]
	TEA^+	4.7	–2.5[b]	–	–	4.6	–4.4[b]	8.5	–0.3[c]	6.4	–0.6[d]	–	–
Toluene	NH_4^+	3.2	–1.8[b]	–	–	3.1	–3.6[b]	6.1	–0.3[c]	4.8	–0.8[d]	–	–
	TMA^+	4.6	–2.1[b]	8.6	–0.2[c]	4.4	–4.3[b]	7.5	–0.6[c]	6.2	–0.5[d]	–	–
	TEA^+	4.7	–2.6[b]	9.5	–0.3[c]	4.6	–4.5[b]	8.6	–0.4[c]	6.7	–0.8[d]	–	–
4-Methylphenol	NH_4^+	3.4	–1.7[b]	–	–	3.2	–2.1[b]	5.8	–0.4[c]	4.9	–0.7[d]	–	–
	TMA^+	4.3	–2.4[b]	8.6	–0.3[c]	4.3	–3.8[b]	7.5	–0.7[c]	6.3	–0.5[d]	9.0	–0.2[e]
	TEA^+	4.7	–2.8[b]	–	–	4.6	–4.1[b]	8.7	–0.5[c]	6.4	–0.9[d]	–	–
3-Methylindole	NH_4^+	4.2	–1.3[b]	–	–	3.2	–3.3[b]	5.7	–0.6[c]	4.9	–0.7[d]	–	–
	TMA^+	4.4	–1.9[b]	–	–	4.3	–3.5[b]	7.5	–0.6[c]	6.3	–0.6[d]	8.7	–0.4[e]
	TEA^+	4.6	–3.3[b]	–	–	4.4	–4.7[b]	8.8	–0.3[c]	6.9	–0.6[d]	8.9	–0.3[e]

[a] r_1 and r_2 are the distances (in Å) where the PMF has its first and second minimum, respectively. PMF(r_1) and PMF(r_2) are the binding free energies between the ion and the ligand at r_1 and r_2, respectively. [b]Cation–π pairs. [c]Water-bridged cation–π pairs. [d]Hydrophobic contacts. [e]Water-bridged hydrophobic contacts.

The solubility of benzene in aqueous quaternary ammonium salt solutions increases with the size of the ion ($NH_4^+ < TMA^+ < TEA^+$).[338] The orientationally averaged free energy minima and the en face binding free energies between the three ions and a given aromatic ligand follow the same trend. The trend in increasing the binding affinity of benzene and the three ions follows qualitatively the trend in increasing benzene solubility. For example while the orientationally averaged PMF for the benzene complex increases (more negative) by 0.9 kcal/mol on going from NH_4^+ to TMA^+, it increases by 0.2 kcal/mol on going from TMA^+ to TEA^+. The salting-in constant for benzene increases by 0.47 L/mol on going from ammonium bromide to tetramethylammonium bromide and increases by 0.21 L/mol on going from the latter to tetraethylammonium bromide.[338] This suggests that cation–π interaction might play a role in the observed solubility trend: the larger the binding affinity between the ion and benzene, the larger the solubility of the latter in water.

7.4. Conclusion

Drude potential models for the interactions of TMA^+ and TEA^+ with water, benzene, toluene, 4-methylphenol, and 3-methylindole are optimized. These models, together with previously reported models for NH_4^+ interactions,[18,30] are used in MD simulations to investigate the binding affinity between the cations and the aromatic compounds in water. Simulations are showing that similar to gas-phase, the en face binding geometry is favored over the edge-on binding for all complexes. The calculations show that, compared to gas phase, the binding affinity is reduced and the trend in binding of the three cations with a given ligand is reversed. The observed trend in binding affinity between the ions and benzene in water follows the trend of benzene solubility in aqueous quaternary ammonium salts[338] and is suggesting a role of cation–π interactions in benzene solubility. The optimized models are important for investigating cation–π interactions in proteins, in protein-ligand interactions, and in understanding the binding affinity and inhibition of potassium channels by quaternary ammonium ions.

8. Computational Investigation of the Selectivity and Inhibition of AmtB and RhCG Ammonium Transport Proteins

Abstract

Ammonium transport through cell membranes provides a source of nitrogen for amino acid synthesis in bacteria and plants. It helps control the acid-base equilibrium in mammals and excretes the ion from the cell when present at high concentration. This transport is mediated by proteins of the Amt/Mep/Rh family. Crystal structures of Amt and Rh proteins reveal some structural differences along the transport pathway. It is also found that Amt proteins are selective for NH_4^+ relative to Na^+ and K^+, yet that their activity is inhibited by ions such as Cs^+ and Tl^+ (Javelle *et al*. *Proc. Natl. Acad. Sci. U.S.A*. **2008**, *105*, 5040−5045). The degree of selectivity and mechanism of inhibition as well as the influence of the structural differences among these protein families on their selectivity and mechanism of function remain however unclear.

Toward understanding these phenomena, we perform molecular dynamics simulations on AmtB and RhCG proteins using a force field calibrated for ion-protein interactions. The results show that both proteins have higher binding affinity toward NH_4^+ compared to NH_3, Na^+, K^+, and Rb^+. On the other hand, Cs^+ and Tl^+ bind the proteins with similar and higher binding affinities to that of NH_4^+, suggesting that inhibition of protein activity is due to competitive binding of Cs^+ and Tl^+. Simulations on the wild structures of AmtB and on its Ile28/Phe mutant as well as on the wild structure of RhCG and on its Phe74/Ile mutant are showing that the larger hydrophobicity of the pore lumen in RhCG prevents water from entering the pore which results in destabilizing NH_4^+ inside the pore. This suggests that RhCG functions as NH_3 rather than NH_4^+ transporter or NH_3/H^+ cotransporter, which are suggested transport mechanisms in AmtB.

8.1. Introduction

The movement of ammonium through cellular membranes is mediated by ammonium transport proteins which are found in all domains of life.[25,39,339–343] Ammonia is a source of nitrogen for amino acid synthesis in bacteria, plants, and yeast. Under low ammonia concentration, ammonium transport (Amt) proteins in bacteria and plants and methylamine permease (Mep) in yeast are expressed and facilitate the transport of ammonia across cell membranes.[25,39,339,340] In mammals, ammonia controls the acid base balance yet is toxic when present at high concentration. Erythrocytic RhAG and non-erythrocytic RhBG and RhCG from the Rh family of proteins mediate ammonium transport in mammals.[341–343]

Functional studies are suggesting that while Amt proteins transport the charged species (NH_4^+),[25,39,339,340] Rh proteins transport the neutral one (NH_3).[341–343] Crystal structures of Amt and Rh proteins have revealed the presence of a hydrophobic pore along the transport pathway and accordingly suggested that both protein families may transport neutral ammonia.[19,20,354–347]

The X-ray crystallographic structures of AmtB protein from *Escherichia coli* (at 1.35 Å resolution)[19] and the human RhCG protein (at 2.1 Å resolution),[20] show that these proteins are homotrimers with one pore at the center of each monomer. A comparison between the two channel structures (see Figure 8.1) reveals conserved features including an external aperture gated by two phenylalanines and a largely hydrophobic pore lined by two coplanar histidines near the center of the channel. Notable differences in the structures of the two pores are also seen. The characteristic tryptophan (Trp148) in AmtB, which is thought to participate in recruitment of NH_4^+ at the periplasmic entry of the pore through cation–π interaction,[19] is absent in RhCG, however Glu166 in the latter may aid in NH_4^+ recruitment.[20] The outer phenylanaline (Phe 130) in RhCG is not blocking the pore as is the case of Phe107 in AmtB. The pore lumen of RhCG is more hydrophobic due to Phe74, compared to Ile28 in AmtB. In addition, four electron density maxima are identified for AmtB: one in the extracellular vestibule (labeled S1) and three in the pore lumen (labelled S2–S4, see Figure 8.1)[348] and a water molecule is identified in the structure of RhCG near His185[20] (labelled W), at a position similar to S2 in AmtB.

Studies on various proteins of the Amt family suggest three transport mechanisms: electroneutral NH_3 transport,[19,21,352,349–354] NH_3/H^+ cotransport,[18,21–23,355] and NH_4^+ transport.[24,25,39,339,340,344] On the other hand, studies on Rh family proteins[20,341–343] are pointing toward an electroneutral transport mechanism. Experimental studies on Amt proteins are

showing that the proteins are selective for NH_4^+ over the biologically abundant Na^+ and K^+ ions,[21,25,339] yet that Cs^+ and Tl^+ inhibit the protein activity with full activity inhibition at 50 mM Cs^+ and 0.5 mM Tl^+.[21] The degree of selectivity of AmtB and RhCG proteins toward various ions is however unknown. Structural variations among the two proteins might play a critical role in their mechanism of function and might also influence their selectivity. Although mutagenesis studies are useful in finding the importance of certain amino acids, computational studies provide detailed information about the exact role of these amino acids at the molecular level.

The computationally demanding nature of ab initio and semiempirical quantum calculations restrict their application to small systems, which makes force fields (FFs) the most suitable for studying protein systems. However since the majority of FFs are not optimized for ion-protein interactions, further reparameterization is required in order to use them for studying the selectivity, ligand binding, and amino acids functional roles in ammonium transport proteins.[18] For this reason, we have developed polarizable FFs for NH_3, NH_4^+, Na^+, and K^+ interacting with model compounds for amino acid side chains that line the permeation pathway of AmtB.[18,356] Models for Rb^+, Cs^+, and Tl^+ interactions have also been optimized (see chapter 6).

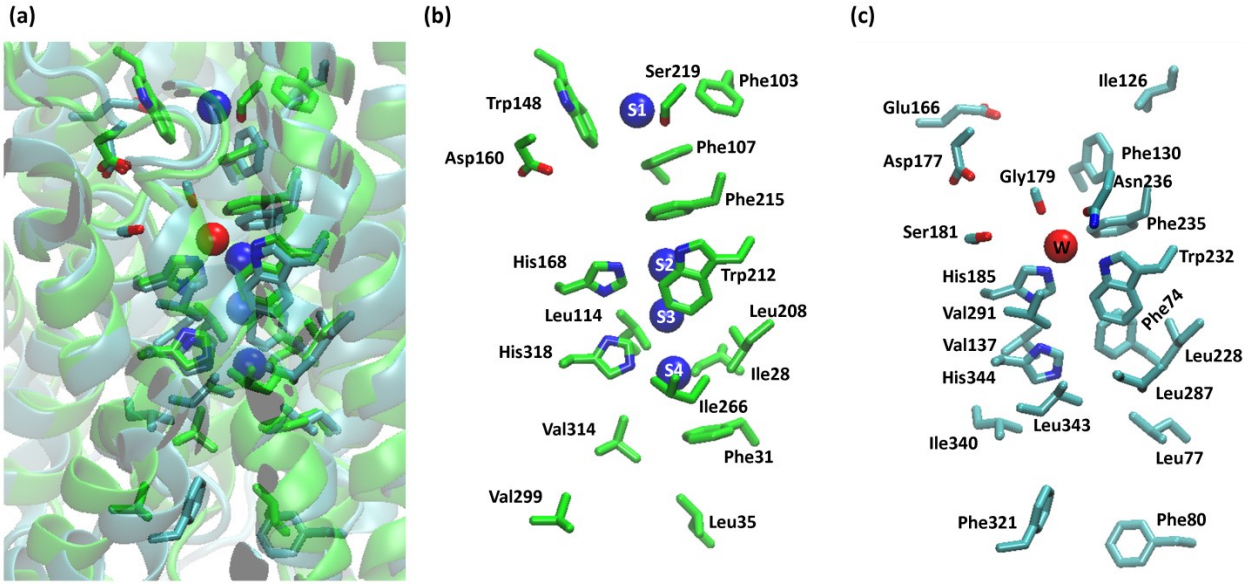

Figure 8.1. Molecular representations of the AmtB and RhCG pore. Panel (a) shows the alignment of the structure of AmtB (PDB ID: IU7G, in green) with that of RhCG (PDB ID: 3HD6, in cyan). Panel (b) shows the key residues lining the pore of AmtB and crystallographically identified four electron densities (shown in blue spheres and labeled S1–S4). Panel (c) presents key residues lining the pore of RhCG and a crystallographically resolved water molecule binding His185 (shown as red sphere and labeled W).

The purpose of this study is to investigate the selectivity, inhibition, and the structural function of amino acids in the permeation pathways of AmtB and RhCG proteins. Toward this, the optimized polarizable models are used in molecular dynamics (MD) simulations on the wild structures of AmtB and RhCG and on mutations that make the pore of one protein similar to that of the other. The pore of RhCG is relatively more hydrophobic than that in AmtB, due to Phe74 in the first, compared to Ile28 in the latter. The effect of pore hydrophobicity on the stability of H_2O and NH_4^+ is investigated by simulations on the Phe74/Ile mutant of RhCG and the Ile28/Phe mutant of AmtB.

8.2. Methods

8.2.1. Simulation System Preparation

The AmtB and RhCG monomer structures used in this work are based on the X-ray structures determined by Khademi *et al*.[19] (PDB ID: 1U7G) and by Gruswitz *et al*.[20] (PDB ID: 3HD6). Mutations F68S, S126P, and K255L in 1U7G are modified back to their native states. RhCG loops that were not resolved (residues 35-52 and 362-383) were modeled[348] using the loop modeling function of the Rosetta program.[357] Unless otherwise stated, the two coplanar histidine residues in the pore lumen of both monomers (His168 and His318 in AmtB and His185 and His344 in RhCG) are kept neutral with His168−H···His318−H and His185−H···His344−H protonation states. This protonation state was shown[358] to better reproduce the experimental density inside the pore of AmtB (sites S2–S4, see Figure 8.1b) compared to the reverse state. The Membrane builder tool of CHARMM-GUI[359] is then used to add a lipid bilayer of dimyristoylphosphatidylcholine (DMPC), water, and KCl to each protein monomer. For AmtB, 185 DMPC lipid molecules, 13111 water molecules, 34 K^+, and 36 Cl^- ions are added.[18] For RhCG, 204 DMPC lipid molecules, 15813 water molecules, 46 K^+, and 40 Cl^- ions are added. The final simulation box is 92.3 Å × 77.4 Å × 91.2 Å for AmtB, and 88 Å × 88 Å × 100 Å for RhCG. The overall simulation system of AmtB is shown in Figure 8.2.

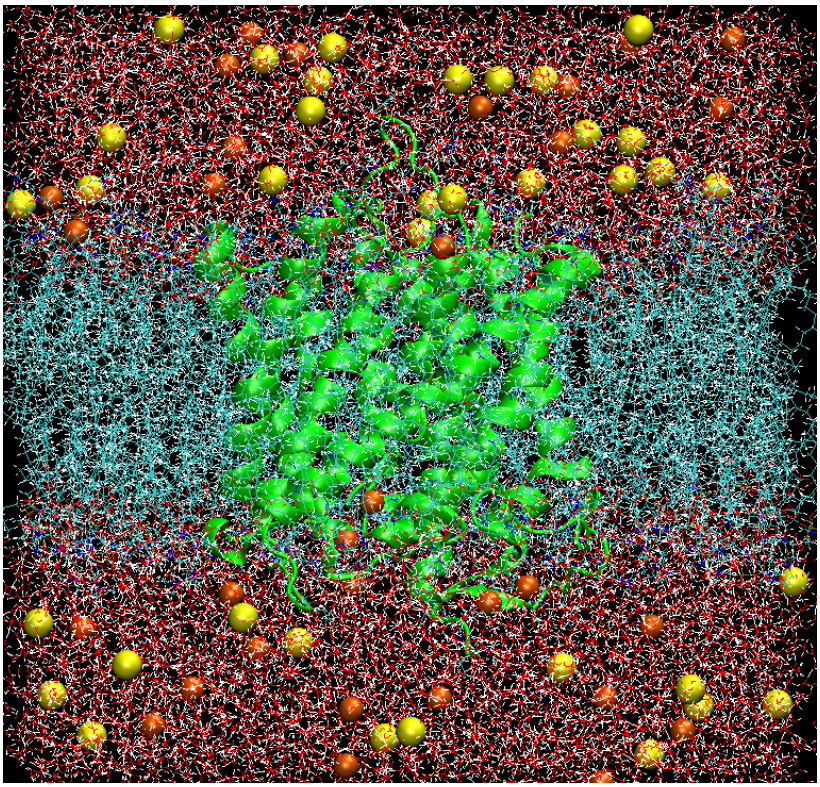

Figure 8.2. AmtB membrane protein model (unit cell) for MD simulations. The structure of AmtB monomer is shown in green cartoon. Atom colors are red for oxygen, blue for nitrogen, cyan for carbon, white for hydrogen, orange for potassium, and yellow for chloride.

8.2.2. Molecular Dynamic Simulations

We use an MD simulation protocol similar to that reported elsewhere.[18] In particular, MD simulations are performed with the CHARMM program,[29] using a hybrid polarizable mechanics/molecular mechanics (PM/MM) description of the system.[18] Ligands (H_2O, NH_3, NH_4^+, Na^+, K^+, Rb^+, Cs^+, and Tl^+) and surrounding water molecules and protein side chains are described by a polarizable force field based on the classical Drude oscillator,[18,30,113,118,123,170,356,360] and parametrized to reproduce both the free energy of hydration and the ion–protein interactions. The rest of the system is described by the nonpolarizable CHARMM param27 force field.[114] For AmtB, we simulate four different conditions. Two of these involve simulating NH_4^+ at S1 and S2 of the protein, and the other two involve simulating water molecules in the pore lumen of the wild type and the Ile28/Phe mutated structures. Four conditions are similarly simulated for RhCG. Two of these involve NH_4^+ in the periplasmic side and in the pore lumen of the protein. The other two correspond to water molecules in the pore lumen of the wild type protein and its Phe74/Ile mutant. To maintain the electroneutrality of this

system, one potassium ion is removed when NH_4^+ is added. In all simulations, periodic boundary conditions are applied, and electrostatic interactions are computed using particle-mesh Ewald method[361] with 1.0 Å grid spacing. The van der Waals interactions are cut off at 12 Å. Velocity Verlet integrator is used and integration time step is 1 fs. All covalent bonds with hydrogen are fixed using the RATTLE/Roll algorithm.[33] All simulations are performed in the NPT ensemble. Modified dual-thermostat Andersen–Hoover equations are used to maintain constant temperature and constant pressure (1 atm).[32] Atoms are kept at 298.15 K and Drude oscillators at 1 K.

8.2.3. Polarizable Mechanics/Molecular Mechanics Setup

To better account for ion-protein interactions, we use a simulation protocol in which the ion and surrounding residues are described with polarizable force field. For simulations involving AmtB two setups are used. In the first (see Figure 8.3a), the polarizable region includes NH_4^+ in the S1 site, the surrounding side chains of (Phe103, Phe107, Phe215, Trp148 and Ser219), and two SWM4 water molecules.[113] In the second setup (see Figure 8.3b), the polarizable region includes NH_4^+ in the S2 site, the surrounding side chains (Phe107, His168, Trp212, Phe215 and His318), and four SWM4 water molecules in the hydrophobic pore. We also simulate the latter system without the ion to study the stability of a water chain in the pore lumen of the wild and of the Ile28/Phe mutated structures.

During all simulations of RhCG, the side chains of Phe74, Phe130, His185, Trp232, Phe235, Asn236, His344, the carbonyl groups of Gly179, and NH_4^+ are kept polarizable. In addition one polarizable water molecule is used when NH_4^+ is present in the periplasmic side of the protein. The stability of a water chain in the pore lumen of RhCG is studied by simulating four polarizable water molecules in the pore lumen of the wild and Phe74/Ile mutated proteins. The protein residues in both AmtB and RhCG are selected because they are the nearest neighbors to the ligands in the binding sites. Both Phe107 and Phe215 in AmtB and Phe130 and Phe235 in RhCG are treated with polarizable models to account for cation–π and π–π interactions.[30] Parameters of the polarizable amino acids side chains are taken from the studied model compound in chapter 6[30,113,118,123,170,360]: $–CH_2$-OH from ethanol for Ser219 in AmtB; $–CH_2$-C_6H_5 from toluene for Phe103, Phe107, and Phe215 in AmtB and for Phe74, Phe130, and Phe235 in RhCG; $–CH_2$-C_8H_6N from 3-methylindole for Trp148 and Trp212 in AmtB and for Trp232 for RhCG; $–CH_2$-$C_3H_3N_2$ from 4-methylimidazole for His168 and His 318 in AmtB and for His185 and His344 for RhCG; CH_2-$CONH_2$ from acetamide for Asn236 in RhCG; and CO from N-

methylacetamide for Gln179 in RhCG. Those polarizable fragments are linked to the α carbons of the corresponding residues. To keep the fragment electrically neutral, the charge on the H atom removed from the model compound is transferred to the polarizable beta-carbon atom. All bonded parameters between polarizable and non-polarizable atoms are taken from CHARMM param27 parameters.[114] While the interaction of the ions with neighboring amino acid side chains are described by the polarizable force field, CHARMM param27 parameters (along with the TIP3P water model[362]) are used for other interactions.

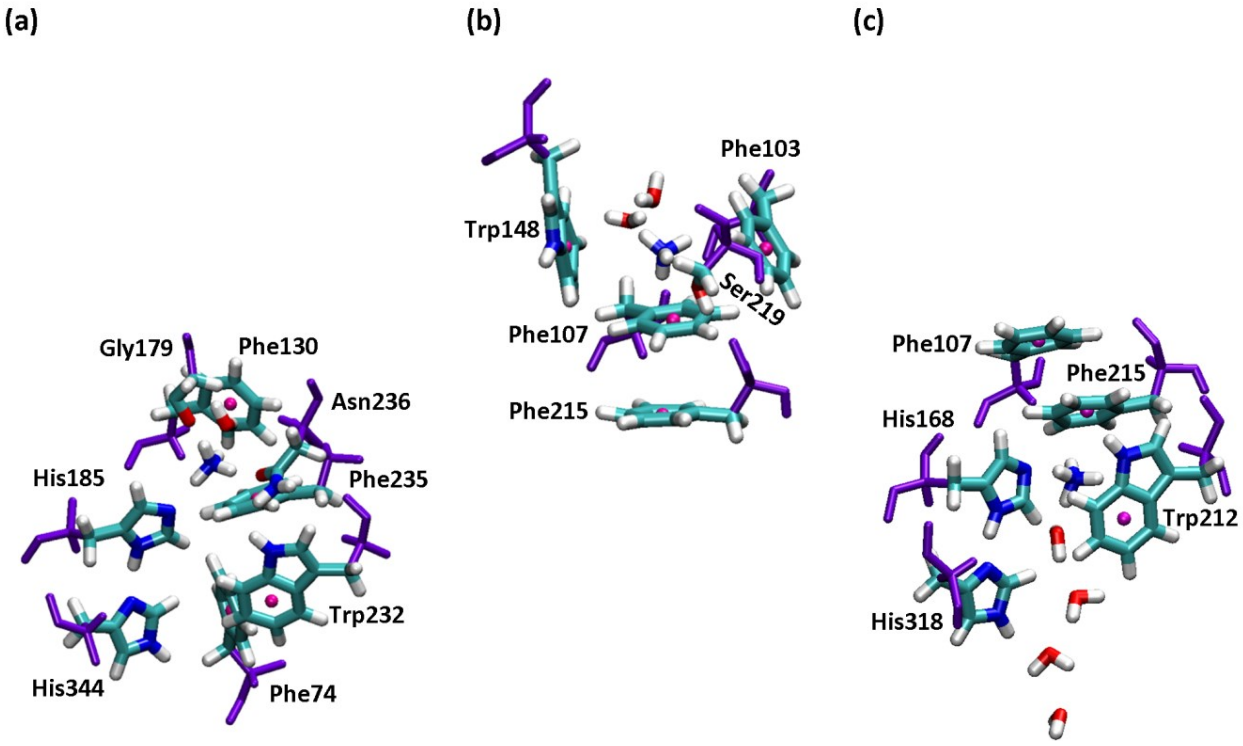

Figure 8.3. Snapshots from MD simulations showing: (a), ammonium ion in the periplasmic vestibule of RhCG and surrounding residues, (b) ammonium ion in S1 of AmtB and surrounding residues, and (c) ammonium ion in S2 of AmtB and surrounding residues. Atom colors are red for oxygen, blue for nitrogen, cyan for carbon, and white for hydrogen. Non-atomic sites in Phe and Trp side chains (see references 18 and 30 for details) are presented as pink spheres and non-polarizable fragments of the amino acids are colored in violet.

8.2.4. Binding Free Energy Calculations

Relative binding free energies ($\Delta\Delta G_{bind}$) are calculated using the standard thermodynamic integration (TI) method,[363] as combinations of free energies of mutation of NH_3, NH_4^+, Na^+, K^+, Rb^+, Cs^+, and Tl^+ to H_2O at S1 and S2 of AmtB, at site W of RhCG, and in bulk water. Mutations are performed using a hybrid residue that corresponds to the polarizable ligand when $\lambda = 0$ and to the SWM4-NDP water model[113] when $\lambda = 1$.[18,30] These residues are created by bonding one fragment with a second "dummy" fragment with a force constant of 5 kcal/mol/Å^2 assigned to the harmonic tether between the two fragments. A weak restraint potential is imposed on the ion to prevent large drifts away from the binding site and to allow for reliable estimation of relative binding free energies. The transition of λ from 0 to 1 is split into 12 windows: 0, 0.05, 0.15, 0.25, 0.35, 0.45, 0.55, 0.65, 0.75, 0.85, 0.95, and 1. Each window corresponds to an independent simulation that includes 100 ps of equilibration and 250 ps of data collection. Five independent calculations are performed to get more reliable results and to estimate errors. The free energy calculations in the protein (ΔG_{mut}^{prot}) use polarizable force fields as described in the previous section. Free energies of hydration (ΔG_{mut}^{wat}) are calculated in a periodic system of 250 SWM4 water molecules.

8.3. Results and Discussion

8.3.1. Ammonium Recruitment in AmtB and RhCG

The ionic form of the substrate, NH_4^+, predominates under physiological pH conditions, and thus NH_4^+ rather than NH_3 is believed to occupy the S1 site of AmtB.[18,19,21–23,345,351–354] While the structure of RhCG is revealing a water molecule interacting with His185 (site W), it is suggested[20,364] that RhCG lacks a periplasmic recruitment site for NH_4^+. In previous work,[18] we used PM/MM MD simulations to investigate the binding of NH_4^+ to S1, S2, and S4 of AmtB. The results showed that the ion binds the protein at the S1 site, where it is stabilized by cation–π interactions with Trp148, Phe103, and Phe107, and by hydrogen bonding to Ser219 and two water molecules (see Figure 8.4a).[18]

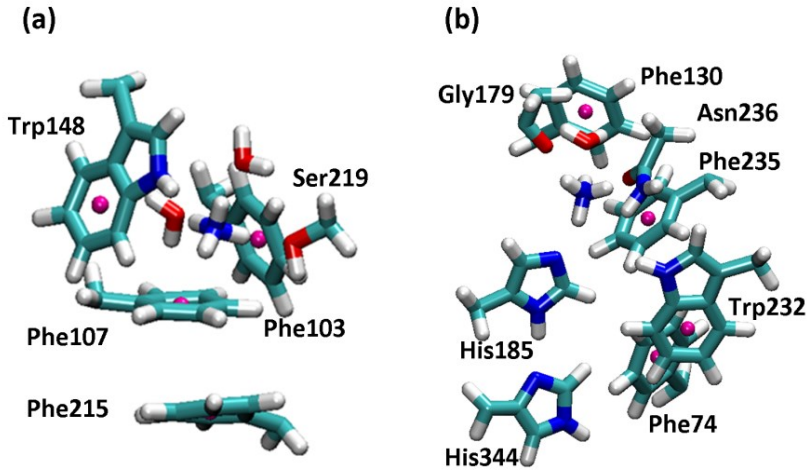

Figure 8.4. Binding of NH_4^+ to the periplasmic vestibule of AmtB (panel a) and RhCG (panel b). In AmtB the ion is coordinated by Phe103, Phe107, Trp148, Ser219, and two water molecules. In RhCG, the ion is bound to Gly179, His185, Phe235, Asn236, and one water molecule.

To investigate the recruitment of NH_4^+ by RhCG, we performed a 50 ns PM/MM MD simulation with NH_4^+ at site W of the RhCG monomer. In order to equilibrate the ion, it was restrained to stay within 3.5 Å of the Nε atom of His185 for the first 10 ns of the simulation. The ion remained bound to His185 throughout the whole simulation. As a control, a second 50 ns simulation was performed with the ion initially restrained to a maximum distance of 3.5 Å from the center of the six membered ring of Phe130. Within 1 ns of removing the restraint, NH_4^+ reached His185 and adopted same binding conformation as in the first simulation (site W). The ion is stabilized in this binding site by hydrogen bonding to His185, Asn236, Gly179, and a water molecule, and by cation–π interaction with Phe235 (see Figure 8.4b). The fact that site W in RhCG closely resemble site S2 in AmtB is clearly suggesting that NH_4^+ can cross the phenylalanine gate in AmtB and reach His168.

8.3.2. Stability of NH_4^+ in the Pore Lumen of AmtB and RhCG

In previous work,[18] MD simulations of NH_4^+ in the pore lumen of AmtB showed that the ion is stabilized at a binding position that closely resembles site S2 in the experimental structure.[19] The ion binds the protein at this site with an affinity comparable to that at S1.[18] Hydrogen bonding to His168 and to a water molecule in addition to cation–π interactions with Phe2015 and Trp212 stabilizes the ion in this position (see Figure 8.5).

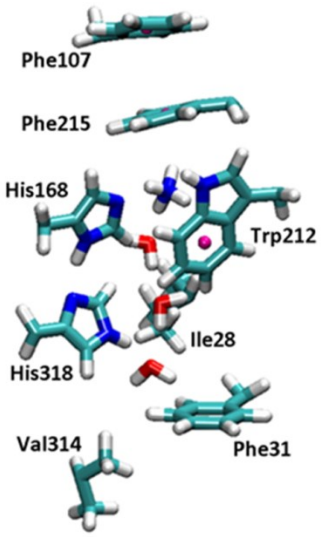

Figure 8.5. Binding of NH_4^+ in the pore lumen of AmtB. The ion is coordinated to His168, Phe215, Trp212, and one water molecule.

To study the stability of NH_4^+ in the pore of RhCG, we performed 45 ns PM/MM MD simulations on the ion inside the pore. The ion was restrained to a minimum distance of 8 Å from Nε of His185 and within a distance of 5 Å from Phe74 ring center in the first 10 ns of the simulation. After the restraint is removed, the ion leaves the pore toward the periplasmic side and occupies site W (see Fig 8.4b). The instability of NH_4^+ in the pore lumen of RhCG is likely due to the larger hydrophobicity of the RhCG pore and the absence of stable water chain in the pore (see section 8.3.3). This suggests that RhCG functions as a NH_3 rather than NH_4^+ transporter.

8.3.3. Water Accessibility to the Pore Lumen of AmtB and RhCG

Based on the X-ray structure of crystals grown in presence of ammonium salts, Khademi *et al.* assigned NH_3 molecules to the crystallographic sites S2–S4.[19] Electronic density is however observed in crystals grown in absence of ammonium salts,[345] suggesting H_2O to be the ligand at these sites. Using MD simulations it has been suggested that these sites are occupied by water molecules.[348,358] In comparison, no electron densities were assigned to H_2O or NH_3 in the pore lumen of RhCG.[20] The nature of the ligand occupying the pore of the channel is critical to the mechanism of action of the protein.[18,348]

To elucidate the stability of water in the pore of AmtB and RhCG, we run a 40-ns PM/MM MD simulation on the monomer of each protein with four water molecules added to the pore. In the first 5 ns of these simulations, water molecules are kept in the pore by applying a

restrain to keep one of them within 3.5 Å from Nε atom of His185 and to keep the water molecules within the same distance from one another. Once the restraint is removed, a stable water chain is observed in the case of AmtB with the four water molecules arranged such that one is H-bond donor to His68, one is H-bond acceptor to His318, and the four molecules are H-bonded to one another (see Figure 8.6a). This finding is in agreement with previous MD simulation results.[348,365] In contrast, no water chain is stabilized in the pore of RhCG. Immediately after the restrain is removed, the chain is broken with the water molecule bound to His185 moving toward the periplasmic side of the protein, occupying site W, and the other three water molecules moving to the cytoplasmic side (see Figure 8.6b).

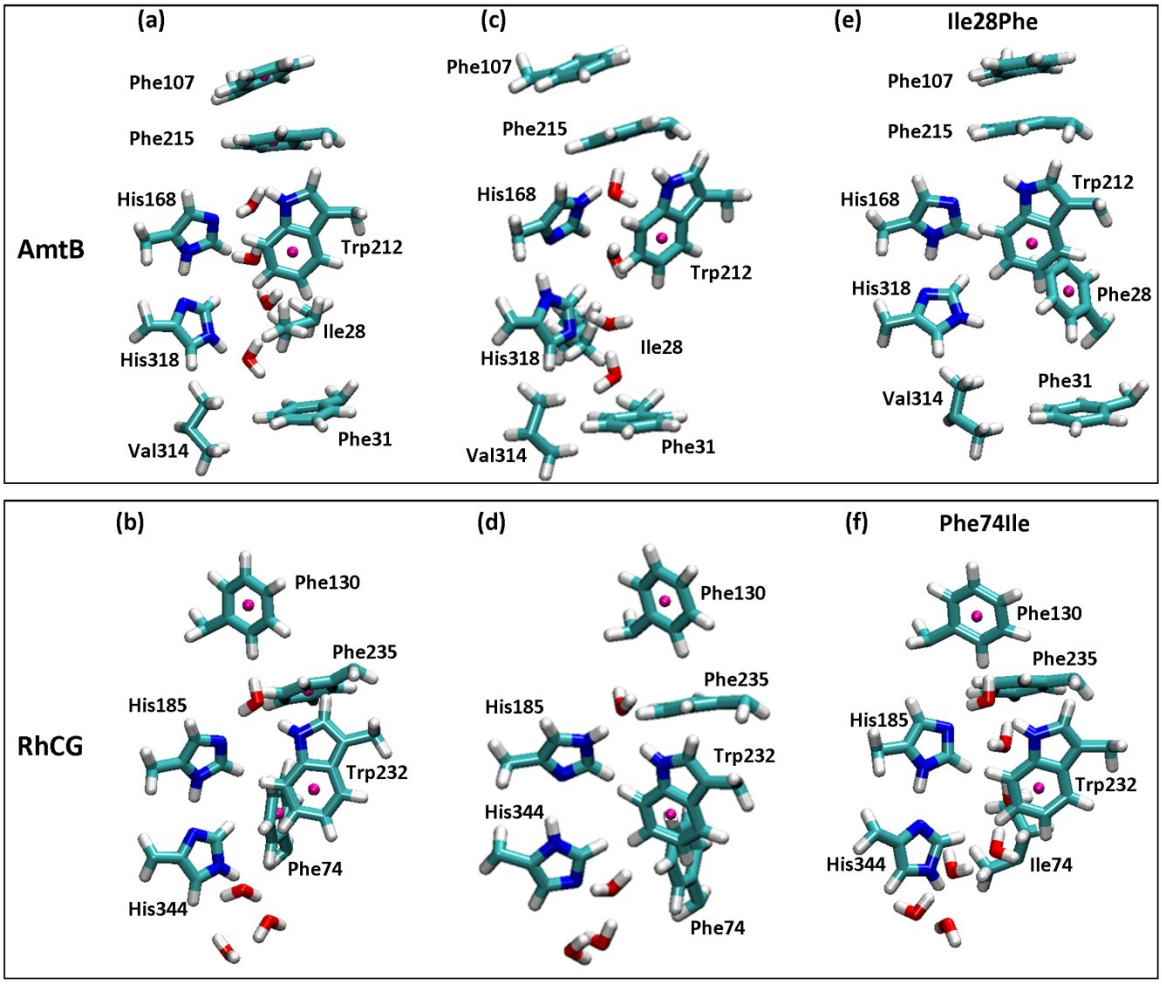

Figure 8.6. Water in the pore lumen of wild type AmtB with H–His168···H–His318 (panel a) and His168–H···His318–H (panel c) protonation structures, of wild type RhCG with H–His185···H–His344 (panels b) and His185–H···His344–H (panel d) structures, of Ile28/Phe mutated AmtB (panel e), and of Phe74/Ile mutated RhCG (panel f).

In a previous study,[18] it was shown that the H–His168···H–His318 protonation state of AmtB stabilizes water molecules in the pore lumen of the protein (Figure 8.6c). To check whether the H–His185···H–His344 protonation state can stabilize water in the pore of RhCG, we performed a 40-ns PM/MM MD simulation on this protonation state with four water molecules kept inside the pore during the first 10 ns. Similar to what is observed for the His185–H···His344–H state, one water molecule occupies site W and the rest are pushed to the cytoplasmic side of the protein upon removal of the restraints (see Figure 8.6d).

To compare the relative stability between His185–H···OH_2 and His185···H–OH, we optimized the gas-phase complexes formed between imidazole and water (Figure 8.7 a,b) at the MP2(full)/6-311++G(d,p) level using Gaussian 09.[26] The binding energy in each complex is calculated and corrected for basis set superposition error (BSSE) using the counterpoise (CP) procedure of Boys and Bernardi.[111] The dimer shows two stable conformers with water acting either as a proton donor or acceptor. The calculated BSSE-uncorrected (E) and corrected (E^{CP}) binding energies together with binding energies calculated with the Drude model (E^{MM}) are reported in Table 8.1. Results show that the binding energies of both conformers are comparable, which is likely the reason for stabilizing a water molecule at the same site (site W) in both protonation states of His185.

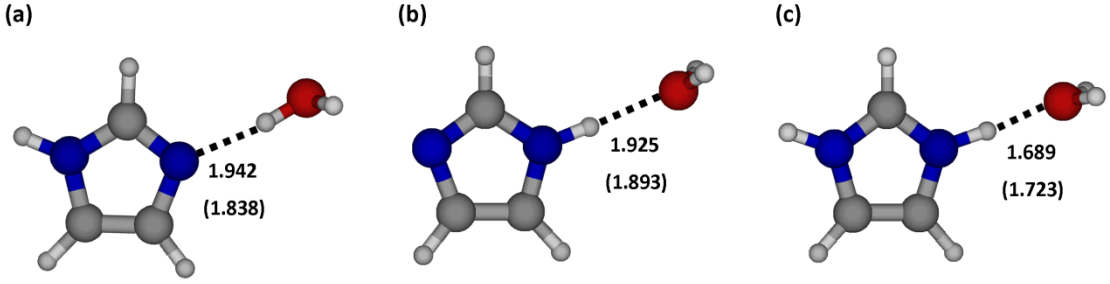

Figure 8.7. Geometries of water–imidazole and water–(imidazolium ion) dimers optimized at the MP2(full)/6-311++G(d,p) level. Numbers represent hydrogen bond distances (in Å) from ab initio and Drude (in brackets) optimized structures.

Table 8.1. BSSE-uncorrected and corrected binding energies (E and E^{CP}, respectively) of energy minima structures for gas-phase complexes of water with imidazole and imidazolium ion. Binding energies calculated with the Drude model (E^{MM}) are also reported. All energies are in kcal/mol.

Structure	E	E^{CP}	E^{MM}
a	–8.28	–6.71	–7.15
b	–7.88	–5.85	–5.58
c	–18.70	–16.14	–15.44

The major difference between the pores of the two proteins is the presence of phenylalanine (Phe74) in the structure of RhCG compared to isoleucine (Ile28) in AmtB. This results in the pore of RhCG being more hydrophobic and might thus destabilize water. To investigate the effect of pore hydrophobicity, we mutated Ile28 of AmtB to Phe and mutated Phe74 of RhCG to Ile and conducted a 50-ns PM/MM MD simulation using same procedure as for the wild types. The results show that while Ile28/Phe mutation of AmtB destabilizes the water chain that is observed in the wild type structure (see Figure 8.6e), the Phe74/Ile mutation in RhCG is stabilizing a water chain (see Figure 8.6f). It is clear thus that the stronger hydrophobicity and the narrowing of the RhCG pore, due to Phe74 side chain prevents the formation of a stable water chain.

The difference in the hydration structure of the pore of AmtB and RhCG likely affects the mechanism of transport. In a previous study we proposed that NH_4^+ reaches site S2 of AmtB and then transfers a proton to His168 leaving the neutral NH_3 which diffuses down the pore. The proton is then transferred to His318 and finally is transferred back to NH_3 leading to a net NH_3/H^+ cotransport mechanism. This results in converting the system from His168–H···His318–H state, required for proton transfer at S2, to the H–His168···H–His318 state. The presence of water molecules in the pore of AmtB is critical for the reset of the protonation state of the two histidines.[18] While NH_4^+ binds His185 in RhCG and is likely to deprotonate at this position, the absence of water molecules in the pore of RhCG makes it unlikely to have an NH_3/H^+ cotransport mechanism in this protein. Accordingly RhCG protein is most likely an NH_3 transporter.

A 40-ns MD simulation on the RhCG monomer with a protonated His185 is also performed. The simulation is showing a periplasmic water chain that ends with a water molecule at site W (see Figure 8.8). This water molecule is stabilized by the strong hydrogen bond that forms between imidazolium cation and water. Ab initio calculations predict a binding energy between water and imidazolium cation that is about three times that between water and neutral histidine (see Figure 8.7 and Table 8.1). It is likely thus that His185 will transfer the proton to periplasm through this water chain.

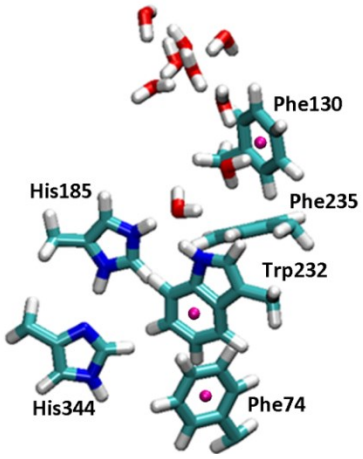

Figure 8.8. A snapshot from simulation of RhCG protein with protonated His185 showing periplasmic water reaching His185.

8.3.4. Binding Selectivity and Activity-Inhibition of RhCG and AmtB

The binding affinity of AmtB and RhCG toward NH_3, NH_4^+, Na^+, K^+, Rb^+, Cs^+, and Tl^+ is calculated as the difference of the free energy for alchemical transformation of the ligand into H_2O at the protein putative binding site (ΔG_{mut}^{prot}) and in bulk water (ΔG_{mut}^{wat}). We calculate the binding affinity of S1 and S2 of AmtB and of site W of RhCG. The results are summarized in Table 8.2. We calculate equivalent dissociation constants for the various ligands (see Table 8.3) as follows:

$$K_d = [W]\cdot\exp(\Delta\Delta G_{bind}/RT) \qquad 8.1$$

where [W] is the concentration of water (55.4 M), T is temperature, and R is the gas constant.

Table 8.2. Relative binding free energies of NH_3, NH_4^+, Na^+, K^+, Rb^+, Cs^+, and Tl^+ at the S1 and S2 sites of AmtB and at site W of RhCG (in kcal/mol)

Mutation	ΔG_{mut}^{wat}	ΔG_{mut}^{prot}			$\Delta\Delta G_{bind} = \Delta G_{mut}^{prot} - \Delta G_{mut}^{wat}$		
		RhCG, W	AmtB, S1	AmtB, S2	RhCG, W	AmtB, S1	AmtB, S2
$H_2O \rightarrow NH_3$	2.0 ± 0.1	3.3 ± 0.3	1.0 ± 0.2	1.2 ± 0.2	+1.2 ± 0.2	–1.0 ± 0.3	–0.8 ± 0.2
$H_2O \rightarrow NH_4^+$	–61.7 ± 0.2	–83.6 ± 1.4	–75.8 ± 1.3	–74.7 ± 1.2	–21.9 ± 1.6	–14.1 ± 1.5[a]	–13.0 ± 1.0[a]
$H_2O \rightarrow Na^+$	–80.3 ± 0.3	–94.7 ± 1.5	–85.2 ± 1.6	–81.9 ± 1.5	–14.4 ± 1.2	–4.9 ± 1.0[a]	–1.6 ± 1.0
$H_2O \rightarrow K^+$	–62.9 ± 0.2	–79.7 ± 0.9	–68.8 ± 1.1	–68.6 ± 1.2	–16.8 ± 1.5	–5.9 ± 0.4[a]	–5.7 ± 0.9
$H_2O \rightarrow Rb^+$	–57.1 ± 0.2	–76.1 ± 1.1	–66.8 ± 0.8	–66.3 ± 1.6	–19.0 ± 1.2	–9.7 ± 0.8	–9.2 ± 0.7
$H_2O \rightarrow Cs^+$	–49.9 ± 0.3	–72.3 ± 1.0	–63.3 ± 1.3	–62.8 ± 1.4	–22.4 ± 1.6	–13.4 ± 1.1	–12.9 ± 1.0
$H_2O \rightarrow Tl^+$	–64.7 ± 0.2	–89.6 ± 1.2	–83.15 ± 1.2	–82.3 ± 1.1	–24.9 ± 1.4	–18.5 ± 1.5	–17.6 ± 1.6

[a] Reproduced from reference 18.

Table 8.3. Dissociation constants (K_d, in M) of the various ligands at site W of RhCG and at sites S1 and S2 of AmtB calculated using *Eq*. 8.1

Ligand	RhCG, site W	AmtB, site S1	AmtB, site S2
NH_3	4.20×10^{2}	10.2	14.4
NH_4^+	4.91×10^{-15}	2.56×10^{-9}	1.64×10^{-8}
Na^+	1.54×10^{-9}	1.42×10^{-2}	3.72
K^+	2.69×10^{-11}	2.62×10^{-3}	3.68×10^{-3}
Rb^+	6.55×10^{-13}	4.30×10^{-6}	1.00×10^{-5}
Cs^+	2.11×10^{-15}	8.34×10^{-9}	1.94×10^{-8}
Tl^+	3.10×10^{-17}	1.52×10^{-12}	6.96×10^{-12}

The data show that the binding affinity of NH_3 is much lower than that of NH_4^+, confirming that the latter is the species that initially binds the protein. Except for NH_3, the binding affinity of RhCG toward all studied ligands is higher than those of sites S1 and S2 of AmtB. The difference in affinity between the two proteins arises from different coordination schemes. In AmtB, NH_4^+ is coordinated by two water molecules, Ser219, Phe107, and Trp148 in S1 and is coordinated by one water, Phe215, Trp212, and His168 in site S2. In comparison, the ion is coordinated to one water, His185, Asn236, Gly179, and Phe235 in RhCG. Table 6.1 of chapter 6 shows that the binding affinities between an ion and the oxygen atom of acetamide and N-methylacetamide are about 10 kcal/mol higher than the binding affinities with water, ethanol, and model compounds to the aromatic amino acid side chains. In comparison calculations at the MP2(full)/6-311++G(d,p) level shows that water binds acetamide with E^{CP} = –8.35 kcal/mol and binds N-methylacetamide with E^{CP} = –6.59 kcal/mol. These are, in respective, 3.86 and 1.76 kcal/mol higher than the binding energy of the water dimer calculated at the same level, E^{CP} = –4.49 kcal/mol. Accordingly, strong interactions between the ions and Asn236 and Gly179 stabilize the ions at site W of RhCG relative to bulk water and result in the higher binding affinity of the protein relative to this of AmtB.

It is experimentally observed that Amt proteins activities are not inhibited by Na^+ or K^+ ions.[20,25,339] It is however found that 50 mM Cs^+ and 0.5 mM Tl^+ cause full inhibition of AmtB activity.[21] The crystal structure of AmtB protein crystallized in presence of 1 mM thallium chloride and 100 mM ammonium sulphate is suggesting binding of Tl^+ at S1.[21] The data in Table 8.2 are consistent with this trend. Na^+, K^+, and Rb^+ bind the two proteins with lower binding

affinities compared to that of NH_4^+ and are thus unlikely, especially for Na^+ and K^+, to compete with ammonium binding. In comparison, the binding affinity of Cs^+ and Tl^+ are comparable and higher than that of NH_4^+. The high affinity toward these two metal ions is the reason for their inhibition of the protein activity. The higher affinity toward Tl^+ compared to Cs^+ explains why the activity of the protein is inhibited by 50 mM of Cs^+ but requires only 0.5 mM of Tl^+.[21]

The increase in binding affinity of both proteins with increasing the size of alkali ions suggests that cation–π interactions play a role in the protein selectivity. It is found that the affinity of alkali ions toward aromatic compounds in aqueous solutions increases with the size of the ion (see chapter 6 and reference 30). The presence of aromatic amino acids at the ion-binding sites stabilizes thus the larger ion (Rb^+ and Cs^+) than the smaller ones (Na^+ and K^+). Cation–π interactions are also responsible for the high binding affinity of both proteins toward Tl^+. It has been found (see Chapter 6) that Tl^+ complexes with aromatic compounds are very stable in aqueous solutions.

Table 8.3 is showing a dissociation constant of NH_4^+ at S1 of AmtB = 2.56 nM. This is consistent with the experimental activity of Amt proteins. It is found that *E. coli* can grow normally without functional AmtB protein down to ammonium concentrations of ~0.1 μM[349] and that AmtB is inactivated at concentrations higher than ~5–50 μM.[365] It is also consistent with nanomolar affinity of benzene-based synthetic receptors.[366] In comparison, a dissociation constant of 4.91 fM is calculated for NH_4^+ at site W of RhCG.

8.4. Conclusion

Binding selectivity of AmtB and RhCG proteins is studied using PM/MM MD simulation set up. The results are showing that among NH_3, Na^+, K^+, Rb^+, Cs^+, and Tl^+, only the last two may compete with NH_4^+ for binding the proteins, and hence cause the experimentally observed inhibition of the protein activity. While the pore lumen of AmtB is experimentally[345] and computationally[348,358] observed to stabilize a chain of water molecules, the pore of RhCG is largely hydrophobic and does not stabilize water. Among transport mechanisms, NH_4^+ transport and NH_3/H^+ cotransport are suggested for AmtB. Water molecules in the pore of AmtB are found critical for the latter mechanism, and are required for stabilizing NH_4^+ during its transport. The absence of water in the pore of RhCG indicates that the protein function as NH_3 transporter.

9. Conclusion and Future Work

9.1. Conclusion

The wide distribution of ions in all domains of life and the critical roles they play in biological systems has been the motivation for the development of molecular models for ion-protein interactions presented in this study.

Toward understanding how proteins discriminate between various metal ions, we have optimized polarizable force field (FF) models for ammonia and hydrogen sulfide (minimal model compound for N and S-containing ligands).[170,262] The models, together with a previously developed model for water,[113] were used in molecular dynamics simulations to study the solvation structure and solvation free energy of alkali metal ions in liquid water, ammonia, and hydrogen sulfide and to study the ion's preferential solvation in aqueous NH_3 and aqueous H_2S solutions. The optimized models for NH_3 and H_2S reproduce the experimental structure and the experimental thermodynamic properties of the pure and aqueous liquids under wide range of temperatures and pressures.[170,262] The models reproduce the ab initio properties of NH_3–NH_3, NH_3–H_2O, NH_3–alkali ion, H_2S–H_2S, H_2S–H_2O, and H_2S–alkali ion clusters without further adjustments.[170,202,262] They also show[4] solvation structures and solvation free energies of alkali ions in liquid ammonia in agreement with experimental data. In addition, they show selectivity of alkali ions toward the three ligands in agreement with the Hard and Soft Acids and Bases theory.[170,202,262] The simulations are giving insight itno the mechanism of metal ion selectivity toward ligands. It is found that the strength of metal-ligand interaction is not the only factor contributing to metal ion selectivity. The size of the ligand and the nature of interactions between first and second shell solvent molecules are also important. For example while alkali metals bind NH_3 more strongly than H_2O in gas phase, it is seen that they are preferentially solvated by water in aqueous ammonia solutions. The small size of H_2O relative to NH_3 and the stronger (H_2O)–H···$O(H_2O)$ and (H_2O)–H···$N(NH_3)$ hydrogen bonds relative to (NH_3)–H···$O(H_2O)$ and (NH_3)–H···$N(NH_3)$ hydrogen bonds result in water being selected over ammonia in the ion's first solvation shell.[202]

Because of the various roles of Mg^{2+} and Ca^{2+} in biological systems, one of the aims of this work was to develop molecular models for the two metals. Due to the limitations of force fields in describing chemical reactions and the computational cost of ab initio quantum mechanical (QM) calculations, we optimize new semiempirical (SE) QM models for the two

metals based on the original AM1 scheme.[28] The models are calibrated on the binding energies and structures of binary complexes of each metal ion with a variety of ligands that model protein groups that can bind the two ions. Two models are optimized for each metal with parameters being compatible with AM1 parameters for H, C, N, O, and S for one model and compatible with RM1 parameters of these elements for the other model. The performance of the models is tested on ~170 binary and water-containing ternary complexes that range in size from the dimer to the heptamer. The optimized models for Ca reliably reproduce the ab initio properties of both training and testing sets. Except for complexes containing sulfur, the optimized models for Mg give good agreement with the calculated ab initio properties. For complexes containing sulfur, Mg models underestimate their binding energies. The fact that Mg^{2+} is a hard metal and does not coordinate sulfur, allows for using its models in studying Mg^{2+}-metalloproteins.

Cation–π interactions are common among biological systems. Toward understanding their roles and measuring their strength and geometry in biological systems, polarizable FFs for the interaction of metal ions (Rb^+, Cs^+, Tl^+) and quaternary ammonium ions (NH_4^+, tetramethylammonium (TMA^+), tetraethylammonium(TEA^+)) with model compounds to aromatic amino acids side chains are calibrated on the ab initio properties of the different cation–π pairs. Polarizable models for the interaction of the three metal ions with acetamide, N-methylacetamide, and imidazole are also optimized in order to compare the strength of cation–π and charge-dipole interactions. Results are showing that while becoming weaker compared to gas-phase, cation–π interactions still persist in aqueous solution. Similar to gas phase, cations bind the face rather than the side of the aromatic compounds in aqueous solutions. Results also show that in contrast to gas phase, cation–π complexes are more stable than charge-dipole complexes in water. The results are suggesting a role of cation–π interactions in the solubility of aromatic compounds in aqueous salt solutions. For example the binding affinity of Rb^+, Cs^+, NH_4^+, TMA^+, and TEA^+ toward benzene[173,338] in water follows the order $Cs^+ > Rb^+$ and $TEA^+ > TMA^+ > NH_4^+$, which follows the same trend for benzene solubility in aqueous salts of these cations.

Membrane proteins of the Amt/Mep/Rh family transport ammonium across cell membranes.[25,39,339–343] A further aim of this work was to measure the binding affinity of AmtB and RhCG protein toward various ligands and to study the structure-function relationship of amino acids that line the transport pathway. For this regard, FF models for ion-protein

interactions from this work and from previous studies[18,30,31,356] are used in MD simulations of both proteins. Results are showing that among NH_3, Na^+, K^+, Rb^+, Cs^+, and Tl^+, only the last two have binding affinities similar or higher than that of NH_4^+ toward the proteins. Only Cs^+ and Tl^+ may thus compete with NH_4^+ for binding the protein. This is in line with the experimental finding that while Na^+ and K^+ do not inhibit the activity of Amt proteins,[21,25,339] 50 mM Cs^+ and 0.5 mM Tl^+ causes a full inhibition of protein activity.[21] Simulations also show that the larger hydrophobicity of the pore of RhCG compared to that of AmtB destabilizes NH_4^+ and prevent the formation of a stable water chain in the pore of RhCG. This results in RhCG functioning as NH_3 transporter rather than NH_4^+ transporter or NH_3/H^+ cotransporter.

9.2. Future Work

The presented work opens various avenues of investigation, such as:

1. Investigating the preferential solvation of alkali metal ions in complex mixtures. While alkali ions are found[202,262] selective to H_2O over NH_3 in aqueous ammonia solutions and are found to be selective to H_2O over H_2S in aqueous hydrogen sulfide solutions, it would be interesting to study the influence of the third component on ion's selectivity. In this regard MD simulations on alkali ions solvated in mixtures of H_2O, NH_3, and H_2S are required. MD simulations on binary and complex mixtures containing other ligands are also important for complete understanding of the selectivity of alkali ions. Ligands that mimic protein groups that coordinate these metal ions seem the most appropriate for this purpose. For example MD simulation on alkali ions solvated in aqueous solutions containing acetate ions (model for Asp and Glu), acetamide (model for Asn, Gln, and peptide backbones), and ethanol (model for Ser and Thr) can be performed. The composition of the ion's first solvation shells can aide in identifying plausible binding sites in biological systems and in designing potential ion selective receptors.

2. Optimized SE models of Mg and Ca can similarly be used to investigate the preferential solvation of the two ions by various ligands. This is of critical importance toward understanding the structural and geometrical requirements for protein binding sites to coordinate the two metal ions and how these binding sites are/can be designed to discriminate between the two metal ions. The models can also be used in SE MD simulations to study the rate of ligand exchange in each ion's first solvation shell. Ca^{2+} has a high ($> 10^8$ s^{-1}) water-exchange rate constant while Mg^{2+} possesses an intermediate rate constant (10^4–10^8 s^{-1}).[367] Calculation of the rate of water exchange

as a function of ligand structure and hardness is required to get insight into the kinetics and mechanism of protein binding as a function of binding site composition. Optimized models can also be used SE QM/MM MD simulations to study the influence of the metal ions on protein stability, to study the mechanisms of reactions in enzymes utilizing these metal ions as cofactors, and to calculate the binding affinity of various proteins toward both metal ions. For example, calmodulin (CaM) is a protein containing the "EF hand" (a helix-loop-helix structural domain found in a large family of calcium-binding proteins), and is involved in a variety of physiological processes. While the apo form of CaM is characterized by a partially unfolded C-terminal domain and an almost fully folded N-terminal domain,[368–370] the holo form is characterized by fully structured domains. The protein is also known to be selective for Ca^{2+} over Mg^{2+}.[227] Optimized SE models can be used to understand the conformational change associated with Ca^{2+} binding, to investigate the influence of Ca^{2+} on the stability of CaM, and to measure the binding affinity of the protein toward Ca^{2+} and Mg^{2+}.

3. Optimized models for cation–π interactions can be used to measure binding stability and roles of these interactions in proteins. An example is understanding the mechanism of activity inhibition of potassium channels by quaternary ammonium (QA) ions such as TMA^+ and TEA^+.[327,328] The structure of the bacterial KcsA channel shows four Tyr82 residues coordinating TEA^+.[371] The structure and computational studies[366–374] are however suggesting an edge-on binding mode between the ion and the four aromatic amino acid side chains. Force fields used in these studies are however not calibrated for cation–π interactions and might thus underestimate the stability of the en face binding mode of the complexes. A properly calibrated force field is needed to understand the mechanism of activity inhibition and the forces playing the roles in ligand binding.

References

1. Cowan, J. A. Inorganic Biochemistry. An Introduction, 2nd ed., Wiley-VCH, New York, **1997**.
2. Crabb, E.; Davies, R.; Janes, R.; Moore, E.; Smart, L.; Walton, P. Metals and Life, Royal Society of Chemistry, **2010**.
3. Pearson, R. G. *J. Am. Chem. Soc.* **1963**, *85*, 3533–3539.
4. Haas, K. L.; Franz, K. J. *Chem. Rev.* **2009**, *109*, 4921–4960.
5. Müller-Dethlefs, K.; Hobza, P. *Chem. Rev*. **2000**, *100*, 143–167.
6. Dougherty, D. A. *Science*, **1996**, *271*, 163–168.
7. Gromiha, M. M.; Santhosh, C.; Ahmad, S. *Int. J. Biolog. Macromol.* **2004**, *34*, 203–211.
8. Prajapati, R. S.; Sirajuddin, M.; Durani, V.; Sreeramulu, S.; Varadarajan, R. *Biochemistry*, **2006**, *45*, 15000–15010.
9. Tayubi, I. A.; Sethumadhavan, R. *Biochemistry-Moscow*, **2010**, *75*, 912–918.
10. Wintjens, R.; Lievin, J.; Rooman, M.; Buisine, E. *J. Mol. Biol.* **2000**, *302*, 395–410.
11. Lummis, S. C. R.; Beene, D. L.; Harrison, N. J.; Lester, H. A.; Dougherty, D. A. *Chem. Biol*. **2005**, *12*, 993–997.
12. Cheng, J. G.; Luo, X. M.; Yan, X. H.; Li, Z.; Tang, Y.; Jiang, H. L.; Zhu, W. L. *Sci. China Ser. B: Chem*. **2008**, *51*, 709–717.
13. Mecozzi, S.; West, A. P.; Dougherty, D. A. *J. Am. Chem. Soc.* **1996**, *118*, 2307–2308.
14. Cubero, E.; Luque, F. J.; Orozco, M. *Proc. Natl. Acad. Sci. U.S.A.* **1998**, *95*, 5976–5980.
15. Soteras, I.; Orozco, M.; Luque, F. J. *Phys. Chem. Chem. Phys.* **2008**, *10*, 2616–2624.
16. Tsuzuki, S.; Yoshida, M.; Uchimaru, T.; Mikami, M. *J. Phys. Chem. A* **2001**, *105*, 769–773.
17. Lamoureux, G.; Javelle, A.; Baday, S.; Wang, S.; Bernèche, S. *Transf. Clin. Biol*. **2010**, *17*, 168–175.
18. Wang, S.; Orabi, E. A.; Baday, S.; Bernèche, S.; Lamoureux, G. *J. Am. Chem. Soc*. **2012**, *134*, 10419–10427.
19. Khademi, S.; O'Connell, J.; Remis, J.; Robles-Colmenares, Y.; Miercke, L. J. W.; Stroud, R. M. *Science*, **2004**, *305*, 1587–1594.
20. Gruswitz, F.; Chaudhary, S.; Ho, J. D.; Schlessinger, A.; Pezeshki, B.; Ho, C. M.; Sali, A.; Westhoff, C. M.; Stroud, R. M. *Proc. Natl. Acad. Sci. U.S.A*. **2010**, *107*, 9638–9643.

21. Javelle, A.; Lupo, D.; Ripoche, P.; Fulford, T.; Merrick, M.; Winkler, F. K. *Proc. Natl. Acad. Sci. U.S.A.* **2008**, *105*, 5040–5045.
22. Boeckstaens, M.; André, B.; Marini, A. M. *J. Biol. Chem*. **2008**, *283*, 21362–21370.
23. Ludewig, U. *Transfus. Clin. Biol*. **2006**, *13*, 111–116.
24. Fong, R. N.; Kim, K. S.; Yoshihara, C.; Inwood, W. B.; Kustu, S. *Proc. Natl. Acad. Sci. U.S.A.* **2007**, *104*, 18706–18711.
25. Ludewig, U.; von Wirén, N.; Frommer, W. B. *J. Biol. Chem.* **2002**, *277*, 13548–13555.
26. Frisch, M. J.; Trucks, G. W.; Schlegel, H. B.; Scuseria, G. E.; Robb, M. A.; Cheeseman, J. R.; Scalmani, G.; Barone, V.; Mennucci, B.; Petersson, G. A.; Nakatsuji, H.; Caricato, M.; Li, X.; Hratchian, H. P.; Izmaylov, A. F.; Bloino, J.; Zheng, G.; Sonnenberg, J. L.; Hada, M.; Ehara, M.; Toyota, K.; Fukuda, R.; Hasegawa, J.; Ishida, M.; Nakajima, T.; Honda, Y.; Kitao, O.; Nakai, H.; Vreven, T.; Montgomery, Jr., J. A.; Peralta, J. E.; Ogliaro, F.; Bearpark, M.; Heyd, J. J.; Brothers, E.; Kudin, K. N.; Staroverov, V. N.; Kobayashi, R.; Normand, J.; Raghavachari, K.; Rendell, A.; Burant, J. C.; Iyengar, S. S.; Tomasi, J.; Cossi, M.; Rega, N.; Millam, J. M.; Klene, M.; Knox, J. E.; Cross, J. B.; Bakken, V.; Adamo, C.; Jaramillo, J.; Gomperts, R.; Stratmann, R. E.; Yazyev, O.; Austin, A. J.; Cammi, R.; Pomelli, C.; Ochterski, J. W.; Martin, R. L.; Morokuma, K.; Zakrzewski, V. G.; Voth, G. A.; Salvador, P.; Dannenberg, J. J.; Dapprich, S.; Daniels, A. D.; Farkas, Ö.; Foresman, J. B.; Ortiz, J. V.; Cioslowski, J.; Fox, D. J. Gaussian, Inc., Wallingford CT Gaussian 09, Revision B.01, **2009**.
27. Murrell, J. N.; Harget, A. J. Semiempirical Self-Consistent-Field Molecular Orbital Theory of Molecules, Wiley, New York, **1972**.
28. Dewar, M. J. S.; Zoebisch, E. G.; Healy, E. H.; Stewart, J. J. P. *J. Am. Chem. Soc.* **1985**, *107*, 3902–3909.
29. Brooks, B. R.; Brooks, C. L.; Mackerell, A. D.; Nilsson, L.; Petrella, R. J.; Roux, B.; Won, Y.; Archontis, G.; Bartels, C.; Boresch, S.; Caflisch, A.; Caves, L.; Cui, Q.; Dinner, A. R.; Feig, M.; Fischer, S.; Gao, J.; Hodoscek, M.; Im, W.; Kuczera, K.; Lazaridis, T.; Ma, J.; Ovchinnikov, V.; Paci, E.; Pastor, R. W.; Post, C. B.; Pu, J. Z.; Schaefer, M.; Tidor, B.; Venable, R. M.; Woodcock, H. L.; Wu, X.; Yang, W.; York, D. M.; Karplus, M. *J. Comput. Chem*. **2009**, *30*, 1545–1614.
30. Orabi, E. A.; Lamoureux, G. *J. Chem. Theory Comput*. **2012**, *8*, 182–193.

31. Lamoureux, G.; Orabi, E. A. *Mol. Simul*. **2012**, *38*, 704–722.
32. Lamoureux, G.; Roux, B. *J. Chem. Phys*. **2003**, *119*, 3025–3039.
33. Martyna, G. J.; Tuckerman, M. E.; Tobias, D. J.; Klein, M. L. *Mol. Phys*. **1996**, *87*, 1117–1157.
34. Lagowski, J. J. *Synth. React. Inorg. Met.-Org. Nano-Metal Chem*. **2007**, *37*, 115–153.
35. Lagowski, J. J. *Pure Appl. Chem*. **1971**, *25*, 429–456.
36. Miflin, B. J.; Lea, P. J. *Annu. Rev. Plant Physiol*. **1977**, *28*, 299–329.
37. Ninnemann, O.; Jauniaux, J.-C.; Frommer, W. B. *EMBO J*. **1994**, *13*, 3464–3471.
38. Marini, A.-M.; Urrestarazu, A.; Beauwens, R.; André, B. *Trends Biochem. Sci*. **1997**, *22*, 460–461.
39. Marini, A.-M.; Soussi-Boudekou, S.; Vissers, S.; André, B. *Mol. Cell. Biol*. **1997**, *17*, 4282–4293.
40. Marini, A.-M.; Vissers, S.; Urrestarazu, A.; André, B. *EMBO J*. **1994**, *13*, 3456–3463.
41. Narten, A. H. *J. Chem. Phys*. **1968**, *49*, 1692–1696.
42. Narten, A. H. *J. Chem. Phys*. **1977**, *66*, 3117–3120.
43. Ricci, M. A.; Nardone, M.; Ricci, F. P.; Andreani, C.; Soper, A. K. *J. Chem. Phys.* **1995**, *102*, 7650–7655.
44. Thompson, H.; Wasse, J. C.; Skipper, N. T.; Hayama, S.; Bowron, D. T.; Soper, A. K. *J. Am. Chem. Soc*., **2003**, *125*, 2572–2581.
45. Kasahara K.; Munakata T.; Uematsu M. *J. Chem. Thermodyn*. **1999**, *31*, 1273–1281.
46. Overstreet, R.; Giauque, W. F.; *J. Am. Chem. Soc*., **1937**, *59*, 254–259.
47. Garroway A. N.; Cotts, R. M. *Phys. Rev. A*, **1973**, *7*, 635–648.
48. O'Reilly, D. E.; Peterson, E. M.; Scheie, C. E. *J. Chem. Phys*. **1973**, *58*, 4072–4075.
49. Groß, T.; Buchhauser, J.; Price, W. E.; Tarassov, I. N.; H.-D. Lüdemann, H.-D.; *J. Mol. Liq*. **1997**, *73–74*, 433–444.
50. Billaud, G.; Demortier, A. *J. Phys. Chem*. **1975**, *79*, 3053–3055.
51. Plank, C. J.; Herschel, H. *J. Am. Chem. Soc*. **1939**, *61*, 3590–3591.
52. Osborne, N. S.; Van Dusen, M. S. *J. Am. Chem. Soc*. **1918**, *40*, 14–25.
53. Howard, M. J.; Burdenski, S.; Giese, C. F.; Gentry, W. R. *J. Chem. Phys*. **1984**, *80*, 4137–4141.

54. Fraser, G. T.; Nelson, D.D.; Charo, A.; Klemperer, W. *J. Chem. Phys*. **1985**, *82*, 2535–2546.
55. Snels, M.; Fantoni, R.; Sanders, R.; Meerts, W. L. *Chem. Phys*. **1987**, *115*, 79–91.
56. Kamke, W.; Herrmann, R.; Wang, Z.; Hertel, I. V. Z. Phys. D: At., Mol. Clusters, **1988**, *10*, 491–497.
57. Marshall, M. D.; Izgi, K. C.; Muenter, J. S. *J. Chem. Phys*. **1997**, *107*, 1037–1044.
58. Lee J. S.; Park, S. Y. *J. Chem. Phys*. **2000**, *112*, 230–237.
59. Kulkarni, S. A.; Pathak, R. K. Chem. Phys. Lett. **2001**, *336*, 278–283.
60. Janeiro-Barral P. E.; Mella, M. *J. Phys. Chem. A*, **2006**, *110*, 11244–11251.
61. Sagarik, K. P.; Ahlrichs R.; Brode, S. *Mol. Phys*. **1986**, *57*, 1247–1264.
62. Greer, J. C.; Ahlrichs, R.; Hertel, I. V. *Chem. Phys*. **1989**, *133*, 191–197.
63. Beu, T. A.; Buck, U. *J. Chem. Phys*. **2001**, *114*, 7848–7852.
64. Janeiro-Barral, P. E.; Mella, M.; Curotto, E. *J. Phys. Chem. A*, **2008**, *112*, 2888–2898.
65. Yu, L.; Yang, Z.-Z. *J. Chem. Phys*. **2010**, *132*, 174109-1–174109-11.
66. Impey, R. W.; Klein M. L. Chem. Phys. Lett. **1984**, *104*, 579–582.
67. Almeida, T. S.; Coutinho, K.; Cabral, B. J. C.; Canuto, S. *J. Chem. Phys*. **2008**, *128*, 014506-1–014506-9.
68. Hinchliffe, A.; Bounds, D. G.; Klein, M. L.; McDonald, I. R.; Righini, R. *J. Chem. Phys*. **1981**, *74*, 1211–1216.
69. Rizzo, R. C.; Jorgensen, W. L. *J. Am. Chem. Soc*. **1999**, *121*, 4827–4836.
70. Kristóf, T.; Vorholz, J.; Liszi, J.; Rumpf, B.; Maurer, G. *Mol. Phys*. **1999**, *97*, 1129–1137.
71. Diraison, M.; Martyna, G. J.; Tuckerman, M. E.; *J. Chem. Phys*. **1999**, *111*, 1096–1103.
72. Kiselev, M.; Kerdcharoen, T.; Hannongbua, S.; Heinzinger, K. Chem. Phys. Lett. **2000**, *327*, 425–428.
73. Hannongbua, S. *J. Chem. Phys*. **2000**, *113*, 4707–4712.
74. Honda, K. *Bull. Chem. Soc. Jpn*. **2000**, *73*, 289–295.
75. Boese, A. D.; Chandra, A.; Martin, J. M. L.; Marx, D. *J. Chem. Phys*. **2003**, *119*, 5965–5980.
76. Tongraar, A.; Kerdcharoen, T.; Hannongbua, S. *J. Phys. Chem. A*, **2006**, *110*, 4924–4929.
77. Eckl, B.; Vrabec, J.; Hasse, H. *Mol. Phys*. **2008**, *106*, 1039–1046.
78. Chowdhuri, S.; Chakraborty D.; Chandra, A. *Ind. J. Phys*. **2009**, *83*, 91–100.

79. Tassaing, T.; Soetens, J.-C.; Vyalov, I.; Kiselev, M.; Idrissi, A. *J. Chem. Phys*. **2010**, *133*, 214505-1–214505-8.
80. Feng, H.; Liu, X.; Gao, W.; Chen, X.; Wang, J.; Chen, L.; Lüdemann, H.-D. *Phys. Chem. Chem. Phys*. **2010**, *12*, 15007–15017.
81. Vyalov, I.; Kiselev, M.; Tassaing, T.; Soetens, J. C.; Idrissi, A. *J. Phys. Chem. B*, **2010**, *114*,15003–15010.
82. Engin, C.; Merker, T.; Vrabec, J.; Hasse, H. *Mol. Phys*. **2011**, *109*, 619–624.
83. Abbaspour, M. *Chem. Phys*. **2011**, *389*, 121–127.
84. Ren, P.; Wu, C.; Ponder, J. W. *J. Chem. Theory Comput*. **2011**, *7*, 3143–3161.
85. Tillner-Roth R.; Friend, D. G. *J. Phys. Chem. Ref. Data*, **1998**, *27*, 45–61.
86. Herbine, P.; Dyke, T. R. *J. Chem. Phys*. **1985**, *83*, 3768–3774.
87. Stockman, P. A.; Bumgarner, R. E.; Suzuki, S.; Blake, G. A. *J. Chem. Phys*. **1992**, *96*, 2496–2510.
88. Fraser, G. T.; Suenram, R. D. *J. Chem. Phys*. **1992**, *96*, 7287–7297.
89. Kuma, S.; Slipchenko, M. N.; Momose, T.; Vilesov, A. F. *Chem. Phys. Lett*. **2007**, *439*, 265–269.
90. Mollner, A. K.; Casterline, B. E.; Ch'ng, L. C.; Reisler, H. *J. Phys. Chem. A*, **2009**, *113*, 10174–10183.
91. Tuma, C.; Boese, A. D.; Handy, N. C. *Phys. Chem. Chem. Phys*. **1999**, *1*, 3939–3947.
92. Sadlej, J.; Moszynski, R.; Dobrowolski, J. Cz.; Mazurek, A. P. *J. Phys. Chem. A*, **1999**, *103*, 8528–8536.
93. Rappé, A. K.; Bernstein, E. R. *J. Phys. Chem. A*, **2000**, *104*, 6117–6128.
94. Rzepkowska, J.; Uras, N.; Sadlej, J.; Buch, V. *J. Phys. Chem. A*, **2002**, *106*, 1790–1796.
95. Huang, N.; MacKerell, A. D. *J. Phys. Chem. A*, **2002**, *106*, 7820–7827.
96. Lane, J. R.; Vaida, V.; Kjaergaard, H. G. *J. Chem. Phys*. **2008**, *128*, 034302-1–034302-11.
97. Donaldson, D. J. *J. Phys. Chem. A*, **1999**, *103*, 62–70.
98. Takaoka, T.; Inamura, M.; Yanagimachi, S.; Kusunoki, I.; Komeda, T. *J. Chem. Phys*. **2004**, *121*, 4331–4338
99. Bacelo, D. E. *J. Phys. Chem. A*, **2002**, *106*, 11190–11196.
100. Karthikeyan, S.; Singh, N. J.; Kim, K. S. *J. Phys. Chem. A*, **2008**, *112*, 6527–6532.
101. Sorkin, A.; Dahlke, E. E.; Truhlar, D. G. *J. Chem. Theory Comput*. **2008**, *4*, 683–688.

102. Tanabe, Y.; Rode, B. M. *J. Chem. Soc., Faraday Trans*. 2, **1988**, *84*, 679–692.
103. Ferrario, M.; Haughney, M.; McDonald, I. R.; Klein, M. L. *J. Chem. Phys*. **1990**, *93*, 5156–5166.
104. Udomsub, S.; Hannongbua, S. *J. Chem. Soc., Faraday Trans*. **1997**, *93*, 3045–3052.
105. Uras, N.; Buch, V.; Devlin, J. P. *J. Phys. Chem. B*, **2000**, *104*, 9203–9209.
106. Dang, L. X.; Garrett, B. C. *Chem. Phys. Lett*. **2004**, *385*, 309–313.
107. Paul, S.; Chandra, A. *J. Chem. Phys*. **2005**, *123*, 174712-1–174712-9.
108. Pártay, L. B.; Jedlovszky, P.; Hoang, P. N. M.; Picaud, S.; Mezei, M. *J. Phys. Chem. C* **2007**, *111*, 9407–9416.
109. Takenaka, N.; Koyano, Y.; Nagaoka, M. *Chem. Phys. Lett*. **2010**, *485*, 119–123.
110. Chakraborty, D.; Chandra, A. *J. Chem. Phys*. **2011**, *135*, 114510-1–114510-10.
111. Boys, S. F.; Bernardi, F. *Mol. Phys*. **1970**, *19*, 553–566.
112. (a) Dunning, T. H. Jr. *J. Chem. Phys*. **1989**, *90*, 1007–1023. (b) Kendall, R. A.; Dunning, T. H. Jr.; Harrison, R. J. *J. Chem. Phys*. **1992**, *96*, 6796–6806. (c) Woon, D. E.; Dunning, T. H. Jr. *J. Chem. Phys*. **1993**, *98*, 1358–1371. (d) Woon, D. E.; Dunning, T. H., Jr. *J. Chem. Phys*. **1994**, *100*, 2975–2988.
113. Lamoureux, G.; Harder, E.; Vorobyov, I. V.; Roux, B.; MacKerell, A. D. *Chem. Phys. Lett*. **2006**, *418*, 245–249.
114. MacKerell, A. D.; Bashford, D.; Bellott, M.; Dunbrack, R. L.; Evanseck, J. D.; Field, M. J.; Fischer, S.; Gao, J.; Guo, H.; Ha, S.; Joseph-McCarthy, D.; Kuchnir, L.; Kuczera, K.; Lau, F. T. K.; Mattos, C.; Michnick, S.; Ngo, T.; Nguyen, D. T.; Prodhom, B.; Reiher, W. E.; Roux, B.; Schlenkrich, M.; Smith, J. C.; Stote, R.; Straub, J.; Watanabe, M.; Wiorkiewicz-Kuczera, J.; Yin, D.; Karplus, M. *J. Phys. Chem. B*, **1998**, *102*, 3586–3616.
115. Essmann, U.; Perera, L.; Berkowitz, M. L.; Darden, T.; Lee, H.; Pedersen, L. G. *J. Chem. Phys*. **1995**, *103*, 8577–8593.
116. Lagüe, P.; Pastor, R. W.; Brooks, B. R. *J. Phys. Chem. B*, **2004**, *108*, 363–368.
117. Deng, Y.; Roux, B. *J. Phys. Chem. B*, **2004**, *108*, 16567–16576.
118. Yu, H.; Whitfield, T.; Harder, E.; Lamoureux, G.; Vorobyov, I.; Anisimov, V. M.; MacKerell, A. D.; Roux, B. *J. Chem. Theory Comput*. **2010**, *6*, 774–786.
119. Benedict, W. S.; Gailar, N.; Plyler, E. K. *Can. J. Phys*. **1957**, **35**, 1235–1241.

120. Shimanouchi, T. Tables of molecular Vibrational frequencies I. National Standard Reference Data Series – National Bureau of Standards 39, Washington, DC, **1972**, http://www.nist.gov/data/nsrds/NSRDS-NBS-39.pdf (accessed on March 13, 2012).
121. Haar, L.; Gallagher, J. S. *J. Phys. Chem. Ref. Data*, **1978**, *7*, 635–792.
122. Lamoureux, G.; MacKerell, A. D.; Roux, B. *J. Chem. Phys*. **2003**, *119*, 5185–5197.
123. Yeh, I.-C.; Hummer, G. *J. Phys. Chem. B*, **2004**, *108*, 15873–15879.
124. Lopes, P. E. M.; Lamoureux, G.; Roux, B.; MacKerell, A. D. *J. Phys. Chem. B*, **2007**, *111*, 2873–2885.
125. Natl. Bur. Std. (U. S.) Circ. No. 142, **1923**.
126. Lemmon, E. W.; McLinden, M. O; Friend, D. G. Thermophysical Properties of Fluid Systems, in NIST Chemistry WebBook, NIST Standard Reference Database Number 69, ed. Linstrom, P. J; Mallard, W. G. National Institute of Standards and Technology, Gaithersburg, MD, 20899, 2000, http://webbook.nist.gov (retrieved March 15, 2012).
127. Lange, N. A. Handbook of Chemistry, 10th ed.; McGraw-Hill: New York, **1961**
128. Guevara-Carrion, G.; Vrabec, J.; Hasse, H. *Int. J. Thermophys.*, **2012**, *33*, 449–468.
129. Idrissi, A.; Vyalov, I. *J. Phys. Chem. B*, **2011**, *115*, 2011, 9646–9652.
130. Jones F. M.; Arnett, E. M. *Prog. Phys. Org. Chem*. **1974**, *11*, 263–332.
131. Ben-Naim, A.; Marcus, Y. *J. Chem. Phys*. **1984**, *81*, 2016–2027.
132. King, H. H.; Hall, J. L.; Ware, G. C. *J. Am. Chem. Soc*., **1930**, *52*, 5128–5135.
133. Appl, M. *Ammonia, 1. Introduction*. In Ullmann's Encyclopedia of Industrial Chemistry; Wiley-VCH: Weinheim, **2011**.
134. Kraus, C. A.; Lucasse, W. W. *J. Am. Chem. Soc*. **1921**, *43*, 2529–2539.
135. Kraus, C. A.; Carney, E. S.; Johnson, W. C. *J. Am. Chem. Soc*. **1927**, *49*, 2206–2213.
136. Johnson, W. C.; Meyer, A. W. *J. Am. Chem. Soc*. **1932**, *54*, 3621–3628.
137. Wasse, J. C.; Hayama, S.; Neal T. Skipper, N. T. *Phys. Rev. B*, **2000**, *61*, 11993–11997.
138. Wasse, J. C.; Hayama, S.; Masmanidis, S.; Stebbings, S. L.; Skipper, N. T. *J. Chem. Phys*. **2003**, *118*, 7486–7494.
139. Wasse, J. C.; Hayama, S.; Skipper, N. T. *J. Phys. Chem. B*, **2003**, *107*, 14452–14456.
140. Thompson, H.; Wasse, J. C.; Skipper, N. T.; Howard, C. A.; Bowron, D. T.; Soper, A. K. *J. Phys. Condens. Matter*, **2004**, *16*, 5639–5652.
141. Salter, T. E.; Mikhailov, V.; Ellis, A. M. *J. Phys. Chem. A*, **2007**, *111*, 8344–8351.

142. Hannongbua, S.; Ishida, T.; Spohr, E.; Heinzinger, K. *Z. Naturforsch. A*, **1988**, *43*, 572–582.
143. Marchi, M.; Sprik, M.; Klein, M. L. *J. Phys. Condens. Matter*, **1990**, *2*, 5833–5848.
144. Gurskii, Z.; Hannongbua, S.; Heinzinger, K. *Mol. Phys.* **1993**, *78*, 461–474.
145. Kerdcharoen, T.; Liedl, K. R.; Rode, B. M. *Chem. Phys*. **1996**, *211*, 313–323.
146. Tongraar, A.; Hannongbua, S.; Rode, B. M. *Chem. Phys.* **1997**, *219*, 279–29.
147. Hannongbua, S. *J. Chem. Phys*. **1997**, *106*, 6076–6081.
148. Hannongbua, S. *Chem. Phys. Lett*. **1998**, *288*, 663–668.
149. Kerdcharoen, T.; Hannongbua, S. *Chem. Phys. Lett*. **1999**, *310*, 333–341.
150. Kerdcharoen, T.; Rode, B. M. *J. Phys. Chem. A*, **2000**, *104*, 7073–7078.
151. Mierzwicki, K.; Latajka, Z. *Chem. Phys.* **2001**, *265*, 301–311.
152. Hannongbua, S.; Remsungnen, T.; Kiselev, M.; Heinzinger, K. *Condens. Matter Phys.* **2003**, *6*, 459–470.
153. Corral, I.; Mó, O.; Yáñez, M.; Radom, L. *J. Phys. Chem. A*, **2005**, *109*, 6735–6742.
154. Salter, T. E.; Ellis, A. M. *Chem. Phys.* **2007**, *332*, 132–138.
155. Chandra, A.; Marx, D. *Angew. Chem. Int. Ed.* **2007**, *46*, 3676–3679.
156. Lim, I. S.; Botschwina, P.; Oswald, R.; Barone, V.; Stoll, H.; Schwerdtfeger, P. *J. Chem. Phys.* **2007**, *127*, 104313-1–104313-12.
157. Pinsook, U.; Scheicher, R. H.; Ahuja, R.; Hannongbua, S. *J. Phys. Chem. A*, **2008**, *112*, 5323–5326.
158. Almeida, T. S.; Cabral, B. J. C. *J. Chem. Phys*. **2010**, *132*, 094307-1–094307-10.
159. Tongraar, A.; Hannongbua, S. *J. Phys. Chem. B*, **2008**, *112*, 885–891.
160. Rode B. M.; Tanabe, Y. *J. Chem. Soc., Faraday Trans. 2*, **1988**, *84*, 1779–1788.
161. Kheawsrikul, S.; Hannongbua, S. V.; Kokpol, S. U.; Rode, B. M. *J. Chem. Soc., Faraday Trans. 2*, **1989**,*85*, 643–649.
162. Tongraar, A.; Rode, B. M. *J. Phys. Chem. A*, **1999**, *103*, 8524–8527.
163. Tongraar, A.; Rode, B. M. *J. Phys. Chem. A*, **2001**, *105*, 506–510.
164. Tongraar, A.; Rode, B. M. *Phys. Chem. Chem. Phys*. **2004**, *6*, 411–416.
165. Tongraar, A.; Rode, B. M. *Chem. Phys. Lett.* **2008**, *466*, 61–64.
166. Pratihar, S.; Chandra, A. *J. Chem. Phys*. **2011**, *134*, 024519-1–024519-8.
167. Glendening, E. D. *J. Am. Chem. Soc*. **1996**, *118*, 2473–2482.

168. The Stuttgart relativistic small core basis set was obtained from EMSL Basis Set Library at the URL https://bse.pnl.gov/bse/portal. For the original valence basis set and ECP reference, see: Bergner, A.; Dolg, M.; Kuechle, W.; Stoll, H.; Preuss, H. *Mol. Phys*. **1993***, 80*, 1431–1441.
169. Coletti, C.; Re, N. *J. Phys. Chem. A*, **2006**, *110*, 6563–6570.
170. Orabi, E. A.; Lamoureux, G. *J. Chem. Theory Comput*. **2013**, *9*, 2035–2051.
171. Lamoureux, G.; Roux, B. *J. Phys. Chem. B*, **2006**, *110*, 3308–3322.
172. Kumar, S.; Bouzida, D.; Swendsen, R. H.; Kollman, P. A.; Rosenberg, J. M. *J. Comput. Chem*. **1992**, *13*, 1011–1021.
173. Souaille, M.; Roux, B. *Comput. Phys. Commun*. **2001**, *135*, 40–57.
174. Woodin, R. L.; Beauchamp, J. L. *J. Am. Chem. Soc*. **1978**, *100*, 501–508.
175. Armentrout, P. B.; Rodgers, M. T. *J. Phys. Chem. A*, **2000**, *104*, 2238–2247.
176. Iceman, C.; Armentrout, P. *Int. J. Mass Spectrom*. **2003**, *222*, 329–349.
177. Džidić, I.; Kebarle, P. *J. Phys. Chem*. **1970**, *74*, 1466–1474.
178. Glendening, E. D.; Feller, D. *J. Phys. Chem*. **1995**, *99*, 3060–3067.
179. Halgren, T. A. *J. Am. Chem. Soc.* **1992**, *114*, 7827–7843.
180. Plambeck, J. A. *Can. J. Chem.* **1969**, *47*, 1401–1410.
181. Tuttle, T. R.; Malaxos, S.; Coe, J. V. *J. Phys. Chem. A*, **2002**, *106*, 925–932.
182. Tissandier, M. D.; Cowen, K. A.; Feng, W. Y.; Gundlach, E.; Cohen, M. H.; Earhart, A. D.; Coe, J. V. *J. Phys. Chem. A* **1998**, *102,* 7787–7794.
183. Marcus, Y. *J. Chem. Soc. Faraday Trans*. 1, **1988**, *84*, 1465–1473.
184. Bagarinao, T. *Aquatic Toxicol.* **1992**, *24*, 21–62.
185. Reiffenstein, R. J.; Hulbert, W. C.; Roth, S. H. *Annu. Rev. Pharmacol. Toxicol*. **1992**, *32*, 109–134.
186. EPA, Report to Congress on Hydrogen Sulfide Air Emissions Associated with the Extraction of Oil and Natural Gas. EPA-453/R-93-045, **1993**.
187. Li, L.; Rose, P.; Moore, P. K. *Annu. Rev. Pharmacol. Toxicol*. **2011**, *51*, 169–187.
188. Soper, A. K.; Bruni, F.; Ricci, M. A. *J. Chem. Phys*. **1997**, *106*, 247–254.
189. Santoli, G.; Bruni, F.; Ricci, F. P.; Ricci, M. A.; Soper, A. K. *Mol. Phys*. **1999**, *97*, 777–786.
190. Clarke, E. C. W.; Glew, D. N. *Can. J. Chem*. **1970**, *48*, 764–775.

191. Ihmels, E. C.; Gmehling, J. *Ind. Eng. Chem. Res*. **2001**, *40*, 4470–4477.
192. Giauque, W. F.; Blue, B. W. *J. Am. Chem. Soc*. **1936**, *58*, 831–837.
193. Liessmann, G.; Schmidt, W.; Reiffarth, S. Recommended thermophysical data; Data compilation of the Saechsische Olefinwerke: Boehlen, Germany, **1995**.
194. Dupré, F.; Piaggesi, D.; Ricci, F. P. *Phys. Lett. A*, **1980**, *80*, 178–180.
195. Havriliak, S.; Swenson, R. W.; Cole, R. H. *J. Chem. Phys*. **1955**, *23*, 134–135.
196. Lemmon, E. W.; McLinden, M. O.; Friend, D. G. "Thermophysical properties of fluid systems" in NIST Chemistry WebBook, NIST Standard Reference Database Number 69, Eds. Linstrom, P. J.; Mallard, W. G. National Institute of Standards and Technology, Gaithersburg MD, 20899, http://webbook.nist.gov (accessed on May 13, 2013).
197. Jorgensen, W. L. *J. Chem. Phys*. **1986**, *90*, 6379–6388.
198. Forester, T. R.; McDonald, I. R.; Klein, M. L. *Chem. Phys*. **1989**, *129*, 225–234.
199. Kristóf, T.; Liszi, J. *J. Chem. Phys. B*, **1997**, *101*, 5480–5483.
200. Kamath, G.; Lubna, N.; Potoff, J. J. *J. Chem. Phys*. **2005**, *123*, 124505-1–124505-7.
201. Riahi, S; Rowley, C. N. *J. Phys. Chem. B*, **2013**, *117*, 5222–5229.
202. Orabi, E. A.; Lamoureux, G. *J. Chem. Theory Comput*. **2013**, *9*, 2324–2338.
203. Herzberg, G. Electronic spectra and electronic structure of polyatomic molecules, Van Nostrand, New York, **1966**.
204. Zezin, D. Yu.; Migdisov, A. A.; Williams-Jones, A. E. *Geochim. Cosmochim. Acta*, **2011**, *75*, 5483–5495.
205. Hoover, W. G. *Phys. Rev. A*, **1985**, *31*, 1695–1697.
206. Martyna, G. J.; Tobias, D. J.; Klein, M. L. *J. Chem. Phys*. **1994**, *101*, 4177–4189.
207. Neumann, M.; Steinhauser, O. *Chem. Phys. Lett*. **1984**, *106*, 563–569.
208. Buckingham, A. D. *Proc. R. Soc. London, Ser. A*, **1956**, *238*, 235–244.
209. Hoy, A. R.; Bunker, P. R. *J. Mol. Spectrosc.* **1979**, *74*, 1–8.
210. Nelson R. D.; Lide, D. R.; Maryott, A. A. Selected values of electric dipole moments for molecules in the gas phase. National Standard Reference Data Series – National Bureau of Standards 10, Washington, DC, **1967**, http://www.nist.gov/data/nsrds/NSRDS-NBS-10.pdf (accessed on May 13, 2014).
211. Olney, T. N.; Cann, N. M.; Cooper, G.; Brion, C. E. *Chem. Phys*. **1997**, *223*, 59–98.

212. Shimanouchi, T. Tables of molecular Vibrational frequencies I. National Standard Reference Data Series – National Bureau of Standards 39, Washington, DC, **1972**, http://www.nist.gov/data/nsrds/NSRDS-NBS-39.pdf (accessed on May 13, 2014).
213. Wilhelm, E.; Battino, R.; Wilcock, R. J. *Chem. Rev*. **1977**, *77*, 219–262.
214. Kubo, M. M.; Gallicchio, E.; Levy, R. M. *J. Phys. Chem. B*, **1997**, *101*, 10527–10534.
215. Riahi, S; Rowley, C. N. *J. Phys. Chem. B*, **2014**, 118, 1373–1380.
216. Suleimenov, O. M.; Krupp, R. E. *Geochim. Cosmochim. Acta*, **1994**, *58*, 2433–2444.
217. Cotton, F. A.; Wilkinson, G. Anorganische Chemie. Weilheim, Germany: Chemie GmbH, **1967**.
218. Weast, R. C. Handbook of Chemistry and Physics. Boca Raton, FL: CRC Press **1987**.
219. Maguire, M. E.; Cowan, J. A. *Biometals*, **2002**, *15*, 203–210.
220. Wacker, W. Magnesium and Man. Cambridge, MA: Harvard University Press; **1980**, 1–184.
221. Elin, R. *J. Dis. Mon*. **1988**, *34*, 161–218.
222. Swaminathan R. Magnesium metabolism and its disorders. *Clin. Biochem. Rev*. **2003**, *24*, 47–66.
223. Feillet-Coudray, C.; Coudray, C.; Gueux, E.; Mazur, A.; Rayssiguier, Y. *J. Nutr*. **2003**, *133*, 1220–1223.
224. Jahnen-Dechent, W.; Ketteler, M. *Clin. Kidney J*. **2012**, *5*(Suppl 1), i3–i14.
225. Saris, N. E.; Mervaala, E.; Karppanen, H.; Khawaja. J. A.; Lewenstam, A. *Clin. Chim. Acta* **2000**, *294*, 1–26.
226. Cunningham, J.; Rodrı´guez, J. M.; Messa, P. *Clin. Kidney J*. **2012**, *5*(Suppl 1), i39–i51.
227. Bertini, I.; Gray, H. B.; Lippard, S. J.; Valentine, J. S.; Forsen, S.; Kördel, J. Calcium in Biological Systems. In Bioinorganic Chemistry; University Science Books: Mill Valley, CA, **1994**, 107–166.
228. Williams, R. J. Biochim. *Biophys. Acta*, **2006**, *1763*, 1139–1146.
229. Case, R. M.; Eisner, D.; Gurney, A.; Jones, O.; Muallem, S.; Verkhratsky, A. *Cell Calcium*, **2007**, *42*, 345–350.
230. Zhou, Y.; Xue, S.; Yang, J. *J. Metallomics*, **2013**, *5*, 29–42.
231. Glusker, J. P.; Katz, A. K.; Bock, C. W. *Rigaku J*. **1999**, *16*, 8–16.

232. Peeraer, Y.; Rabijns, A.; Gollet, J. F.; Van Schaftingen, E.; De Ranter, C. Eur. J. Biochem. **2004**, *271*, 3421–3427.
233. Pople, J. A, Santry, D. P.; Segal, G. A. *J. Chem. Phys*. **1965**, *43*, S129–S135.
234. Pople, J. A.; Beveridge, D. L.; Dobosh, P. A. *J. Chem. Phys*. **1967**, *47*, 2026–2033.
235. Stewart, J. J. P. *J. Comput. Chem*. **1989**, *10*, 209–220.
236. Stewart, J. J. P. *J. Comput. Chem*. **1989**, *10*, 221–264.
237. Stewart, J. J. P. *J. Comput. Chem*. **1991**, *12*, 320–341.
238. Stewart, J. J. P. *J. Mol. Model*. **2007**, *13*, 1173–1213.
239. Stewart, J. J. P.. *J. Mol. Model*. **2013**, *19*, 1–32.
240. Rocha, G. B, Freire, R. O.; Simas, A. M.; Stewart, J. J. P. *J. Comput. Chem*. **2006**, *27*, 1101–1111.
241. Bräuer, M.; Kunert, M.; Dinjus, E.; Klußmann, M.; Döring, M.; Görls, H.; Anders, E. *J. Mol. Struct. THEOCHEM*, **2000**, *505*, 289–301.
242. Troya, D.; García-Molina, E. *J. Phys. Chem. A*, **2005**, *109*, 3015–3023.
243. Nam, K.; Cui, Q.; Gao, J.; York, D. M. *J. Chem. Theory Comput*. **2007**, *3*, 486–504.
244. Korth, M.; Thiel, W. *J. Chem. Theory Comput*. **2011**, *7*, 2929–2936.
245. Choi, T. H.; Liang, R.; Maupin, C. M.; Voth, G. A. *J. Phys. Chem. B*, **2013**, 117, 5165–5179.
246. Wang, S.; MacKay, L.; Lamoureux, G. *J. Chem. Theory Comput*. **2014**, *10*, 2881–2890.
247. Stewart, J. J. P. *J. Comput.-Aided Mol. Des*. **1990**, *4*, 1–103.
248. Stewart, J. J. P. *J. Mol. Model*. **2004**, *10*, 155–164.
249. Hutter, M. C.; Reimers, J. R.; Hush, N. S. *J. Phys. Chem. B*, **1998**, *102*, 8080–8090.
250. Cundari, T. R.; Deng, J.; Fu, W. Int. *J. Quantum Chem*. **2000**, *77*, 421–432.
251. Brothers, E. N.; Merz, K. M., Jr. *Phys. Chem. B*, **2002**, *106*, 2779–2785.
252. Giese, T. J.; Sherer, E. C.; Cramer, C. J.; York, D. M. *J. Chem. Theory Comput*. **2005**, *1*, 1275–1285.
253. McNamara, J. P.; Sundararajan, M.; Hillier, I. H. *J. Mol. Graph. Model*. **2005**, *24*, 128–137.
254. Giese, T. J.; York, D. M. *J. Chem. Phys*. **2005**, *123*, 164108-1–164108-9.
255. Tejero, I.; González-Lafont, À.; Lluch, J. M. *J. Comput. Chem*. **2007**, *28*, 997–1005.

256. Williams, D. E.; Peters, M. B.; Wang, B.; Merz, K. M. *J. Phys. Chem. A*, **2008**, *112*, 8829–8838.
257. Tafipolsky, M.; Schmid, R. *J. Phys. Chem. B*, **2009**, *113*, 1341–1352.
258. Mane, J. Y.; Klobukowski, M. *Chem. Phys. Lett*. **2010**, *500*, 140–143.
259. Isegawa, M.; Fiedler, L.; Leverentz, H. R.; Wang, Y.; Nachimuthu, S.; Gao, J.; Truhlar, D. G. *J. Chem. Theory Comput*. **2013**, *9*, 33–45.
260. Charbonneau, P. *Astrophys*. *J. Suppl. Ser*. **1995**, *101*, 309–334.
261. Nelson R. D.; Lide, D. R.; Maryott, A. A. Selected values of electric dipole moments for molecules in the gas phase. National Standard Reference Data Series – National Bureau of Standards 10, Washington, DC, 1967, http://www.nist.gov/data/nsrds/NSRDS-NBS-10.pdf (accessed on January 10, 2015).
262. Orabi, E. A.; Lamoureux, G. *J. Chem. Theory Comput.* **2014**, 10, 3221–3235.
263. Suárez, D.; Rayón, V. M.; Díaz, N.; Valdés, H. *J. Phys. Chem. A*, **2011**, *115*, 11331–11343.
264. Johnson, E. R.; Keinan, S.; Mori-Sánchez, P.; Contreras-García, J.; Cohen A. J.; Yang, W. *J. Am. Chem. Soc.*, **2010**, *132*, 6498–6506.
265. Watson, J. D.; Crick, F. H. C. *Nature*, **1953**, *171*, 737–738.
266. Guerra, C. F.; Bickelhaupt, F. M.; Snijders, J. G.; Baerends, E. J. *J. Am. Chem. Soc*. **2000**, *122*, 4117–4128.
267. Meyer, E. A.; Castellano, R. K.; Diederich, F. *Angew. Chem. Int. Ed*. *Engl*. **2003**, *42*, 1210–1250.
268. Stauffer, D. A.; Barrans, R. E.; Dougherty, D. A. *J. Org. Chem.* **1990**, *55*, 2762–2767.
269. Gallivan, J. P.; Dougherty, D. A. *Proc. Natl. Acad. Sci. U. S. A.* **1999**, *96*, 9459–9464.
270. Ma, J. C.; Dougherty, D. A. *Chem. Rev.* **1997**, *97*, 1303–1324.
271. Kumpf, R. A.; Dougherty, D. A. *Science*, **1993**, *261*, 1708–1710.
272. Mecozzi, S. *Proc. Natl. Acad. Sci. U. S. A.* **1996**, *93*, 10566–10571.
273. Caldwell, J. W.; Kollman, P. A. *J. Am. Chem. Soc.* 1995, *117*, 4177–4178.
274. Minoux, H.; Chipot, C. *J. Am. Chem. Soc.* **1999**, *121*, 10366–10372.
275. Dehez, F.; Ángyán, J. G.; Gutiérrez, I. S.; Luque, F. J.; Schulten, K.; Chipot, C. *J. Chem. Theory Comput*. **2007**, *3*, 1914–1926.
276. Archambault, F.; Chipot, C.; Soteras, I.; Luque, F. J.; Schulten, K.; Dehez, F. *J. Chem. Theory Comput*. **2009**, *5*, 3022–3031.

277. Burley, S. K.; Petsko, G. A. *FEBS Letters*, **1986**, *203*, 139–143.
278. Singh, J.; Thornton, J. M. *J. Mol. Biol.* **1990**, *211*, 595–615.
279. Mitchell, J. B.; Nandi, C. L.; McDonald, I. K.; Thornton, J. M.; Price, S. L. *J. Mol. Biol.* **1994**, *239*, 315–331.
280. Shi, Z.; Olson, C. A.; Kallenbach, N. R. *J. Am. Chem. Soc.* **2002**, *124*, 3284–3291.
281. Andrew, C. D.; Bhattacharjee, S.; Kokkoni,N.; Hirst, J. D.; Jones, G. R.; Doig, A. J. *J. Am. Chem. Soc.* **2002**, *124*, 12706–12714.
282. Tsou, L. K.; Tatko, C. D.; Waters, M. L. *J. Am. Chem. Soc.* **2002**, *124*, 14917–14921.
283. Tatko, C. D.; Waters, M. L. *Prot. Sci.* **2003**, *12*, 2443–2452.
284. Riemen, A. J.; Waters, M. L. *Biochemistry*, **2009**, *48*, 1525–1531.
285. Imai, Y. N.; Inoue, Y.; Yamamoto, Y. *J. Med. Chem.* **2007**, *50*, 1189–1196.
286. Prajapati, R. S.; Sirajuddin, M.; Durani, V.; Sreeramulu, S.; Varadarajan, R. *J. Phys. Chem. A*, **2000**, *104*, 11414–11419.
287. Jay C. Amicangelo, J. C.; Armentrout, P. B. *J. Phys. Chem. A*, **2000**, *104*, 11420–11432.
288. Amunugama, R.; Rodgers, M. T. *J. Phys. Chem. A*, **2002**, *106*, 9718–9728.
289. Kim, D.; Hu, S.; Tarakeshwar, P.; Kim, K. S.; Lisy, J. M. *J. Phys. Chem. A*, **2003**, *107*, 1228–1238.
290. Reddy, A. S.; Sastry, G. N. *J. Phys. Chem. A*, **2005**, *109*, 8893–8903.
291. Ruan, C.; Yang, Z.; Hallowita, N.; Rodgers, M. T. *J. Phys. Chem. A*, **2005**, *109*, 11539–11550.
292. Min, S. K; Lee, E. C.; Lee, H. M.; Kim, D. Y.; Kim, D.; Kim, K. S. *J. Comput. Chem*. **2008**, *29*, 1208–1221.
293. Amunugama, R.; Rodgers, M. T. *J. Phys. Chem. A*, **2002**, *106*, 5529–5539.
294. Singh, N. J.; S. K.; Kim, D. Y.; Kim, K. S. *J. Chem. Theory Comput.* **2009**, *5*, 515–529.
295. Marshall, M. S.; Steele, R. P.; Thanthiriwatte, K. S.; Sherrill, C. D. *J. Phys. Chem. A*, **2009**, *113*, 13628–13632.
296. Xu, Y.; Shen, J.; Zhu, W.; Luo, X.; Chen, K.; Jiang, H. *J. Phys. Chem. B*, **2005**, *109*, 5945–5949.
297. Gallivan, J. P.; Dougherty, D. A. *J. Am. Chem. Soc.* **2000**, *122*, 870–874.
298. Frontera, A.; Quiñonero, D.; Garau, C.; Costa, A.; Ballester, P.; Deyà, P. M. *J. Phys. Chem. A*, **2006**, *110*, 9307–9309.

299. Vijay, D.; Sastry, G. N. *Chem. Phys. Lett.* **2010**, *485*, 235–242.
300. Wireduaah, S.; Parker, T. M.; Lewis. M. *J. Phys. Chem. A*, **2013**, *117*, 2598–2604.
301. Lebowitz, E.; Greene, M. W.; Fairchild, R.; Bradley-Moore, P. R.; Atkins, H. L.; Ansari, A. N.; Richards, P.; Belgrave, E. *J. Nucl. Med*. **1975**, *16*, 151–155.
302. Mudring, A.; Rieger, F. *Inorg. Chem.* **2005**, *44*, 6240–6243.
303. Akhbari, K.; Morsali, A. *Coord. Chem. Rev*. **2010**, *254*, 1977–2006.
304. Marcus, Y. *J. Chem. Soc., Faraday Trans,* **1991**, *87*, 2995–2999.
305. Stevens, W. J.; Krauss, M.; Basch, H.; Jasien, P. G. *Can. J. Chem*. **1992**, *70*, 612–630.
306. Vchirawongkwin, V.; Hofer, T. S.; Randolf, B. R.; Rode, B. M.; *J. Comput. Chem*. **2007**, *28*, 1006–1016.
307. Anisimov, V. M.; Vorobyov, I. V.; Roux, B.; Mackerell, A. D.; *J. Chem. Theory Comput*. **2007**, *3*, 1927–1946.
308. Harder, E.; Anisimov, V. M.; Whitfield, T.; MacKerell, A. D.; Roux, B. *J. Phys. Chem. B*, **2008**, *112*, 3509–3521.
309. Lev, B. B.; Salahub, D. R.; Noskov, S. Y.; *Interdiscip. Sci. Comput. Life Sci*. **2010**, *2*, 12–20.
310. McDevit, W. F.; Long, F. A. *J. Am. Chem. Soc.* **1952**, *74*, 1773–1777.
311. Caracelli, I.; Haiduc, I.; Zukerman-Schpector, J.; Tiekink, E. R. T.; *Coord. Chem. Rev*. **2014**, *281*, 50–63.
312. PDB Protein Data Bank: http://www.pdb.org/pdb/home/home.do
313. Kiser, P. D.; Lorimer, G. H.; Palczewski, K.; *Acta Crystallogr. F65*, **2009**, *65*, 967–971.
314. Gill, H. S.; Eisenberg, D. *Biochemistry*, **2001**, *40*, 1903–1912.
315. Rife, C. L.; Pharris, R. E.; Newcomer, M. E.; Armstrong, R. N. *J. Am. Chem. Soc*. **2002**, *124*, 11001–11003.
316. Crowley, P. B.; Golovin, A. *Proteins: Struct. Funct. Bioinf.* **2005**, *59*, 231–239.
317. Lehn, J.-M.; Meric, R.; Vigneron, J.-P.; Cesario, M.; Guilhem, J.; Pascard, C.; Asfari, Z.; Vicens, *J. Supramol. Chem*. **1995**, *5*, 97–103.
318. Mavri, J.; Koller, J.; Hadži, D. *J. Mol. Struc.-THEOCHEM*, **1993**, *283*, 305–312.
319. Kim, K. S.; Lee, J. Y.; Lee, S. J.; Ha, T.-K.; Kim, D. H. *J. Am. Chem. Soc.* **1994**, *116*, 7399–7400.

320. Lee, J. Y.; Lee, S. J.; Choi, H. S.; Cho, S. J.; Kim, K. S.; Ha, T.-K. *Chem. Phys. Lett*. **1995**, *232*, 67–71.
321. Pullman, A.; Berthier, G.; Savinelli, R. *J. Comput. Chem.* **1997**, *18*, 2012–2022.
322. Zhu, W.-L.; Tan, X.-J.; Puah, C. M.; Gu, J.-D.; Jiang, H.-L.; Chen, K.; Felder, C. E.; Silman, I.; Sussman, J. L. *J. Phys. Chem. A*, **2000**, *104*, 9573–9580.
323. C.E. Felder, C. E.; Jiang, H.-L.; Zhu, W.-L.; Chen, K.; Silman, I.; Botti, S. A.; Sussman, J. L. *J. Phys. Chem. A*, **2001**, *105*, 1326–1333.
324. Pullman, A; Berthier, G; Savinelli, R. *J. Mol. Struc.-THEOCHEM,* **2001**, *537*, 163–172.
325. Couture, J.F.; Hauk, G.; Thompson, M. J.; Blackburn, G. M.; Trievel, R. C. *J. Biol. Chem*. **2006**, *281*, 19280–19287.
326. Daze, K. D.; Hof, F. *Acc. Chem. Res.* **2013**, *46*, 937–945.
327. Armstrong, C. M. *J. Gen. Physiol.* **1971**, *58*, 413–437.
328. French, R. J.; Shoukimas, J. *J. Biophys. J.* **1981**, *34*, 271–291.
329. Deakyne, C. A.; Meotner, M. *J. Am. Chem. Soc.* **1985**, *107*, 474–479.
330. Gao, J.; Chou, L. W.; Auerbach, A. *Biophys. J.* **1993**, *65*, 43–47.
331. Duffy, E. M.; Kowalczyk, P. J.; Jorgensen, W. L. *J. Am. Chem. Soc.* **1993**, *115*, 9271–9275.
332. Chipot, C.; Maigret, B.; Pearlman, D. A.; Kollman, P. A. *J. Am. Chem. Soc.* **1996**, *118*, 2998–3005.
333. Gaberšček, M.; Mavri, *J. Chem. Phys. Lett*. **1999**, *308*, 421–427.
334. Sa, R.; Zhu, W.; Shen, J.; Gong, Z.; Cheng, J.; Chen, K.; Jiang, H. *J. Phys. Chem. B*, **2006**, *110*, 5094–5098.
335. Lopes, P. E. M.; Lamoureux, G.; MacKerell, A. D. *J. Comput. Chem.* **2009**, *30*, 1821–1838.
336. Luzhkov, V. B.; Åqvist, J. *FEBS Lett*. **2001**, *495*, 191–196.
337. Meot-Ner, M.; Deakyne, C. A. *J. Am. Chem. Soc* **1985**, *107*, 469–474.
338. Desnoyers, J. E.; Pelletier, G. E.; Jolicoeur, C. *Can. J. Chem.* **1965**, *43*, 3232–3237.
339. Ninnemann, O.; Jauniaux, J. C.; Frommer, W. B. *EMBO J.* **1994**, *13*, 3464–3671.
340. Siewe, R. M.; Weil, B.; Burkovski, A.; Eikmanns, B. J.; Eikmanns, M.; Krämer, R. *J. Biol. Chem.* **1996**, *271*, 5398–5403.
341. Ludewig U. *J. Physiol.* **2004**, *559*, 751–759.

342. Ripoche, P.; Bertrand, O.; Gane, P.; Birkenmeier, C.; Colin, Y.; Cartron, J-P. P. *Proc. Natl. Acad. Sci. U.S.A.* **2004**, *101*, 17222–17227.
343. Mouro-Chanteloup, I.; Cochet, S.; Chami, M.; Genetet, S.; Zidi-Yahiaoui, N.; Engel, A.; Colin, Y.; Bertrand, O.; Ripoche, P. *PLoS One*, **2010**, *5*, e8921.
344. Wacker, T.; Garcia-Celma, J. J.; Lewe. P.; Andrade. S. L. *Proc. Natl. Acad. Sci. U.S.A.* **2014**, *111*, 9995–10000.
345. Zheng, L.; Kostrewa, D.; Bernèche, S.; Winkler, F. K. Li, X. D. *Proc. Natl. Acad. Sci. U.S.A.* **2004**, *101*, 17090–17095.
346. Andrade, S. L.; Dickmanns, A.; Ficner, R.; Einsle, O. *Proc. Natl. Acad. Sci. U.S.A.* **2005**, *102*, 14994–14999.
347. Lupo, D.; Li, X-D. D.; Durand, A.; Tomizaki, T.; Cherif-Zahar, B.; Matassi, G.; Merrick, M.; Winkler, F. K. *Proc. Natl. Acad. Sci. U.S.A.* **2007**, *104*, 19303–19308.
348. Baday, S.; Wang, S.; Lamoureux, G.; Bernèche, S. *Biochemistry*, **2013**, *52*, 7091–7098.
349. Soupene, E.; He, L. H.; Yan, D. L.; Kustu, S. *Proc. Natl. Acad. Sci. U.S.A.* **1998**, *95*, 7030–7034.
350. Soupene, E.; Chu, T.; Corbin, R. W.; Hunt, D. F.; Kustu, S. *J. Bacteriol*. **2002**, *184*, 3396–3400.
351. Luzhkov, V. B.; Almlöf, M.; Nervall, M.; Åqvist, J. *Biochemistry*, **2006**, *45*, 10807–10814.
352. Nygaard, T. P.; Rovira, C.; Peters, G. H.; Jensen, M. O. *Biophys. J.* **2006**, *91*, 4401–4412.
353. Ishikita, H.; Knapp, E. W. *J. Am. Chem. Soc*. **2007**, *129*, 1210–1215.
354. Nygaard, T. P.; Alfonso-Prieto, M.; Peters, G. H.; Jensen, M. O.; Rovira, C. *J. Phys. Chem. B*, **2010**, *114*, 11859–11865.
355. Neuhäuser, B.; Ludewig, U. *J. Biol. Chem*. **2014**, *289*, 11650–11655.
356. Orabi, E. A. Molecular modeling of cation–π interactions and ammonium permeation in AmtB, Msc. Thesis, Department of Chemistry and Biochemistry, Concordia University, Montréal, Canada, **2011**.
357. Wang, C.; Bradley, P.; Baker, D. *J. mol. Biol.* **2007**, *373*, 503–519.
358. Lamoureux, G.; Klein, M. L.; Bernèche, S. *Biophys. J.* **200**7, *92*, L82–L84.
359. Jo, S.; Kim, T.; Iyer, V. G.; Im, W. *J. Comput. Chem.* **2008**, *29*, 1859–1865.
360. Lopes, P. E. M.; Roux, B.; MacKerell, A. D. *Theor. Chem. Acc*. **2009**, *124*, 11–28.
361. Darden, T.; York, D.; Pedersen, L., *J. Chem. Phys*. **1993**, *98*, 10089–10092.

362. Jorgensen, W. L.; Chandrasekhar, J.; Madura, J. D.; Impey, R. W.; Klein, M. L., *J. Chem. Phys*. **1983**, *79*, 926–935.
363. Kollman, P. *Chem. Rev*. **1993**, *93*, 2395–2417.
364. Hub, J. S.; Winkler, F. K.; Merrick, M.; de Groot, B. L. *J. Am. Chem. Soc.* **2010**, *132*, 13251–13263.
365. Javelle, A.; Severi, E.; Thornton, J.; Merrick, M. J. Biol. Chem. **2004**, *279*, 8530–8538.
366. Ahn, K. H.; Ku, H. Y.; Kim, Y.; Kim, S. G.; Kim, Y. K.; Son, H. S.; Ku, J. K. *Org. Lett*. **2003**, *5*, 1419–1422.
367. Silva J. J. R. F. D.; Williams, R. J. P. The Biological Chemistry of the Elements, Clarendon Press: Oxford, **1991**.
368. Finn, B. E.; Evenas, J.; Drakenberg, T.; Waltho, J. P.; Thulin, E.; Forsen, S. *Nature Struct. Biol.* **1995**, *2*, 777–783.
369. Kuboniwa, H.; Tjandra, N.; Grzesiek, S.; Ren, H.; Klee, C. B.; Bax, A. *Nature Struct. Biol.* **1995**, *2*, 768–776.
370. Masino, L.; Martin, S. R.; Bayley, P. M. *Prot. Sci.* **2000**, *9*, 1519–1529.
371. Doyle, D. A.; Cabral, J. M.; Pfuetzner, R. A.; Kuo, A.; Gulbis, J. M.; Cohen, S. L.; Chait, B. T.; MacKinnon, R. *Science*, **1998**, *280*, 69–77.
372. Crouzy, S.; Bernèche, S.; Roux, B. *J. Gen. Physiol*. **2001**, *118*, 207–217.
373. Guidoni, L.; Carloni, P. *J. Recept. Signal Transduct*. **2002**, *22*, 315–331.
374. Luzhkov, V. B.; Österberg, F.; Åqvist, J. *FEBS Lett*. **2003**, *554*, 159–164.